AFRL-VS-HA-TR-98-0046   SAIC-98/3012

REGIONAL ATTENUATION AT PIDC STATIONS AND THE TRANSPORTABILITY OF THE *S/P* DISCRIMINANT

Richard D. Jenkins
Thomas J. Sereno
Douglas A. Brumbaugh

Science Applications International Corporation
10260 Campus Point Drive
San Diego, CA 92121-1578

31 March 1998

Final Report
8 June 1995 - 31 March 1998

Approved for public release; distribution unlimited

DEPARTMENT OF ENERGY
Office of Non-Proliferation
    and National Security
WASHINGTON, DC 20585

AIR FORCE RESEARCH LABORATORY
Space Vehicles Directorate
29 Randolph Road
AIR FORCE MATERIEL COMMAND
HANSCOM AFB, MA 01731-3010

SPONSORED BY
Department of Energy
Office of Non-Proliferation and National Security

MONITORED BY
Air Force Research Laboratory
CONTRACT No. F19628-95-C-0097

KATHARINE KADINSKY-CADE
Contract Manager

CHARLES P. PIKE, Deputy Director
Integration and Operations Division

REPORT DOCUMENTATION PAGE	Form Approved OMB No. 0704-0188

1. AGENCY USE ONLY (Leave blank)	2. REPORT DATE March 31, 1998	3. REPORT TYPE AND DATES COVERED Final Report 8 Jun 95 - 31 Mar 98

4. TITLE AND SUBTITLE	5. FUNDING NUMBERS
Regional Attenuation at PIDC Stations and the Transportability of the S/P Discriminant	F19628-95-C-0097 PE69120G PR DENN TA GM WU AO

6. AUTHOR(S)

Richard D. Jenkins, Thomas J. Sereno, and Douglas A. Brumbaugh

7. PERFORMING ORGANIZATION NAME(S) AND ADDRESS(ES) Science Applications International Corporation 10260 Campus Point Drive San Diego, CA 92121-1578	8. PERFORMING ORGANIZATION REPORT NUMBER SAIC-98/3012

9. SPONSORING/MONITORING AGENCY NAME(S) AND ADDRESS(ES) Air Force Research Laboratory 29 Randolph Road Hanscom AFB, MA 01731-3010 Contract Manager: Katharine Kadinsky-Cade/VSBS	10. SPONSORING/MONITORING AGENCY REPORT NUMBER AFRL-VS-HA-TR-98-0046

11. SUPPLEMENTARY NOTES

12a. DISTRIBUTION AVAILABILITY STATEMENT	12b. DISTRIBUTION CODE

13. ABSTRACT *(Maximum 200 words)*

Frequency-dependent regional-wave amplitudes for nine subnetworks of the pIDC in varying geologic and tectonic environments were inverted for source and attenuation models. These models were used to normalize and evaluate variants of the S/P regional discriminant (e.g., various frequency bands and regional phases) using a data set of earthquakes, presumed industrial explosions, and a few nuclear explosions from the Lop Nor test site. Path and source corrections derived from the models were effective at removing the distance and magnitude dependence of the S/P ratios. Several variants of the normalized S/P ratios were successful at separating nuclear explosions from earthquakes. In particular, low- to mid-frequency bands performed best. As expected, nuclear explosions are characterized by lower S/P ratios than earthquakes. However, the average S/P ratios are only slightly lower for industrial explosions than for earthquakes, and there is considerable overlap. Average "stable" and "tectonic" attenuation models were developed that are generally within one standard deviation of the region-specific models. Thus, the models and normalized S/P discriminant appear to be transportable to uncalibrated regions.

14. SUBJECT TERMS Keywords: Discrimination, Frequency-Dependent Attenuation, Regional Seismicity, Transportability, Regionalization, S/P Ratios, Source-Level Correction, Software Development	15. NUMBER OF PAGES 186
	16. PRICE CODE

17. SECURITY CLASSIFICATION OF REPORT Unclassified	18. SECURITY CLASSIFICATION OF THIS PAGE Unclassified	19. SECURITY CLASSIFICATION OF ABSTRACT Unclassified	20. LIMITATION OF ABSTRACT Unlimited

Table of Contents

Preceding Page Blank

1. Introduction

1.1 Objectives

Results from previous empirical studies indicate that variants of high-frequency *S/P* amplitude ratios are some of the most promising discriminants at regional distances. However, many of these studies are based on co-located earthquakes and explosions in limited geographic regions, and their results must be recalibrated for each new source region. Our objective is to develop and apply distance and source corrections for up to 10 stations in the primary seismic network of the prototype International Data Center (pIDC) to evaluate the transportability of *S/P* discriminants to uncalibrated regions. We will also examine the sensitivity of the discriminants to the accuracy of the attenuation models, and attempt to generalize them by geologic and tectonic environment.

1.2 Background

Several early studies proposed the use of *S/P* ratios as regional event discriminants for earthquakes and nuclear explosions [e.g., *Willis et al.*, 1963; *Blandford*, 1981; *Gupta and Burnetti*, 1981; *Nuttli*, 1981; *Pomeroy et al.*, 1982; *Murphy and Bennett*, 1982; *Bennett and Murphy*, 1986; *Taylor et al.*, 1989]. These studies found that *S/P* discriminants provide some separation between nuclear explosions and earthquakes, but that there is significant overlap between the two populations. More recent studies have exploited higher frequencies to improve the *S/P* discriminant and have extended the application to include industrial chemical explosions. For example, high-frequency (2-16 Hz) *S/P* ratios have been shown to be successful in discriminating between earthquakes and mining explosions in northern and central Europe [e.g., *Baumgardt and Young*, 1990; *Dysart and Pulli*, 1990; *Baumgardt et al.*, 1992; *Wuster*, 1993], and earthquakes and underground nuclear explosions in Eurasia [e.g., *Bennett et al.*, 1989; *Chan et al.*, 1990; *Bennett et al.*, 1992]. The practice of mining can also induce stress-release events such as rockbursts. Often these stress-release events are much larger than the actual mining explosions. *Bennett et al.* [1993] show that stress-release events in central Europe and South Africa have *S/P* ratios that are similar to earthquakes (> 1.0) across broad frequency bands, and these are higher than the ratios for underground nuclear explosions (< 1.0) at frequencies above 2 Hz. Most of these studies use co-located explosions and earthquakes to minimize propagation differences. A concern expressed in recent research is that propagation characteristics may have a significant effect on the *S/P* discriminant, and that transportability may be problematic [e.g,. *Lynnes and Baumstark*, 1991; *Bennett et al.*, 1992].

1.3 Outline of Report

The report is divided into eight sections and three appendices. Section 2 is an overview of our technical approach. Section 3 describes the data sets and how they were selected. Section 4 describes the data processing and our estimates of frequency-dependent amplitudes of regional phases. Section 5 discusses our regional-wave attenuation and

source models. Section 6 describes the application of the attenuation and source models to evaluate normalized *S/P* ratios as regional discriminants. Section 7 evaluates the transportability of the *S/P* discriminants to uncalibrated regions. Section 8 contains the primary conclusions of this study.

Many of the details are provided in the three appendices. Appendix A shows maps with ray paths for all regional arrivals used in this study. Attenuation and source models derived from the regional-wave amplitudes are presented in Appendix B. Finally, Appendix C provides validation of our distance corrections along with histograms of normalized *S/P* ratios for several frequency bands for earthquakes, presumed industrial explosions, and a few nuclear explosions.

2. Technical Approach

The pIDC data set is summarized in Section 2.1. Our parameterization of regional-wave amplitudes is summarized in Section 2.2. The software that we used for measuring frequency-dependent amplitudes and inverting them for source and attenuation models is summarized in Section 2.3. Lastly, our approach for evaluating *S/P* discriminants is summarized in Section 2.4.

2.1 Prototype International Data Center (pIDC)

This study used regional waveform data collected at the pIDC for a global network of more than 130 stations during the Group of Scientific Experts Third Technical Test called GSETT-3 (for an overview of GSETT-3, see *Kerr* [1993]). The waveform data and analyst-reviewed event bulletins produced at the pIDC were provided to us by the Center for Monitoring Research (CMR) located in Rosslyn, Virginia.

The pIDC acquires waveform data from each station and performs automatic processing to detect and characterize signals and form preliminary event hypotheses. These event hypotheses are reviewed by an analyst. Events that are confirmed by an analyst and their associated arrivals form what is called the Reviewed Event Bulletin (REB). Events in the REB must satisfy conformation criteria specified by the pIDC. These criteria can include, for example, the minimum number of stations that must record an event.

Our study used events in the REB from September 1, 1995 to September 1, 1996. There were just under 24,000 events in the REB in this time period. However, we applied distance and depth constraints in the event selection criteria for this study. First, we only used events whose depth in the REB was ≤33 km. However, some of these events may be deeper than 33 km because depths in the REB are constrained to the earth surface if they cannot be determined by the available data. Next, we only considered events that were within 20° (i.e., regional distance) of at least one station in the pIDC primary seismic network. Approximately 6,700 events in the REB satisfied these constraints, and they formed the basis for this study.

2.2 Parameterization of Regional-Wave Amplitudes

We used the method of estimating source and attenuation models developed by *Sereno* [1990]. Briefly, the frequency-dependent (either time-domain or spectral) amplitude of the kth wave recorded at the ith station from the jth source is parameterized as:

$$\log A_{ijk}(f) = \log A^0_{jk}(f) + B_k(\Delta_{ij}, \Delta_0, f) + \delta_{ik} \tag{1}$$

where $A^0_{jk}(f)$ is the amplitude at a reference distance Δ_0, $B_k(\Delta_{ij}, \Delta_0, f)$ is the attenuation from the reference distance to the epicentral distance Δ_{ij}, and δ_{ik} is a station correction. The reference distance was chosen at a distance where geometrical spreading changes from

3

spherical to a more complicated function based upon the regional phase analyzed. The amplitude at the reference distance is expressed as:

$$\log A_{jk}^0(f) = \log S_{0j} + \log s_j(f) + \log \kappa_k + \gamma_k \log f - \log e \cdot \alpha_k^0 \cdot f \tag{2}$$

where S_{0j} is the long-period level (proportional to seismic moment), $s_j(f)$ is the shape of the source spectrum, κ_k is a wave-dependent excitation factor, and γ_k accounts for different pulse shapes of crustal and upper mantle phases at the reference distance. For example, if the reference distance is near the critical distance, then Pn and Sn can be approximated as head waves at Δ_0 and their pulse shapes are integrals of the direct or turning waves [e.g., *Aki and Richards*, 1980]. Therefore γ_k is set to -1 for Pn and Sn and 0 for Pg and Lg. The last term in (2) describes the total attenuation between the source and reference distance.

The source spectrum is assumed to decay as f^{-2} beyond a corner frequency that scales inversely with the cube root of the long-period level. The following model is used to parameterize the shape of the source function, $s_j(f)$:

$$s(f) = \frac{f_c^2}{(f_c^4 + (1 - 2\beta)f_c^2 f^2 + \beta^2 f^4)^{1/2}} \tag{3}$$

$$f_c = \frac{c}{S_0^{1/3}} \tag{4}$$

where f_c is the corner frequency, c is a scaling parameter that relates corner frequency to long-period source level for all events in the data set, and β determines the shape of the spectrum near the corner frequency [*Mueller and Murphy*, 1971]. This model was used by *Sereno* [1990] to represent mining explosions in Scandinavia. We use this model for earthquakes or explosions. The value of β was selected to provide a generic set of source curves with f^{-2} decay and cube root corner frequency scaling. Figure 1 shows a family of these curves for $\beta = 0.6$ which is the value that we used in our study.

The total attenuation from the reference distance to the epicentral distance is parameterized in terms of a power-law distance dependence with a frequency-dependent exponent:

$$B_k(\Delta_{ij}, \Delta_0, f) = n_k(f) \cdot \log(\Delta_0 / \Delta_{ij}) \tag{5}$$

$$n_k(f) = a_k f + b_k \tag{6}$$

The total attenuation includes geometrical spreading, scattering and anelasticity. It is difficult to separate these terms since the geometrical spreading of regional phases is a complicated function of the crustal and upper mantle velocity structure [e.g., *Sereno and Given*, 1990]. Fortunately, it is not important to separate these terms for application to the *S/P* discriminant.

The system of equations governing the relationship between the data (log amplitudes) and model parameters is formulated by subtracting theoretical data computed from an assumed

Source Spectra
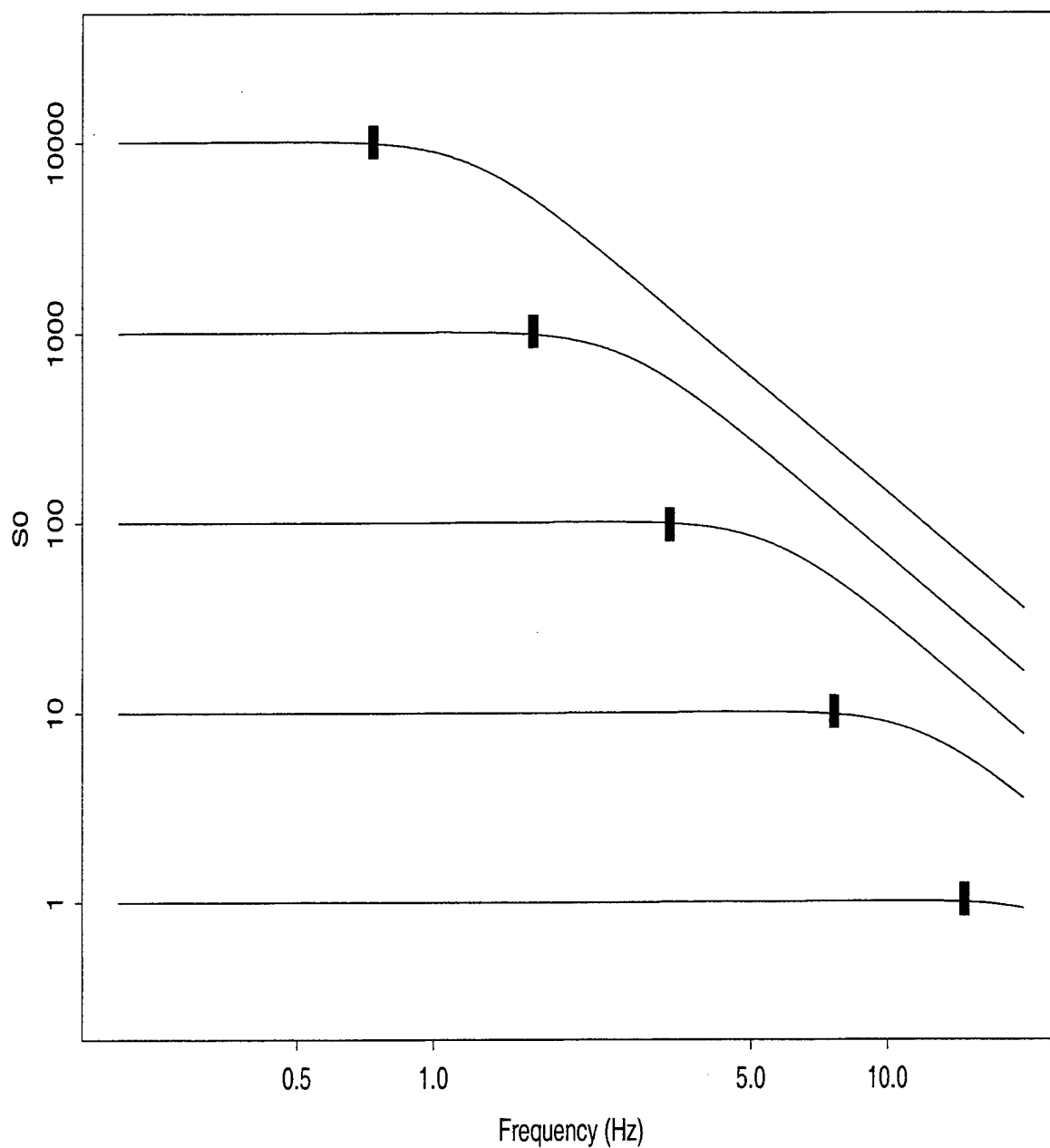
Figure 1. This shows a family of source spectra as a function of source level based on Eq (3) and (4). Vertical bars denote approximate corner frequencies.

starting model from the observed data, and solving iteratively for the model perturbations that minimize the data residuals in the least-squares sense.

2.3 Software for Amplitude Measurements and Inversion

We used two software programs in conjunction with a centralized Data Management System (DMS) as shown in Figure 2 to estimate frequency-dependent amplitudes and invert them for source and attenuation parameters. The first program called DFX (Detection and Feature eXtraction) was developed for the pIDC to perform seismic signal detection and feature extraction [*Wahl*, 1996]. It was used to compute regional-wave amplitudes in the time- and frequency-domains. DFX can be configured to compute amplitudes from beams or single channels and a variety of filter choices are available. The spectra can be computed from a single channel or they can be array-averaged. AmpInv is a new program that we developed under this contract to read the regional-wave amplitudes from the DMS and invert them for source and attenuation parameters. AmpInv also has options to generate synthetic data sets for testing purposes. The AmpInv User's Guide describes all of the program options in detail [*Jenkins*, 1998].
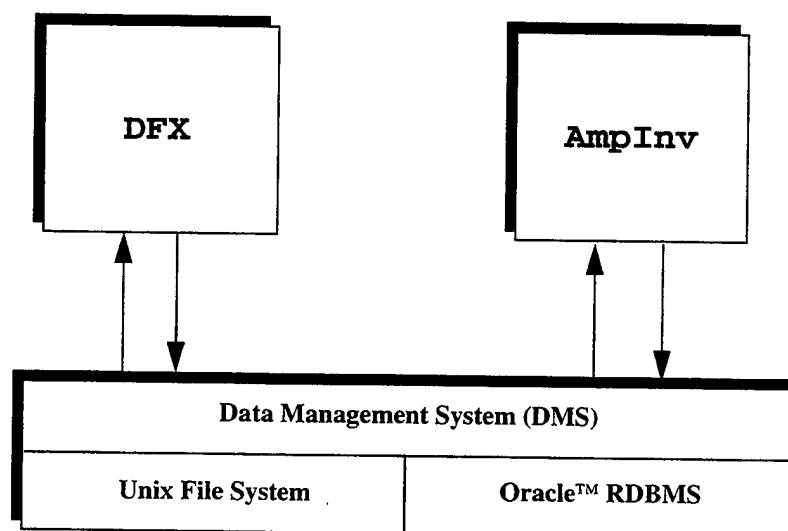
Figure 2. DFX and AmpInv are the two major software components for this project. Both programs interface with the pIDC Data Management System.

2.4 Discrimination

The regional discriminants used in this study are based on the regional phases *Pn*, *Pg*, *Sn*, and *Lg* as defined in the REB. That is, we only considered phases that were confirmed by a pIDC analyst to be associated with an event at a regional distance. We normalized the *S/P* amplitude ratio by applying both distance and source corrections. Cross-spectral ratios

such as *Lg*(0.5-1 Hz)/*Pn*(2-4 Hz) required normalization for the source corner frequency [e.g., *Taylor and Hartse*, 1998]. We examined normalized *S/P* amplitude ratios using a variety of frequency bands subject to the constraint that the *P*-wave frequency is greater than or equal to the *S*-wave frequency. Three types of amplitude ratios are evaluated: *Lg/Pn*, *Sn/Pn*, and Largest *S* / Earliest *P*. Results were compared for earthquakes, presumed industrial explosions and a few nuclear explosions.

3. Data Sets

This section describes the data sets for our attenuation and discrimination studies. We searched the REB for events and their associated arrivals based on the depth and distance criteria summarized in Section 2.1 to support our attenuation study. Waveform data were retrieved from stations in the pIDC primary and auxiliary seismic networks. We augmented the data sets with nuclear explosions and presumed industrial explosions. The nuclear explosions were not used to construct the attenuation models, but they were used to evaluate the effectiveness of the *S/P* discriminant.

In general, we will not have *ground-truth* information for most of the events. Instead, we will rely on knowledge of the local natural and industrial seismicity to qualitatively evaluate the effectiveness of the *S/P* discriminant.

3.1 Station Selection

The pIDC acquired data from 46 primary and 87 auxiliary stations during the time period examined for this study. As shown in Figure 3, the primary stations are distributed globally. The data from the primary network are sent continuously to the pIDC where they are processed and analyzed. Auxiliary stations expand the coverage of the primary network, but these stations are used by the pIDC only when data are requested to improve the location solutions for events defined by the primary network. We select stations from the pIDC primary and auxiliary networks to form subnetworks of multiple stations in close proximity. This allows events recorded by multiple stations at regional distances to be available for the attenuation study. We also selected stations based on tectonic regionalization and the availability of analyst-verified regional phases in the REB.

3.1.1 Subnetworks

Most primary stations have other primary and auxiliary stations in close proximity. We grouped stations into subnetworks if they are within 40° of each other (we use 20° as an upper limit for a regional event). A subnetwork can be comprised of both primary and auxiliary stations. Some pIDC stations may not be included because they do not have a sufficient number of regional phases in the REB. Using these criteria, we defined the eleven subnetworks shown in Figure 3. Unfortunately, we could not develop attenuation models for the Thailand region since only one IMS station is available (multiple stations are needed to resolve source and path contributions to the amplitudes). This reduced the number of subnetworks used in this study to ten.

3.1.2 Tectonic Regionalization

Eight tectonic regions based on a 2° by 2° grid are defined by *O. Gudmundsson* of the Australian National University [personal communication]. His regionalization is shown in Figure 4 and includes the following regions: Young Ocean (< 25 Ma), Intermediate Ocean (25-100 Ma), Old Ocean (> 100 Ma), Tectonic, Cenozoic Continental, Paleozoic and Mesozoic (150-800 Ma), Proterozoic (800-1700 Ma), and Archean (> 1700 Ma). The Young, Intermediate, and Old Ocean categories represent the age of the ocean floor. The Tectonic category represents young and active regions. The Cenozoic Continental,
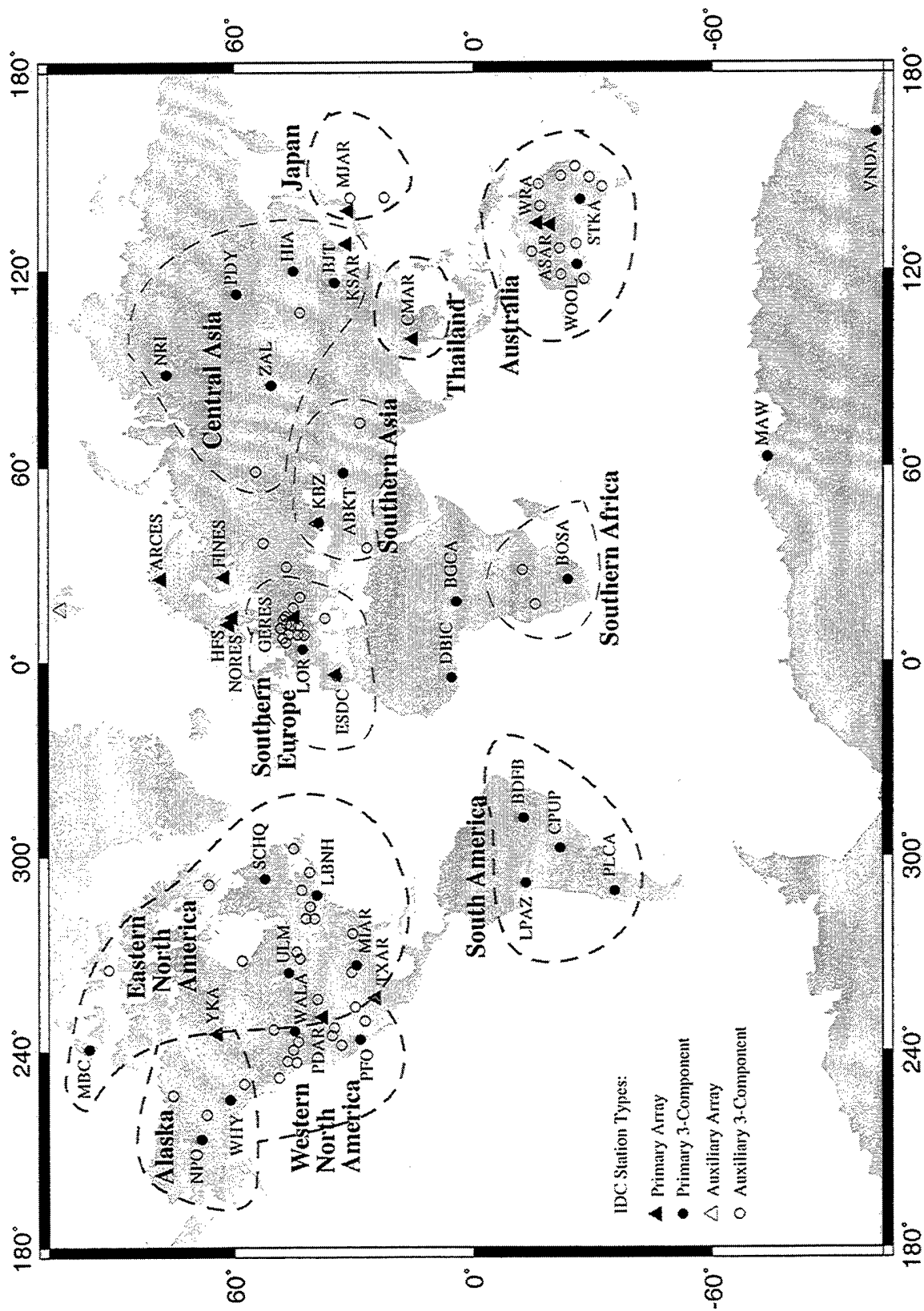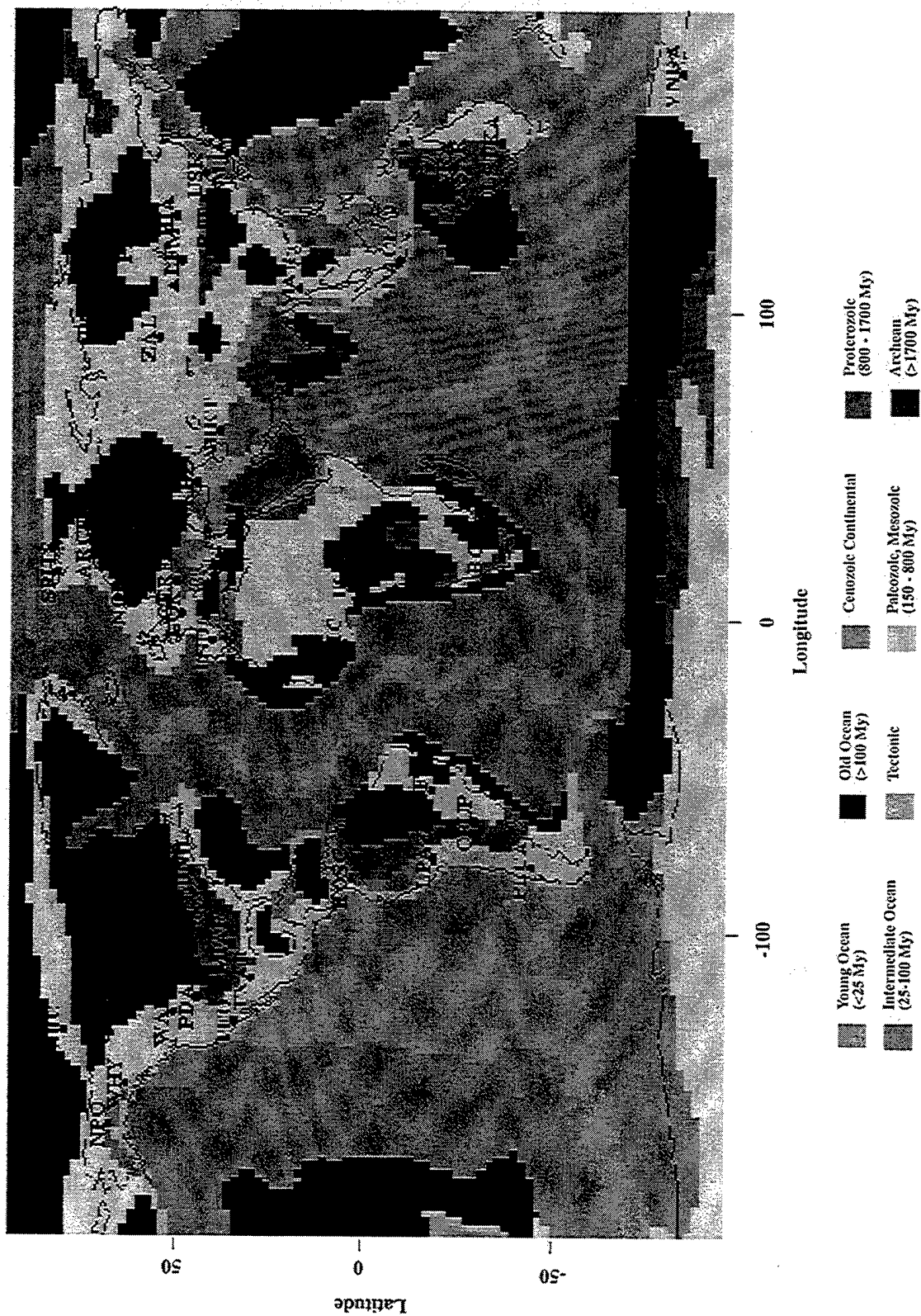
Figure 3. Map of subnetworks defined for this study. The pIDC "primary" stations are labeled.

IDC Station Types:
- ▲ Primary Array
- ● Primary 3-Component
- △ Auxilliary Array
- ○ Auxilliary 3-Component

Alaska
Eastern North America
Western North America
South America
Southern Europe
Southern Asia
Central Asia
Japan
Thailand
Australia
Southern Africa

MBC, NPO, WHY, YKA, SCHQ, ULM, LBNH, WALA, PDAR, PFO, TXAR, MIAR

BDFB, CPUP, PLCA, LPAZ

HFS, NORES, ARCES, FINES, GERES, LOR, ESDC, KBZ, ABKT, DBIC, BGCA, BOSA

NRI, ZAL, PDY, HIA, KSAR, BJT, MJAR, CMAR

WRA, ASAR, WOOL, STKA, MAW, VNDA

Figure 4. Tectonic regionalization map showing locations of pIDC primary stations. This tectonic map is based on a 2° by 2° grid provided by O. *Gudmundsson* of the Australian National University [personal communication].

Paleozoic and Mesozoic, Proterozoic, and Archean represent young to old relatively stable continental environments. Overlaid on Figure 4 is the distribution of pIDC primary stations in the various geologic and tectonic environments. Note that some station locations fall on the boundary of adjacent environments. For this reason, azimuthal constraints must be applied to arrivals when forming data sets for some subnetworks. For the purposes of this study, we combine Cenozoic Continental, Paleozoic and Mesozoic, Proterozoic, and Archean into a single "stable" category and consider this and "tectonic" as our only categories of interest.

3.2 Event Selection for Attenuation

The data set for our attenuation study is based on events in the REB occurring between September 1, 1995 through September 1, 1996. We only use arrivals that were verified by a pIDC analyst. It is difficult for our automated software to screen arrivals otherwise. The review process provided by the analyst provides the necessary level of quality control that is difficult to perform automatically.

We limited our data sets to Pn, Pg, Sn, and Lg phases from events ≤ 33 km depth. We further constrained these phases by distance. Pn and Sn were limited to $15°$ or less. Lg was limited to $20°$; and Pg was limited to $6°$. This reduced the maximum number of events in our data set to approximately 3,280. Table 1 lists each subnetwork name, its tectonic region, its component stations, and the number of phases and events used in our attenuation data set. Each subnetwork includes between 2 and 19 stations, and is declared to be in a stable or tectonic region based on the map in Figure 4. This data set was input into AmpInv where snr constraints were then applied. The snr of arrivals were required to be above a threshold or else they were not used in the inversion. The events listed in Table 1 range in magnitude from m_L 1.8 to m_L 6.0 as reported in the REB. Most events are presumed to be earthquakes, and some are presumed to be industrial explosions.

Table 1: Subnetworks of pIDC Primary and Auxiliary Stations.

SubNetwork	Tectonic Name	Stations	Pn	Pg	Sn	Lg	Number of Events
Alaska/NW Canada	Tectonic	DAWY, DLBC, INK, NPO, WHY, YKA	505	80	210	246	211
Western North America	Tectonic	ALQ, BBB, DUG, EDM, ELK, MNV, NEW, PDAR, PFO, PGC, PMB, PNT, RSSD, TUC, TXAR, WALA	819	125	158	386	285
Southern Europe	Tectonic	APL, AQU, BFO, BRG, BUG, CLL, CLZ, ESDC, FUR, GERES, GRFO, HGN, LOR, MOX, PAB, PSZ, TNS, VRAC	1316	666	444	1092	502
Southern Asia	Tectonic	ABKT, BGIO, KBZ, KVAR, NIL	91	7	26	17	75
Japan	Tectonic	MJAR, OGS, TSK	819	41	308	70	564
South America	Tectonic	CPUP, LPAZ, PLCA	62	1	15	4	48

Table 1: Subnetworks of pIDC Primary and Auxiliary Stations.

SubNetwork	Tectonic Name	Stations	Pn	Pg	Sn	Lg	Number of Events
Eastern North America	Stable	ALQ, EDM, EEO, GAC, LBNH, LMN, LMQ, MIAR, PDAR, RSSD, SADO, SCHQ, TBO, TKL, TUL, TXAR, ULM, WALA, YKA	262	36	66	201	100
Central Asia	Stable	ARU, BJT, NRI, PDY, ULN, ZAL	53	11	23	49	38
Australia	Stable	ARMA, ASAR, CTA, FORT, MEEK, QIS, RMQ, STKA, TOO, WARB, WOOL, WRA	323	33	203	157	107
Southern Africa	Stable	BOSA, TSUM	41	34	6	41	41
TOTAL			4291	1034	1459	2263	1971

The coverage provided by the arrivals summarized in Table 1 is plotted as ray paths on maps in Appendix A for each subnetwork. An example is provided in Figure 5 which shows the ray paths for the Alaska subnetwork.

The coverage for Alaska, Australia, eastern and western North America, and southern Europe is extremely good for all regional phases. However, there was not a sufficient amount of data to estimate the attenuation in southern Africa. Therefore, the remainder of this report is based on the other nine subnetworks in Table 1. The South American data set is also sparse. However, we were able to obtain a stable estimate of the Pn attenuation in this region. The coverage for southern Asia is good for Pn, marginal for Sn, and poor for the crustal phases Pg and Lg. Stations ABKT, KBZ, and KVAR provide most of the data in this region. The coverage for central Asia is good for Pn and Lg, marginal for Sn, and poor for Pg. The coverage for Japan is good for Pn and Sn, but Pg and Lg are limited to short distances.

3.3 Event Selection for Discrimination

Our discrimination data set includes earthquakes, presumed industrial explosions (e.g., mining events) and known nuclear explosions. We used events in the REB recorded between September 1, 1995 and September 1, 1996 to build our data set. The same phase-dependent distance limitations, and depth and azimuthal constraints applied during formation of the attenuation data set were applied here. We augmented this with four known nuclear explosions from May and August, 1995, and July and August, 1996.

The events listed in the REB are not identified as earthquakes, industrial or nuclear explosions. Therefore, we apply contextual information along with the previous work of others to form our data sets.
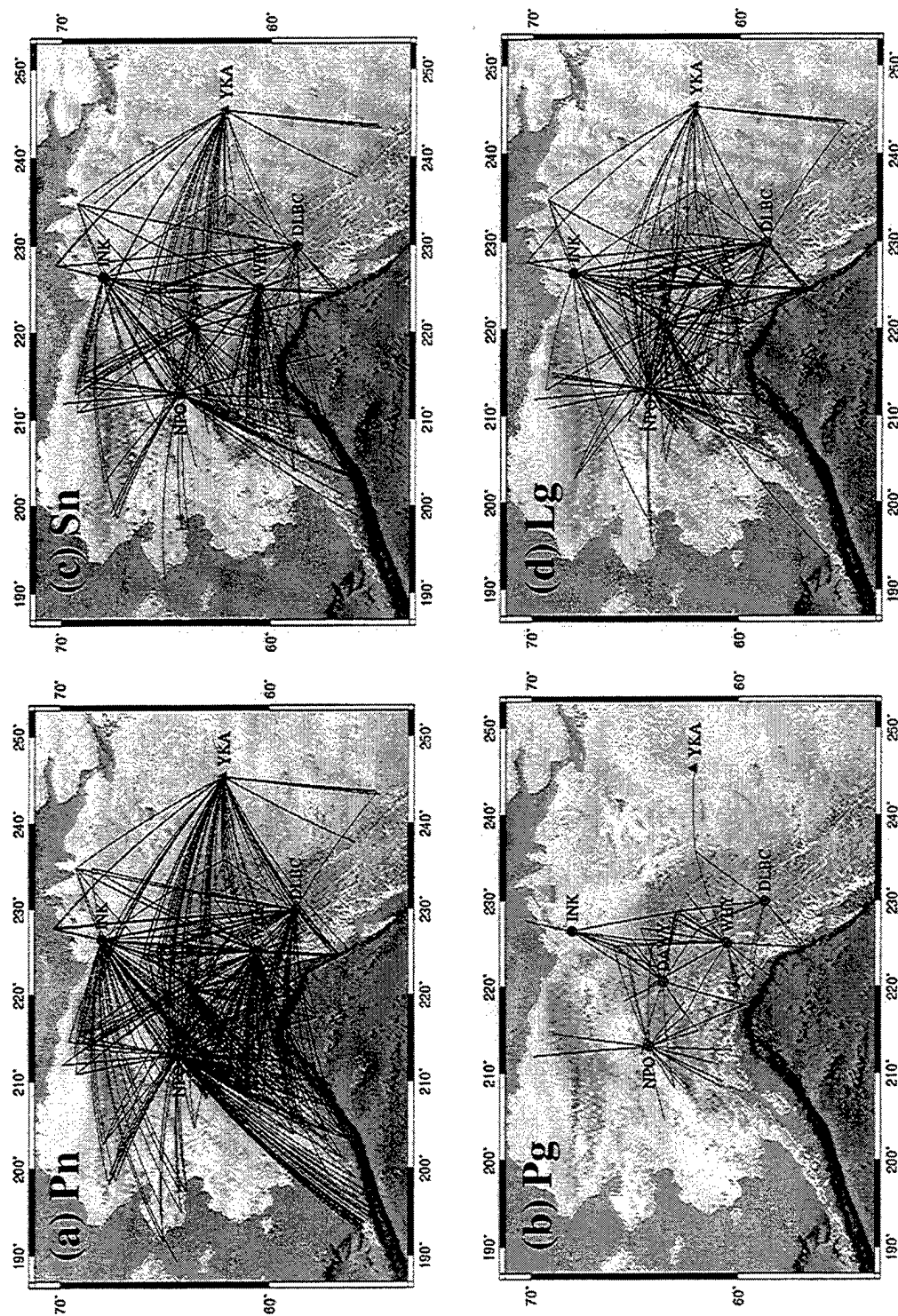
Figure 5. Ray paths of regional arrivals used for Alaska. a) 505 *Pn*. b) 80 *Pg*, c) 210 *Sn*, and d) 246 *Lg* arrivals.

13

3.3.1 Earthquakes

There were approximately 6,700 regional events available in our data set (see Section 2.1). Approximately 4,700 of these events are presumed to be earthquakes within 20° from stations in our subnetworks. For our discrimination study, we presumed all events in seismically-active regions that were not characterized as probable industrial explosions or nuclear explosions (see Section 3.3.2 and Section 3.3.3) are earthquakes. The magnitude and origin time distribution of these events is shown in Figure 6, and the epicenters are shown on a map in Figure 7. These events are presumed to be earthquakes because they occur in seismically-active regions and their magnitudes and origin times are consistent with the expected distributions. That is, the number of events as a function of magnitude is consistent with earthquake recurrence models, and the origin times are random with respect to day-of-the-week and local time-of-day.

3.3.2 Industrial Explosions

We presumed events in the REB to be industrial (or mining) explosions on the basis of location, origin time, and magnitude. Events from active mines are expected to be tightly clustered in their location (e.g., numerous events from a small epicentral region). The origin time of mining events is expected to be clustered by day-of-week and time-of-day, consistent with a normal work schedule. Finally, magnitudes are expected to span a limited range, unlike the typical recurrence models for earthquakes.

For location clustering, we counted the number of regional events in the REB recorded between September 1, 1995 and September 1, 1996 in 1° latitude by 1° longitude grid cells. If the number of events in a given grid cell exceeded a user-defined threshold (which varied by subnetwork, but typically was set to 10 events per grid cell) and the grid cell was located in an area with low natural seismicity, then this group was identified as a potential source of industrial explosions.

The origin times of the events were used to determine the day-of-week and local time-of-day. Histograms of these parameters were visually inspected for non-random distributions indicative of a cultural source. For example, if the events typically occurred on weekdays between mid-morning and mid-afternoon (local time) in a region of historically low seismicity, then that grid cell was classified as a potential area for industrial explosions.

The results of this procedure for the 52° N latitude by 14° E longitude grid cell located in southern Europe are shown in Figure 8. Here we found 29 events in the grid cell. None of the events occurred on Saturday or Sunday. Furthermore, the time-of-day distribution was limited to a small range between late-morning and early-afternoon. The magnitudes for these events spanned a limited range below m_L 4.0. Therefore, we have identified all of the events in this grid cell to be presumed industrial explosions. The results presented for this grid cell are typical of those found in other grid cells containing presumed industrial explosions.

Using this technique, we identified potential industrial explosion areas in northeastern Wyoming, southwestern New Mexico, West Virginia, southeastern British Columbia, northeastern Queensland, South Australia, south-central Spain, and a vast mining district extending from Germany to Czechoslovakia and Poland (just north of the GERESS array).

(a) Magnitude

m_b

(b) Day of Week
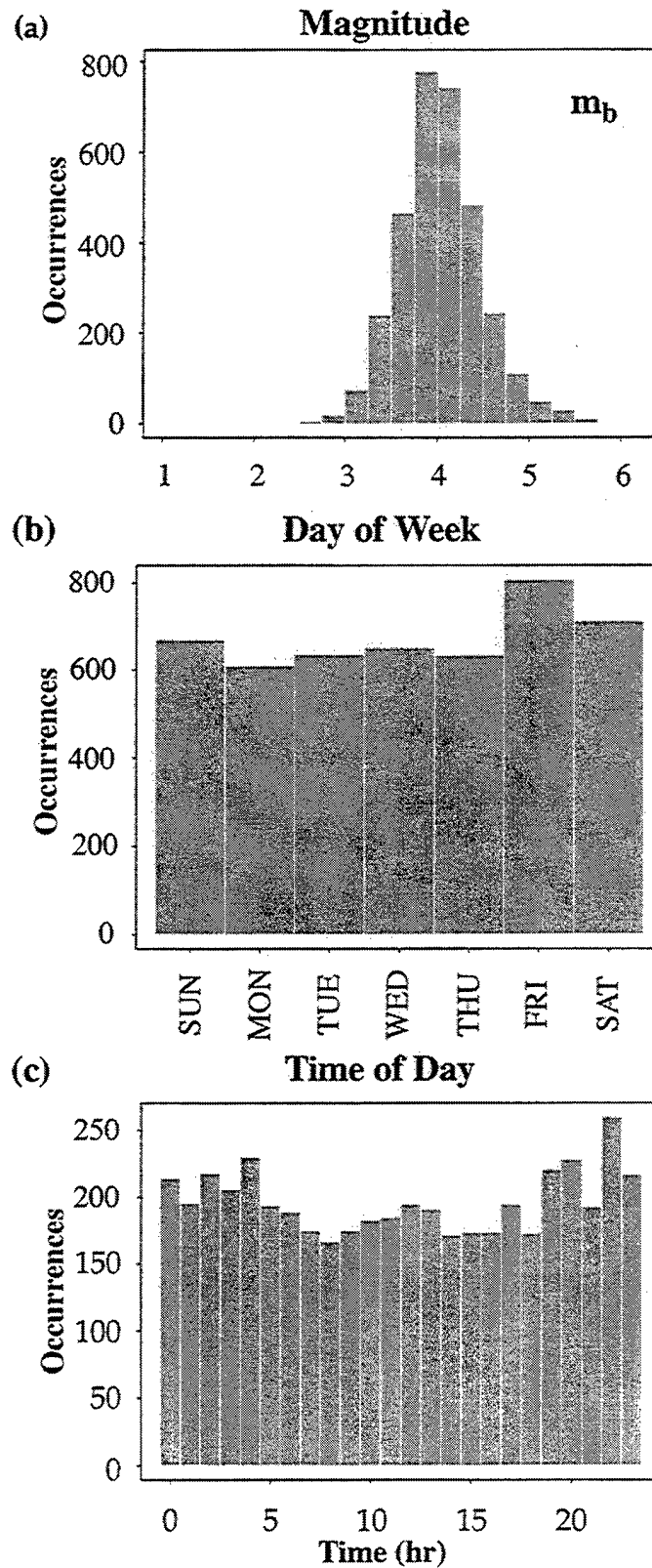
(c) Time of Day

Figure 6. Distributions of presumed earthquakes in our discrimination data set. (a) magnitude distribution, (b) day-of-the-week distribution, and (c) local time-of-day distribution.
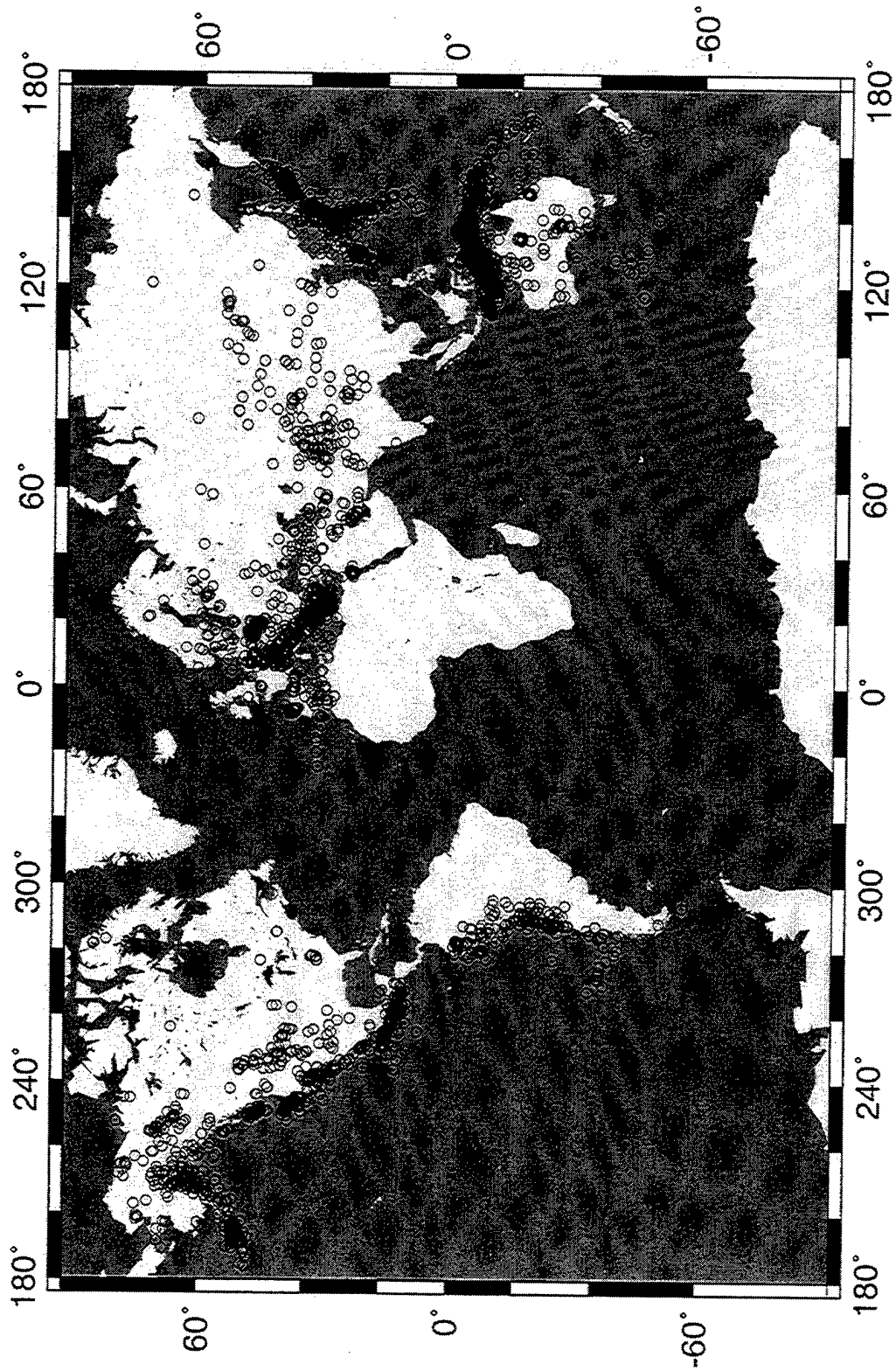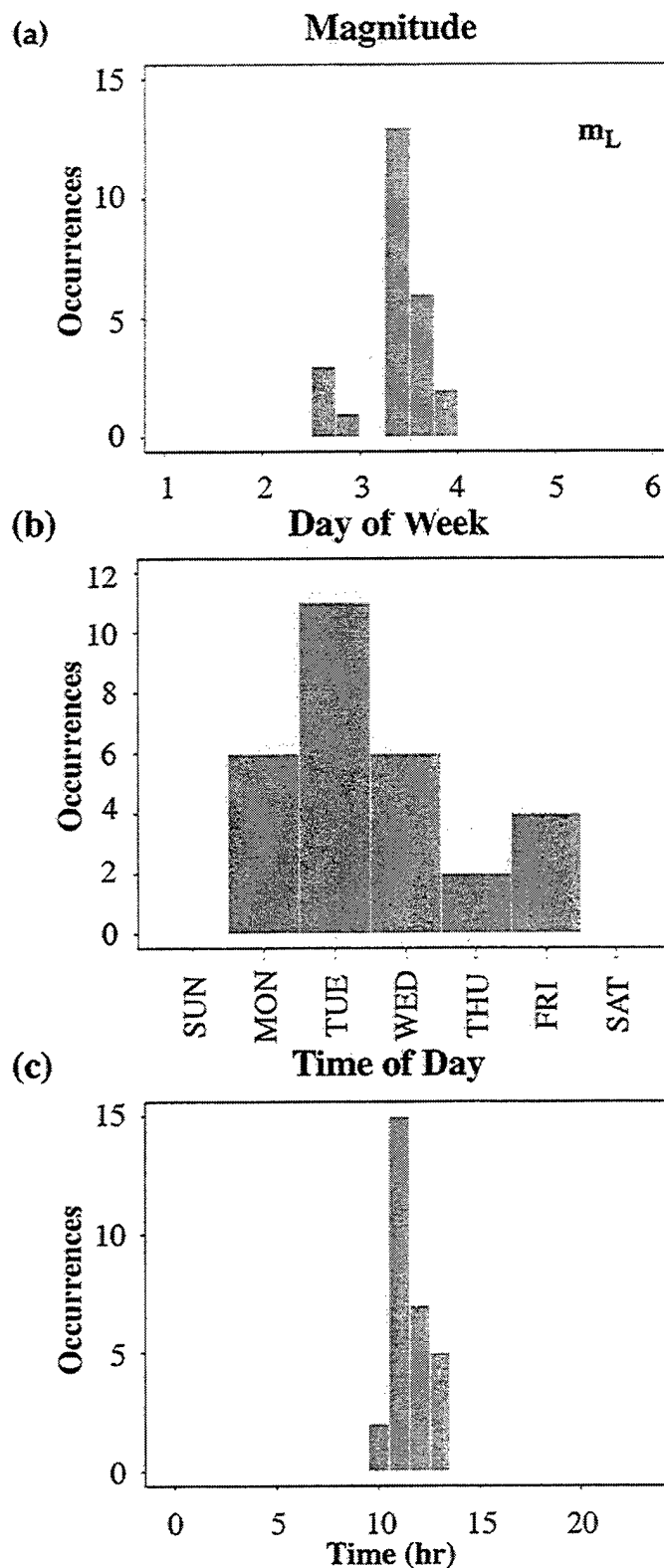
Figure 7. The locations of 4725 presumed earthquakes used to evaluate S/P discriminants are plotted. We only plot those events within 20° of stations in our subnetworks.

Figure 8. Magnitude distribution and origin time distributions of presumed industrial explosions for the (52° N, 14° E) grid cell located in southern Europe. Distribution by (a) magnitude, (b) day-of-week, and (c) local time-of-day. A total of 29 events were found in this grid cell.

We were able to confirm that the three regions in the United States were indeed active mining regions by comparing the location of the grid cells with areas of known mining activity as reported by the USGS in their internet pages (http:// earthquake.usgs.gov/neis/mineblast/). In addition, a few events in southwestern Wyoming were added to the list of presumed industrial explosions since they had locations that placed them in active mining regions as classified by the USGS, and they satisfied the day-of-week and time-of-day requirements. Unfortunately, we are unable to obtain independent confirmation that the remainder of the areas are indeed active mining regions.

Three events in central Russia were also added to the list of presumed industrial explosions by comparing the locations of large blasts ($m_b > 3.5$) in the Kuzbass mining region, acquired from *Khalturin et al.,* 1996, with the locations of events in our data set.

Based on this procedure, 60 events in North America, 14 in Australia, 317 in southern Europe, and 3 in Asia are presumed to be industrial explosions. These events have an approximate median magnitude of 3.25 m_L. The magnitude distribution and locations of our presumed industrial explosions are plotted in Figure 9. These events will be used to evaluate the *S/P* discriminant in eastern and western North America, Australia, southern Europe, and central Asia subnetworks.

3.3.3 Nuclear Explosions

We also included four Lop Nor nuclear explosions in our data set. These events were confirmed to be nuclear explosions as referenced by previous authors [*Hartse et al.,* 1997; *Yang et al.,* 1997]. The REB event solutions and recording stations within a regional distance from these nuclear events are shown in Table 2. At some stations, the pIDC analyst only found one regional arrival acceptable for association for these events. For example, only a *Pn* arrival was associated at the Nilore, Pakistan (NIL) station for the July 29, 1996 Lop Nor event. The location of these events is shown on a map represented by star symbols in Figure 9.

Table 2: Nuclear Explosion Event Solutions.

m_b	Latitude	Longitude	Origin Time	Recording Stations	Distance (km)
5.73	41.6305	88.8701	05/15/95 04:06:00	ULN	1593
5.54	41.5965	88.8575	08/17/95 00:59:59	ULN	1596
5.69	41.6455	88.7641	06/08/96 02:55:59	NIL	1628
4.71	41.6921	88.3534	07/29/96 01:48:59	ZAL, NIL	1353

Presumed Industrial Explosions
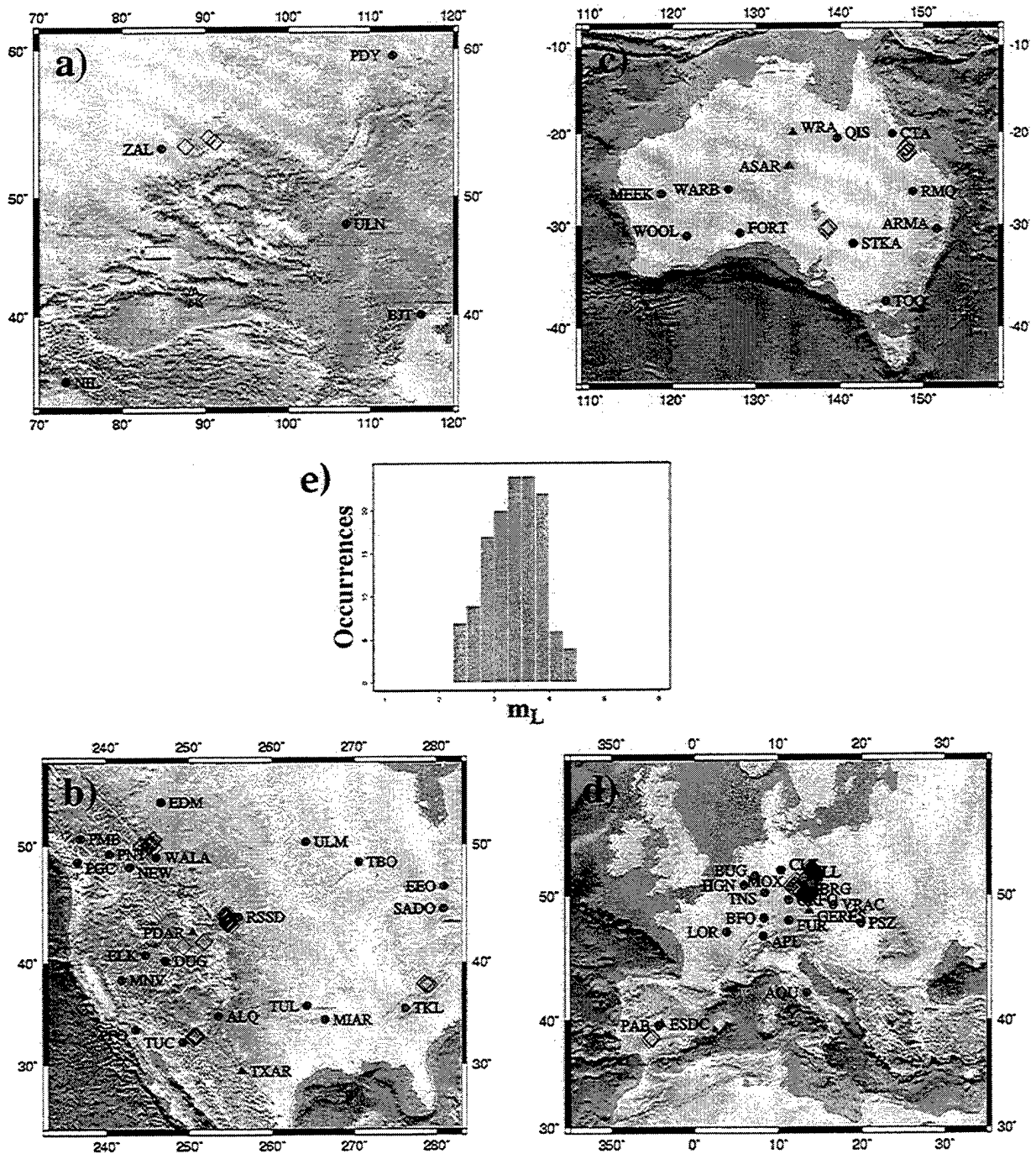
Figure 9. Maps showing the locations of presumed industrial explosions (diamonds) and known nuclear explosions (stars) for the (a) central Asia, (b) western and eastern North America, (c) Australia, and (d) southern Europe subnetworks. (e) The magnitude distribution for all presumed industrial explosions.

4. Data Processing

We use frequency-dependent amplitudes as the basis for our attenuation study. All amplitude measurements were made automatically using the DFX software. In this section we describe and evaluate various types of temporal and spectral amplitude measures and determine a preferred amplitude type to use in estimating attenuation.

4.1 Amplitude Measurements

We measured six different time-domain amplitudes and computed amplitude spectra for each arrival in our data set. All measurements were based on vertical components. Three types of time-domain measurements were made: root mean-square (*rms*), short-term average (*stav*), and average absolute amplitude in the time window after removing the *rms* (*abs*). These types were made on both coherent (i.e., stack then filter) and incoherent (i.e., filter, rectify, and stack) beams. All time-domain measurements were made using up to eight one-octave wide overlapping frequency bands beginning with 0.5 to 1.0 Hz and extending to 8.0 to 16.0 Hz when supported by the instrument. Fourier amplitude spectra were also computed for each arrival. These spectra were array-averaged for array stations. All amplitude measures were corrected for the instrument response. For time-domain amplitudes the instrument correction was applied for the center of the one-octave wide frequency band.

The time window started 0.3 s before the observed arrival time and had a duration of 10 s for *Pn*, *Pg*, and *Sn* arrivals. The window was reduced to 5 s when the epicentral distance was less than 3.5 degrees. A group velocity window between 3.0 km/s and 3.6 km/s was used for the *Lg* arrival. Noise amplitudes were measured for each arrival using a 5.0-s window beginning 5.5 s before the signal. Measurements were also made using theoretical arrival times for regional phases that were not associated by a pIDC analyst. However, we required that at least one of the phases (*Pn*, *Pg*, *Sn*, or *Lg*) must have been associated. Theoretical arrival times were determined using the REB location solution and the IASPEI travel-time model [*Kennett,* 1991].

A sample waveform from the Charters Towers station in Australia (CTA) is shown in Figure 10. The m_L 3.5 event is from a local mining region approximately 3 degrees away. The top waveform is unfiltered followed by filtered waveforms in six frequency bands used for this study (the two highest frequency bands were outside the passband of the instrument for this station). Each waveform shows the pIDC arrival times for the four regional phases, *Pn*, *Pg*, *Sn*, and *Lg*. We also display the spectrum for the *Pn* arrival for this event in Figure 10. The raw signal and noise spectra are shown overlaid by smoothed curves.

4.2 Evaluation

4.2.1 Coherent and Incoherent Beams

We compare the log *rms* amplitudes for coherent and incoherent beams for *Pn* arrivals in our Australian data set in Figure 11. The coherent beams were steered using the theoretical
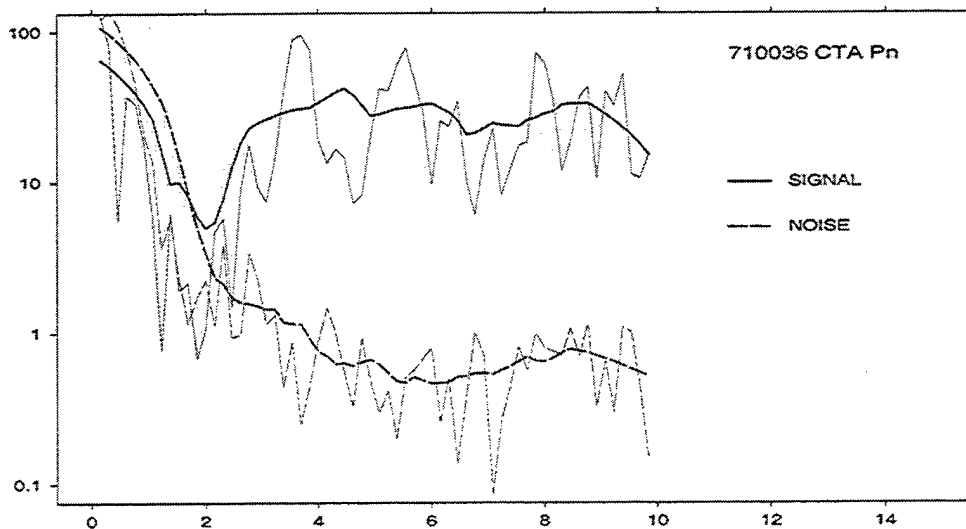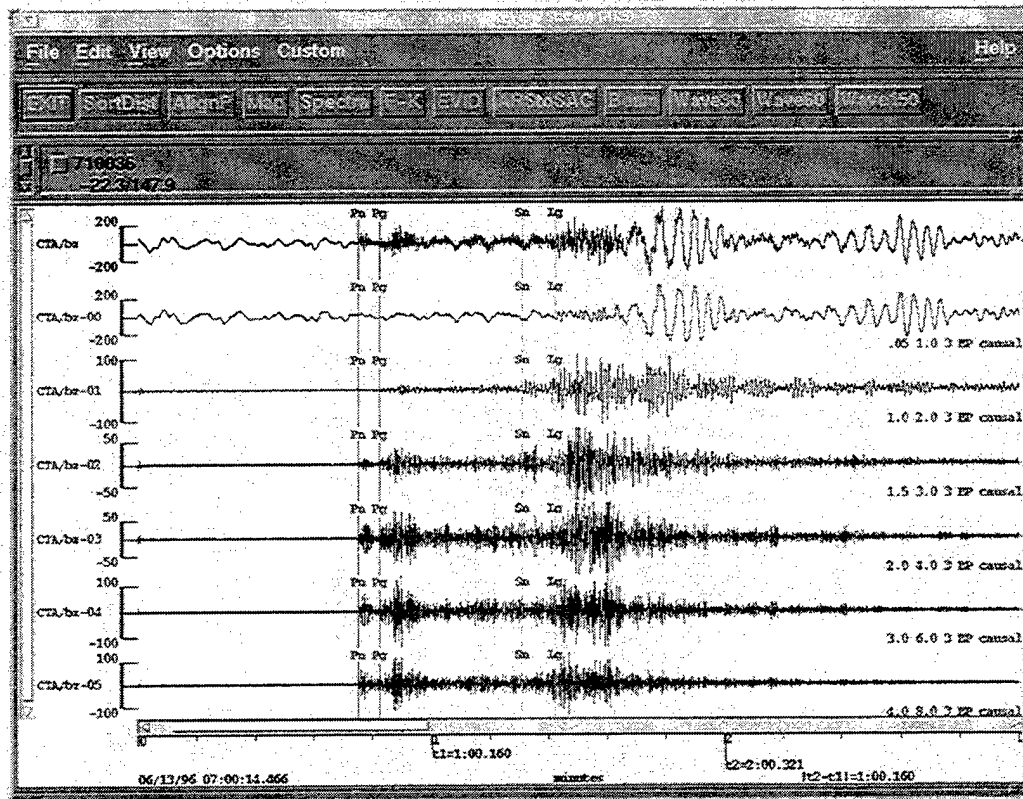
Figure 10. Sample waveform recorded at the Charters Towers, Australia station. This event is located in a local mining region approximately 3 degrees away. The size of the event is m_L 3.5. a) Unfiltered and filtered waveforms. Vertical channels are shown and frequency bands are listed beneath each waveform. b) Amplitude spectra of the Pn arrival and ambient noise. Raw and smoothed spectra are shown.

slowness and azimuth based on the REB location solution. Figure 11 shows the comparison at 3 Hz and 6 Hz. As expected, the two measures are identical for single stations (pluses). However, the measures are different for array stations (circles), especially at higher frequencies. This is due to a lack of signal coherence across the array. Although a coherent beam tends to increase *snr*, using amplitudes from this beam will corrupt our attenuation estimates at higher frequencies. For this reason, we do not recommend the use of amplitudes made from coherent beams.
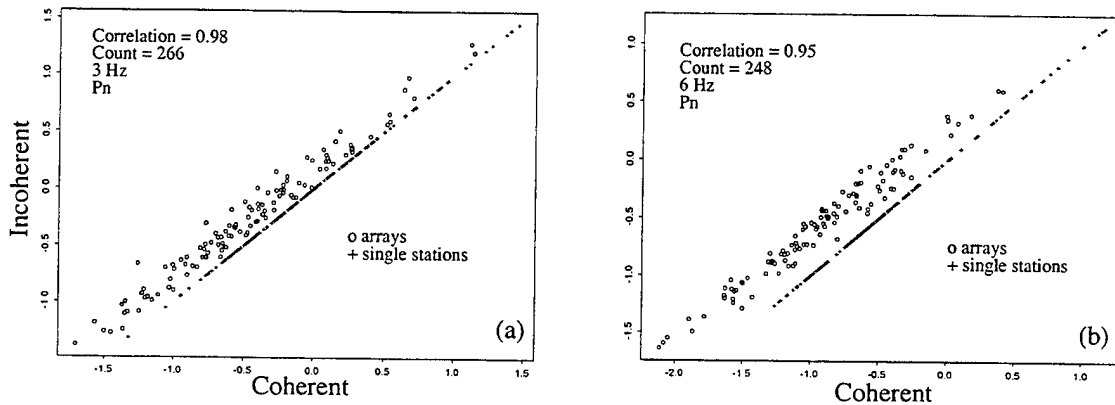
Figure 11. Comparison of log *rms* amplitudes measured on coherent and incoherent beams. (a) *Pn* at 3 Hz. (b) *Pn* at 6 Hz. Arrays are denoted by circles and single stations by pluses.

4.2.2 Amplitude Types

We compare the three different types of amplitudes using incoherent beams for *Pn* arrivals in our Australian data set in Figure 12. Figure 12a compares log *rms* amplitudes and log *stav* amplitudes. Figure 12b compares log *rms* amplitudes and log *abs* amplitudes. Both plots show amplitudes measured in a 4-8 Hz band (referred to as 6 Hz). As expected, the three amplitude measures on incoherent beams have a high degree of correlation but, *abs* amplitudes appear to have a higher variance. Like coherent beam measurements, *abs* amplitudes produce a separation between arrays and single stations at higher frequencies. In this case, the single station amplitudes are larger than those of the arrays. This is because the incoherent beam from an array averages the amplitudes at individual stations. For this reason, we do not recommend the use of *abs* amplitudes for attenuation studies. Either *rms* or *stav* amplitude measurements could be used since they are nearly the same.

We also computed the spectral amplitude for each signal. We compare log *rms* amplitude and log spectral amplitude in Figure 13 for *Pn* arrivals in our Australian data set. Figure 13a shows log amplitudes at 3 Hz and Figure 13b shows them at 6 Hz. The correlation decreases as frequency increases probably because the time-domain measurements are based on 2-4 Hz and 4-8 Hz filters whereas the spectral amplitudes are measured at 3 Hz and 6 Hz. There is no guarantee that the dominant signal frequency is the center of the passband. Furthermore, leakage outside the intended filter band could reduce the correlation [*Rodgers et al.*, 1997].

22
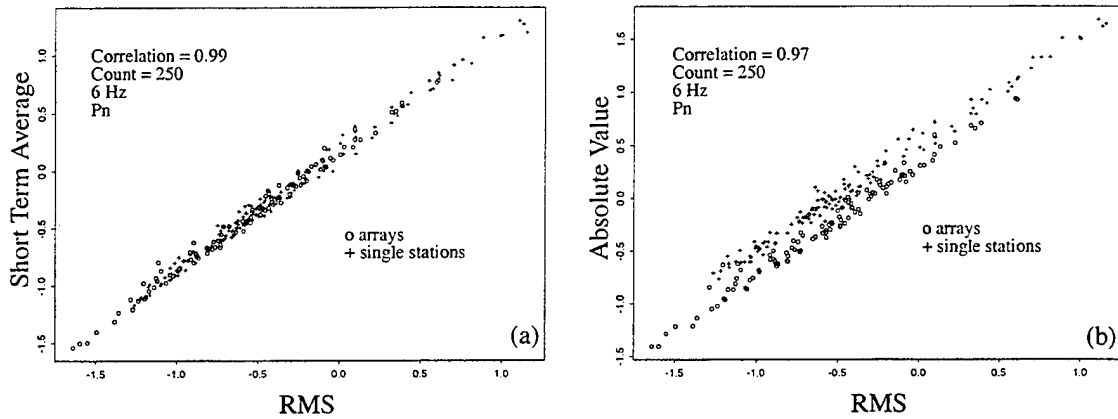
Figure 12. Comparison of three different types of log amplitudes made on 6 Hz *Pn* arrivals using incoherent beams. (a) root-mean square and short-term average comparison. (b) root-mean square and absolute value comparison. Arrays are denoted by circles and single stations by pluses.
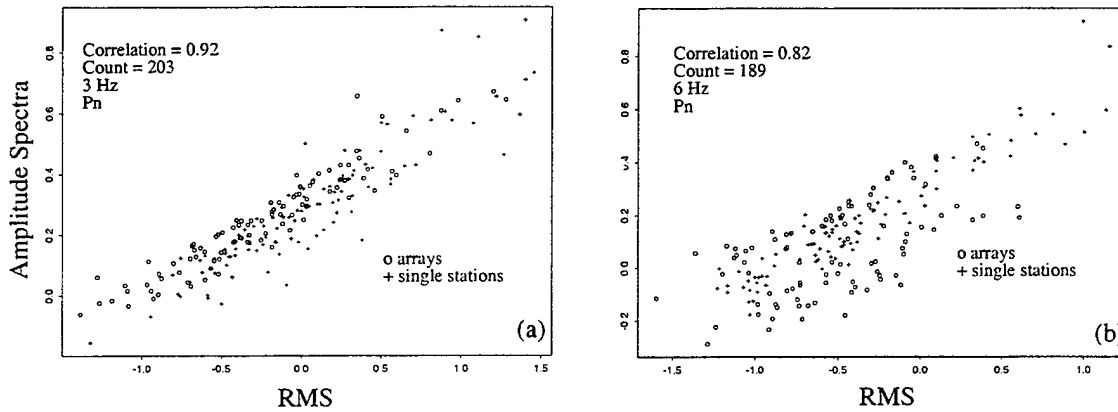
Figure 13. Comparison of root-mean square log amplitudes and log amplitude spectra measurements from *Pn* arrivals examined in this study. The time-domain amplitudes were made on an incoherent beam. (a) Comparison at 3 Hz. (b) Comparison at 6 Hz. Arrays are denoted by circles and single stations by pluses.

4.2.3 Quality Control

The automated amplitude measurements computed by DFX required visual inspection in some cases. For example, energy unrelated to *Lg* was found in some of the *Lg* group velocity windows thus contaminating the amplitude measurement. This was most frequent at long distances where the *Lg* window is nearly 2 minutes in duration for an event 20° away. An example of this is shown in Figure 14. This shows waveforms from an m_b 3.3 event from West Virginia (a suspected mine blast at 37.9076 latitude, -81.1089 longitude) recorded by a station in Schefferville, Canada approximately 2170 km away. The waveform for this event clearly shows Lg energy in the 2.0 to 4.0 Hz band but no energy is

visible in higher frequency bands. However, a high-frequency signal unrelated to *Lg* is contained in the group velocity window. This type of unrelated signal is difficult to detect in automated quality control. The problem of contamination by unrelated signals will require a method for screening unrelated signals to improve the reliability of automated measurements for estimating attenuation.
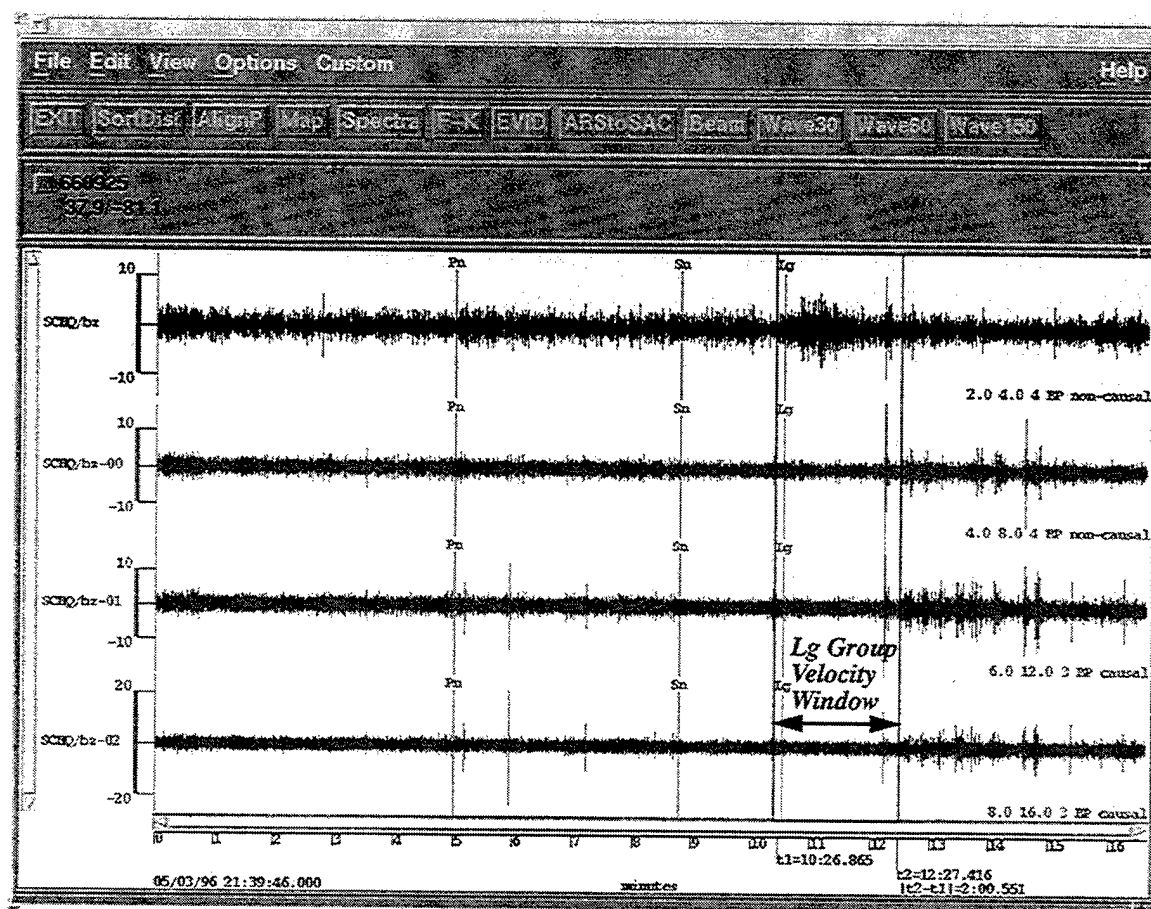
Figure 14. Suspected mine blast from West Virginia recorded by a 3-component station in Schefferville, Canada. *Lg* energy is absent for the 4-8 Hz and higher frequency bands. However, the automated *Lg* amplitude at high frequency is contaminated by unrelated signals. Analyst picks are annotated. Vertical channels are shown and frequency bands are listed beneath each waveform.

4.2.4 Preferred Amplitude Measure

Because of the ease at which temporal measurements can be made and the small amount of storage required, we do not consider spectral measurements any further for this study. It is expected that spectra would produce similar results as we've obtained here. After evaluating the variance of our source and attenuation estimates for a preliminary Australian data set using the temporal *stav* and *rms* amplitudes, we determined that *rms* log amplitudes measured on incoherent beams are the most stable measurements to use for this attenuation study. All remaining results are based on these amplitudes.

24

5. Inversion Results

We estimated source, attenuation and site parameters for each subnetwork by applying AmpInv to the log *rms* amplitudes measured on an incoherent beam. A common set of AmpInv parameters was used for each subnetwork including distance and frequency constraints, *snr* thresholds, and others. These are described in Section 5.1. Our results for source, attenuation and site parameters are summarized in Section 5.2, and described in detail for each subnetwork in Appendix B. In general, we obtained stable results as evidenced by an average standard deviation of 0.27 log amplitude units for all subnetworks. However, a few regions such as South America had an insufficient amount of regional data for some regional phases after applying our *snr* criterion.

5.1 AmpInv Configuration

We applied a single configuration of AmpInv for all subnetworks. The complete set of AmpInv parameters is described by *Jenkins* [1998]. Table 3 summarizes the primary constraints used in this study.

Table 3: Phase-Dependent AmpInv Constraints.

Constraint	Pn	Pg	Sn	Lg
Minimum Epicentral Distance	1.8 $^\circ$	1.8 $^\circ$	1.8 $^\circ$	1.8 $^\circ$
Maximum Epicentral Distance	15.0°	6.0°	15.0°	20.0°
Lower Frequency Cut-off	1.0 Hz	1.0 Hz	0.5 Hz	0.5 Hz
Upper Frequency Cut-off	15.0 Hz	15.0 Hz	10.0 Hz	6.0 Hz
Minimum *snr* Threshold	3.5 dB	2.0 dB	3.5 dB	2.0 dB

We constrained each regional phase to the frequency bands specified in Table 3. *Pn* and *Pg* amplitudes were used if the center frequency of the pass band was between 1.0 and 15.0 Hz. *Sn* amplitudes were restricted to the 0.5 to 10 Hz band, and *Lg* amplitudes were restricted to the 0.5 to 6.0 Hz band. It was found that the use of higher frequencies for regional *S*-phases introduced more outliers than real signals (e.g., the type of unrelated signals described in Section 4). The distance constraints were also applied to reduce the possibility of contamination by unrelated signals. These constraints are based on typical distances ranges for each regional phase in the REB.

We applied phase-dependent *snr* thresholds of 3.5 dB for *Pn* and *Sn*, and 2.0 dB for *Pg* and *Lg* for all subnetworks except western North America and Japan. For these subnetworks we applied a higher *snr* since there were more data available. The *snr* is the ratio of the signal amplitude and the pre-signal noise amplitude. For example, for *Lg* the *snr* is the *Lg* signal amplitude divided by the pre-*Lg* noise. The pre-*Lg* noise is typically much larger than the ambient (pre-*Pn*) noise because it includes the coda of earlier phases.

We also found it necessary to remove some outliers prior to the inversion based on visual inspection. We examined the waveforms for arrivals with anomalous amplitudes. As described earlier, most of the prominent outliers consisted of *Lg* arrivals from events recorded at distances greater than 1000 km that were contaminated by interfering signals. All amplitude measurements related to these arrivals were removed from the data set. All other automated amplitude measurements were retained.

The parameters that control the inversion process were also consistently applied for each subnetwork. For example, the same stopping criteria and degree of damping were applied. The stopping criteria included the maximum number of iterations and a target variance. The degree of damping was reduced for each iteration until a negligible amount of damping was applied. All of our results converged below the target variance before the maximum number of iterations was reached.

All AmpInv model parameters were estimated except the corner frequency scaling parameter called "c" in Equation 4. This parameter relates corner frequency to long-period level assuming cube-root scaling. We found it necessary to fix this parameter as it was not well-constrained by our data. For each subnetwork we repeated the inversion using a range of fixed values for c. The value was selected to provide a uniform corner frequency as a function of magnitude for all subnetworks.

5.2 AmpInv Results

5.2.1 Source

We estimated the long-period source level, S_0, for each event. The long-period levels estimated from the inversion are evaluated for each subnetwork in Appendix B by comparing them to magnitude. As expected, log S_0 (which is proportional to seismic moment) increases with magnitude at a rate between 2/3 and 1 for most subnetworks. The median rate of change of log S_0 as a function of m_L for all subnetworks is 0.83. An example for the Alaska subnetwork is provided in Figure 15.

The long-period levels are related to corner frequency by the scaling parameter, c. The corner frequency scales inversely with the cube root of the long-period level. The parameter, c, was fixed such that the corner frequency is approximately 10 Hz for an m_L 3.0 event for all subnetworks.

Two additional phase-dependent parameters estimated by AmpInv are α and κ. Both terms contribute to the amplitude at the reference distance, A^0, and are therefore included in this discussion of source parameters. The α term represents the total attenuation between the source and reference distance. The κ term is the phase-dependent source excitation parameter which is estimated for *Pg*, *Sn*, and *Lg* relative to *Pn*. Neither of these parameters are dependent on epicentral distance. Estimates for α and κ are included in Appendix B.

5.2.2 Attenuation

The primary product of this study is the estimate of the frequency-dependent attenuation of *Pn*, *Pg*, *Sn* and *Lg* for each subnetwork. These estimates will be used to normalize the discriminants based on *S/P* ratios to a common reference distance.
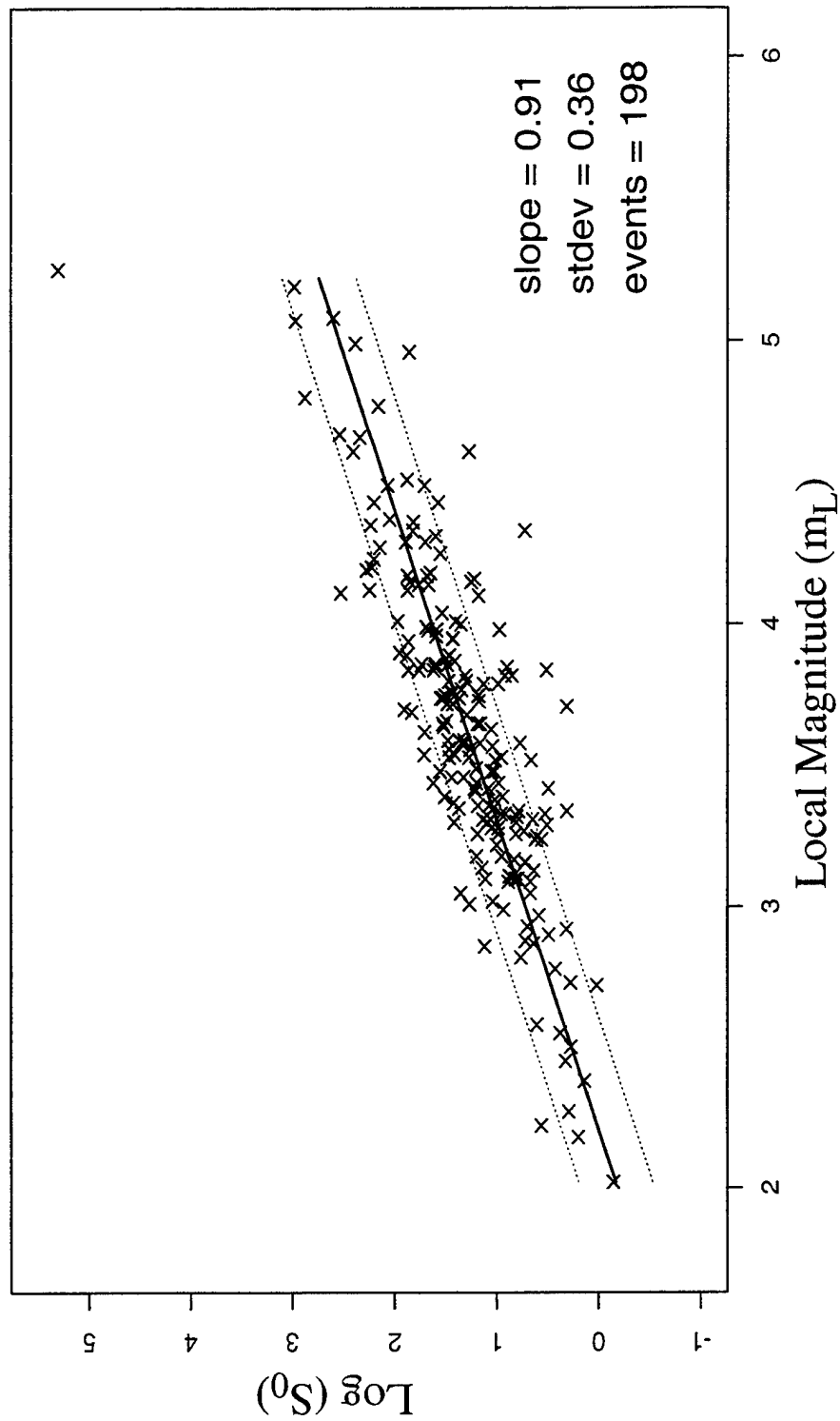
Figure 15. Estimated long-period source level versus local magnitude for the Alaska subnetwork.

The attenuation results for each subnetwork are presented in Appendix B. An example of the attenuation for the Alaska subnetwork is shown in Figure 16. The results for six frequencies for each regional phase are plotted. The points are the observed log amplitudes minus log A^0 and site response (as determined by the inversion) as a function of distance. The solid curve represents the power-law attenuation model for each frequency. The dashed curves indicate one standard deviation. The rate of attenuation (i.e., $\Delta^{-n(f)}$) and the standard deviation are annotated in each plot. In general, the attenuation increases as expected with increasing frequency for each phase and the crustal phases Pg and Lg attenuate more rapidly (particularly at high frequencies) than the mantle phases Pn and Sn.

Table 4 shows the attenuation rates at 3 Hz for each regional phase and subnetwork. Details for each subnetwork are provided in Appendix B. A dash in Table 4 indicates that there were too few arrivals (<15) to estimate the attenuation with confidence. This was the case for all phases for the Southern Africa subnetwork. The one exception is the Lg attenuation rate for Japan which was not included for other reasons as described below. The results for Scandinavia are from *Sereno* [1990] who used the same method to estimate regional-wave attenuation.

Table 4: Attenuation Results at 3 Hz.

Subnetwork	Tectonic Name	Attenuation Coefficient (n) at 3 Hz, Δ^{-n}			
		Pn	Pg	Sn	Lg
Alaska/NW Canada	Tectonic	2.2	2.3	3.3	3.5
Western N. America	Tectonic	2.4	3.1	3.6	3.4
Southern Europe	Tectonic	1.9	2.4	2.4	2.2
Southern Asia	Tectonic	1.7	-	2.6	-
Japan	Tectonic	1.8	1.3	1.9	-
South America	Tectonic	2.1	-	-	-
Eastern N. America	Stable	1.9	3.0	2.4	2.6
Central Asia	Stable	2.1	-	2.6	3.7
Australia	Stable	1.3	1.5	2.1	2.4
Southern Africa	Stable	-	-	-	-
Scandinavia[a]	Stable	1.6	2.7	2.0	2.2

a. The results for Scandinavia are from *Sereno* [1990].

Our estimates of the attenuation rates for Pn, Sn and Lg for Alaska, western North America, and South America are relatively high as would be expected for tectonic regions. The South America subnetwork had substantially fewer arrivals, most of which were
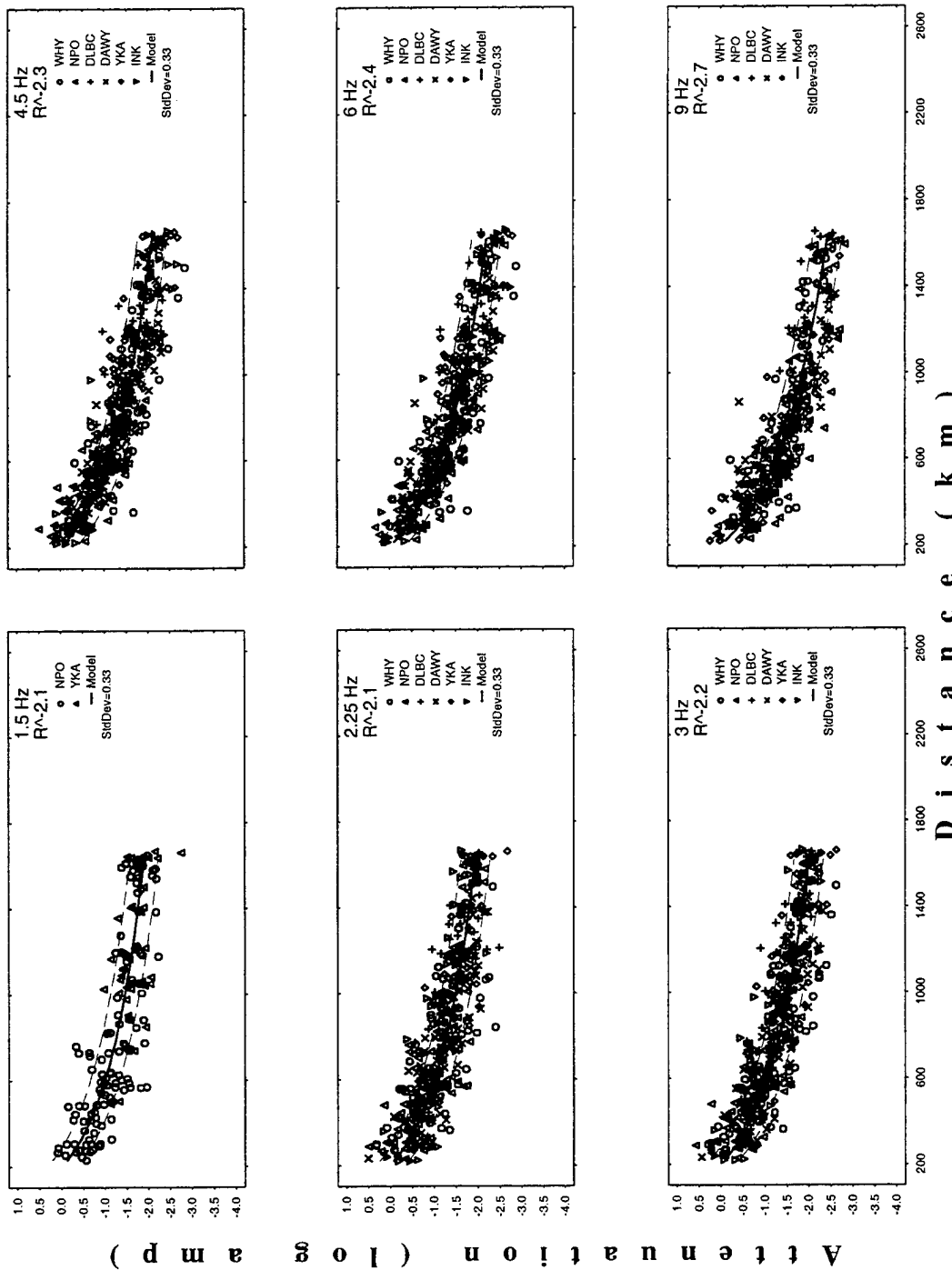
Figure 16. Attenuation curves at various frequencies for the Alaska subnetwork. a) *Pn*, b) *Pg*, and c) *Sn* attenuation curves at 1.5, 2.25, 3.0, 4.5, 6.0, and 9.0 Hz. d) *Lg* attenuation curves at 0.75, 1.5, 2.25, 3.0, 4.5, and 6.0 Hz.
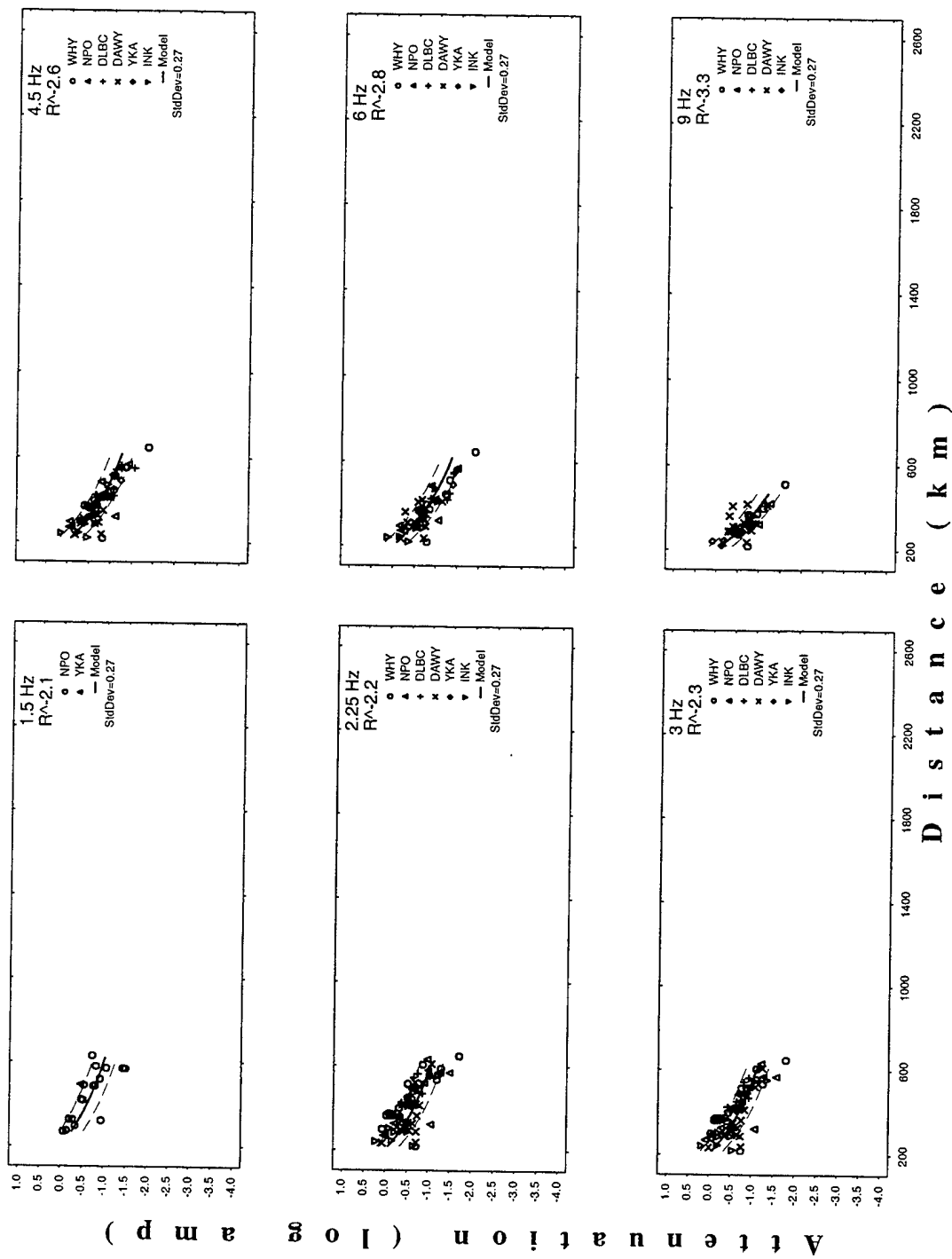
Figure 16. continued.

Figure 16. continued.

31

Figure 16. continued.

32
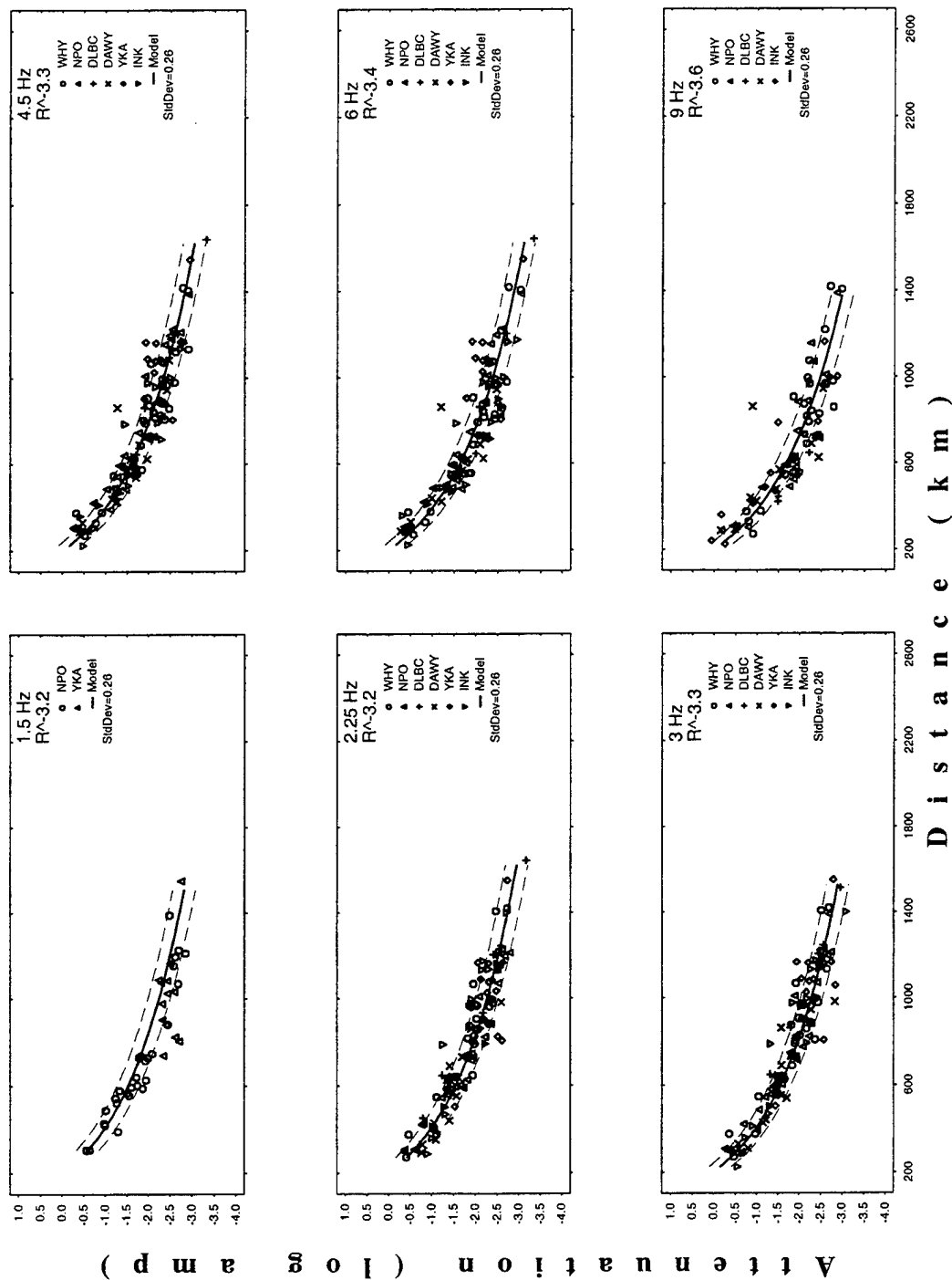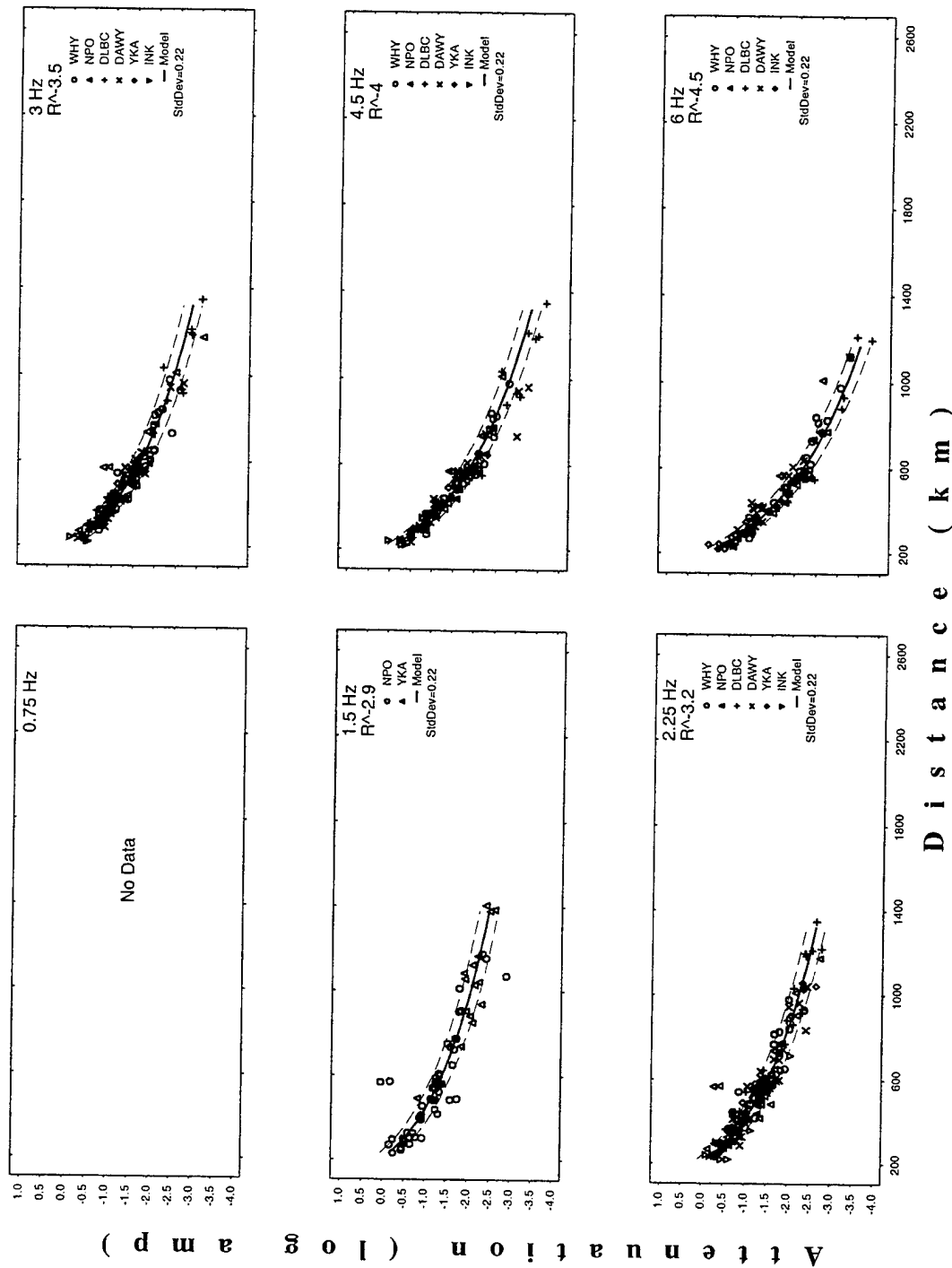
classified as *Pn*. The *Pg* attenuation for all regions is difficult to determine because it is recorded over a very limited distance range. The attenuation rates in southern Europe are surprisingly low for a tectonic region. However, much of the data was from events recorded along stable paths at distances less than 600 km suggesting this subnetwork should be classified as a "*mixed*" environment. The *Pn* and *Sn* attenuation in southern Asia is also low for a tectonic region. Although we could not determine the *Lg* attenuation rate in southern Asia we expect that it is very high since few arrivals were associated in the REB. This may be related to the Moho topography.

Japan appears to have low *Pn* and *Sn* attenuation rates. However, this is a complicated tectonic region that may not be properly characterized by our simple model. Also, it is possible that some of the REB events included for this subnetwork are deeper than 40 km. The *Lg* attenuation rate for Japan is not meaningful because *Lg* was only reported in the REB for distances less than about 350 km (see Appendix B). This is probably because *Lg* is blocked for many paths which include an oceanic segment.

The attenuation rates for *Pn*, *Sn* and *Lg* in eastern North America and Australia are relatively low as expected for stable regions. They are also quite similar to the attenuation rates determined by *Sereno* [1990] for Fennoscandia. Central Asia has a higher attenuation rate (especially for *Lg*), but some of the ray paths appear to cross tectonic regions (see Appendix A). There were too few data from southern Africa to estimate the attenuation in that region.

5.2.3 Site

A phase-dependent site response is estimated for each station in the subnetwork. We impose the constraint that all site responses for one phase must sum to zero.

The average of the median absolute values of the site responses of regional phases in all subnetworks combined is 0.24 (see Appendix B). The estimated values for *Pn* and *Pg* were slightly lower than those found for *Sn* and *Lg*. We verified the need for site corrections by comparing the data variances of two inversions: one with site corrections fixed at zero for all stations, and the other with site corrections as free parameters. The data variance increased with the site corrections fixed, but the attenuation models were not much different.

6. Discrimination

This section evaluates a variety of normalized *S/P* amplitude ratios as regional discriminants. We evaluated three types of discriminants:

1. *Lg/Pn*

2. *Sn/Pn*

3. Largest *S*/Earliest *P*

Pg is not included in the first two discriminants because there are too few *Pg* phases in our data set. Each discriminant is evaluated in several frequency bands. The frequency bands for *Lg* are 0.5-1, 1-2, 2-4, 3-6, and 4-8 Hz. The same bands were used for *Sn* plus an additional one at 6-12 Hz. The frequency bands for *Pn* are 1-2, 2-4, 3-6, 4-8, 6-12, and 8-16 Hz. We consider all phase ratios (e.g., 1-2 Hz *Lg/Pn*) and cross-spectral ratios (e.g., 1-2 Hz *Lg* / 3-6 Hz *Pn*) subject to the constraint that the *P*-wave frequency is greater than or equal to the *S*-wave frequency.

First, we discuss our distance and source corrections and show that we were able to remove these dependencies in the data. Then, we evaluate the performance of 76 variants of the *S/P* discriminant for each subnetwork. To simplify the discussion, we define 0.5-1 Hz and 1-2 Hz as low-frequency (LF) bands, 2-4, 3-6, and 4-8 Hz as mid-frequency (MF) bands, and 6-12 Hz and 8-16 Hz as high-frequency (HF) bands.

6.1 Distance Corrections

This section demonstrates that our attenuation models are effective at removing the distance dependence of the *S/P* ratios. The attenuation models for each regional phase can be used to compute distance corrections for any variant of the *S/P* discriminant. Other studies derive distance corrections directly from the amplitude ratios [*Taylor*, 1997]. That approach can be effective and simple for studying a particular discriminant in one region. However, distance corrections must be developed for each variant of the discriminant, and the results are difficult to transport to uncalibrated regions.

Figure 17 shows uncorrected and distance-corrected log *S/P* amplitude ratios versus distance for events recorded in Alaska. This figure is for the Largest *S*/Earliest *P* discriminant. The corrections include the site and path terms for each regional phase. Results are provided for *rms* amplitudes measured on incoherent beams in three frequency bands; 1-2 Hz, 3-6 Hz, and 6-12 Hz. A least-squares fit (assuming a power-law model) of the log amplitude ratios as a function of distance is overlaid on each plot with boundaries representing one standard deviation. The attenuation rate of the *S/P* ratio, standard deviation, and number of measurements are also displayed in the legend. It is clear from this figure that the attenuation models are effective at removing the primary distance dependence of the *S/P* ratio at all three frequencies. Appendix C shows that similar results were obtained for all other subnetworks.

Alaska

Uncorrected
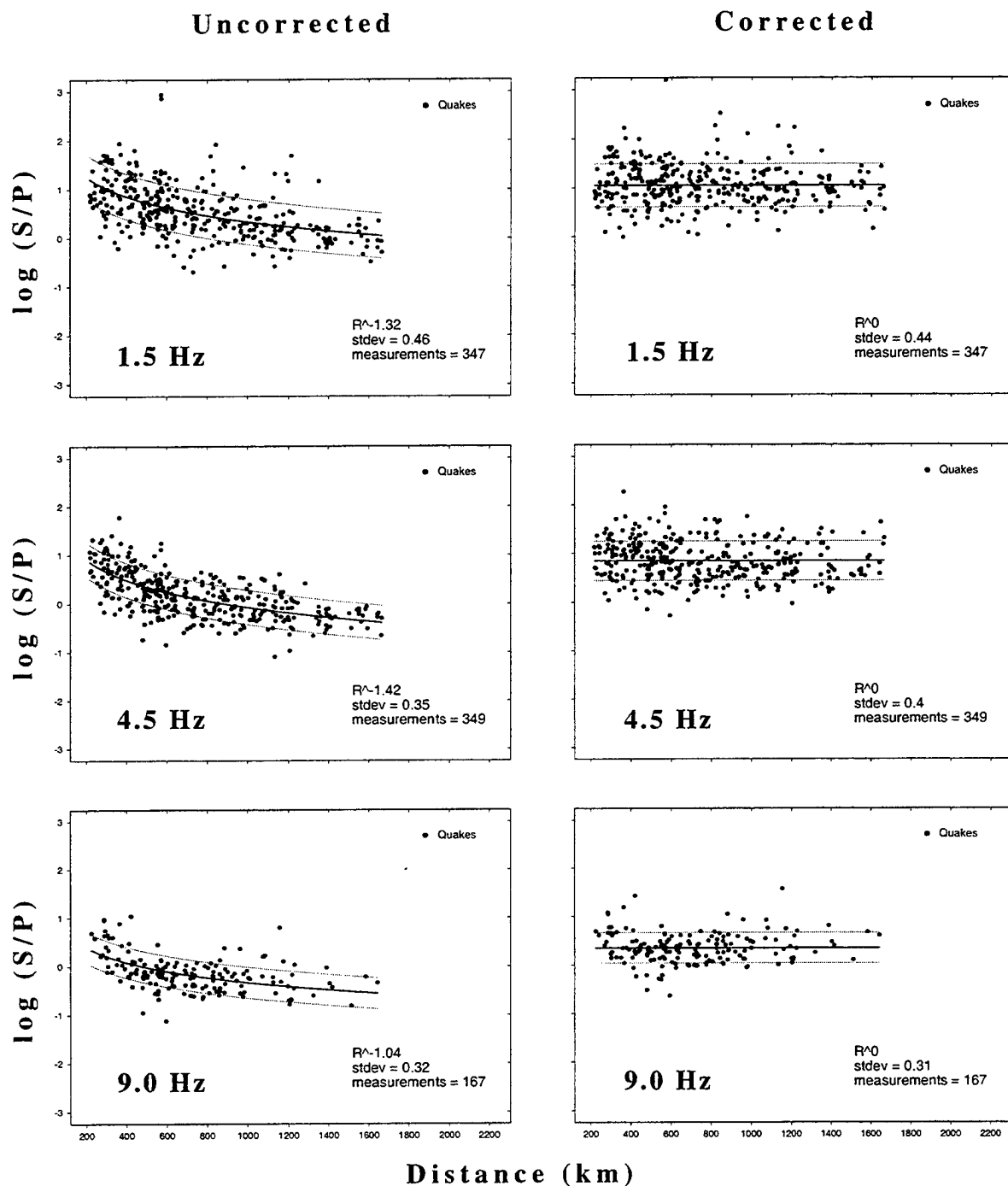
Corrected

Figure 17. Uncorrected and distance-corrected S/P ratios in 1-2, 3-6, and 6-12 Hz (referred to as 1.5, 4.5, and 9.0 Hz) frequency bands for Alaska.

6.2 Source Corrections

A source correction is necessary for evaluation of cross-spectral ratios since the S-wave amplitude is measured at a different frequency than the P-wave amplitude. The source correction is defined as:

$$\text{Source Correction} = \log s(f_S) - \log s(f_P) \qquad (7)$$

where $s(f)$ defines the shape of the source function, f_S is the frequency of the S-wave amplitude measurement, and f_P is the frequency of the P-wave amplitude measurement. The source correction ranges from zero for same frequency ratios to approximately 1.0 log amplitude unit for a m_L 5.0 event and cross-spectral ratios between LF S and HF P. An example of the source correction is shown in Figure 18 using events recorded in the Alaska subnetwork. This figure shows the distance-corrected ratio between 0.5-1 Hz (i.e., referred to as 0.75) Lg and 6.0-12.0 Hz (i.e., referred to as 9) Pn amplitudes as a function of magnitude. The curve is the predicted magnitude dependence based on our source model. The lower plot shows our source-corrected ratio. The source correction is effective at removing the magnitude dependence in the cross-spectral ratio.

6.3 Discriminants

The performance of normalized S/P ratios as regional discriminants is evaluated using our set of earthquakes, presumed industrial explosions and four nuclear explosions. The nuclear explosions were from the Lop Nor test site in China recorded by stations in the central and southern Asia subnetworks (see Figures 19-22). Although there is clearly a large variability in the regional waveforms from nuclear explosions, all four events in our data set have relatively low S/P ratios. Unfortunately, we have too few known explosions to make meaningful conclusions about the effectiveness of the discriminants in most regions. For example, we are not aware of any explosions in our data sets for Alaska and Japan. However, we are able to characterize the distributions of normalized S/P ratios for earthquakes in each region which can be used by statistical algorithms that detect outliers [Fisk et al., 1993].

We consider events with both P-waves and S-waves at the same station. We require the snr of either the P-wave or S-wave to be above a threshold. We use a threshold of 1.5 for Pn or Pg and 1.3 for Sn or Lg. A lower threshold was used for S-phases because the noise is the pre-signal noise which includes the coda of earlier arrivals. Our S/P ratio is a lower bound if the S-wave exceeds the snr threshold but the P-wave does not. This is observed for some earthquakes. Similarly, our S/P ratio is an upper bound if the P-wave exceeds the snr threshold and the S-wave does not. This is typical for Lop Nor nuclear explosions which generally do not have an Sn or Lg arrival above the snr threshold in our data set.

6.3.1 Lg/Pn

The normalized Lg/Pn ratio is summarized in Figure 23 for the central Asia subnetwork. We use this subnetwork as an example because it includes nuclear explosions, presumed
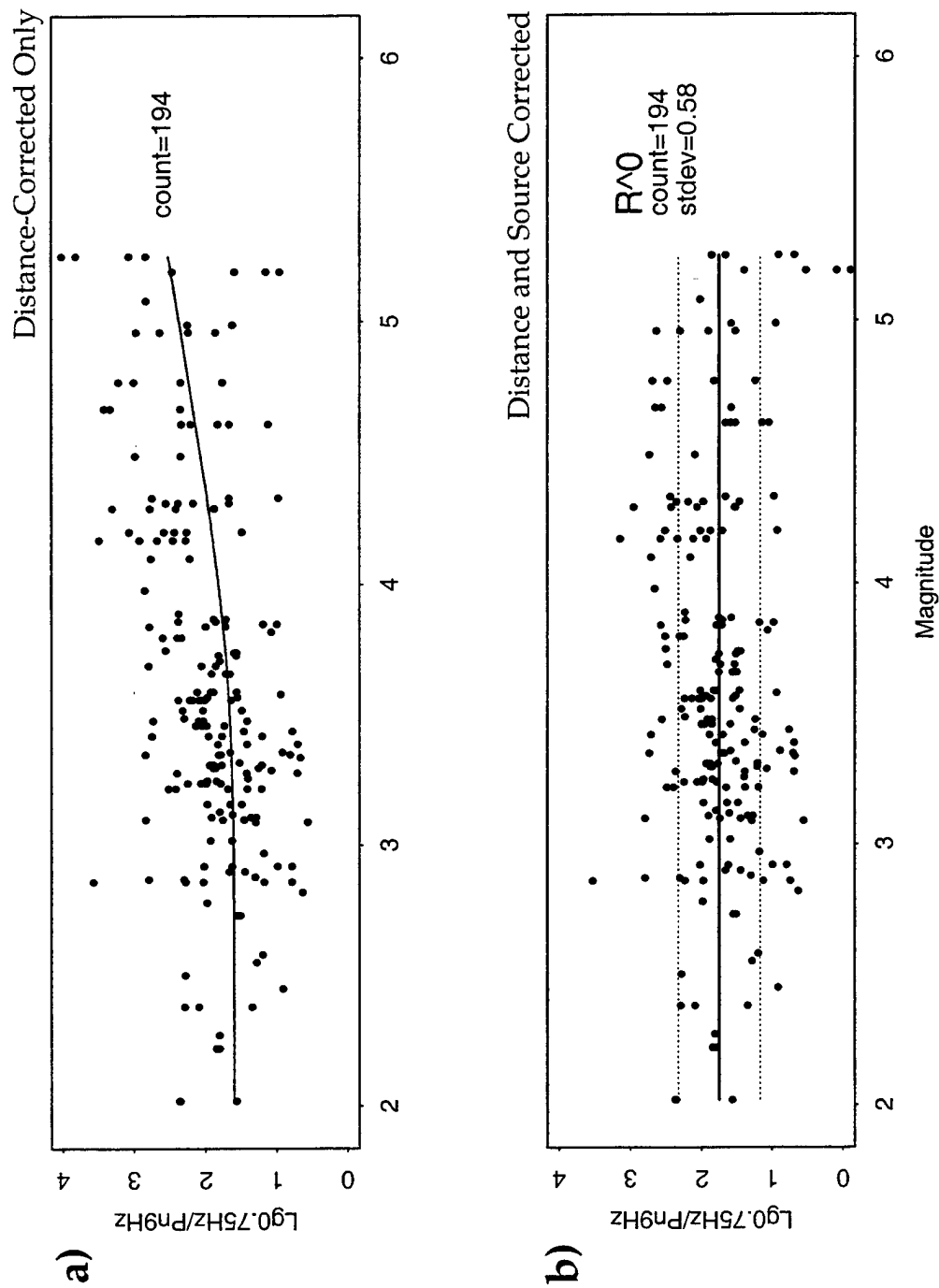
Figure 18. (a) Distance-corrected ratio of L_g (0.5-1 Hz) and P_n (6-12 Hz) amplitudes for 194 events recorded in Alaska. Solid line shows the predicted magnitude dependence in this ratio. (b) The predicted magnitude dependence has been removed from the ratio shown in (a).

37
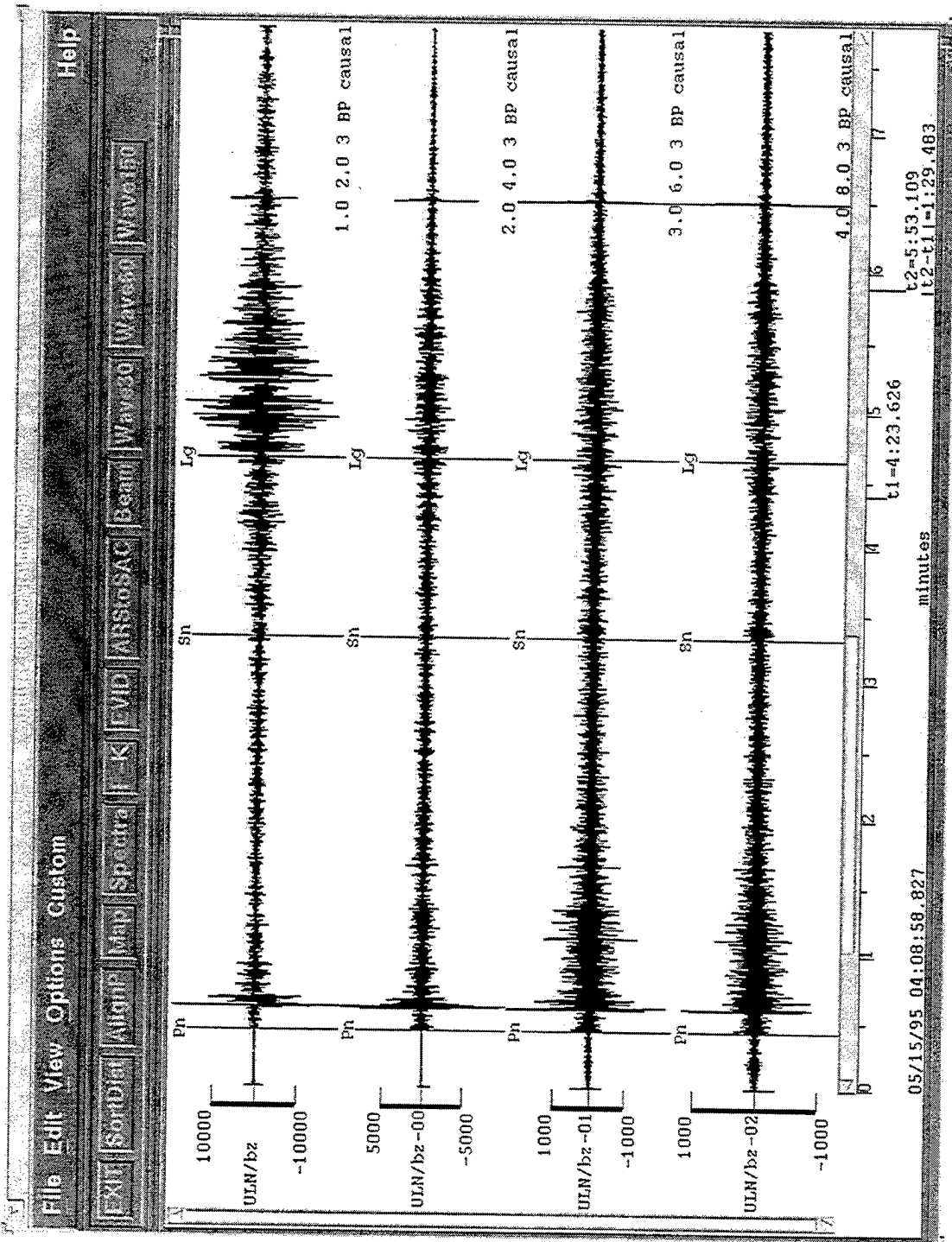
Figure 19. Waveforms from the May 1995 Lop Nor nuclear explosion recorded at station ULN located in Ulaanbaatar, Mongolia (latitude 47.87, longitude 107.05) in the central Asia subnetwork approximately 1600 km away. The event size was mb 5.73. Vertical channels are shown and frequency bands are listed beneath each waveform.
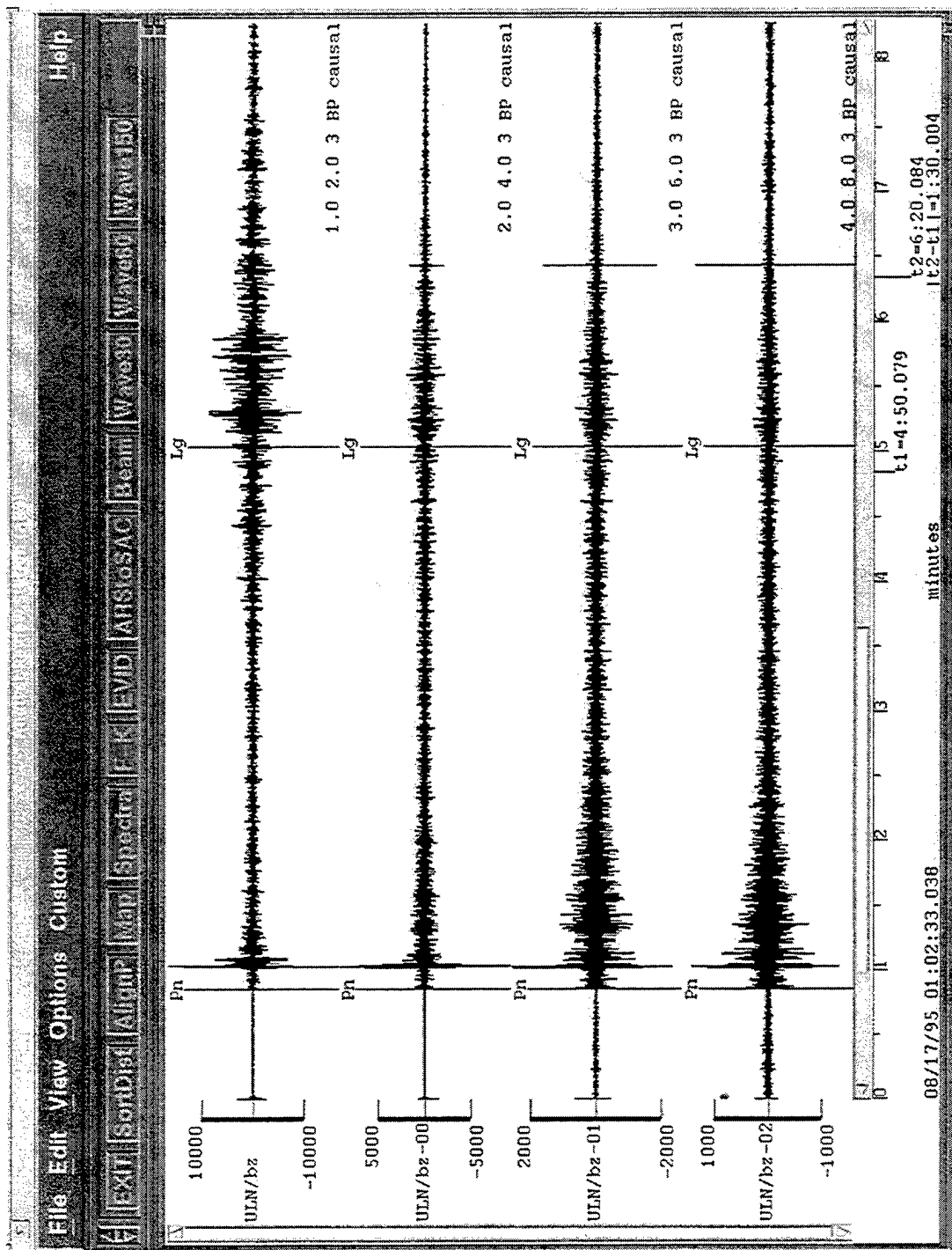
Figure 20. Waveforms from the August 1995 Lop Nor nuclear explosion recorded at station ULN located in Ulaanbaatar, Mongolia (latitude 47.87, longitude 107.05) in the central Asia subnetwork approximately 1600 km away. The event size was mb 5.54. Vertical channels are shown and frequency bands are listed beneath each waveform.
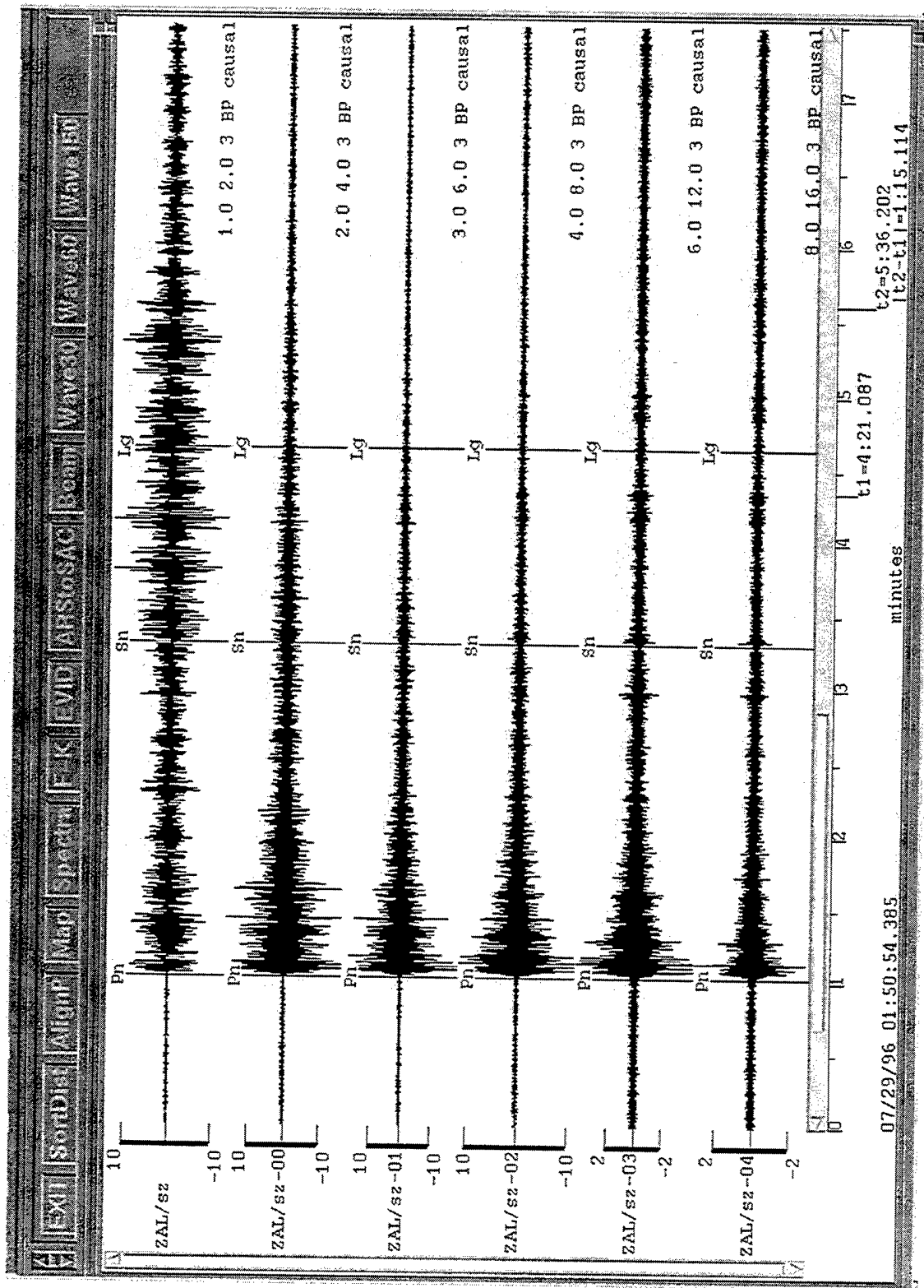
Figure 21. Waveform from the July 1996 Lop Nor nuclear explosion recorded at station ZAL located in Zalesovo, Russia (latitude 53.62, longitude 84.79) in the central Asia subnetwork approximately 1350 km away. The event size was mb 4.71. Vertical channels are shown and frequency bands are listed beneath each waveform.
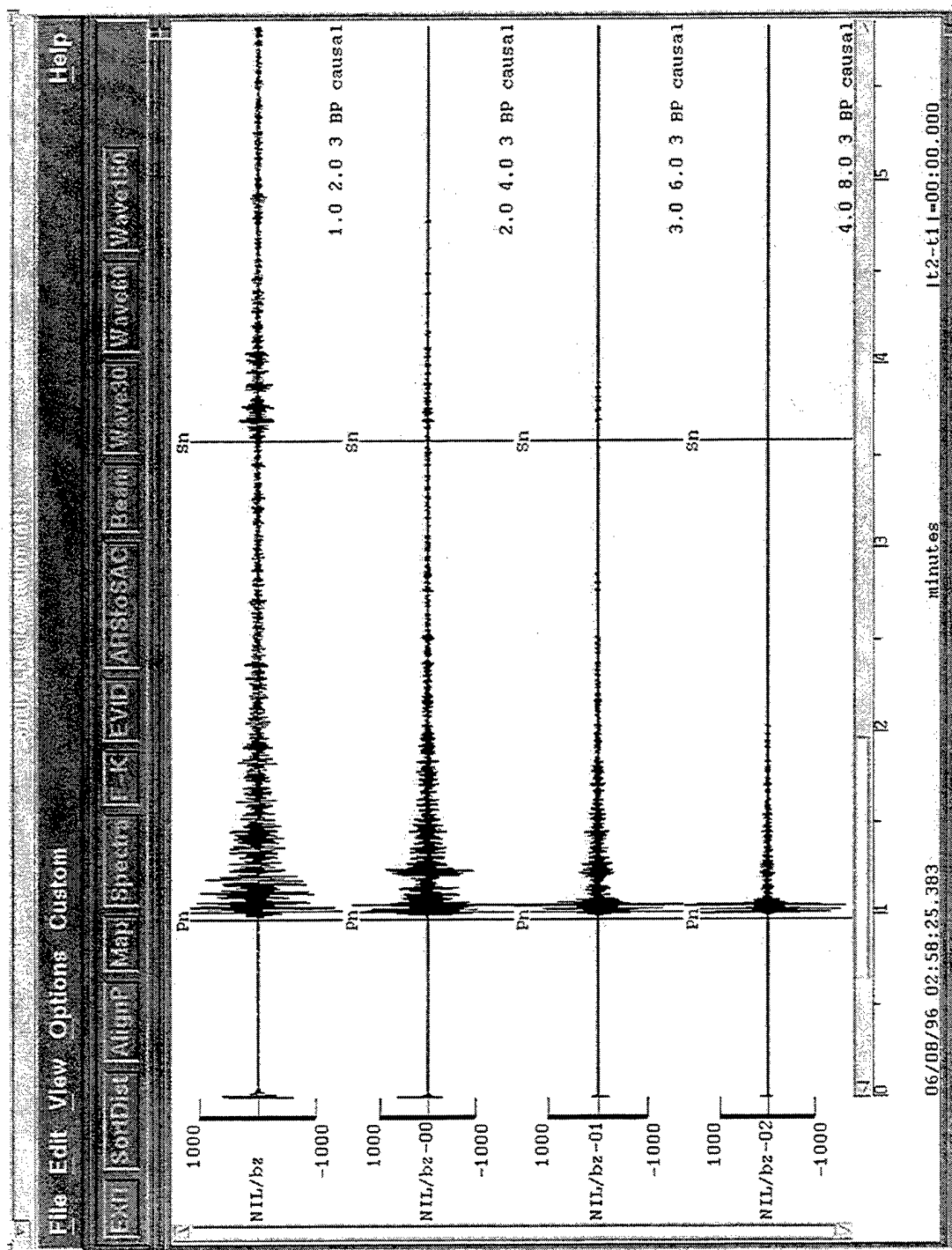
Figure 22. Waveforms from the June 1996 Lop Nor nuclear explosion recorded at station NIL located in Nilore, Pakistan (latitude 43.47, longitude 85.60) in the southern Asia subnetwork approximately 1600 km away. The event size was mb 5.69. Vertical channels are shown and frequency bands are listed beneath each waveform.
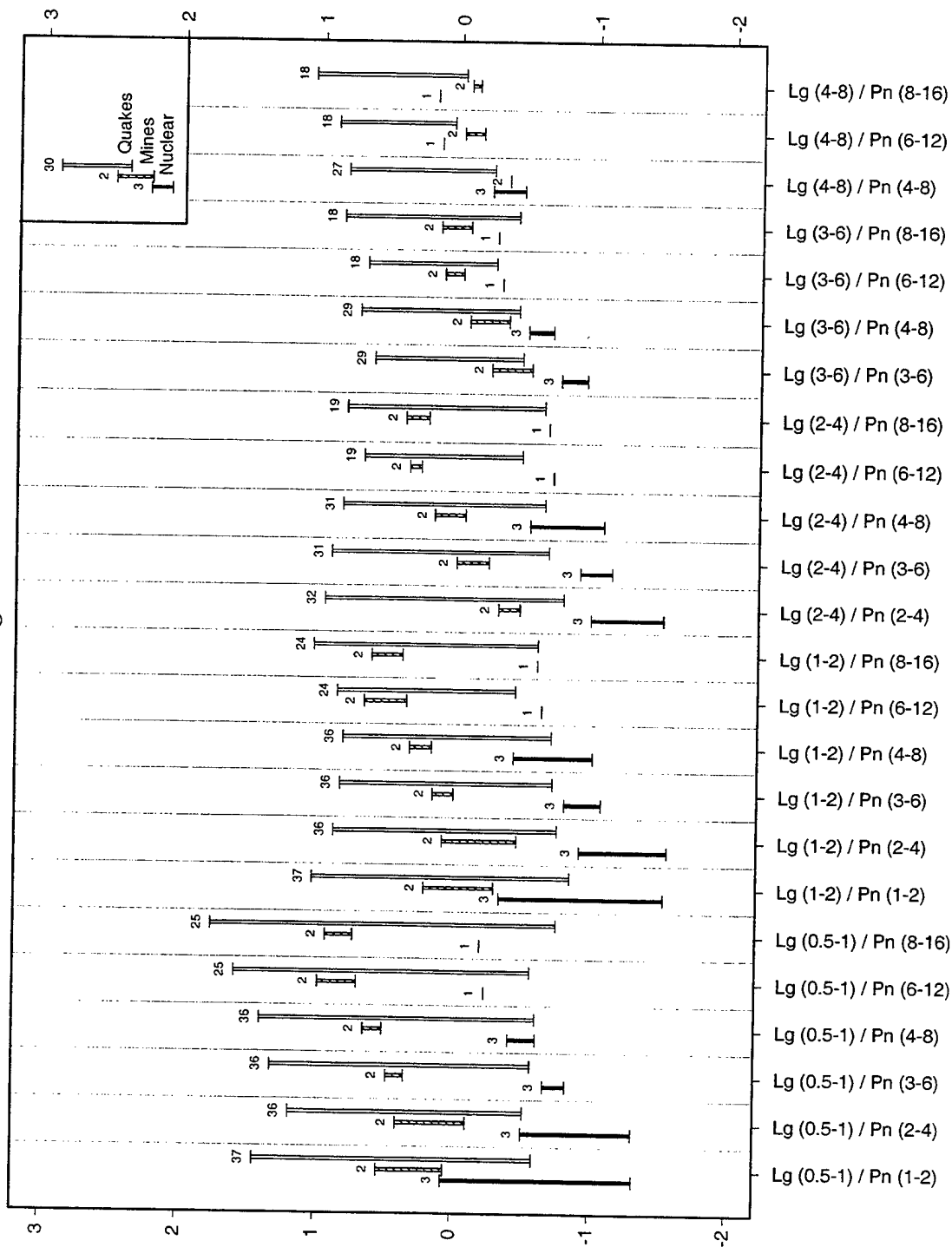
Figure 23. Summary of normalized Lg/Pn amplitude ratios for earthquake and explosions populations found in central Asia. Bars represent range of Lg/Pn ratios. The number of events in each population is indicated.

industrial explosions, and earthquakes. The *Lg/Pn* ratios for all other subnetworks are provided in Appendix C. The *Lg/Pn* ratio tends to be lowest for the nuclear explosions. The mean ratio is only slightly lower for the industrial explosions than for the earthquakes. Unfortunately there is considerable overlap between all three populations in some cases.

The best separation between nuclear explosions and earthquakes is provided by the *Lg*(LF)/*Pn* (MF) and *Lg*(MF)/*Pn*(MF) ratios. The ratios that include *Pn*(LF) or *Lg*(HF) are poor discriminants. Some of the ratios with *Pn*(HF) are good discriminants, but they are limited to fewer data because of the *snr* criteria.

The actual *Lg/Pn* ratios for the nuclear explosions are probably much lower than our estimates. Our estimates are upper bounds since *Lg* did not satisfy the *snr* criterion. We used the amplitude in the *Lg* time window which, for these events, is *P*-wave coda. We expect the *Lg/Pn* discriminant to perform better at closer distances where a meaningful *Lg* amplitude could be measured.

The automated measures of the *Lg/Pn* ratios for two of the nuclear explosions were higher than the ratios for the other two nuclear explosions and were within the typical range for earthquakes and mining explosions (see Figures 19 and 20). These events were recorded at the ULN station at a distance of about 1600 km. Both events have two prominent *P* arrivals and our original automated amplitude measurements were based on the first (or smaller) of them. Unfortunately, our time window for *Pn* did not include the second (or larger) *P* arrival. Therefore, we adjusted the time window for these two events to measure the larger *P* arrival. These corrected amplitudes were used to calculate our ratios. The resulting *S/P* ratios are consistent with the other Lop Nor explosions.

The fact that the *Lg/Pn* ratio does not provide unambiguous separation of nuclear explosions and earthquakes implies that there must be some earthquakes with low *Lg/Pn* ratios (similar to those from the nuclear explosions). Figure 24 is an example of an earthquake and a nuclear explosion both from the Lop Nor region and were recorded at the ZAL station. The earthquake is recorded at 1130 km and the nuclear explosion at 1350 km. Both events have low *S/P* ratios, and particularly low *Lg/Pn* ratios. A variety of factors such as source depth, radiation pattern, and lateral variations in crustal structure could account for low *Lg* amplitudes for some earthquakes.

6.3.2 Sn/Pn

The *Sn/Pn* discriminant performs about the same as the *Lg/Pn* discriminant for low and mid-frequency ratios. Results of the normalized *Sn/Pn* ratio are summarized in Figure 25 for the central Asia subnetwork. This ratio is provided in Appendix C for all other subnetworks. The *Sn/Pn* ratio tends to be lowest for nuclear explosions and only slightly lower for industrial explosions than for earthquakes. There are few *Sn* signals for mining explosions in central Asia because they were recorded at a close epicentral distance. Again, there is considerable overlap between all three populations in some cases.

The *Sn*(LF)/*Pn*(MF) and *Sn*(MF)/*Pn*(MF) ratios are the best discriminants. The *Sn*(LF)/*Pn*(LF) and *Sn*(LF)/*Pn*(HF) ratios are poor discriminants. Since *Sn* attenuates less rapidly than *Lg* at mid- to high-frequencies, the *Sn/Pn* discriminant is expected to perform better than *Lg/Pn* at longer distances.
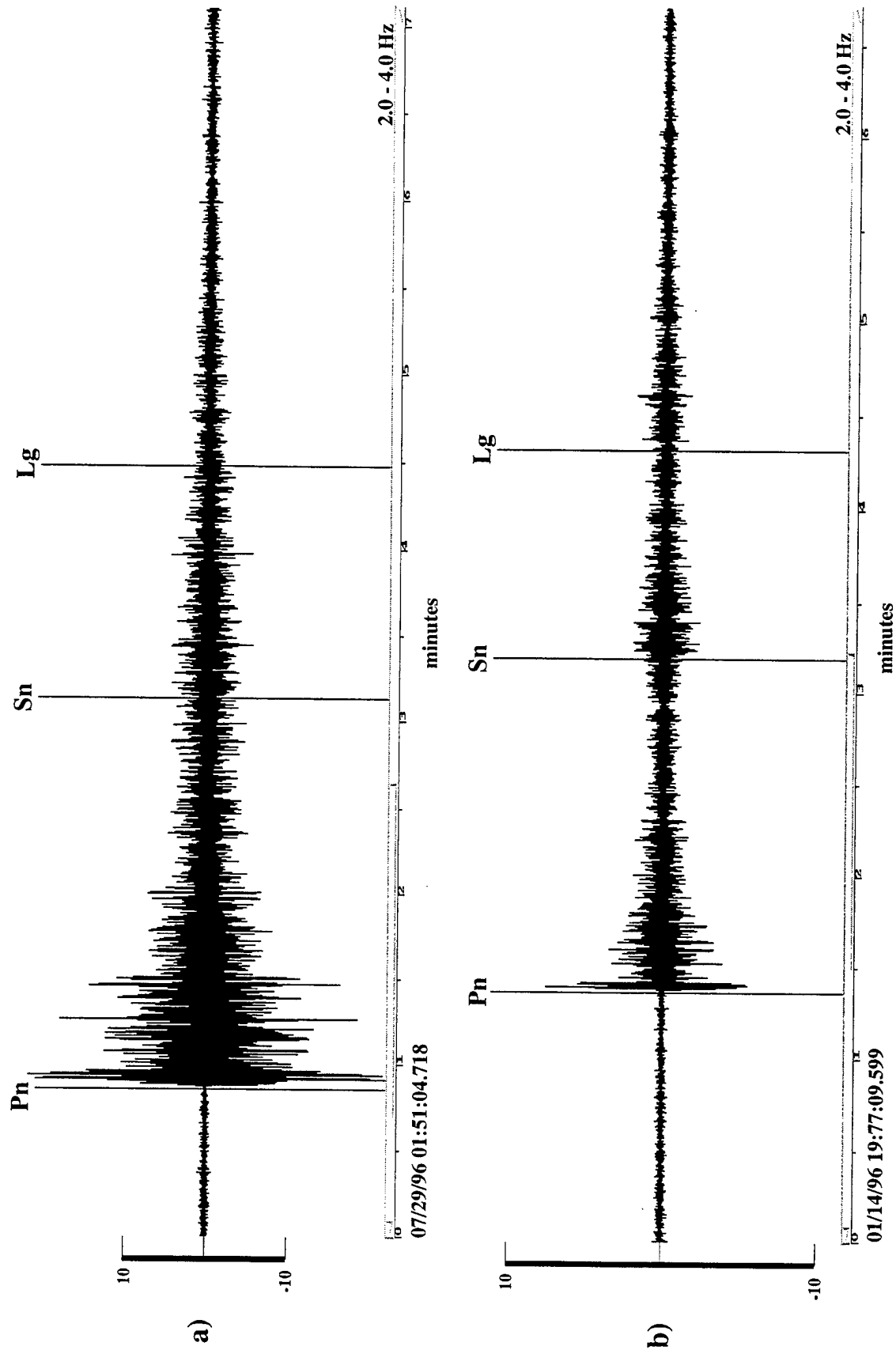
Figure 24. Comparison of two events from the Lop Nor region recorded at ZAL. a) July 1996 Lop Nor nuclear explosion with magnitude 4.7 mb recorded approximately 1350 km away. (b) earthquake with magnitude 3.7 mb recorded
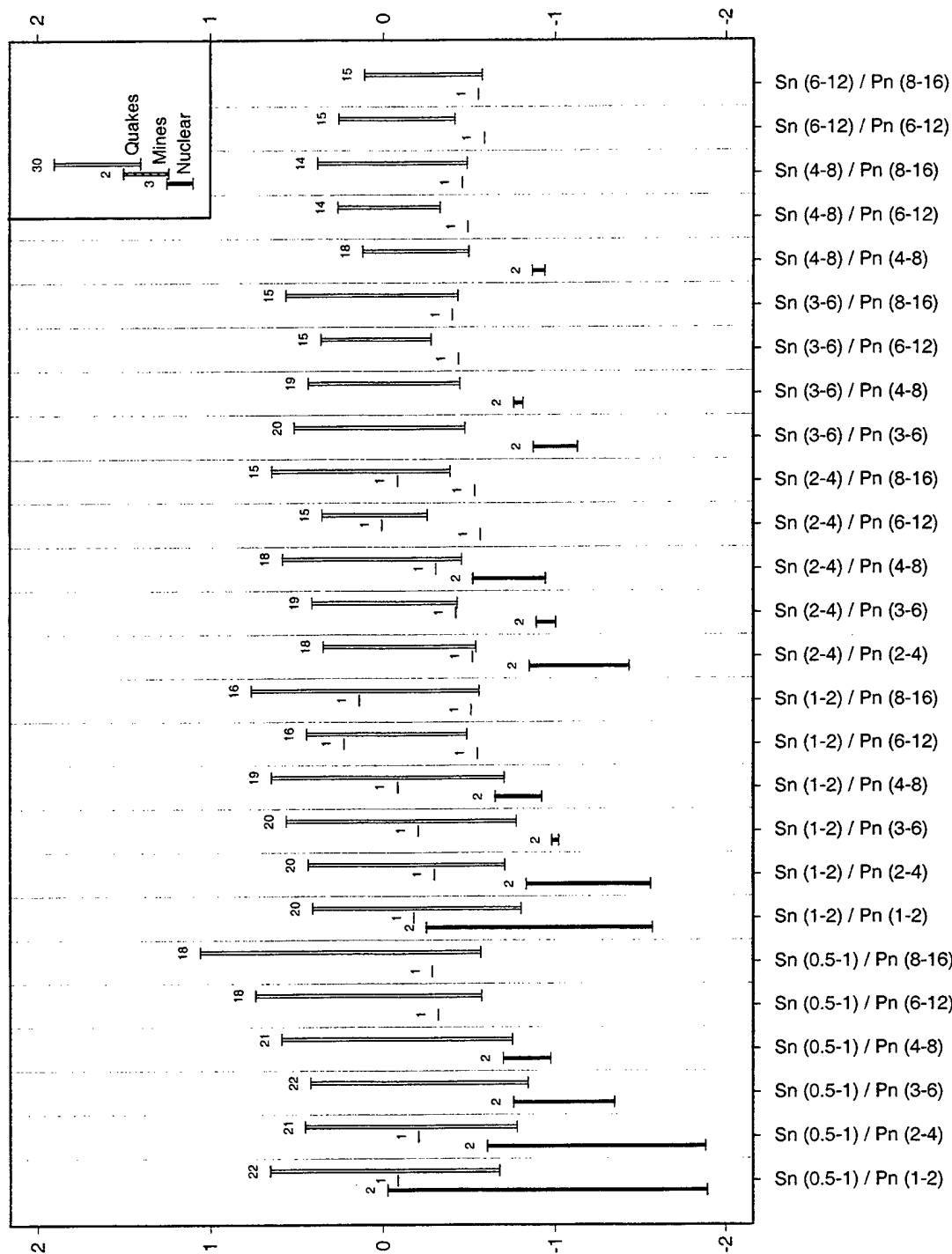
Figure 25. Summary of normalized Sn/Pn amplitude ratios for earthquake and explosion populations found in central Asia. Bars represent range of Sn/Pn ratios. The number of events in each population is indicated.

6.3.3 Largest *S* / Earliest *P*

The normalized ratio between the Largest *S* (*Sn* or *Lg*) and Earliest *P* (*Pn* or *Pg*) performs similarly to the *Lg/Pn* or the *Sn/Pn* discriminants. An advantage is that it can be computed for more stations and more events than a phase-specific ratio. Results from this ratio are summarized in Figure 26 for the central Asia subnetwork. The ratio for all other subnetworks is provided in Appendix C. As determined for the other variants of the *S/P* discriminant, this ratio tends to be lowest for nuclear explosions and only slightly lower for industrial explosions than for earthquakes. Again, there is considerable overlap between all three populations in some cases.

Similar to *Lg/Pn* and *Sn/Pn*, the best separation is provided by the *S*(LF)/*P*(MF) and *S*(MF)/*P*(MF) ratios. Typically, the largest *S* is *Lg* at short distances and in the lower frequency bands where *Lg/Pn* worked best. Conversely, *Sn* is typically the largest *S* at longer distances and higher frequencies. All high-frequency (6-12 and 8-16 Hz) *S* phases are *Sn* as we did not derive distance corrections for *Lg* above 6 Hz. Also, several stations were excluded from the high-frequency bands because their Nyquist frequency was only 10 Hz.
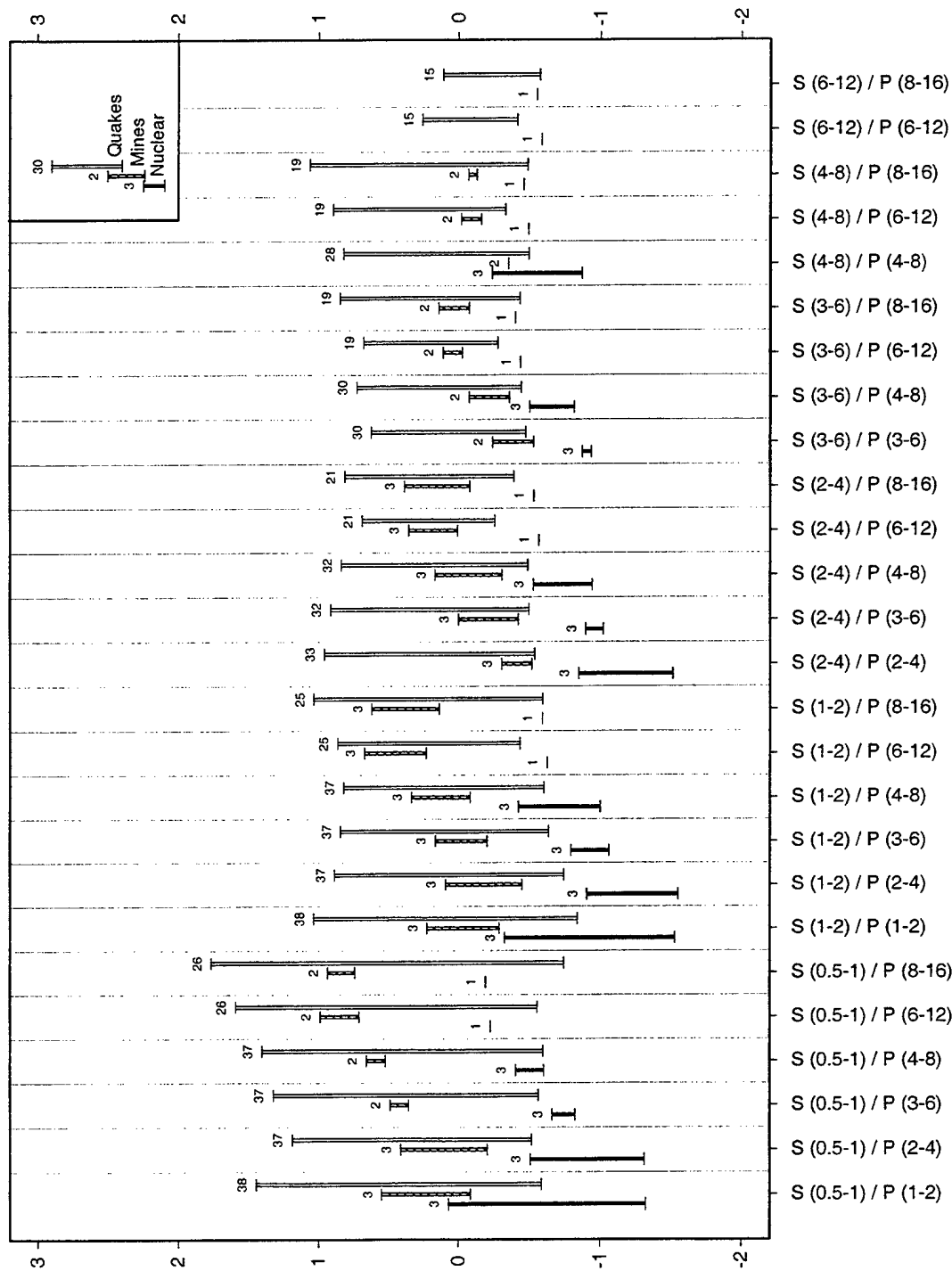
Figure 26. Summary of normalized Largest *S* / Earliest *P* amplitude ratios for earthquake and explosion populations found in central Asia. Bars represent range of *S/P* ratios. The number of events in each population is indicated.

7. Transportability

This section evaluates the transportability of the attenuation models and *S/P* discriminant to uncalibrated regions. We address transportability of the attenuation by estimating average models for stable and tectonic environments and comparing them to region specific models. We evaluate transportability of the *S/P* discriminant by combining distance- and source-corrected *S/P* ratios for all regions and categorizing them by source-type: earthquake, industrial explosion and nuclear explosion.

7.1 Attenuation

We combined data sets from subnetworks with similar geologic and tectonic environments to estimate the average attenuation for *"tectonic"* and *"stable"* regions. Southern Europe was excluded from the combined tectonic model because many paths crossed both tectonic and stable regions. Japan was excluded because of the overall complexity of the structural setting. Southern Africa was also excluded due to inadequate coverage of regional phases.

AmpInv was applied to both of the combined data sets to estimate frequency-dependent source and attenuation parameters for tectonic and stable environments.

7.1.1 Tectonic Environments

The data set for the tectonic environment includes amplitude measurements from the Alaska, western North America, southern Asia, and South America subnetworks. AmpInv results are shown in Table 5.

Table 5: Tectonic Model Inversion Results.

phase	*count*	*c*	κ	α	*a*	*b*	|*site*|	σ
Pn	1201	20.0	0.00	-0.08	0.04	2.28	0.26	0.40
Pg	180	20.0	0.24	0.14	0.19	2.12	0.31	0.34
Sn	182	20.0	0.88	0.00	0.06	3.19	0.45	0.29
Lg	378	20.0	0.82	0.26	0.34	2.29	0.35	0.32

Estimated values for the long-period source level S_0 were as expected with log S_0 increasing linearly with magnitude with a slope near one. This model achieved an overall standard deviation of 0.38. The median site corrections for this model range between 0.26 to 0.45 for all phases. The estimated attenuation model is shown in Figure 27 along with one standard deviation. This figure shows the estimated attenuation in log amplitude units versus distance at 3 Hz for each regional phase. Our results for the individual models (see Appendix B) are also plotted in Figure 27 using different line types for each subnetwork. The average tectonic attenuation model shown also fits our amplitude measurements made in other frequency bands. Most of the region-specific models fit within one standard deviation of the combined tectonic model with the exception of southern Asia for Pn and Sn.

Tectonic Attenuation Model
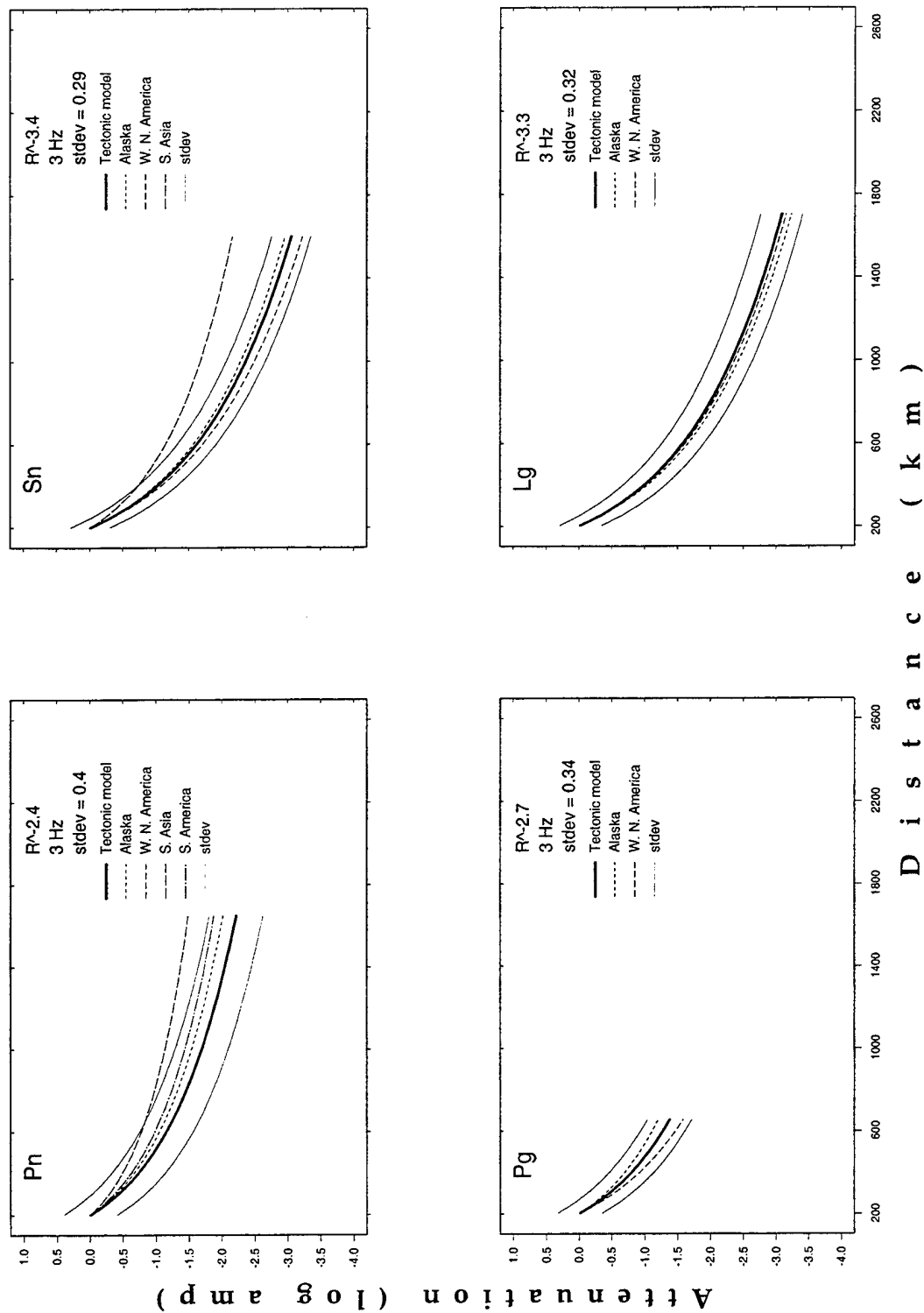
Figure 27. Attenuation curves at 3 Hz for each regional phase recorded along paths travelled in a tectonic environment. The Pn curve for western North America is nearly equivalent to the Tectonic model curve.

7.1.2 Stable Environments

The data set for the stable environment includes amplitudes from the eastern North America, Australia, and central Asia subnetworks. AmpInv results are shown in Table 6.

Table 6: Stable Model Inversion Results.

phase	*count*	*c*	κ	α	*a*	*b*	|*site*|	σ
Pn	561	15.0	0.00	-0.25	0.08	1.44	0.82	0.30
Pg	72	15.0	0.72	-0.02	0.22	2.15	1.02	0.25
Sn	241	15.0	0.78	-0.25	0.12	1.85	0.79	0.24
Lg	365	15.0	1.14	0.06	0.41	1.46	0.86	0.27

The long-period source levels for this data set were also as expected with log S_0 increasing linearly with magnitude with a slope near one. This model achieved an overall standard deviation of 0.28. The median site corrections range between about 0.8 and 1.0. The estimated attenuation model at 3 Hz is shown in Figure 28. Our results for the individual models (see Appendix B) are also plotted in Figure 28 using different line types for each subnetwork. The fit of the model shown in Figure 28 is similar to that found at the other frequencies. The region-specific models fit within one standard deviation of the combined stable model in most cases with the exception of Australia for Pg and central Asia for Lg.

7.1.3 Comparison of Tectonic and Stable Environments

The attenuation rates for the average stable and tectonic models are compared in Figure 29. The models are plotted for 3 Hz along with their standard deviations. As expected, the attenuation is greater for the tectonic model than for the stable model for *Pn, Sn,* and *Lg*. There was not enough *Pg* data to make a meaningful conclusion. Also as expected, the variance of the tectonic model is greater than the variance of the stable model.

The average tectonic and stable models are expected to provide adequate path and source corrections for *S/P* discriminants in uncalibrated regions. However, region-specific models are preferred when sufficient data are available.

7.2 Discrimination

Earthquakes were used to estimate source parameters. Therefore, the normalized *S/P* ratios are expected to have zero mean for earthquakes independent of geographic region. An example is shown in the top panel of Figure 30. This shows the *Sn*(2-4 Hz)/*Pn*(3-6 Hz) ratio for all subnetworks after application of region-specific path and source corrections. The mean is -0.06 and the standard deviation is 0.32. The middle panel shows the same ratio for presumed industrial explosions. The mean is less than the earthquakes but there is substantial overlap between the two populations, which is consistent with earlier studies [*Bennett et al.*, 1993]. All four nuclear explosions have much lower ratios than the earthquakes or industrial explosions.

Stable Attenuation Model
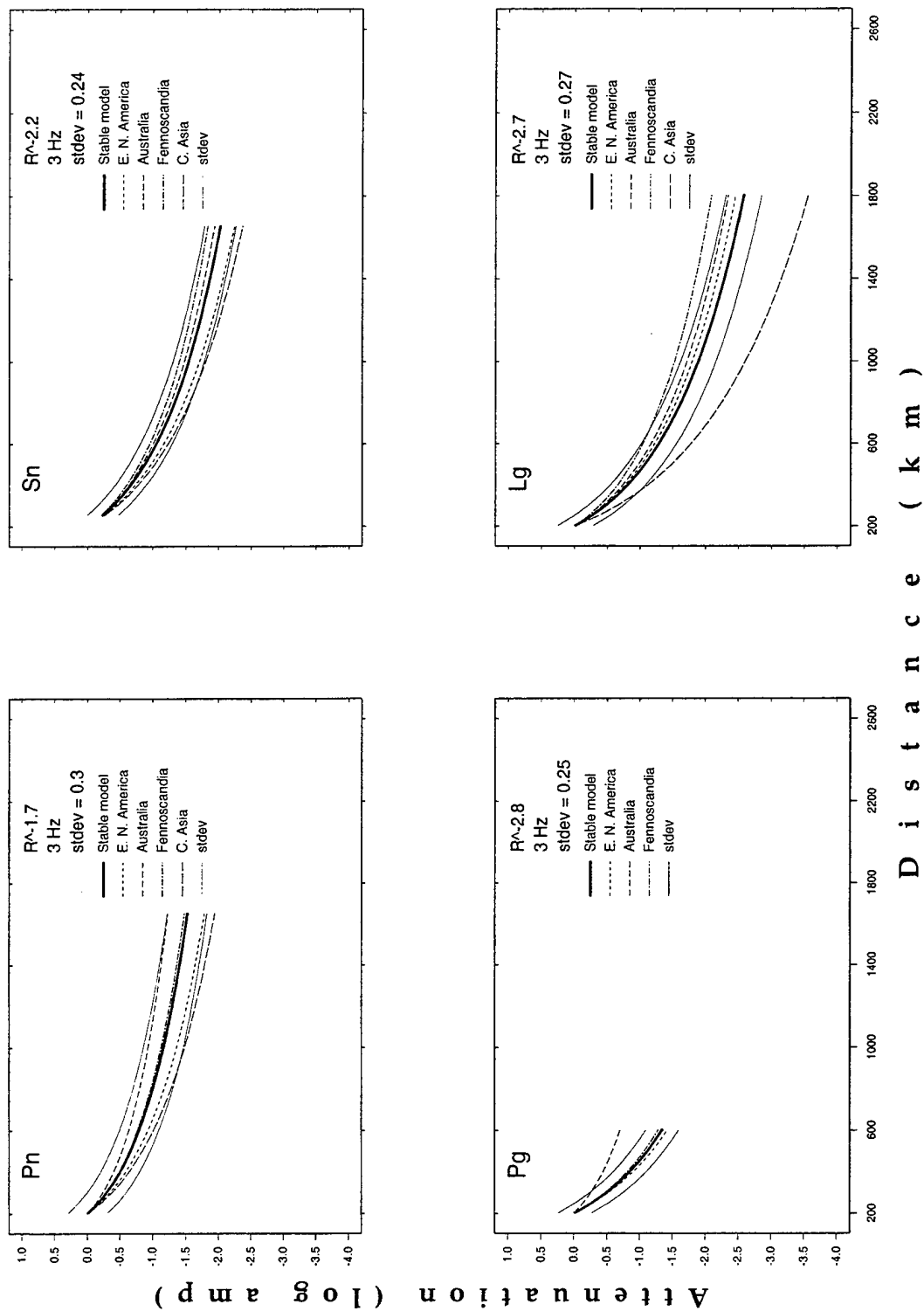
Figure 28. Attenuation curves at 3 Hz for each regional phase recorded along stable paths.

Tectonic and Stable Attenuation Models
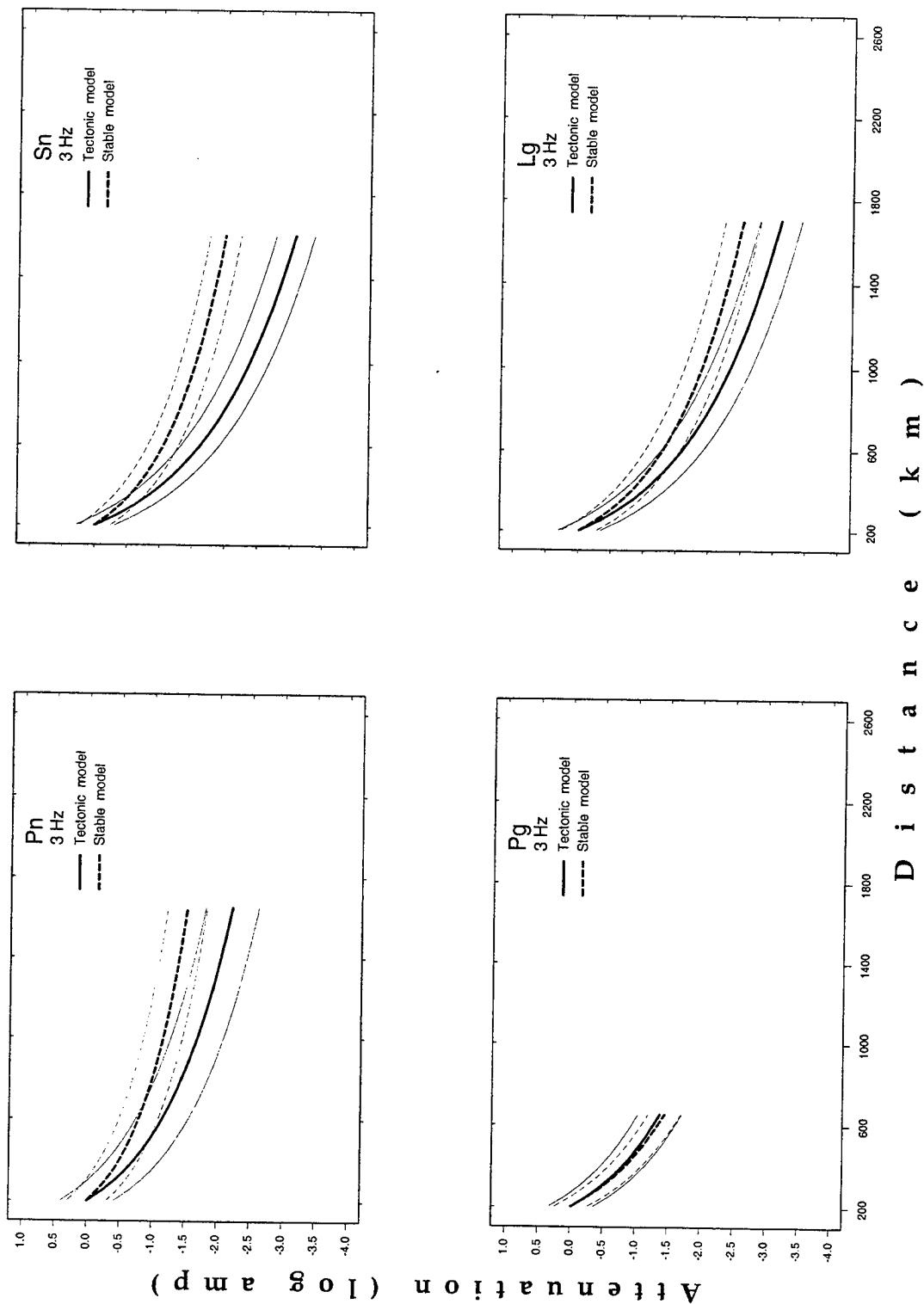
Figure 29. Comparison of attenuation curves for each regional phase at 3 Hz as estimated for tectonic and stable environments.

All Data Sets Combined
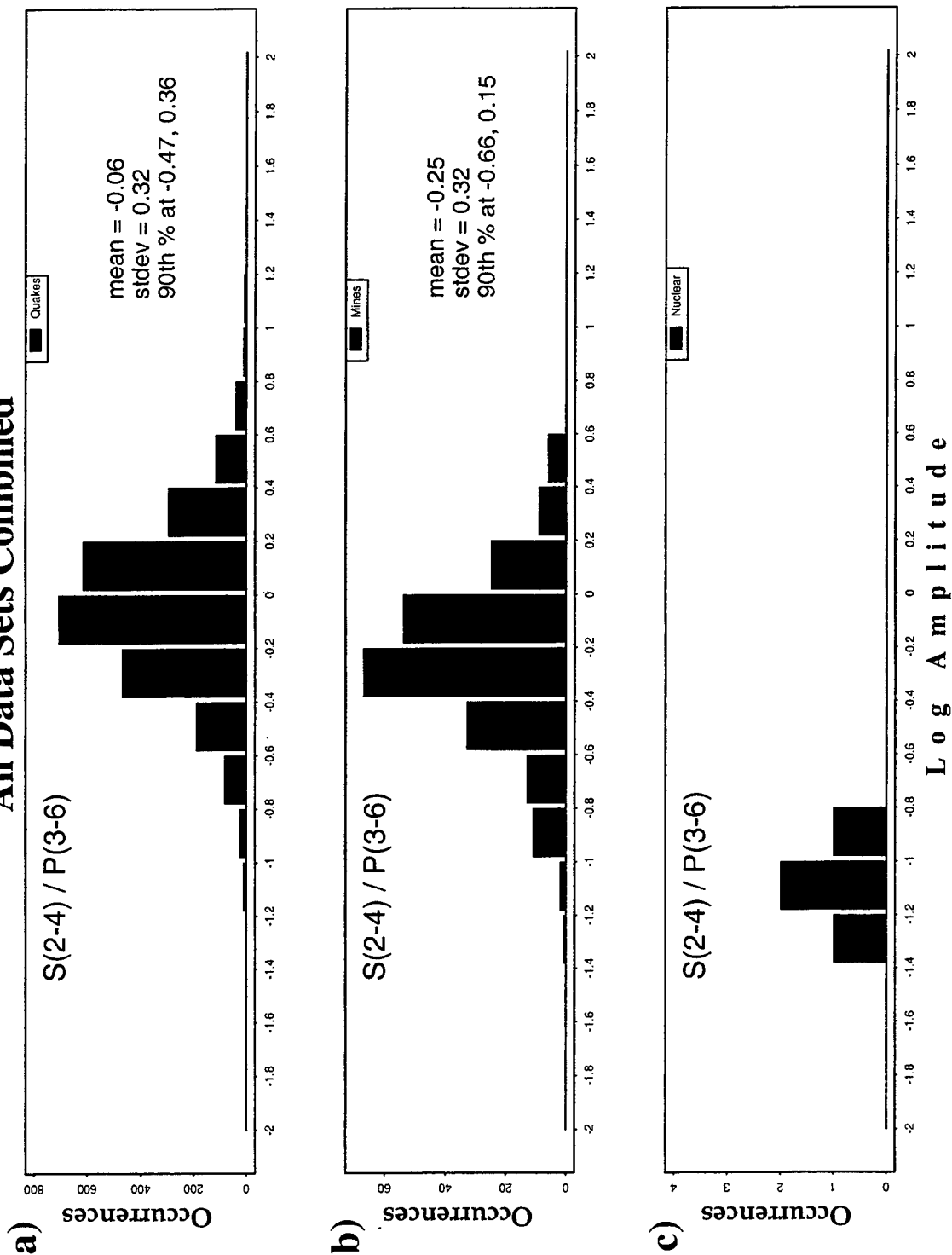
Figure 30. Evaluation of normalized S_n (2-4 Hz) / P_n (3-6 Hz) discriminant using a) earthquakes, b) presumed industrial explosions, and c) nuclear explosions combined from our subnetworks.

a)

Occurrences

0   200   400   600   800

S(2-4) / P(3-6)

Quakes

mean = -0.06
stdev = 0.32
90th % at -0.47, 0.36

b)

Occurrences

0   20   40   60

S(2-4) / P(3-6)

Mines

mean = -0.25
stdev = 0.32
90th % at -0.66, 0.15

c)

Occurrences

0   1   2   3   4

S(2-4) / P(3-6)

Nuclear

L o g   A m p l i t u d e

53

The consistency of the earthquake and industrial explosion populations for many regions suggests that the *S/P* discriminant is likely to be transportable as long as attenuation and source models are available for each region. Unfortunately, we do not have nuclear explosions for more than one region in our data set. However, comparison to previous studies suggests that nuclear explosions in other regions have low *S/P* ratios in comparison to earthquakes [e.g., *Gupta and Burnetti*, 1981; *Bennett and Murphy*, 1986; *Walter et al.*, 1995; *Hartse et al.*, 1997; and *Kim et al.*, 1997].

8. Conclusions

We inverted frequency-dependent regional-wave amplitudes recorded by nine subnetworks of the pIDC in varying geologic and tectonic environments for source and attenuation models. These models were used to normalize and evaluate variants of the *S/P* regional discriminant using a data set of earthquakes, presumed industrial explosions, and a few nuclear explosions from the Lop Nor test site. We evaluated the performance of *S/P* discriminants for each subnetwork and the transportability of these discriminants to uncalibrated regions. The primary conclusions are:

1. The *rms* or *stav* amplitude measurements on filtered incoherent beams provide stable results for regional attenuation and discrimination studies. It was determined that peak amplitudes have greater variance and that high-frequency amplitudes on coherent beams are contaminated by signal loss. Spectral amplitudes were not thoroughly evaluated, but they are expected to be a good alternative.

2. Automated quality control of measurements is difficult, especially for *Lg* which uses a group velocity window that can be up to two minutes in duration at far-regional distances. Unrelated signals from local noise sources or other events can contaminate the regional-wave amplitude measures. We found it necessary to restrict our analysis to phases that were confirmed by pIDC analysts to avoid these type of problems in our data set.

   The length of the *Pn* measurement window was also a problem for two of the Lop Nor nuclear explosions. These had to be re-measured after visual inspection of the waveforms. The original automated measurements produced an *S/P* ratio that was typical for earthquakes.

3. Regional-wave attenuation and source models were developed for each of nine pIDC subnetworks using *rms* measurements. The standard deviation of the observed log amplitudes with respect to the model is about 0.27.

   The source models are consistent with independent magnitude estimates. The long-period level increases linearly with magnitude with a slope between 2/3 and 1. The corner frequency as a function of magnitude is consistent with previous studies [*Bungum et al.*, 1982; *Mueller and Cranswick* 1985].

   The attenuation results are consistent with previous studies [*Chun*, 1989; *Sereno*, 1990]. *Lg* attenuates more rapidly than *Sn* or *Pn*, and *Sn* attenuates more rapidly than *Pn*. The attenuation of *Pn*, *Sn*, and *Lg* increases with frequency, as expected. The *Pg* attenuation was not well-constrained for most regions because too few data were available.

4. The distance and source dependence of *S/P* ratios can be effectively removed by applying corrections based on the source and attenuation models. Attenuation models remove the distance dependence. Source models (including corner frequency) remove the magnitude dependence

5. Variants of the normalized *S/P* regional discriminant are successful at separating nuclear explosions from earthquakes. The discriminants: *Lg/Pn*, *Sn/Pn* and Largest *S/Earliest P* all perform reasonably well. The Largest S/Earliest P is available for more events than

the phase-specific ratios. We find that $S(LF)/P(MF)$ and $S(MF)/P(MF)$ ratios perform better than the other S/P variants. None of the ratios with $P(LF)$ performed very well. The results in the HF bands were mixed. In most cases the use of HF limited the number of events that could be evaluated due to the *snr* criterion.

6. Variants of the normalized S/P regional discriminant were not very successful at separating industrial explosions from earthquakes. The median S/P was generally lower for industrial explosions than for earthquakes, but there was substantial overlap.

7. The attenuation and source models appear to be transportable to uncalibrated regions. In most cases, subnetworks in similar geologic/tectonic environments exhibit similar regional-wave attenuation rates and their models are generally within one standard deviation of the average "stable" or "tectonic" model. The standard deviation obtained for the average stable model is about 0.28 log amplitudes units. It is about 0.38 for the average tectonic model. These are not much different than the region-specific models. As expected, the attenuation in tectonic regions is greater than in stable regions.

8. The S/P discriminant is likely to be transportable to uncalibrated regions, assuming attenuation and source models are available. Normalized S/P ratios for earthquakes in all nine subnetworks are consistent with a normal distribution with a mean near zero and standard deviation of about 0.32. Similar results were obtained for industrial explosions in several subnetworks. The normalized S/P distributions for earthquakes and industrial explosions can be used by outlier detection algorithms to flag events as possible nuclear explosions [*Fisk et al.*, 1993]. The Lop Nor explosions in our data set have lower S/P ratios than earthquakes in central or southern Asia. Previous studies have found similar results in other regions [e.g., *Gupta and Burnetti*, 1981; *Bennett and Murphy*, 1986; *Walter et al.*, 1995; *Hartse et al.*, 1997; and *Kim et al.*, 1997].

References

Baumgardt, D., and G. Young, Regional seismic waveform discriminants and case-based event identification using regional arrays, *Bull. Seismol. Soc. Am.*, *80*, 1874-1892, 1990.

Baumgardt, D., J. Carney, M. Maxson and S. Carter, Evaluation of regional seismic discriminants using the Intelligent Seismic Event Identification System, *Tech. Rep. SAS-TR-93-38*, ENSCO, Inc., Springfield, Virginia, 96 pp., 1992.

Bennett, J., and J. Murphy, Analysis of seismic discrimination capabilities using regional data from western United States events, *Bull. Seismol. Soc. Am.*, *76*, 1069-1086, 1986.

Bennett, J., B. Barker, K. McLaughlin, and J. Murphy, Regional discrimination of quarry blasts, earthquakes, and underground nuclear explosions, *Final Rep. GL-TR-89-0114*, 146 pp., 1989, ADA223148

Bennett, J., A. Campanella, J. Scheimer, and J. Murphy, Demonstration of regional discrimination of Eurasian seismic events using observations at Soviet IRIS and CDSN stations, *Final Rep. PL-TR-92-2090*, 122 pp., 1992, ADA253275

Bennett, J., J. Scheimer, A. Campanella, and J. Murphy, Seismic characteristics of rockbursts for use in discrimination, *Sci. Rep. PL-TR-93-2059*, 89 pp., 1993, ADA266063

Blandford, R., Seismic discrimination problems at regional distances, in *Identification of Seismic Sources - Earthquake or Nuclear Explosion*, E. S. Husebye and S. Mykkeltveit (Ed.), D. Reidel Publishing Co., Dordrecht, The Netherlands, 695-740, 1981.

Bungum, H., S. Vaage, and E. Husebye, The Meløy earthquake sequence, northern Norway; Source parameters and their moment scaling relations, *Bull. Seismol. Soc. Am.*, *72*, 197-206, 1982.

Chan, W., R. Baumstark, and R. Cessaro, Spectral discrimination between explosions and earthquakes in central Eurasia, *Tech. Rep. GL-TR-90-0217*, 38 pp., 1990, ADA230048

Chun, K., R. Kokoski, and G. West, High-frequency *Pn* attenuation in the Canadian Shield, *Bull. Seismol. Soc. Am.*, *79*, 1039-1053, 1989.

Dysart, P., and J. Pulli, Regional seismic event classification at the NORESS array: seismological measurements and the use of trained neural networks, *Bull. Seismol. Soc. Am.*, *80*, 1910-1933, 1990.

Fisk, M. D., H. L. Gray, and G. D. McCartor, Applications of generalized likelihood ratio tests to seismic event identification, *Final Rep. PL-TR-93-2221*, 96 pp., 1993, ADA279479.

Gupta, I., and J. Burnetti, An investigation of discriminants for events in Western USSR based on regional phases recorded at station Kabul, *Bull. Seismol. Soc. Am.*, *71*, 263-274, 1981.

Hartse, H. E., S. R. Taylor, W. S. Phillips, and G. E. Randall, A Preliminary Study of Regional Seismic Discrimination in Central Asia with Emphasis on Western China. *Bull. Seis. Soc. Am.* 87, 551-568, 1997.

Jenkins, R.D., Users's Guide for the Amplitude Inversion Software (AmpInv), *Tech. Rep. SAIC-96/1132*, Science Applications International Corporation, 20 pp., 1998.

Kennett, B., (ed.), IASPEI 1991 Seismological Tables, Research School of Earth Sciences, Aus-

tralian National University, 167 pp., 1991.

Kerr, A., (ed.), Overview GSETT-3. Report prepared by the GSE Working Group on Planning, 9 pp., October, 1993.

Khalturin, Vitaly I., Tatyana G. Rautian, and Paul G. Richards. Statistics on Mine Blasting and Blasting Signals for the Former Soviet Union. F19628-95-C-0100, in *Proceedings of the 18th Annual Seismic Research Symposium on Monitoring a Comprehensive Test Ban Treaty, 4-6 September 1996*. PL-TR-96-2153, 918-925, 1996, ADA313692.

Kim, W.-Y., V. Aharonian, A. L. Lerner-Lam, and P. G. Richards, Discrimination of earthquakes and explosions in southern Russia using regional high-frequency three-component data from the IRIS/JSP Caucasus Network, *Bull. Seismol. Soc. Am., 87*, 569-588, 1997.

Lynnes, C., and R. Baumstark, Phase and spectral ratio discrimination in North America, *Tech. Rep. PL-TR-91-2212(II)*, 68 pp., 1991, ADA246673

Mueller, C. and E. Cranswick, Source parameters from locally recorded aftershocks of the 9 January 1982 Miramichi, New Brunswick, earthquake, *Bull. Seismol. Soc. Am., 75*, 337-360, 1985.

Mueller, R. and J. Murphy, Seismic characteristics of underground nuclear detonations, *Bull. Seismol. Soc. Am., 61*, 1675-1692, 1971.

Murphy, J., and J. Bennett, A discrimination analysis of short-period regional seismic data recorded at Tonto Forest Observatory, *Bull. Seismol. Soc. Am., 72*, 1351-1366, 1982.

Nuttli, O., On the attenuation of Lg waves in western and central Asia and their use as a discriminant between earthquakes and explosions, *Bull. Seismol. Soc. Am., 71*, 249-261, 1981.

Pomeroy, P., W. Best, and T. McEvilly, Test ban treaty verification with regional data - a review, *Bull. Seismol. Soc. Am., 72*, S89-S129, 1982.

Rodgers, A. J., T. Lay, W. R. Walter, and K. M. Mayeda, A comparison of regional-phase amplitude ratio measurement techniques, *Bull. Seismol. Soc. Am., 87*, 1613-1621, 1997.

Sereno, T.J., Attenuation of regional seismic phases in Fennoscandia and estimates of arrival time and azimuth uncertainty using data recorded by regional arrays, *Tech. Rep. SAIC-90/1472*, Science Applications International Corporation, 115 pp., 1990.

Sereno, T. and J. Given, Pn attenuation for a spherically symmetric earth model, *Geophys. Res. Lett., 17*, 1141-1144, 1990.

Taylor, S. R. and H. E. Hartse, A procedure for estimation of source and propagation amplitude corrections for regional seismic discriminants, *J. Geophys. Res., 103*, 2781-2789, 1998.

Taylor, S., M. Denny, E. Vergino, and R. Glaser, Regional discrimination between NTS explosions and western United States earthquakes at regional distances, *Bull. Seismol. Soc. Am., 79*, 1142-1176, 1989.

Walter W. R., K. M. Mayeda, and H. J. Patton, Phase and Spectral Ratio Discrimination between NTS earthquakes and explosions. Part I: Empirical Observations, *Bull. Seismol. Soc. Am., 85*, 1050-1067, 1995.

Wahl, D., Programmer's Guide for the Detection and Feature Extraction Program (DFX), *Tech. Rep. SAIC-96/1069*, Science Applications International Corporation, 77 pp., April 1996.

Willis, D., J. DeNoyer, and J. Wilson, Differentiation of earthquakes and underground nuclear explosions on the basis of amplitude characteristics, *Bull. Seismol. Soc. Am., 53*, 979-987, 1963.

Wuster, J., Discrimination of chemical explosions and earthquakes in central Europe - a case study, *Bull. Seismol. Soc. Am., 83*, 1184-1212, 1993.

Yang, X. R. North, and C. Romney, CMR Nuclear Explosion Database, *Tech. Rep. CMR-97/19*, Center for Monitoring Research, 81pp., May, 1997.

Appendix A: Ray Paths

This appendix contains maps with ray paths that display regional phase (e.g., *Pn*, *Pg*, *Sn*, *Lg*) coverage for ten subnetworks being evaluated for this study. Four shaded relief maps pertaining to *Pn*, *Pg*, *Sn*, and *Lg* arrivals are displayed for each subnetwork with the relevant stations overlaid on each map. See Section 3.2 for discussion of the criteria used in selecting the arrivals. The subnetworks displayed here include: 1) Alaska, 2) western North America, 3) eastern North America, 4) southern Europe, 5) southern Asia, 6) central Asia, 7) Australia, 8) Japan, 9) South America, and 10) southern Africa.
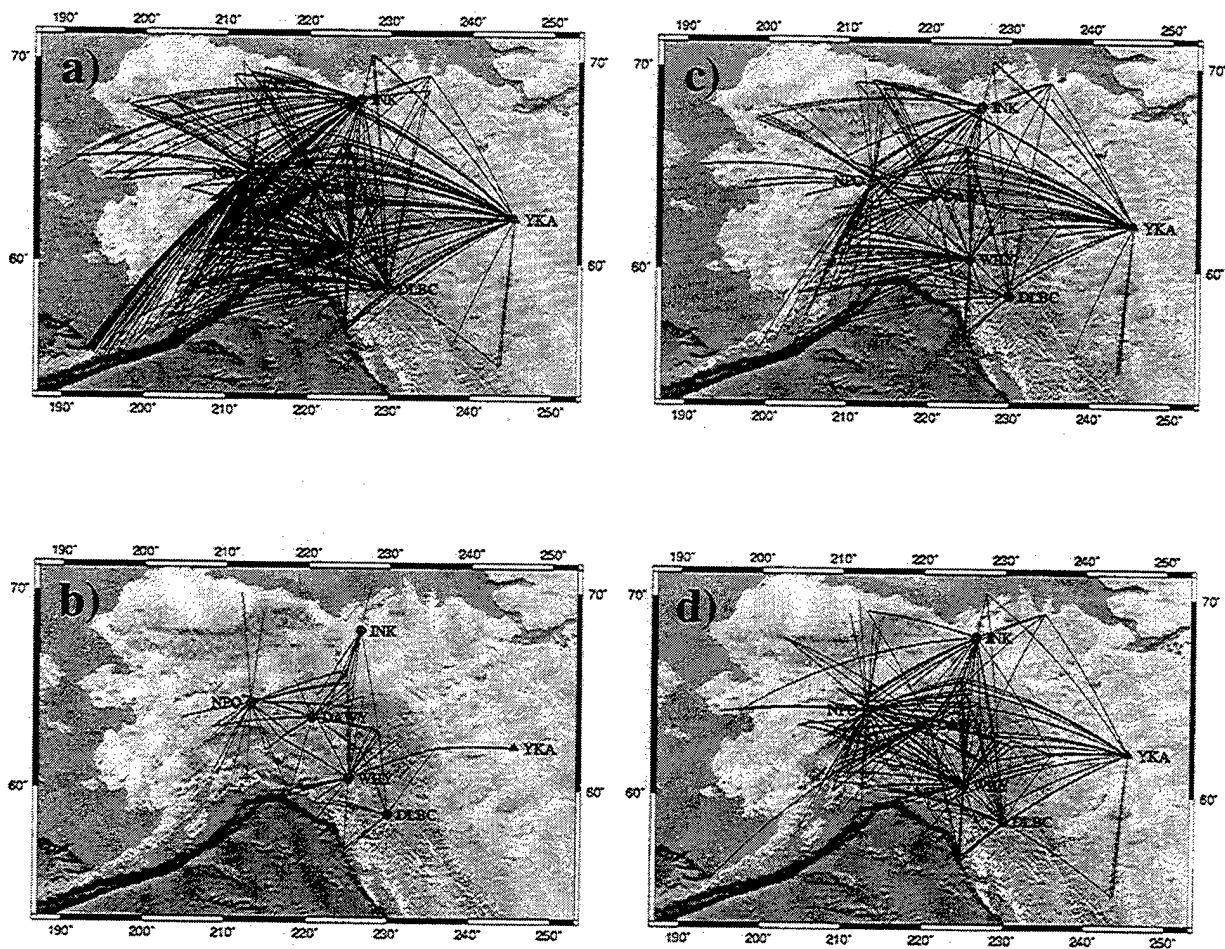
Figure A.1. Ray-path maps of regional arrivals used for Alaska. a) 505 *Pn* arrivals. b) 80 *Pg* arrivals. c) 210 *Sn* arrivals. d) 246 *Lg* arrivals.
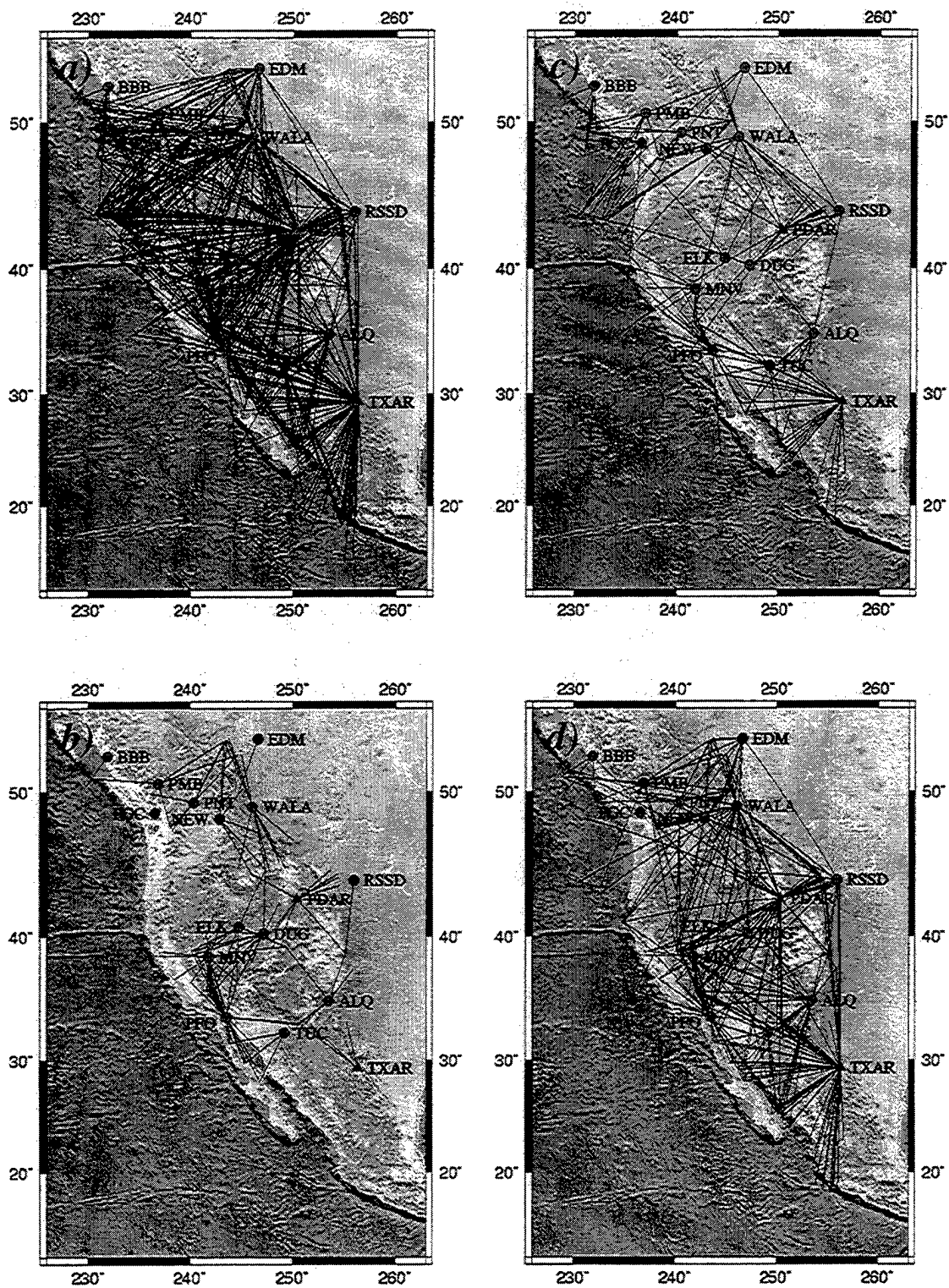
Figure A.2. Ray-path maps of regional arrivals used for western North America. a) 819 *Pn* arrivals. b) 125 *Pg* arrivals. c) 158 *Sn* arrivals. d) 386 *Lg* arrivals.
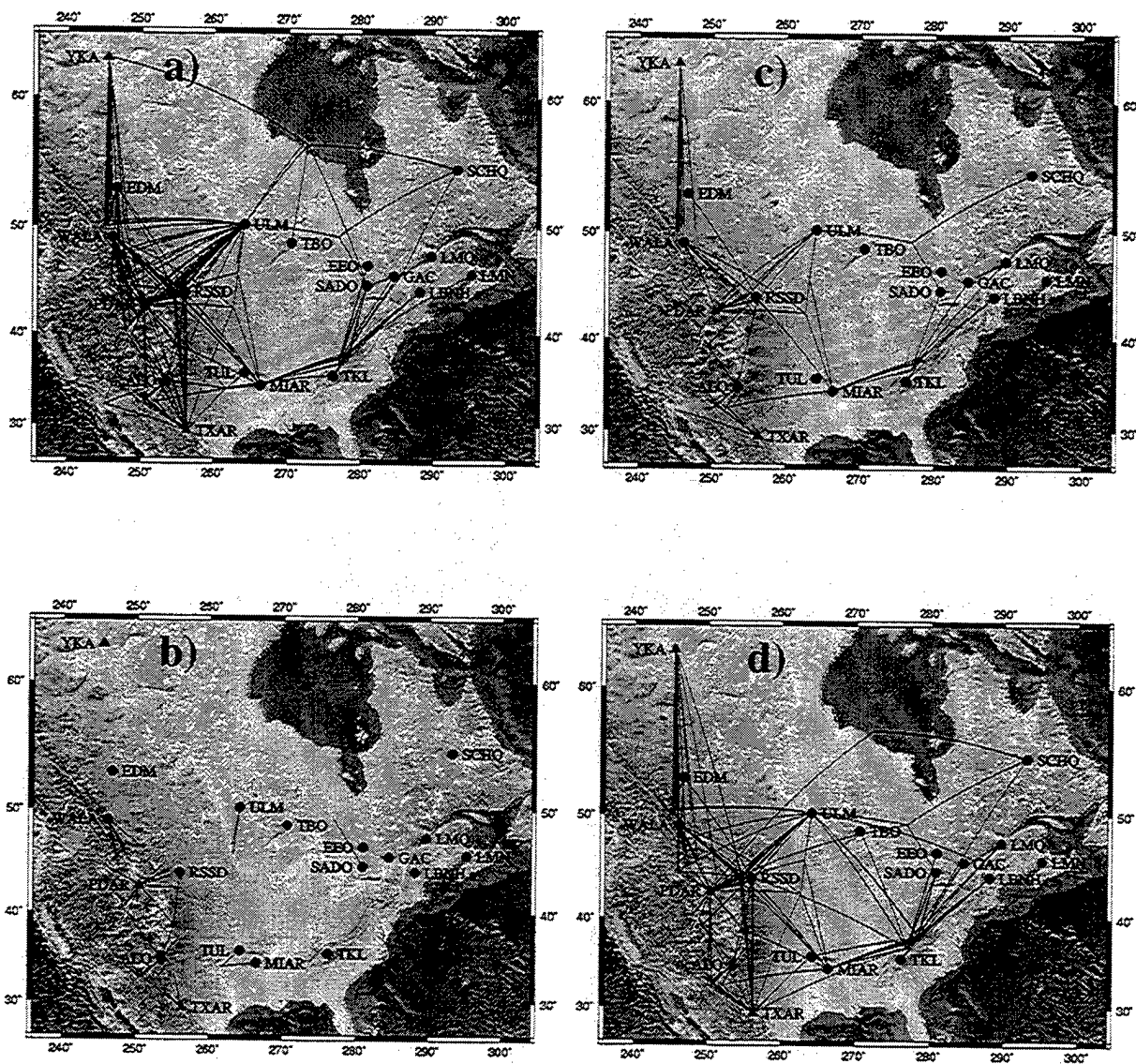
Figure A.3. Ray-path maps of regional arrivals used for eastern North America. a) 262 *Pn* arrivals. b) 36 *Pg* arrivals. c) 66 *Sn* arrivals. d) 201 *Lg* arrivals.
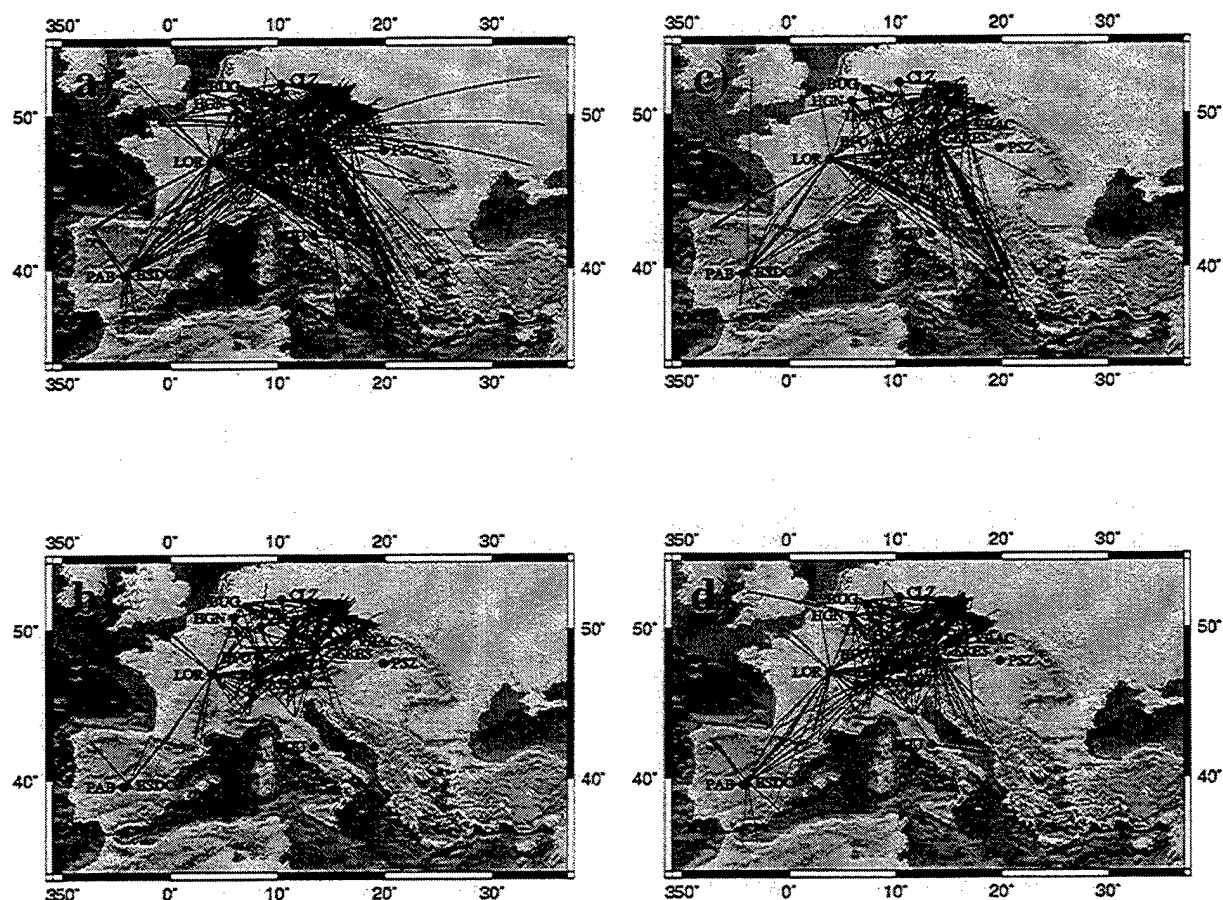
Figure A.4. Ray-path maps of regional arrivals used for southern Europe. a) 1316 *Pn* arrivals. b) 666 *Pg* arrivals. c) 444 *Sn* arrivals. d) 1092 *Lg* arrivals.
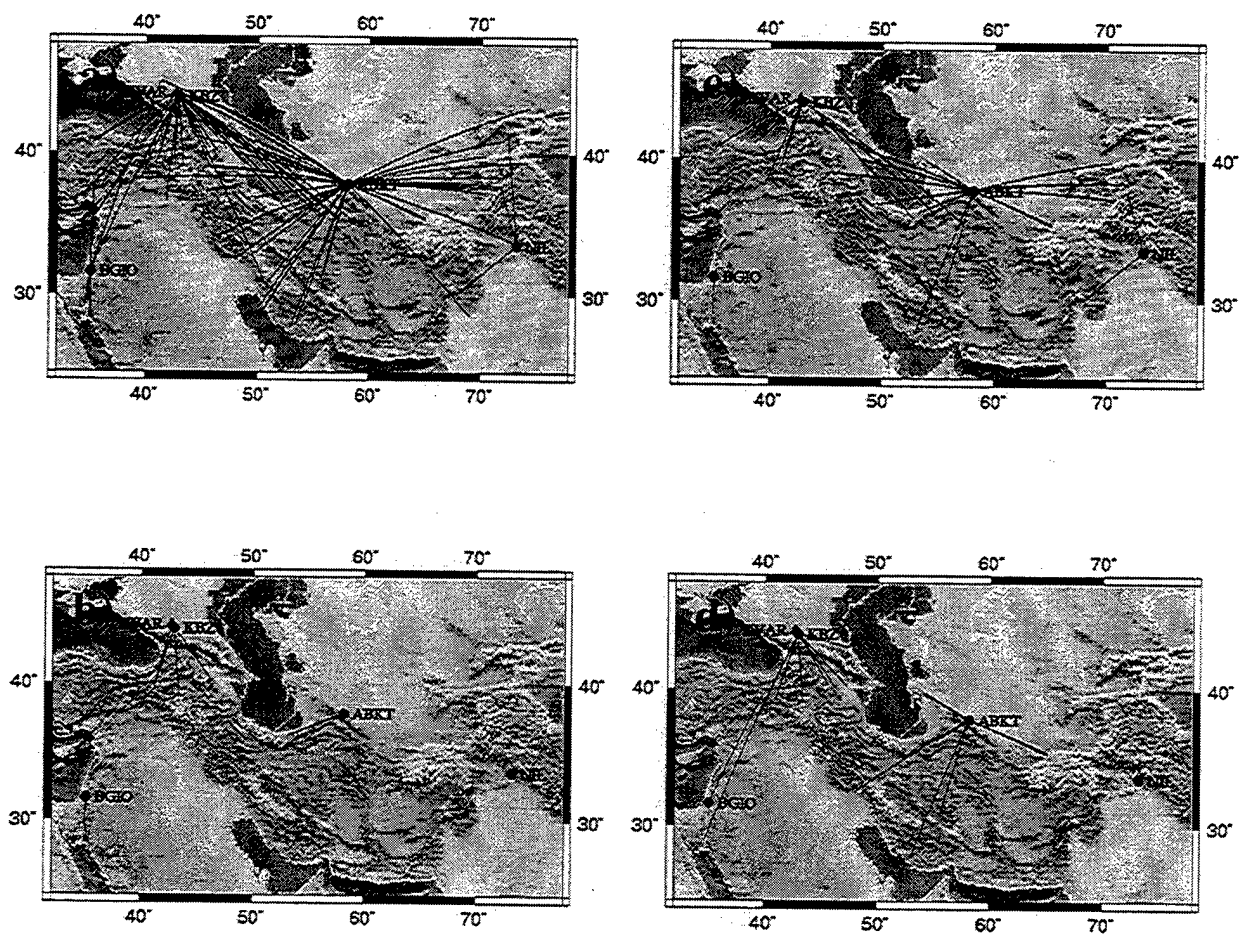
Figure A.5. Ray-path maps of regional arrivals used for southern Asia. a) 91 *Pn* arrivals. b) 7 *Pg* arrivals. c) 26 *Sn* arrivals. d) 17 *Lg* arrivals.
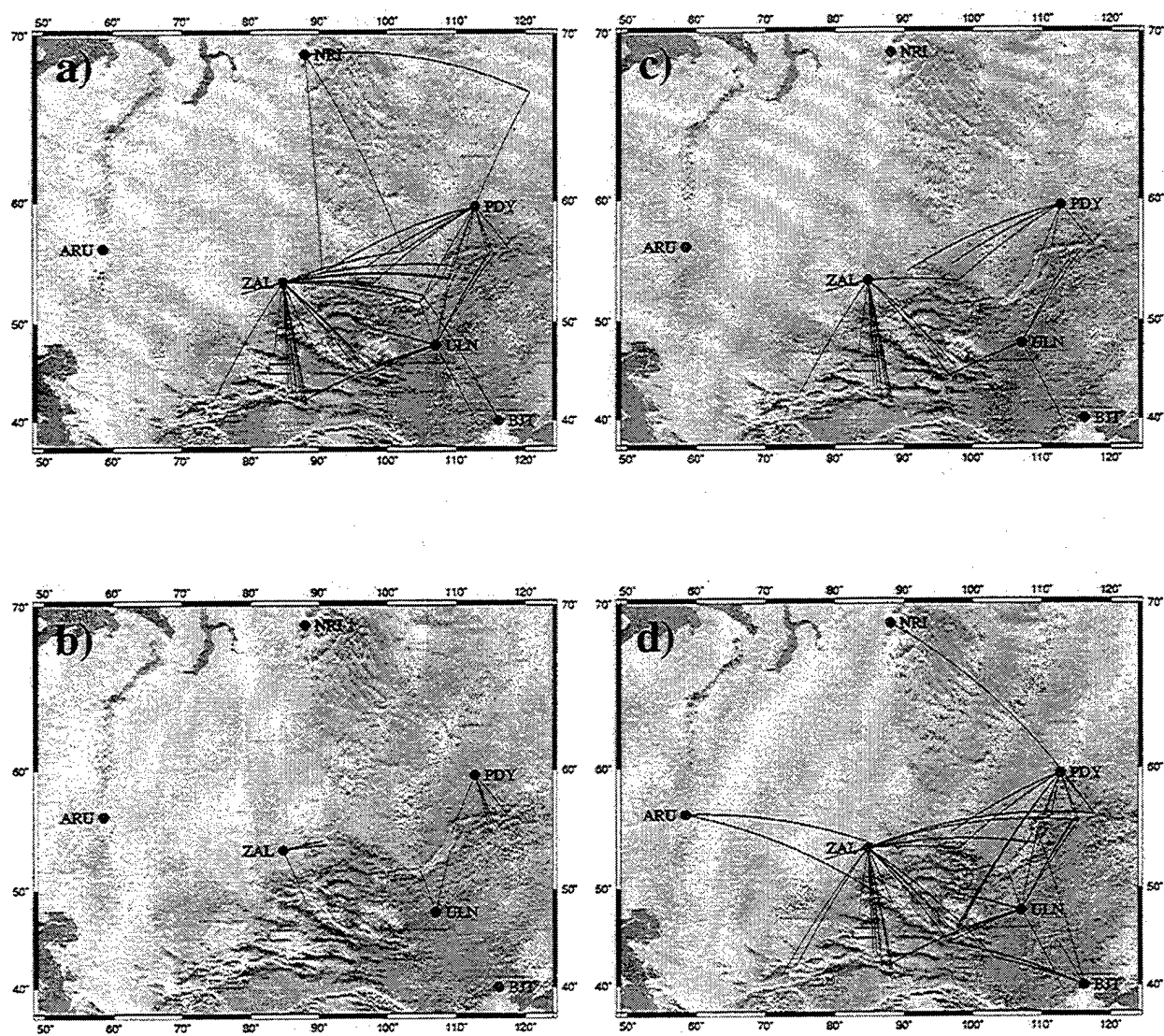
Figure A.6. Ray-path maps of regional arrivals used for central Asia. a) 53 *Pn* arrivals. b) 11 *Pg* arrivals. c) 23 *Sn* arrivals. d) 49 *Lg* arrivals.
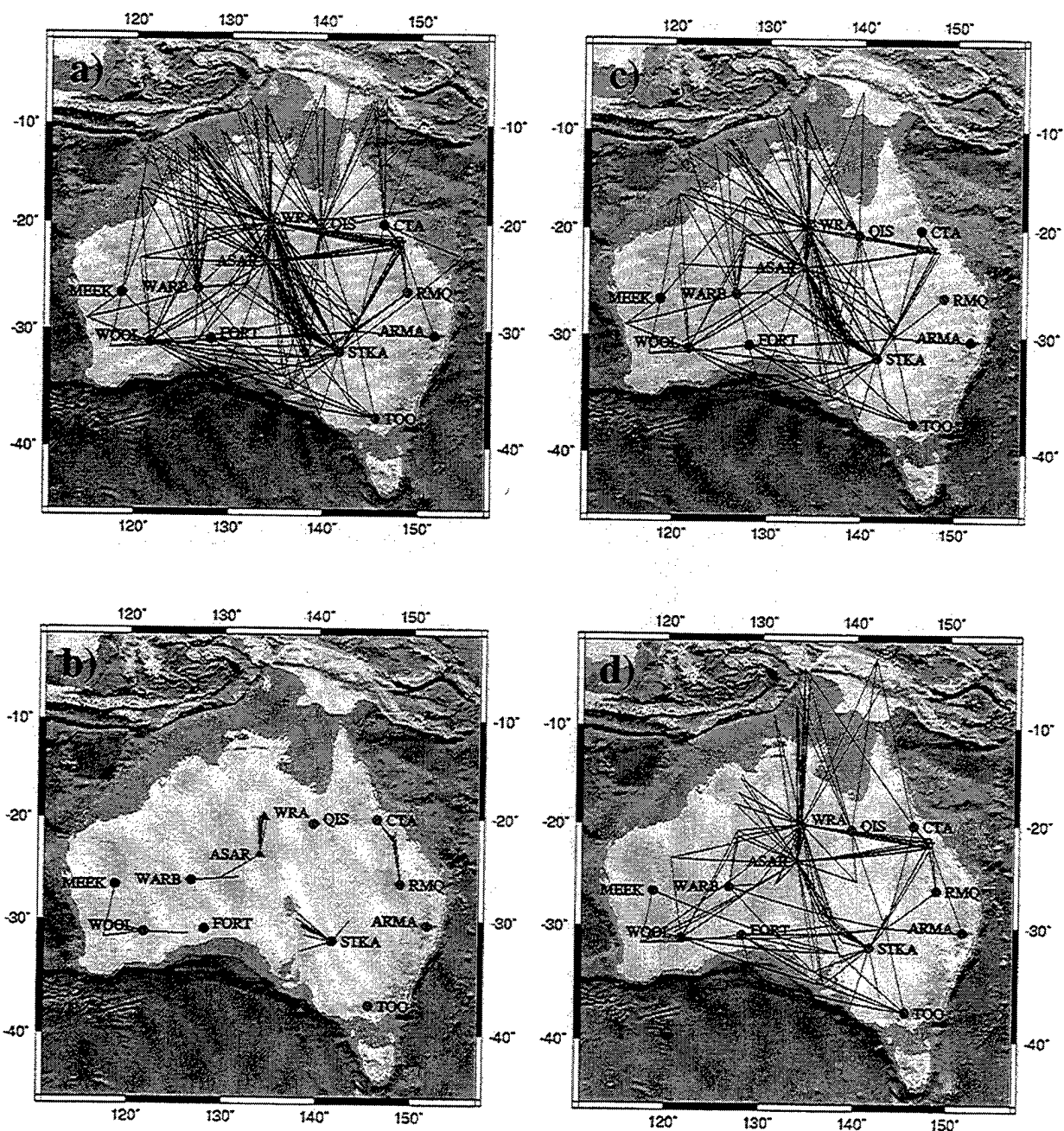
Figure A.7. Ray-path maps of regional arrivals used for Australia. a) 323 *Pn* arrivals. b) 33 *Pg* arrivals. c) 203 *Sn* arrivals. d) 157 *Lg* arrivals.
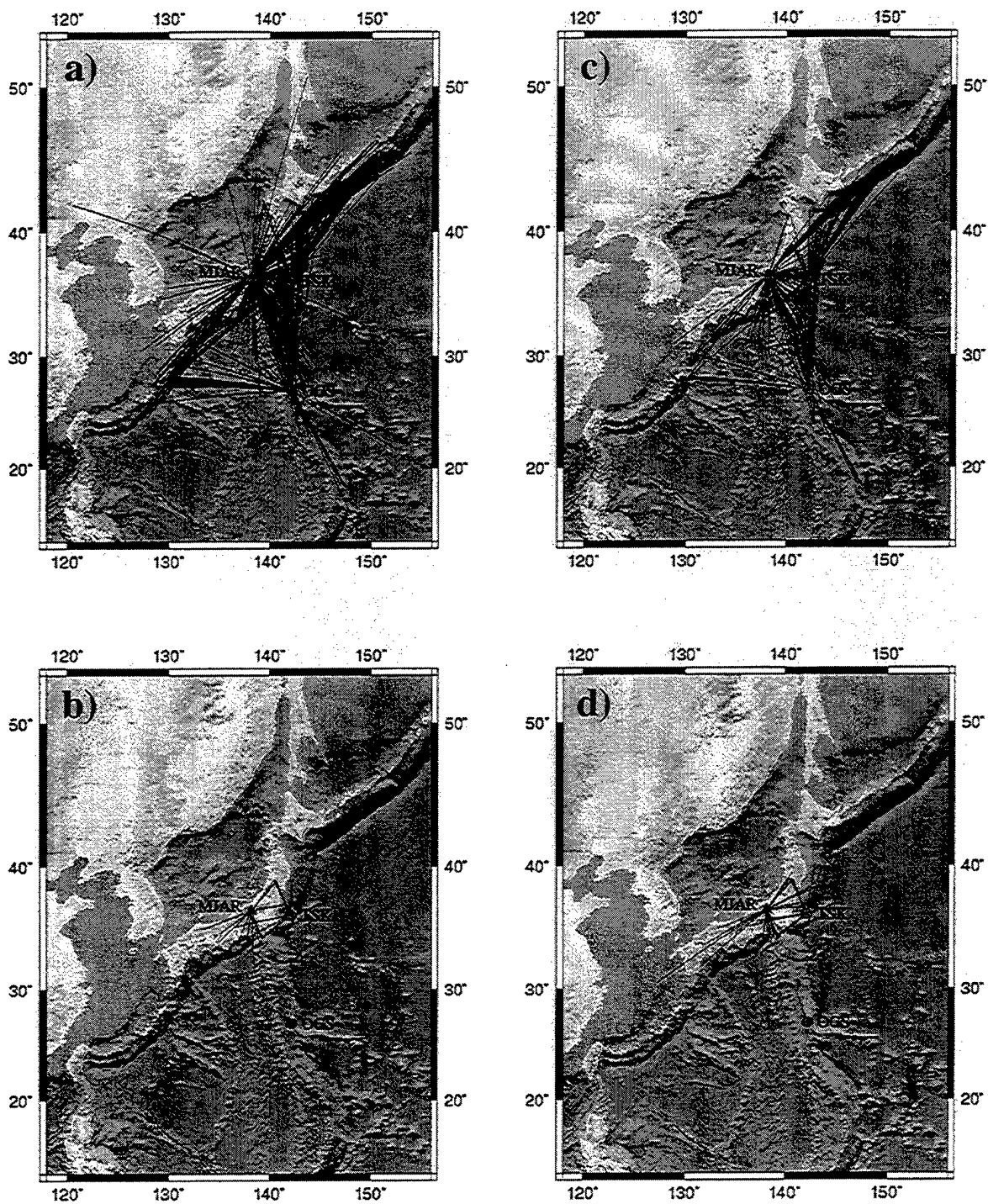
Figure A.8. Ray-path maps of regional arrivals used for Japan. a) 819 *Pn* arrivals. b) 41 *Pg* arrivals. c) 308 *Sn* arrivals. d) 70 *Lg* arrivals.
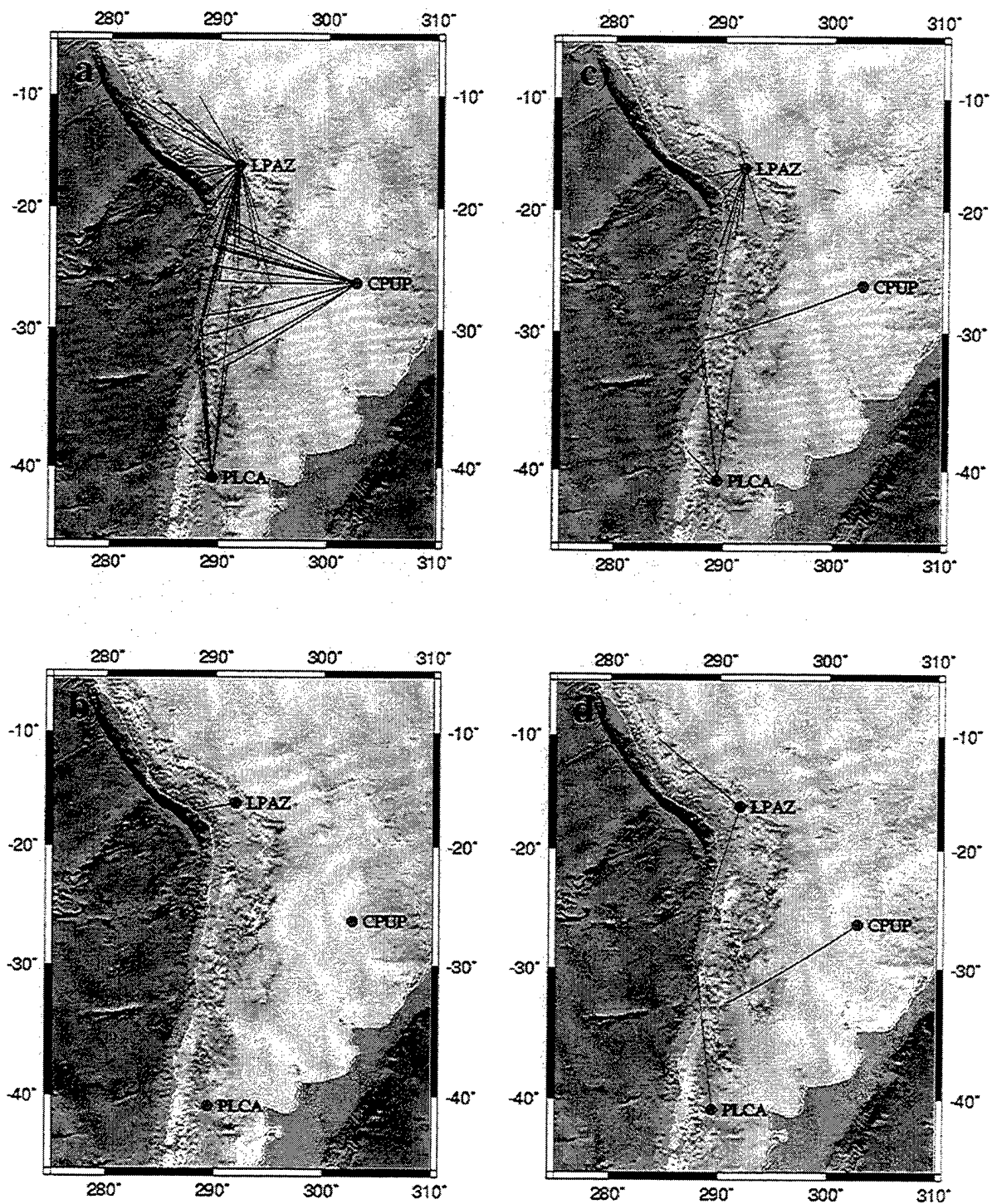
Figure A.9. Ray-path maps of regional arrivals used for South America. a) 62 *Pn* arrivals. b) 1 *Pg* arrival. c) 15 *Sn* arrivals. d) 4 *Lg* arrivals.

70
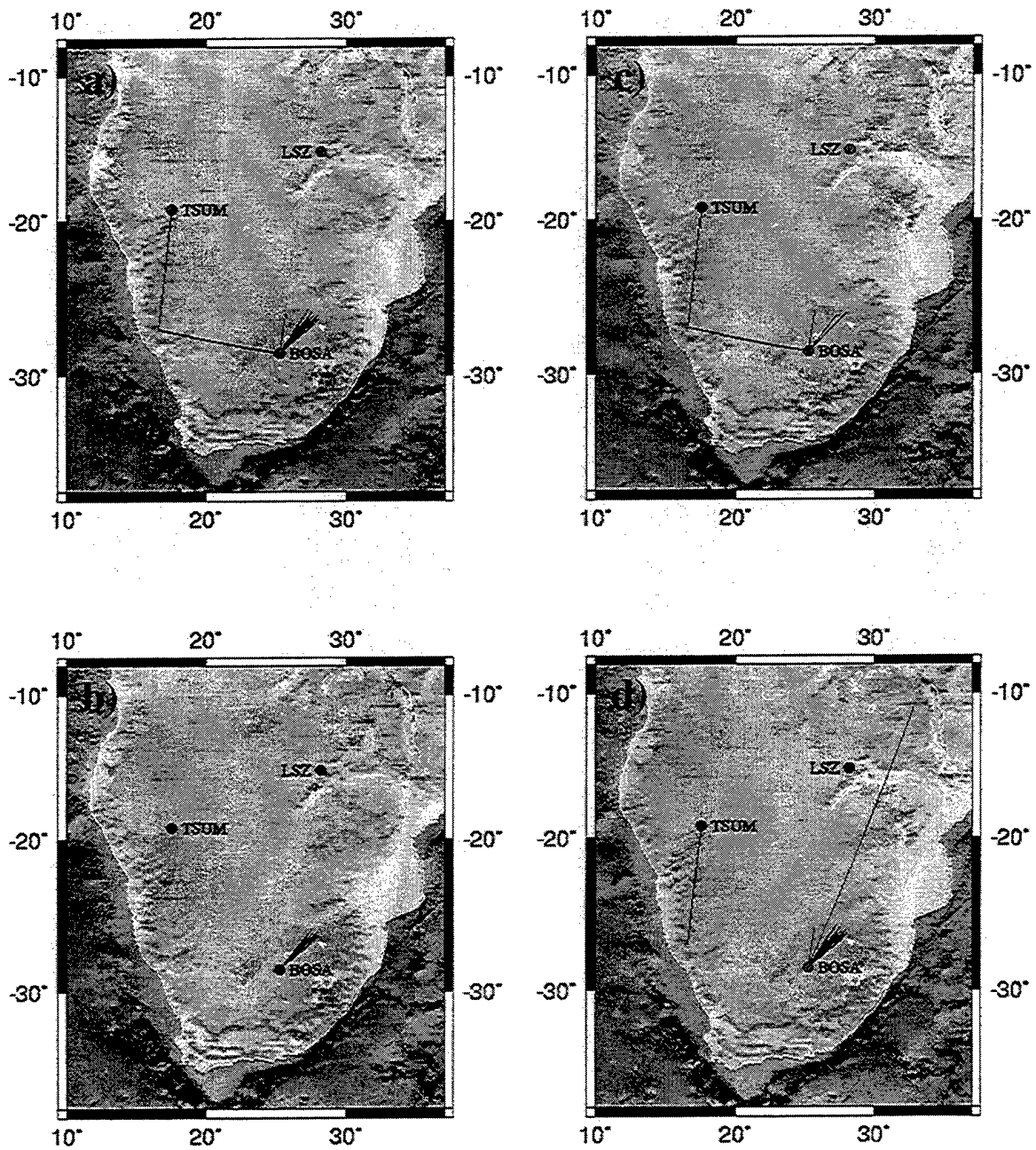
Figure A.10. Ray-path maps of regional arrivals used for southern Africa. a) 41 *Pn*
arrivals. b) 34 *Pg* arrivals. c) 6 *Sn* arrivals. d) 41 *Lg* arrivals.

Appendix B: Source and Attenuation Models

This appendix summarizes the results of our inversion for nine subnetworks: 1) Alaska, 2) western North America, 3) eastern North America, 4) southern Europe, 5) southern Asia, 6) central Asia, 7) Australia, 8) Japan, and 9) South America. Each subnetwork has five pages associated with it.

The first page contains a table summarizing the inversion results along with a plot of source level versus magnitude. The *count* variable represents the total number of arrivals per phase with amplitude measurements that passed the distance, frequency, and *snr* screening. The phase-dependent parameters a, b, κ, and α, along with a phase-dependent standard deviation (σ) were estimated by AmpInv using the c value shown in each table. The $|site|$ parameter represents the median of the absolute value of the site responses estimated by AmpInv. See Section 2.2 for a discussion of all parameters shown in the table headings.

The source-level figure is a plot of the log of the long-period source level (S_0) against local magnitude (m_L) for the events recorded in each subnetwork. Each source-level figure has a solid best-fit line through the data, along with two dashed lines bracketing it. The dashed lines share the same slope as the best-fit line, but are shifted vertically one standard deviation. The slope of the best-fit line, standard deviation, and number of events are denoted in the lower right-hand corner of each figure. Note that some of the events recorded in each subnetwork did not have an m_L magnitude available in the REB; hence the discrepancy between the number of events shown on this plot and the number of events listed in Table 1 of the text.

The second through fifth pages associated with each subnetwork plot attenuation curves. Each of the four pages is devoted to the attenuation of a particular phase. *Pn* is first, followed by *Pg*, *Sn*, and *Lg*. On each page, six different plots of attenuation versus distance are shown. Each of these attenuation curves were estimated using log amplitude measurements from different frequency bands. The *Pn*, *Pg*, and *Sn* curves are shown for the 1-2, 1.5-3, 2-4, 3-6, 4-8, and 6-12 Hz bands, whereas the *Lg* curves are shown for the 0.5-1, 1-2, 1.5-3, 2-4, 3-6, and 4-8 Hz bands. The central point of the frequency band, rate of attenuation (i.e., $R^{-n(f)}$), station legend, and standard deviation of the attenuation model are all shown on the right-hand side of each plot. Note that in some cases, a particular subnetwork did not have any amplitude measurements for a given phase in a particular frequency range. In this case, a figure outline is shown, but the words "No Data" are entered (i.e., Alaska *Lg* 0.5-1 Hz band).

73

B.1 Alaska

B.1.1 Inversion Results

Table B.1:   Inversion Results for the Alaska subnetwork

phase	*count*	*c*	κ	α	*a*	*b*	*|site|*	σ
Pn	479	20.0	0.00	-0.12	0.08	1.96	0.06	0.33
Pg	74	20.0	0.27	0.10	0.16	1.87	0.10	0.27
Sn	157	20.0	1.11	0.04	0.05	3.14	0.13	0.26
Lg	186	20.0	1.04	0.19	0.36	2.41	0.08	0.22

B.1.2 Source

slope = 0.91
stdev = 0.36
events = 198
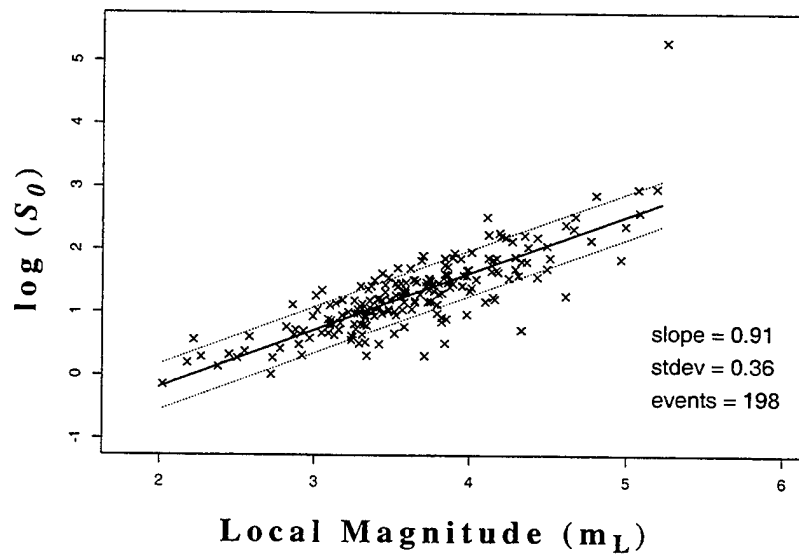
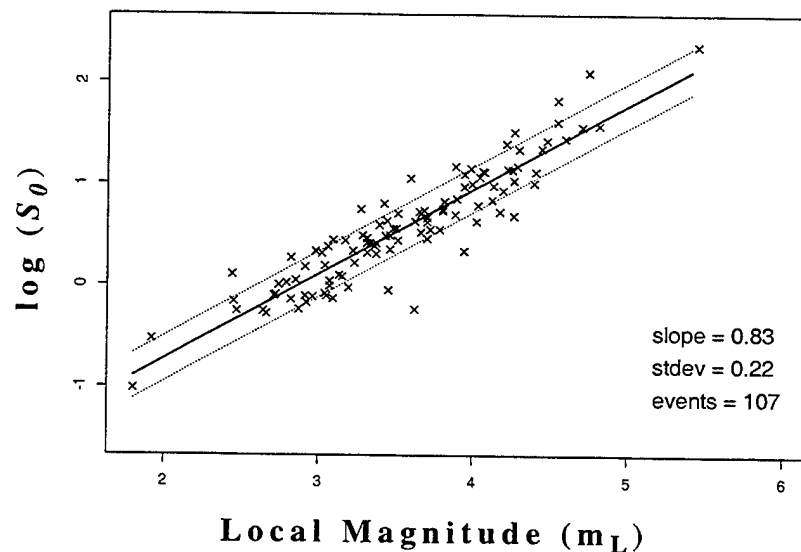**Figure B.1.1** Estimated long period source level (S_0) plotted against local magnitude for the Alaska subnetwork.

B.1.3 Path

Alaska Pn
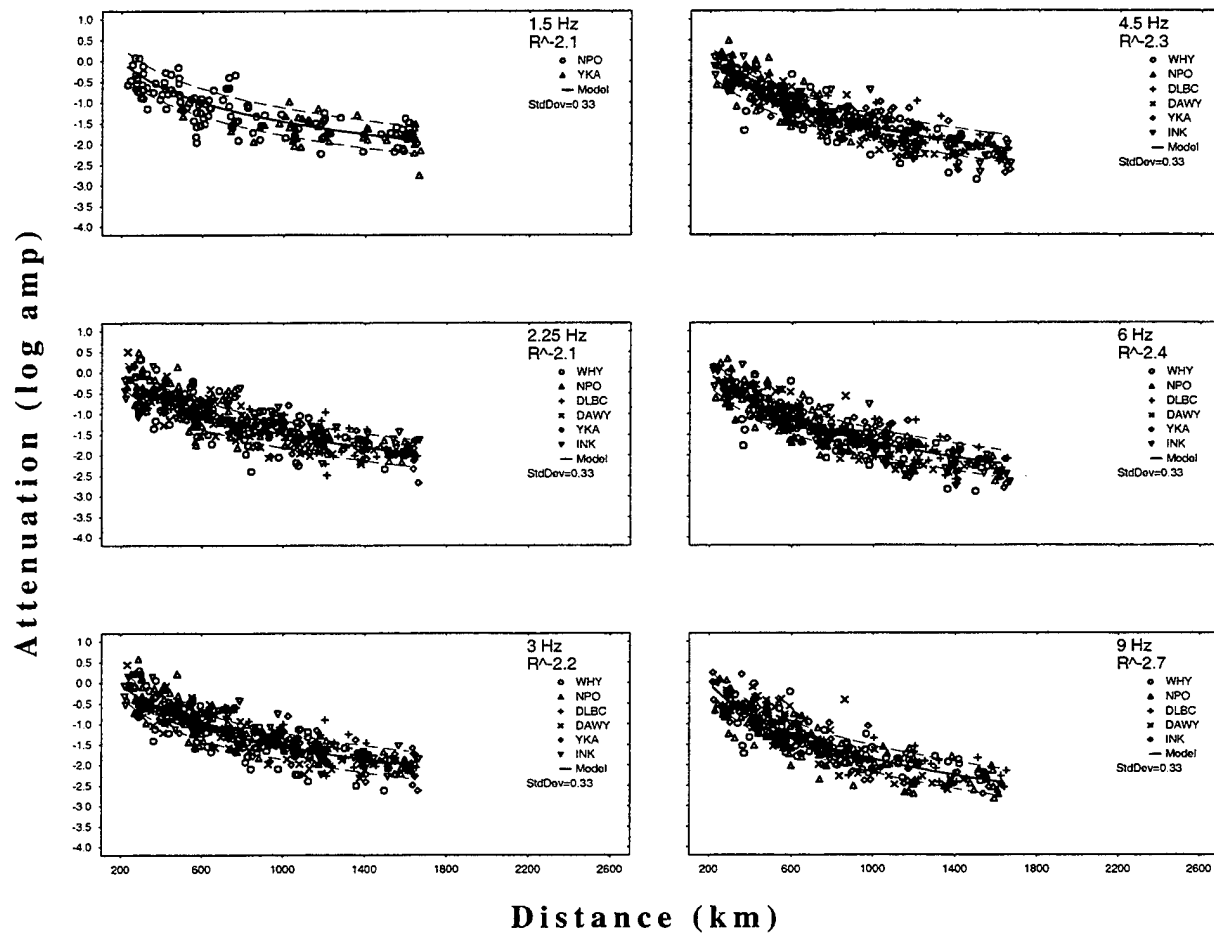
Figure B.1.2 Attenuation curves at various frequencies for *Pn*, *Pg*, *Sn*, and *Lg* phases determined with the Alaska subnetwork.

Alaska Pg
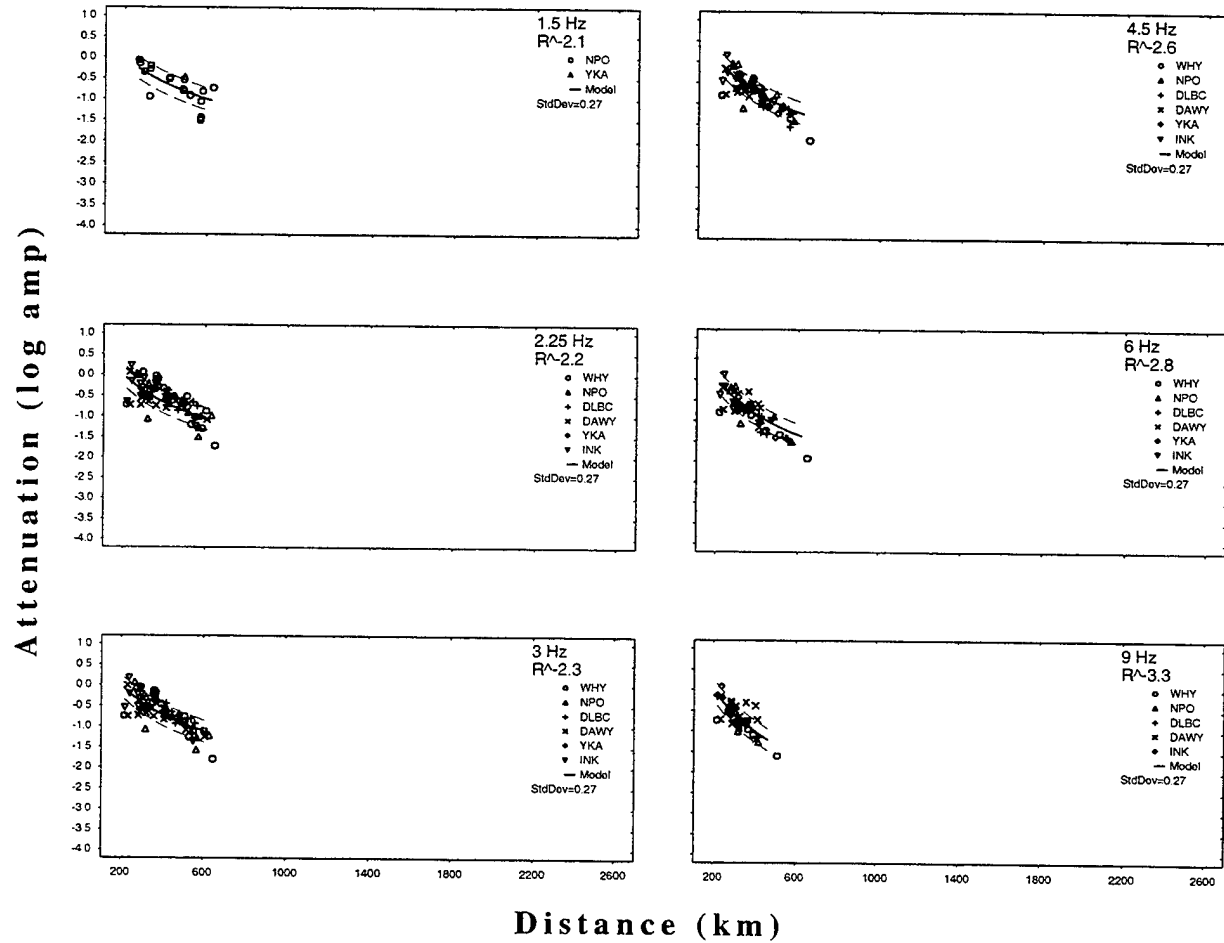
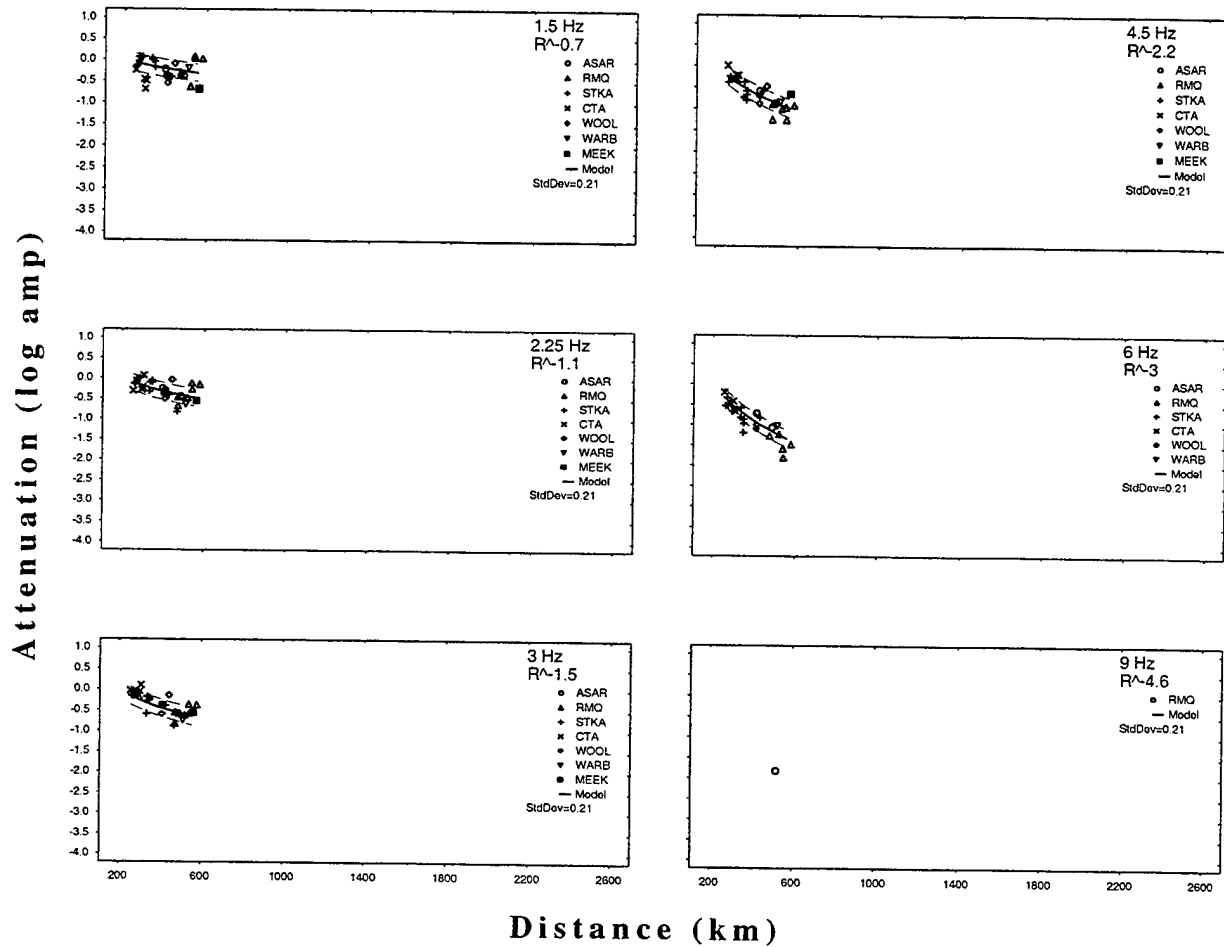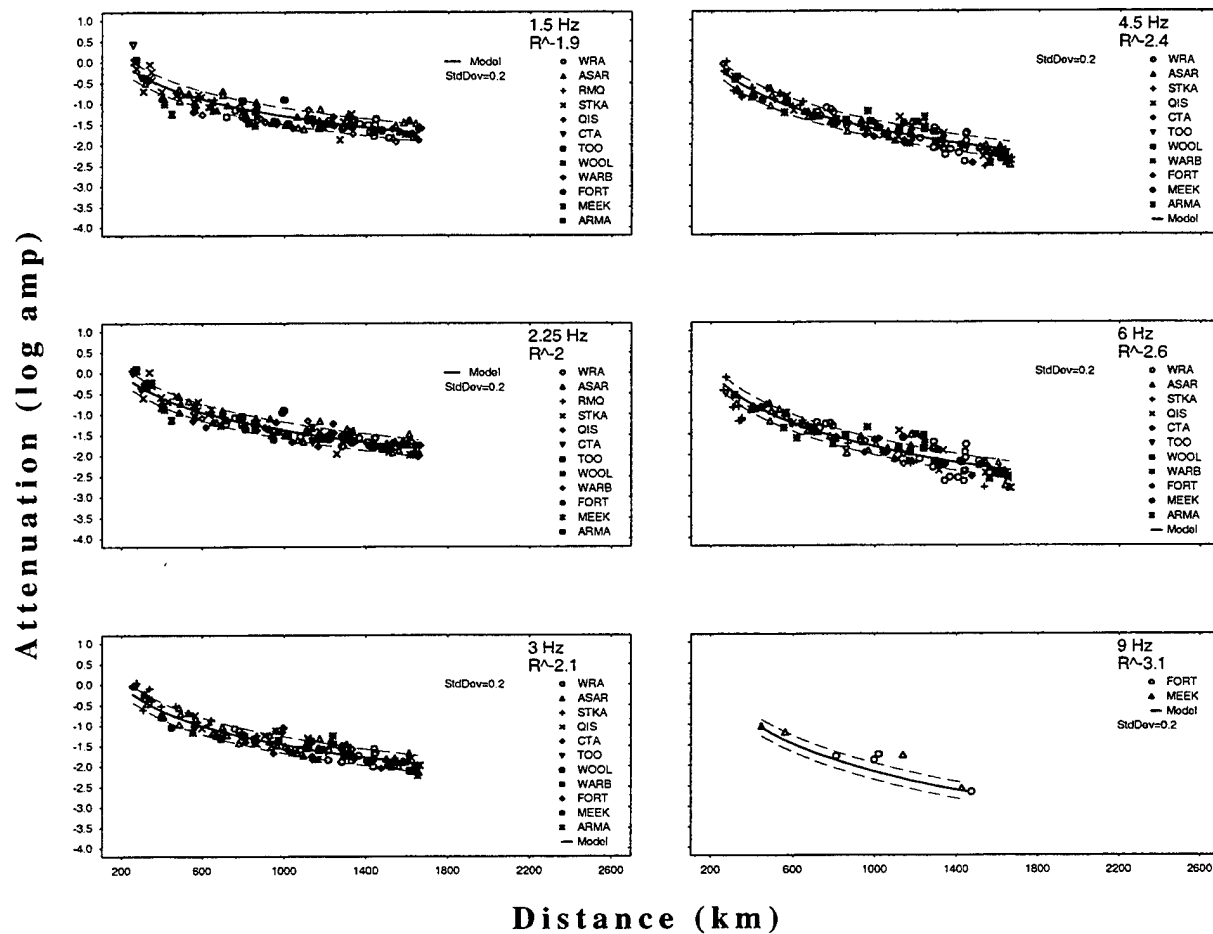**Figure B.1.2** Continued.

Alaska Sn
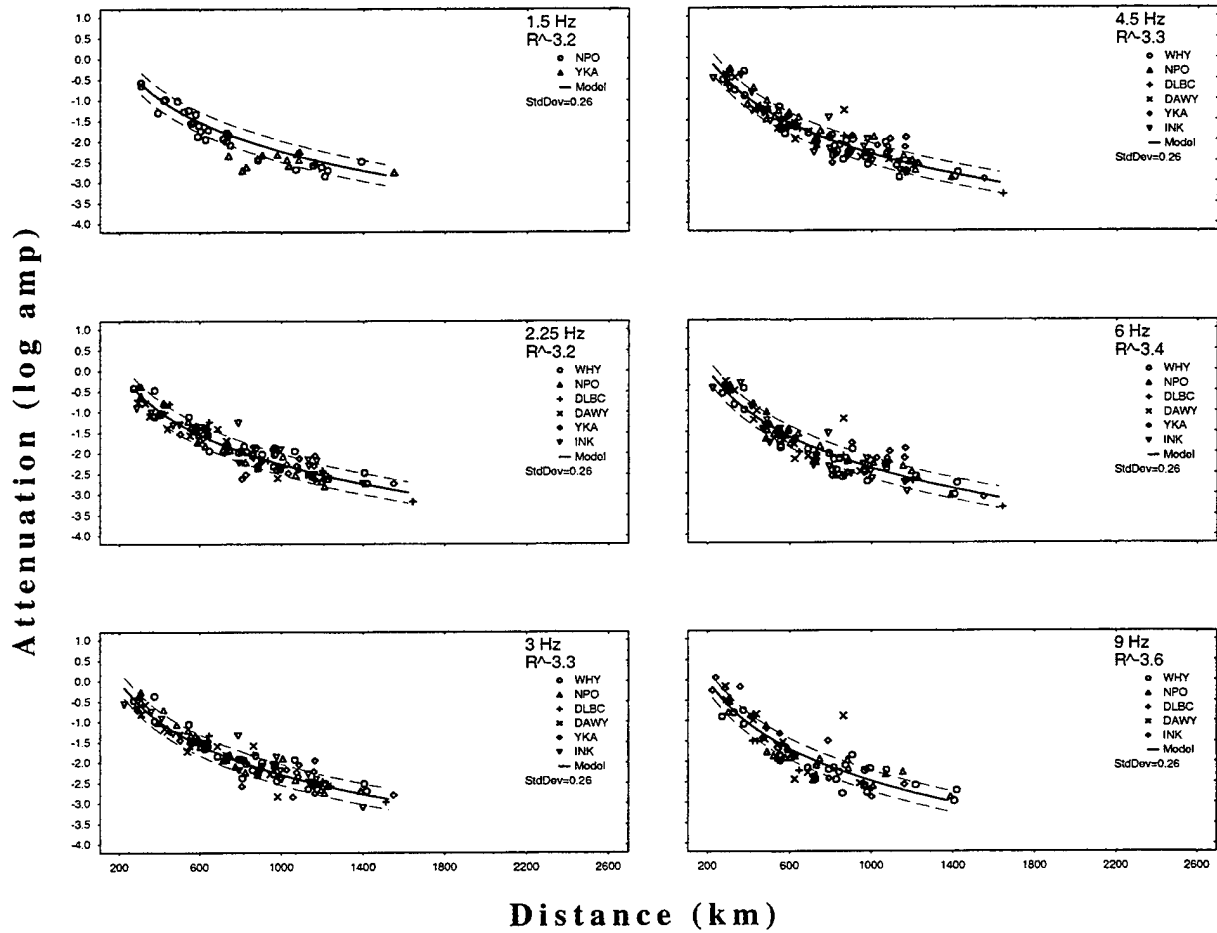
Figure B.1.2 Continued.

Alaska Lg
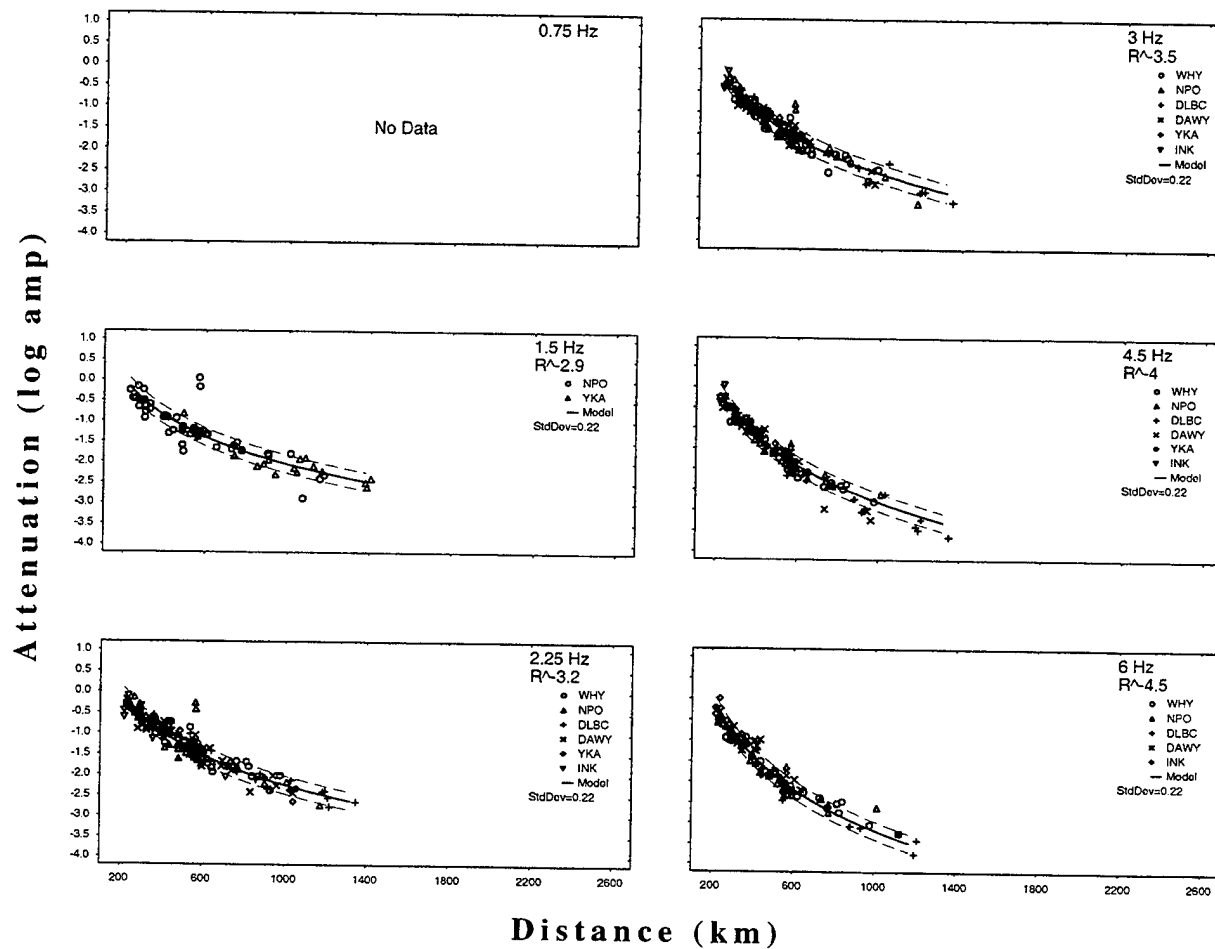
Figure B.1.2 Continued.

B.2 Western North America

B.2.1 Inversion Results

Table B.2: Inversion Results for the western North America subnetwork

phase	*count*	*c*	κ	α	*a*	*b*	*|site|*	σ
Pn	617	15.0	0.00	-0.11	0.06	2.22	0.33	0.50
Pg	106	15.0	0.45	0.18	0.18	2.54	0.33	0.37
Sn	67	15.0	0.86	0.00	0.03	3.47	0.34	0.38
Lg	246	15.0	0.85	0.28	0.35	2.34	0.45	0.37

B.2.2 Source
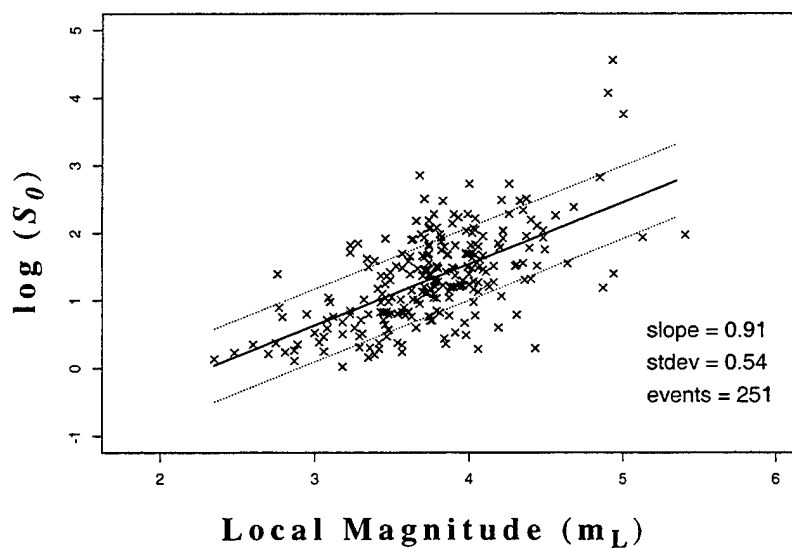
Figure B.2.1 Estimated long period source level (S_0) plotted against local magnitude for the western North America subnetwork.

B.2.3 Path

Western North America Pn
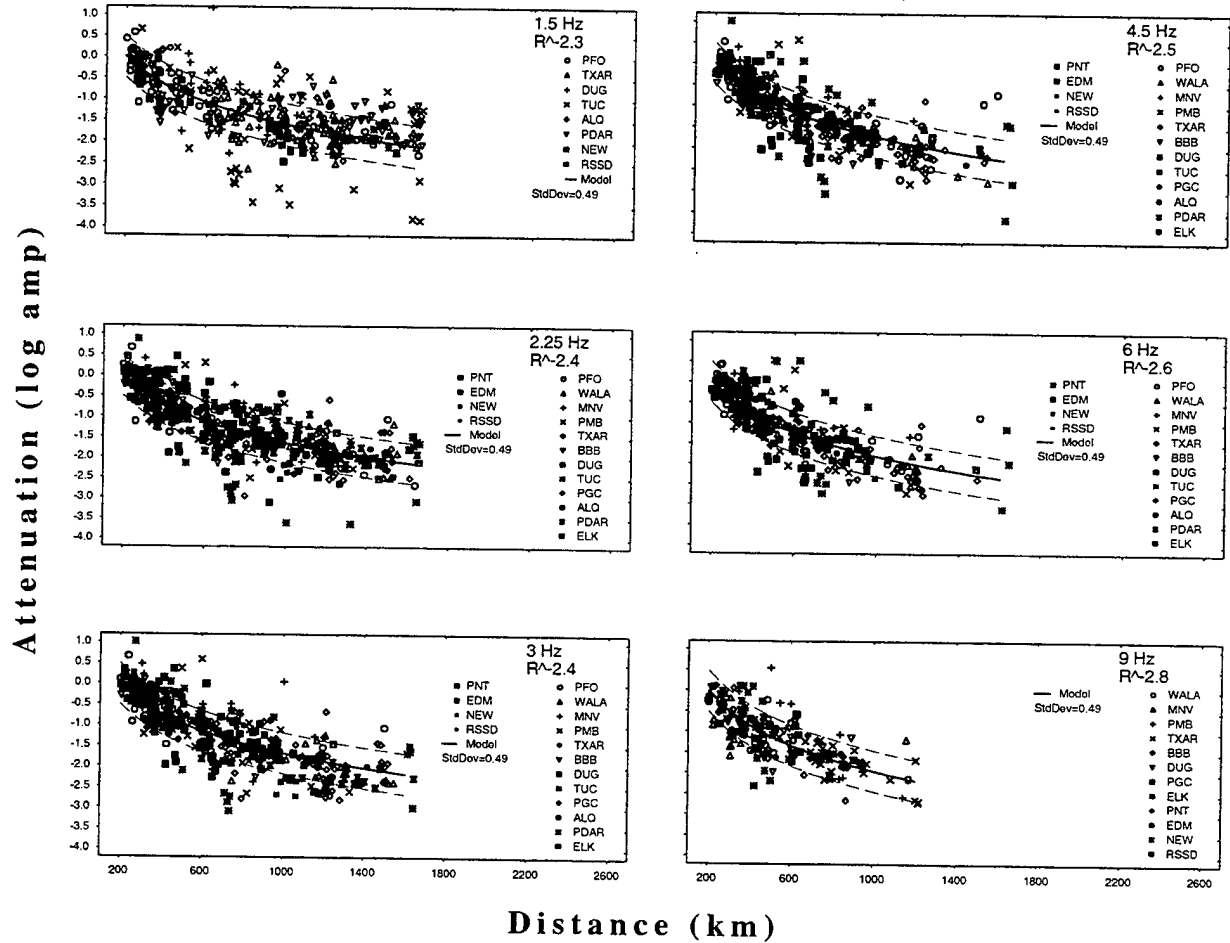
Figure B.2.2 Attenuation curves at various frequencies for *Pn, Pg, Sn,* and *Lg* phases determined with the western North America subnetwork.

Western North America Pg
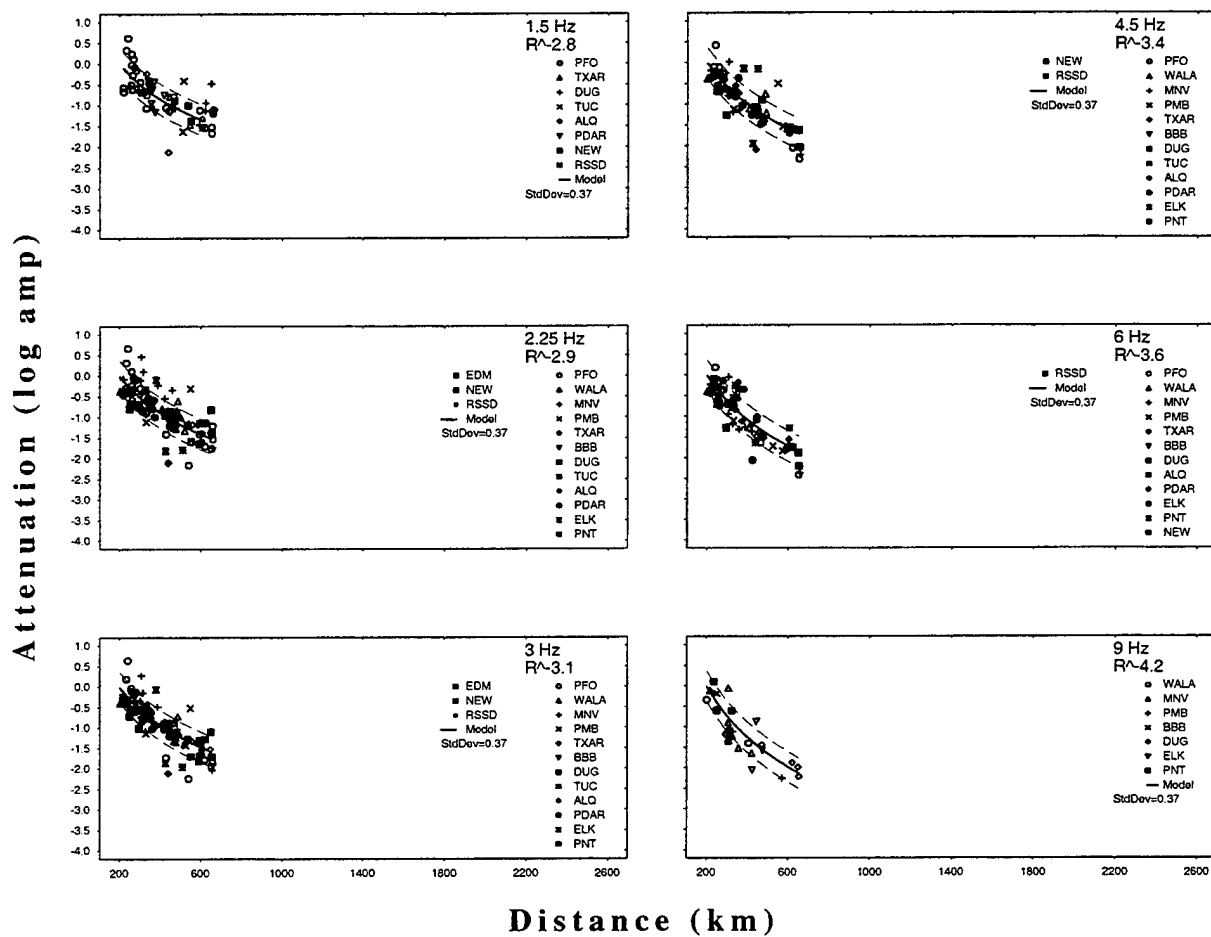
Figure B.2.2 Continued.

Western North America Sn
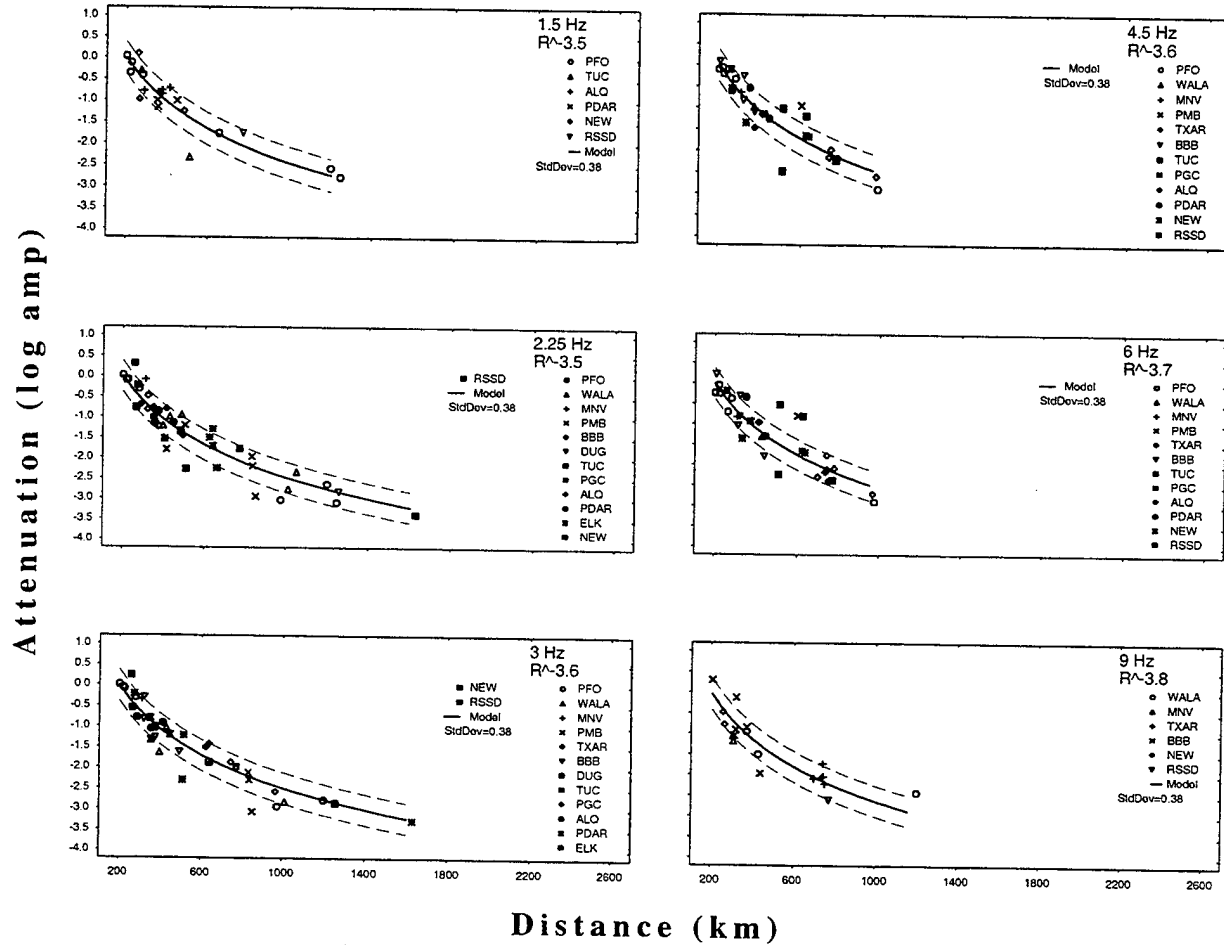
Figure B.2.2 Continued.

Western North America Lg
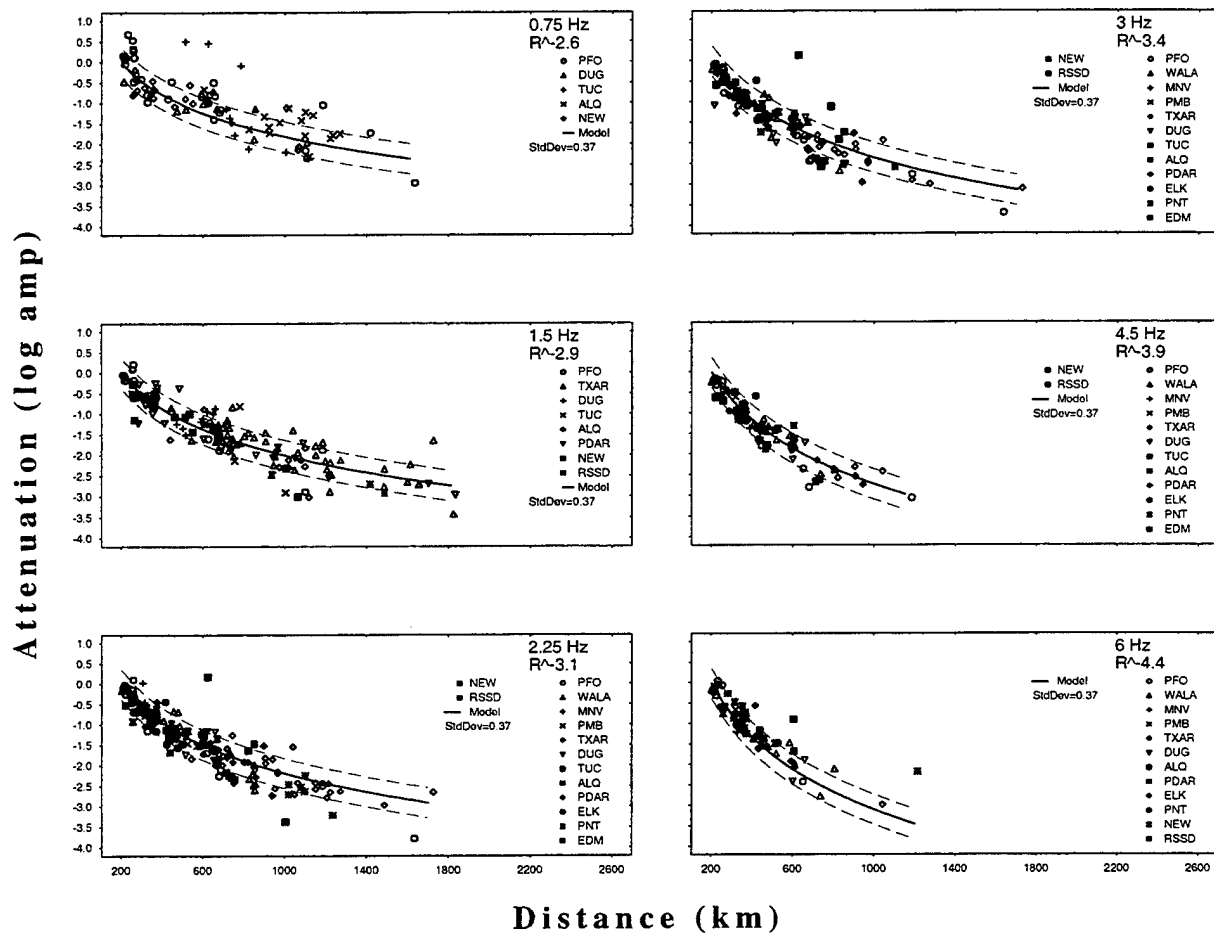
Figure B.2.2 Continued.

B.3 Eastern North America

B.3.1 Inversion Results

Table B.3:   Inversion Results for the eastern North America subnetwork

| *phase*	*count*	*c*	κ	α	*a*	*b*	*|site|*	σ
Pn	218	15.0	0.00	-0.15	0.06	1.77	0.29	0.34
Pg	31	15.0	0.29	0.13	0.09	2.72	0.32	0.27
Sn	41	15.0	0.85	0.06	-0.03	2.53	0.14	0.34
Lg	174	15.0	0.83	0.23	0.37	1.45	0.25	0.30

B.3.2 Source
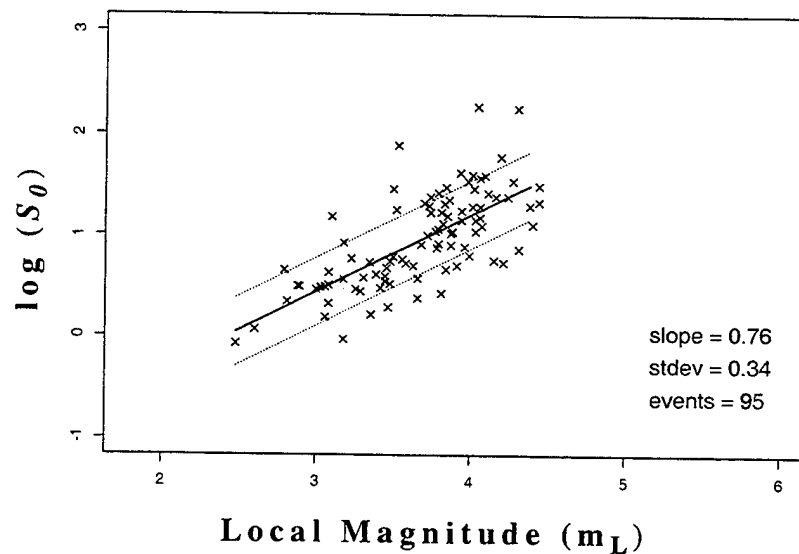
Figure B.3.1 Estimated long period source level (S_0) plotted against local magnitude for the eastern North America subnetwork.

B.3.3 Path

Eastern North America Pn
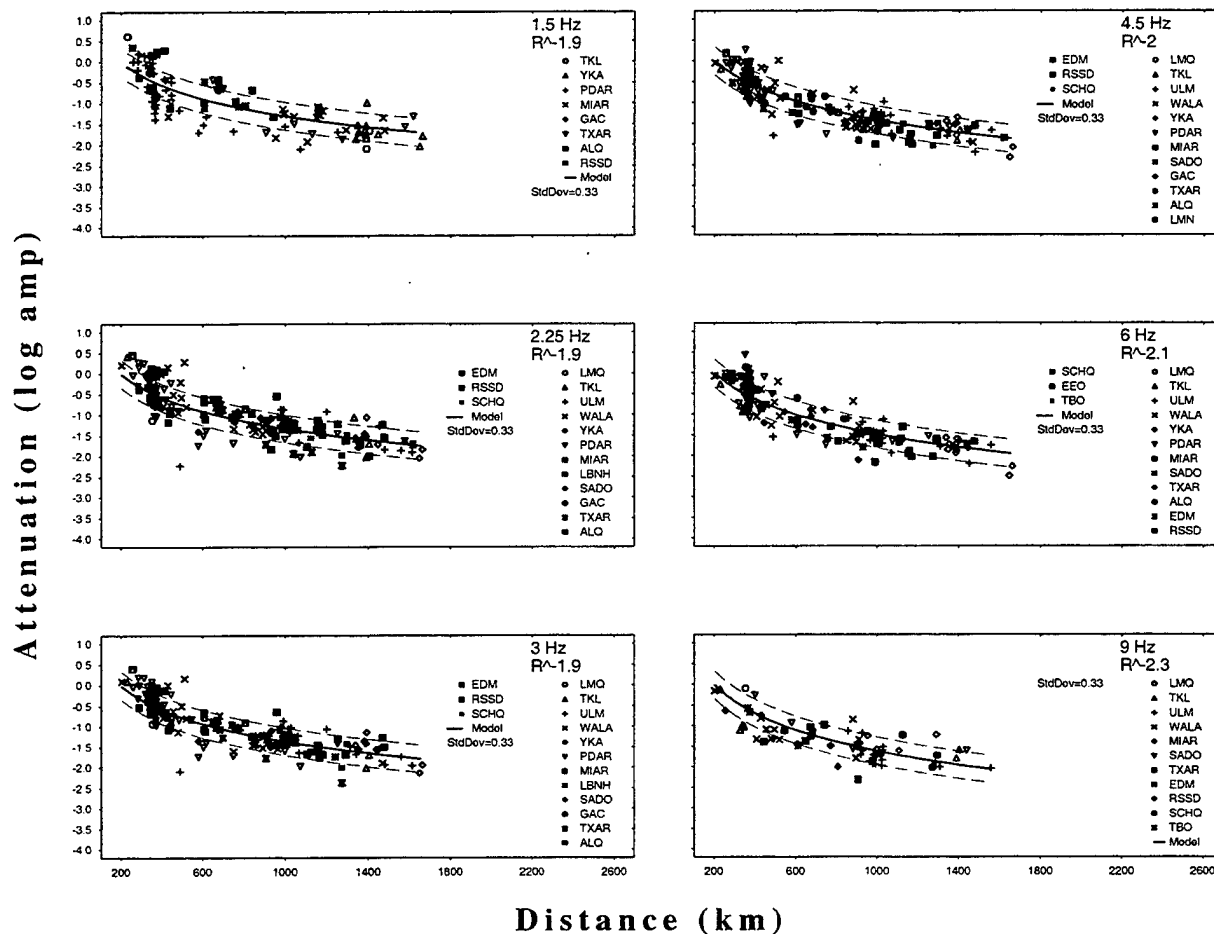
Figure B.3.2 Attenuation curves at various frequencies for *Pn*, *Pg*, *Sn*, and *Lg* phases determined with the eastern North America subnetwork.

Eastern North America Pg
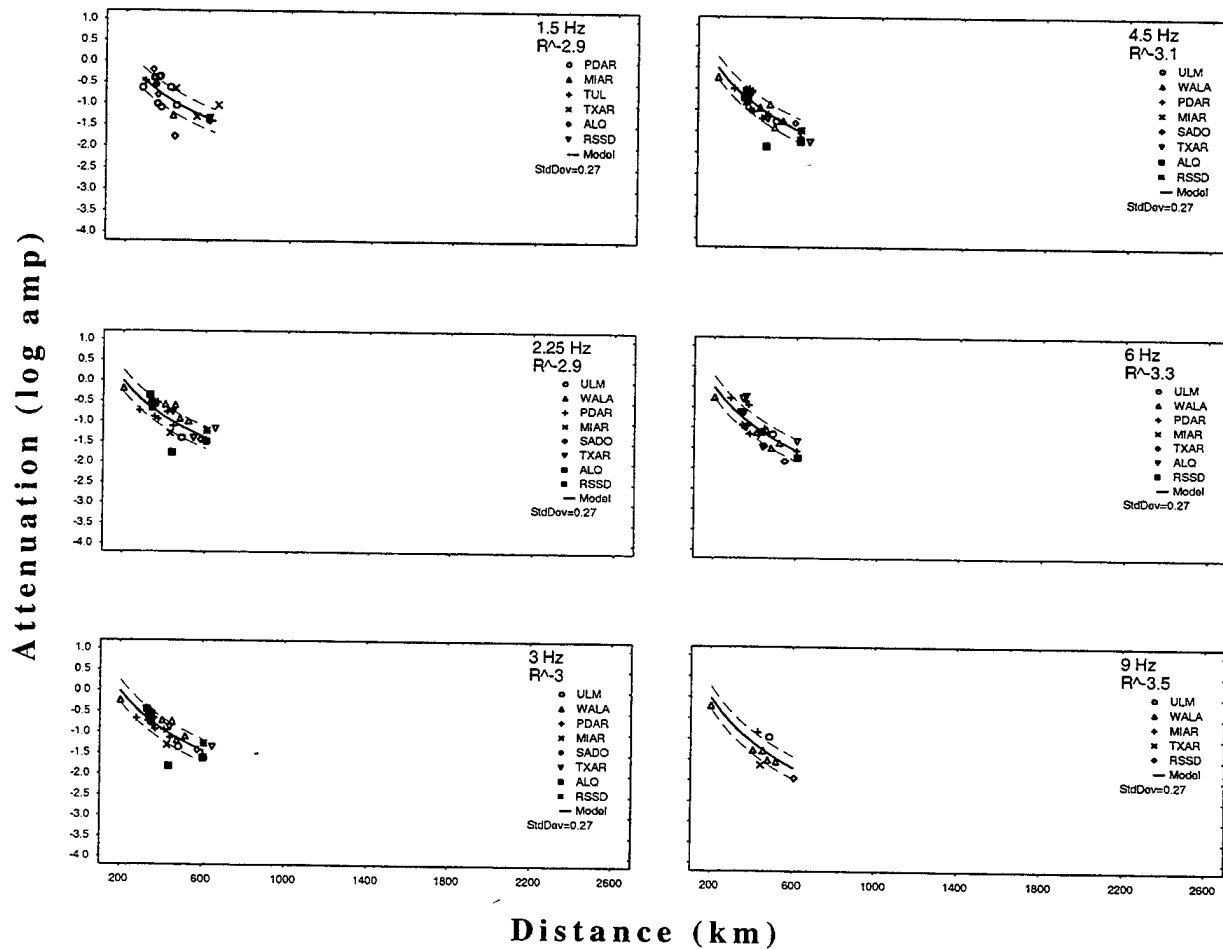
Figure B.3.2 Continued.

Eastern North America Sn
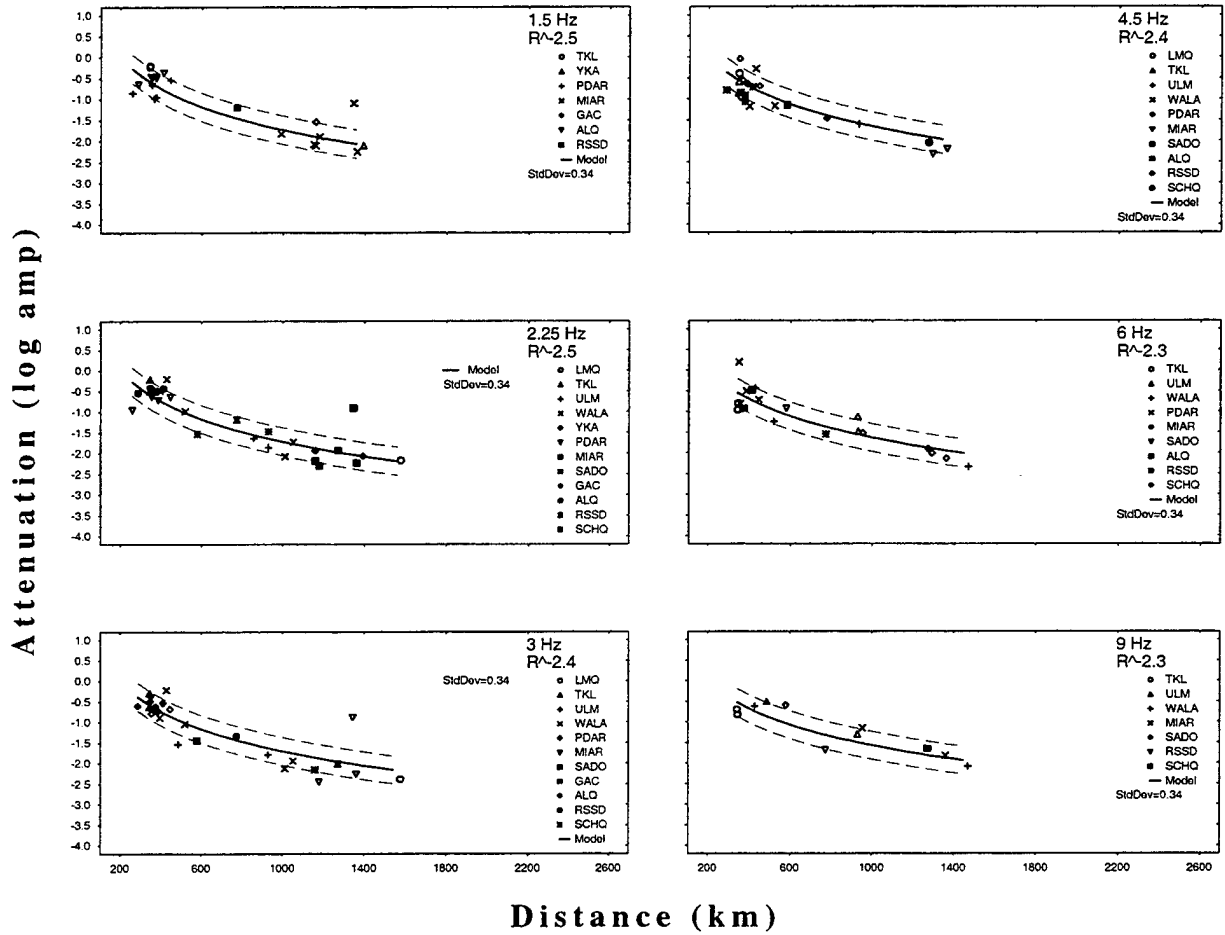
Figure B.3.2 Continued.

Eastern North America Lg
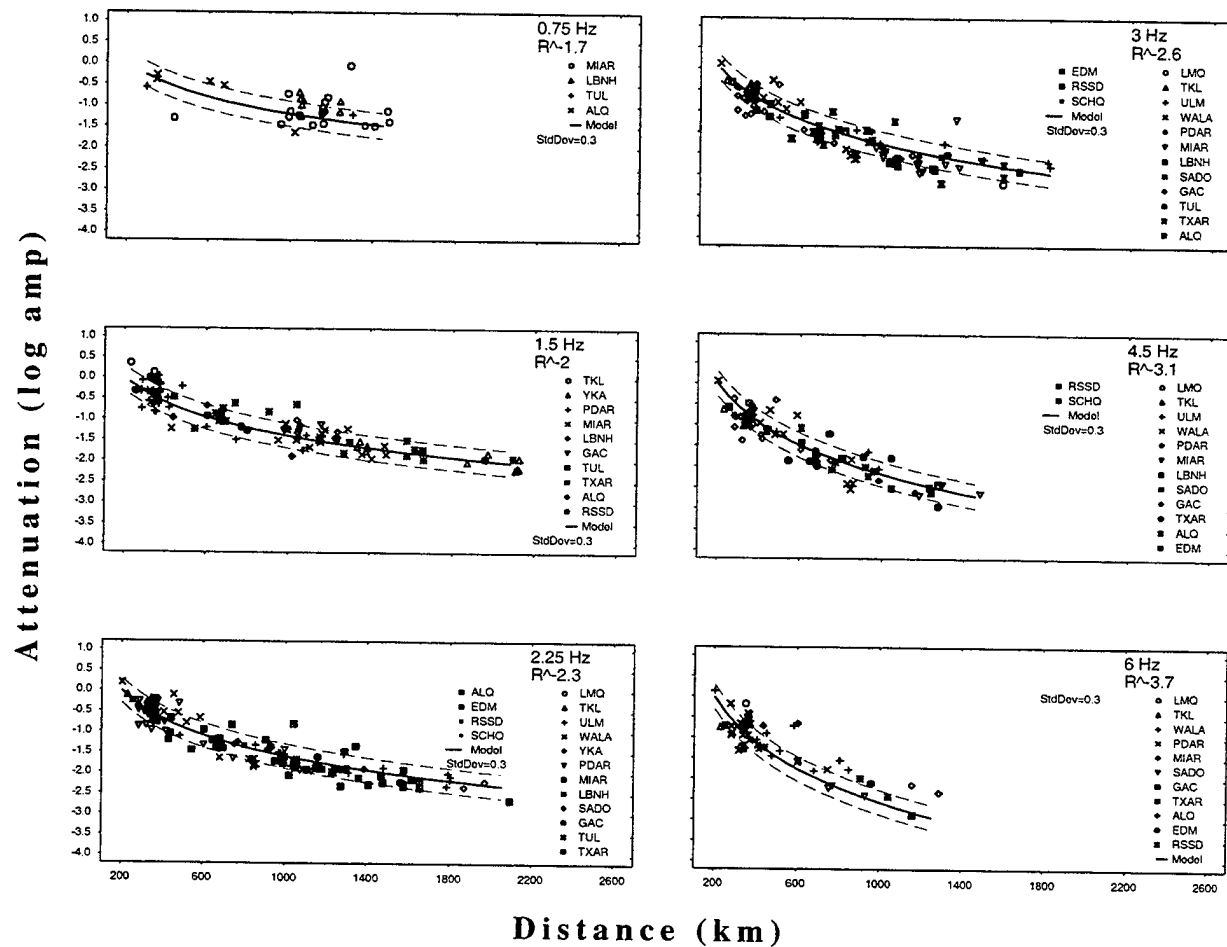
Figure B.3.2 Continued.

B.4 Southern Europe

B.4.1 Inversion Results

Table B.4:   Inversion Results for the southern Europe subnetwork

phase	*count*	*c*	κ	α	*a*	*b*	|*site*|	σ
Pn	1105	15.0	0.00	-0.04	-0.04	1.97	0.12	0.25
Pg	604	15.0	0.22	0.19	0.00	2.39	0.09	0.21
Sn	262	15.0	0.59	0.01	-0.01	2.42	0.05	0.21
Lg	949	15.0	0.41	0.22	0.21	1.60	0.14	0.17

B.4.2 Source
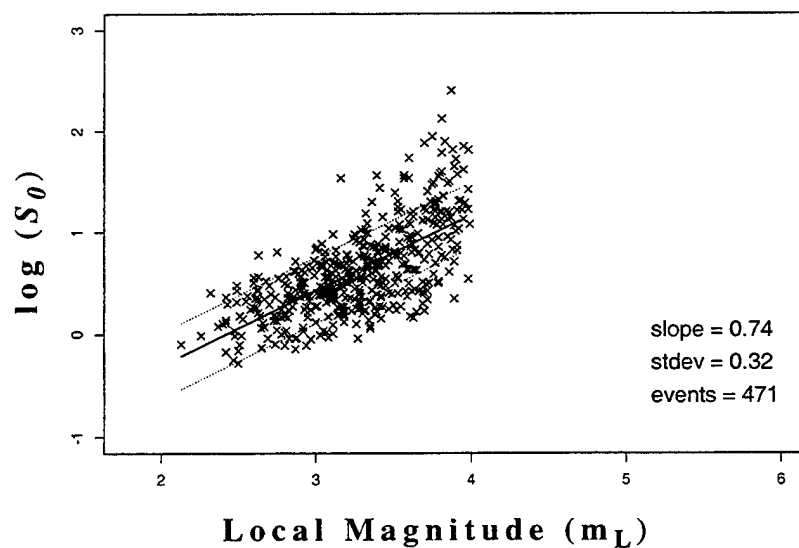
Figure B.4.1 Estimated long period source level (S_0) plotted against local magnitude for the southern Europe subnetwork.

B.4.3 Path

Southern Europe Pn
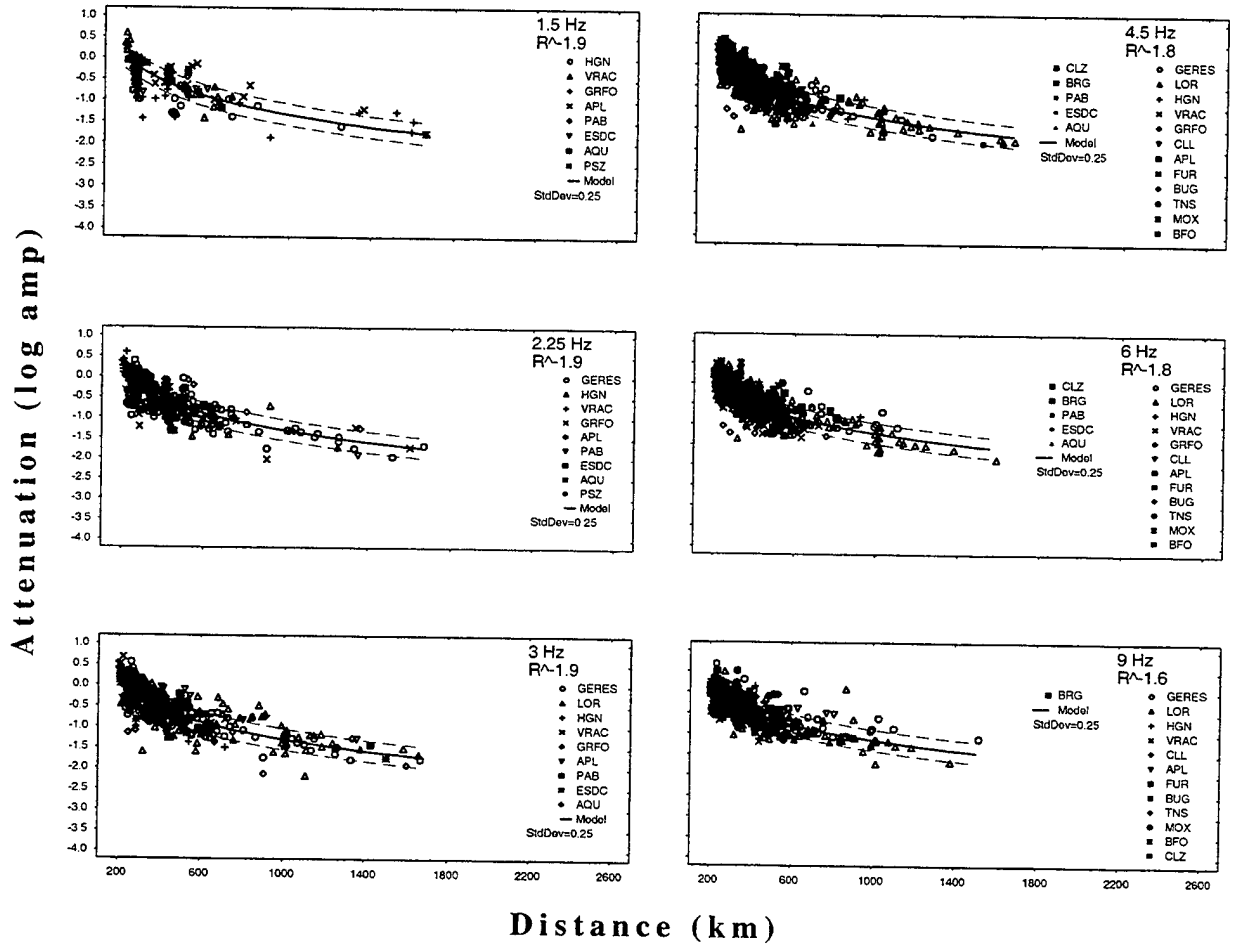
Figure B.4.2 Attenuation curves at various frequencies for *Pn*, *Pg*, *Sn*, and *Lg* phases determined with the southern Europe subnetwork.

# Southern Europe Pg
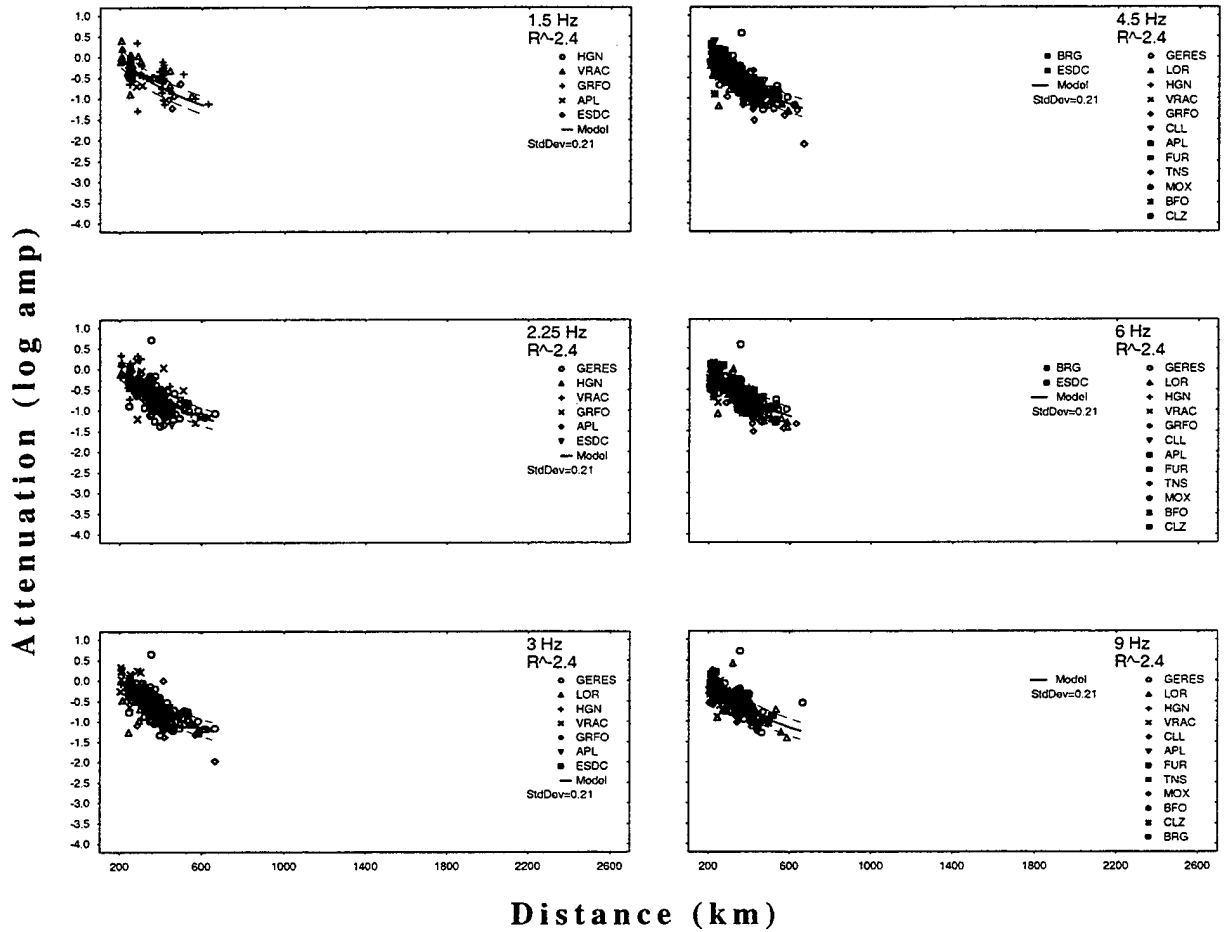
Figure B.4.2 Continued.
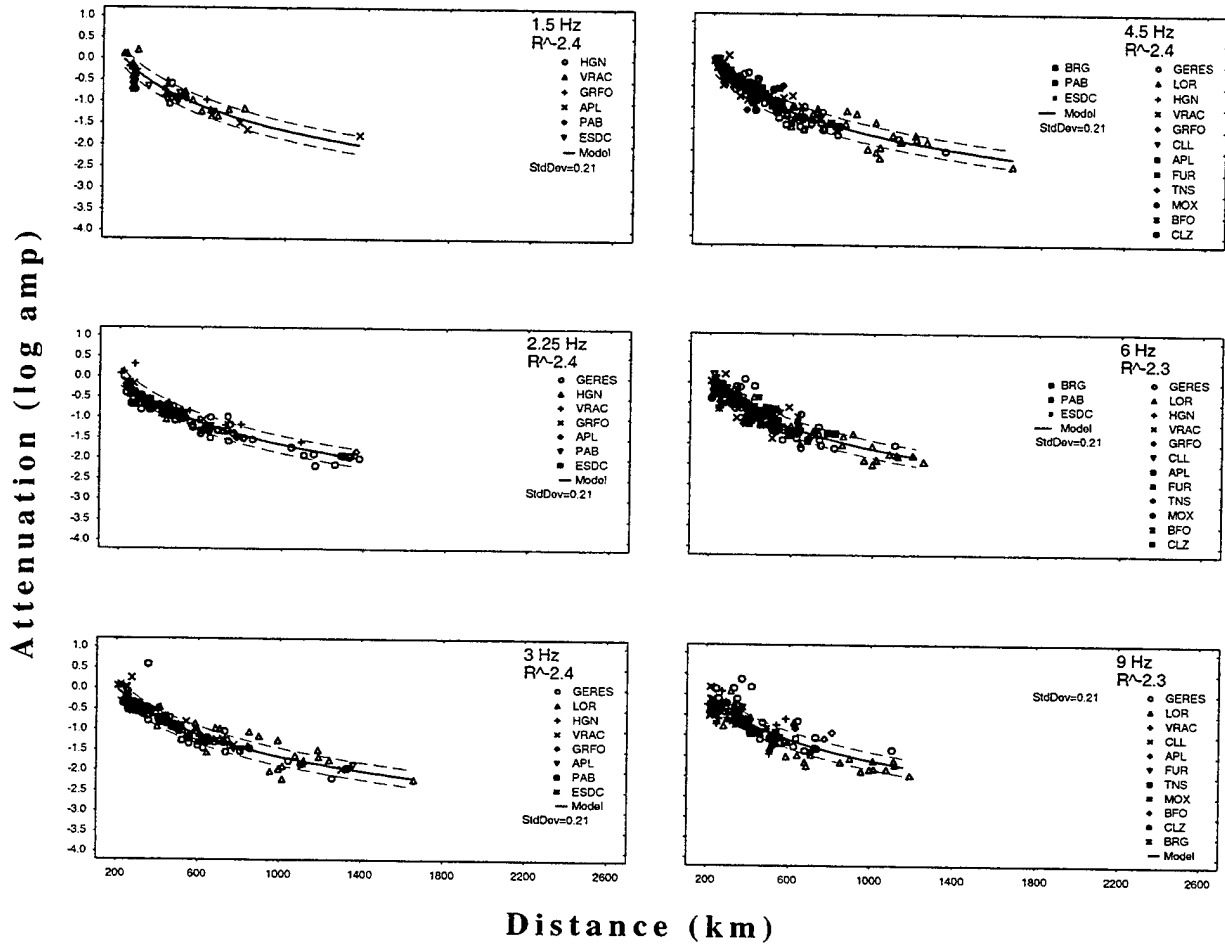
Southern Europe Sn

Figure B.4.2 Continued.

Southern Europe Lg
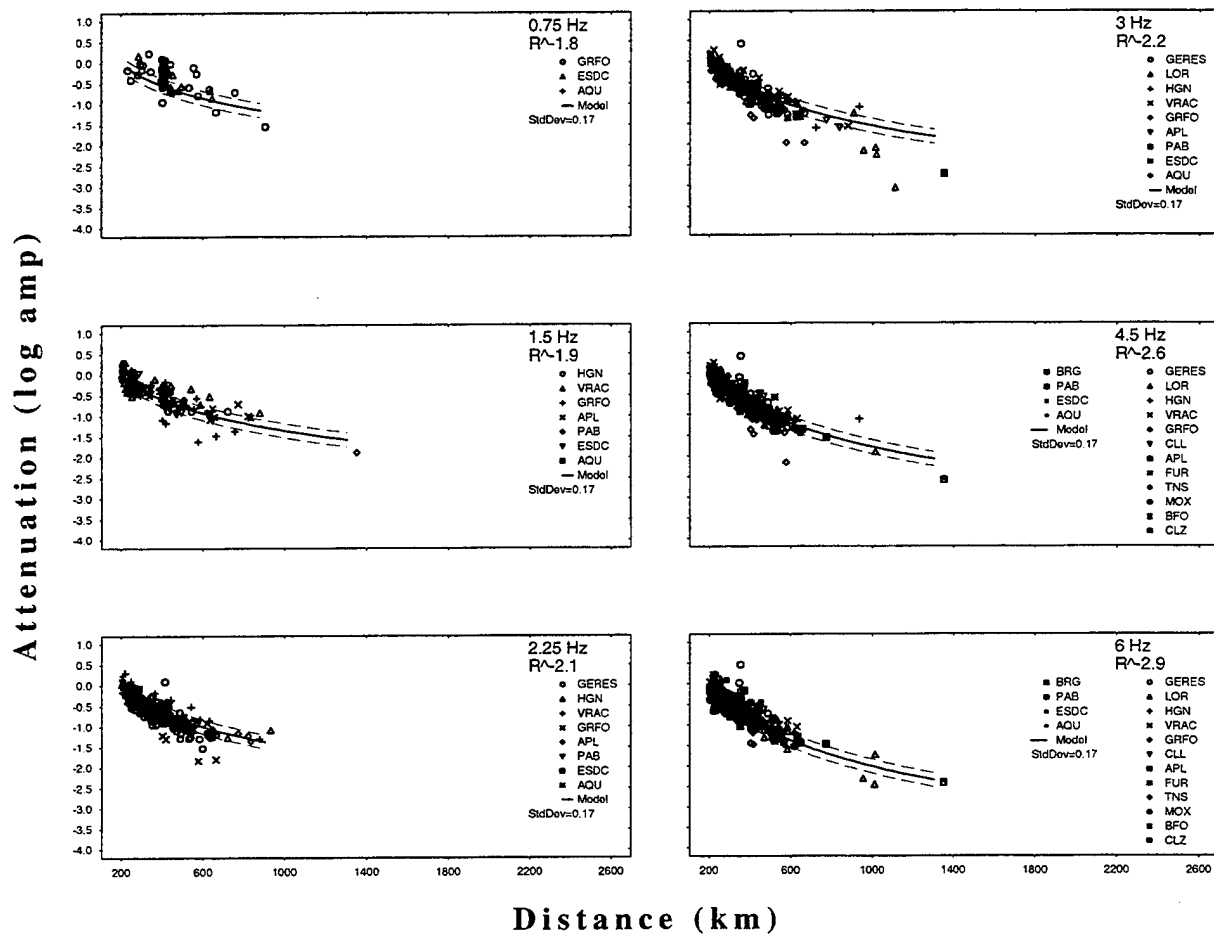
Figure B.4.2 Continued.

B.5 Southern Asia

B.5.1 Inversion Results

Table B.5:   Inversion Results for the southern Asia subnetwork

phase	count	c	κ	α	a	b	|site|	σ
Pn	89	20.0	0.00	-0.10	0.04	1.54	0.38	0.27
Pg	7	20.0	0.97	0.25	-0.09	3.32	0.40	0.20
Sn	21	20.0	0.44	-0.36	0.30	1.66	0.79	0.19
Lg	12	20.0	1.03	-0.01	0.77	1.65	0.40	0.17

B.5.2 Source
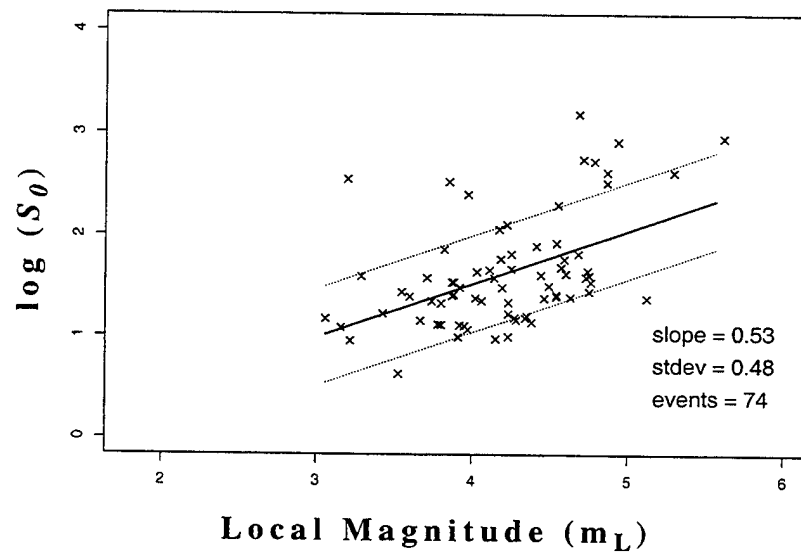
Figure B.5.1 Estimated long period source level (S_0) plotted against local magnitude for the southern Asia subnetwork.

B.5.3 Path

Southern Asia Pn
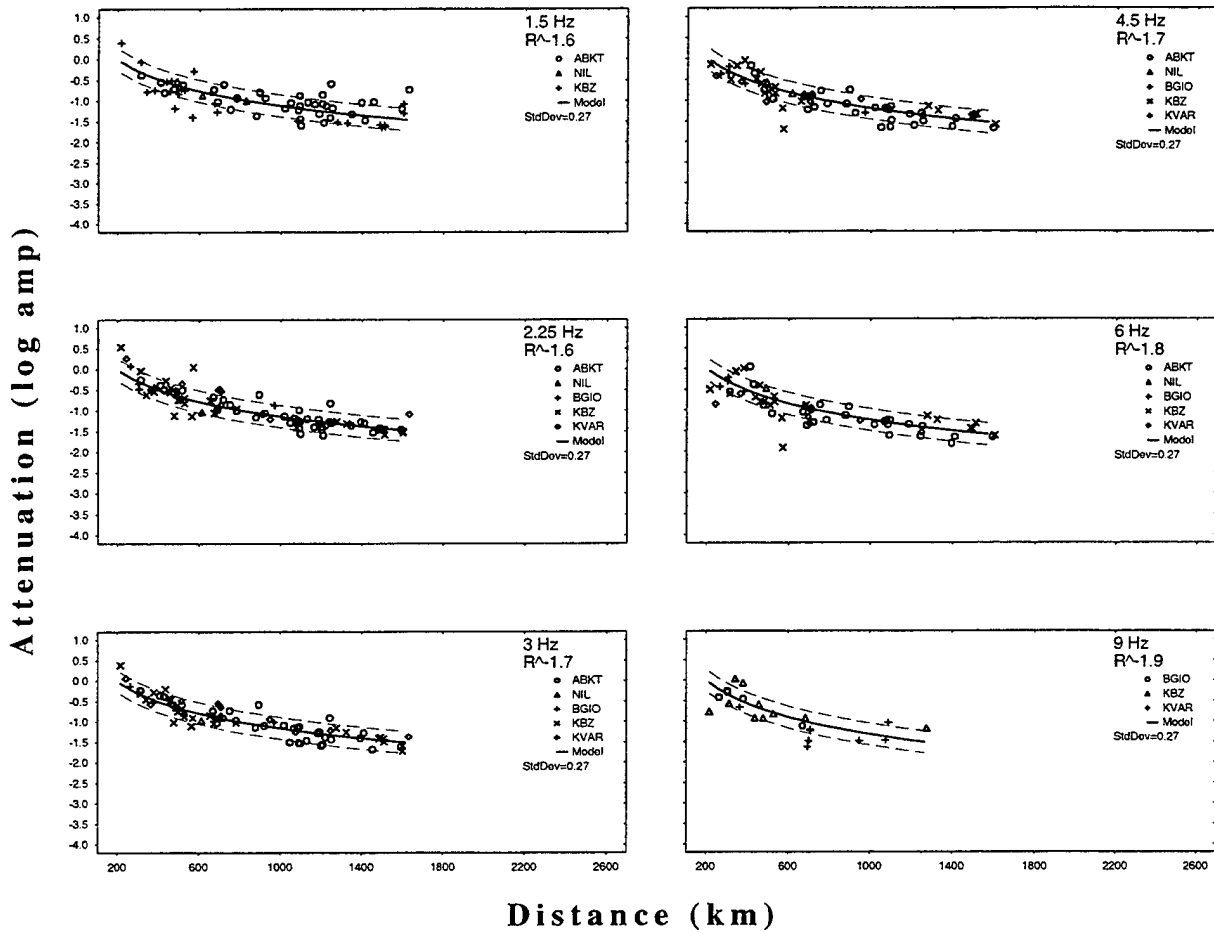
Figure B.5.2 Attenuation curves at various frequencies for *Pn*, *Pg*, *Sn*, and *Lg* phases determined with the southern Asia subnetwork.

Southern Asia Pg
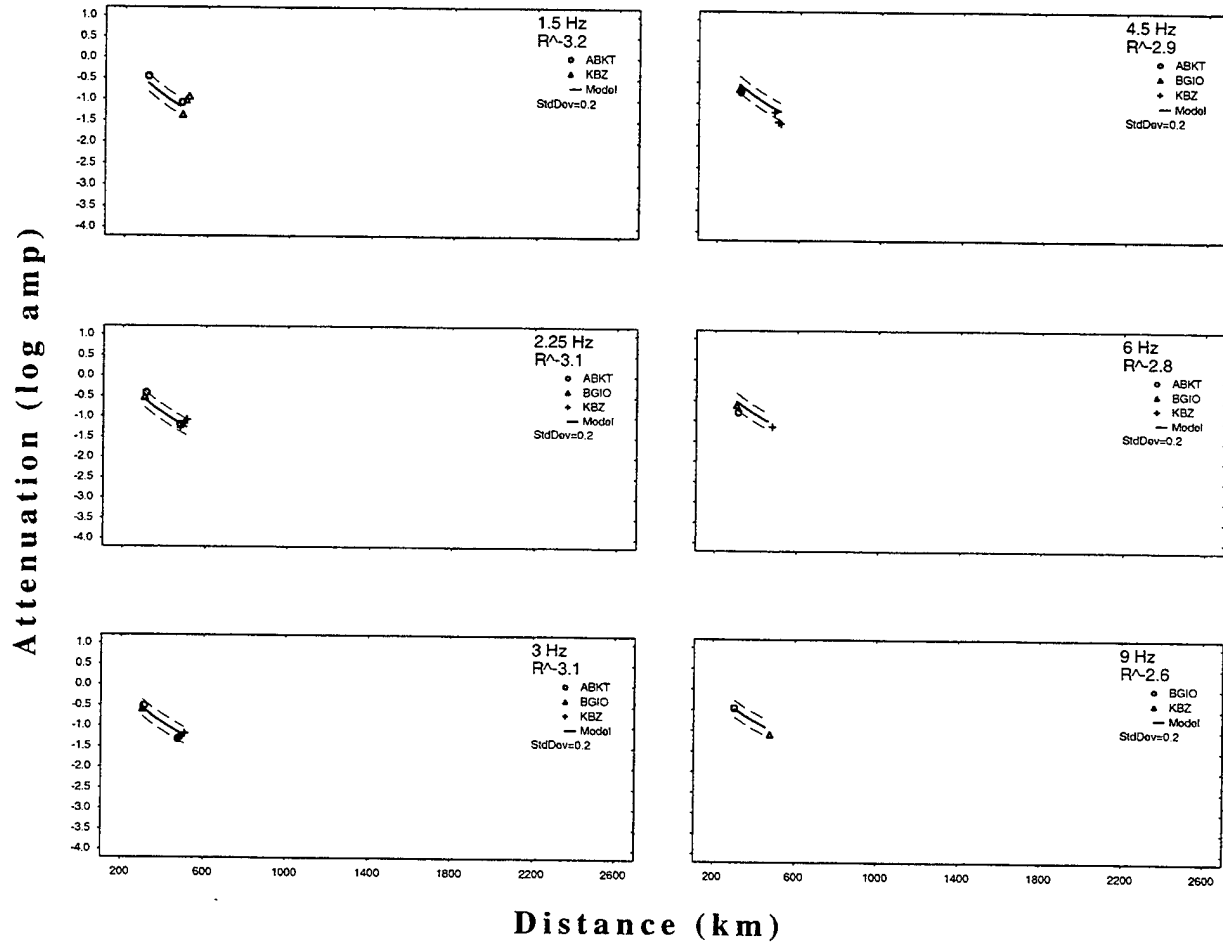
Figure B.5.2 Continued.

Southern Asia Sn
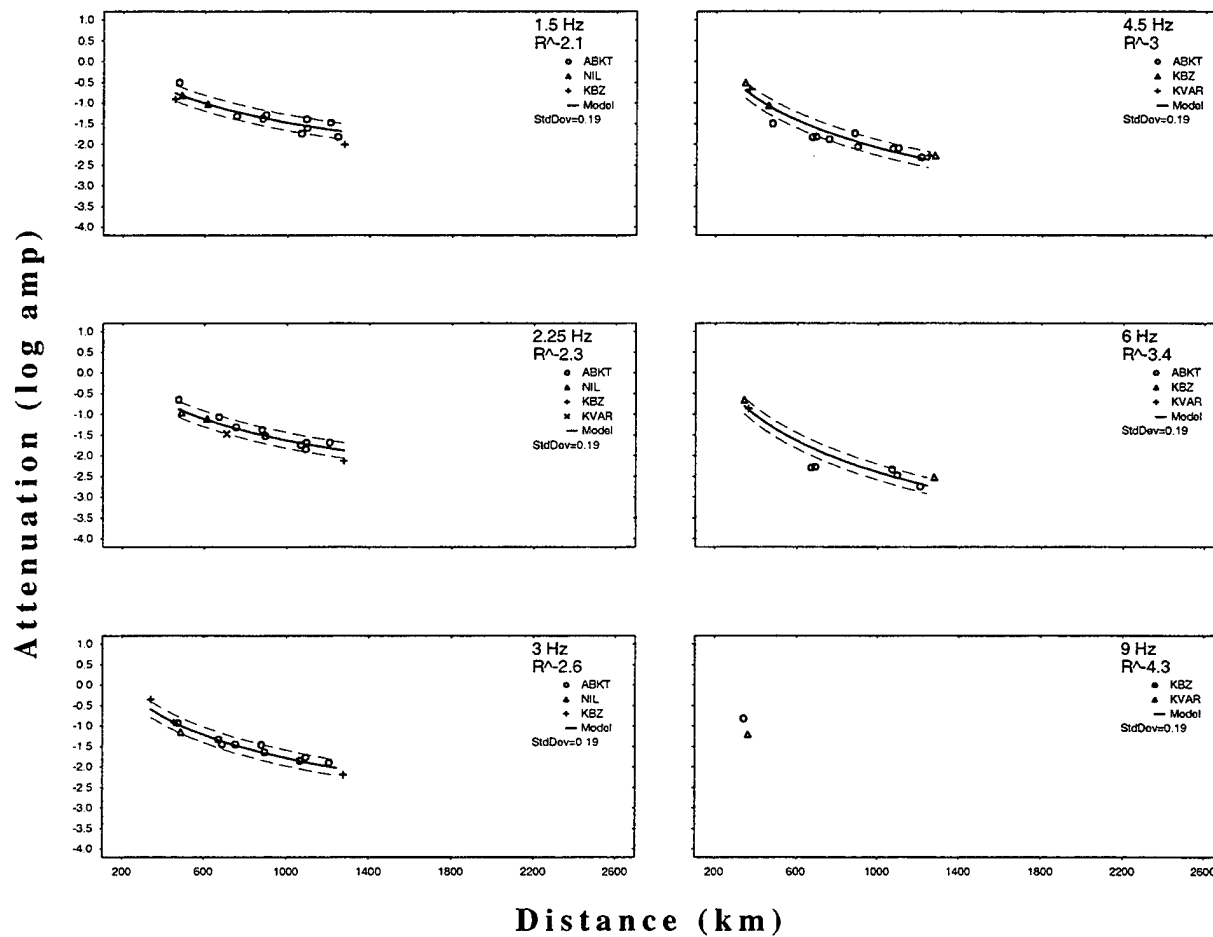
Figure B.5.2 Continued.

Southern Asia Lg
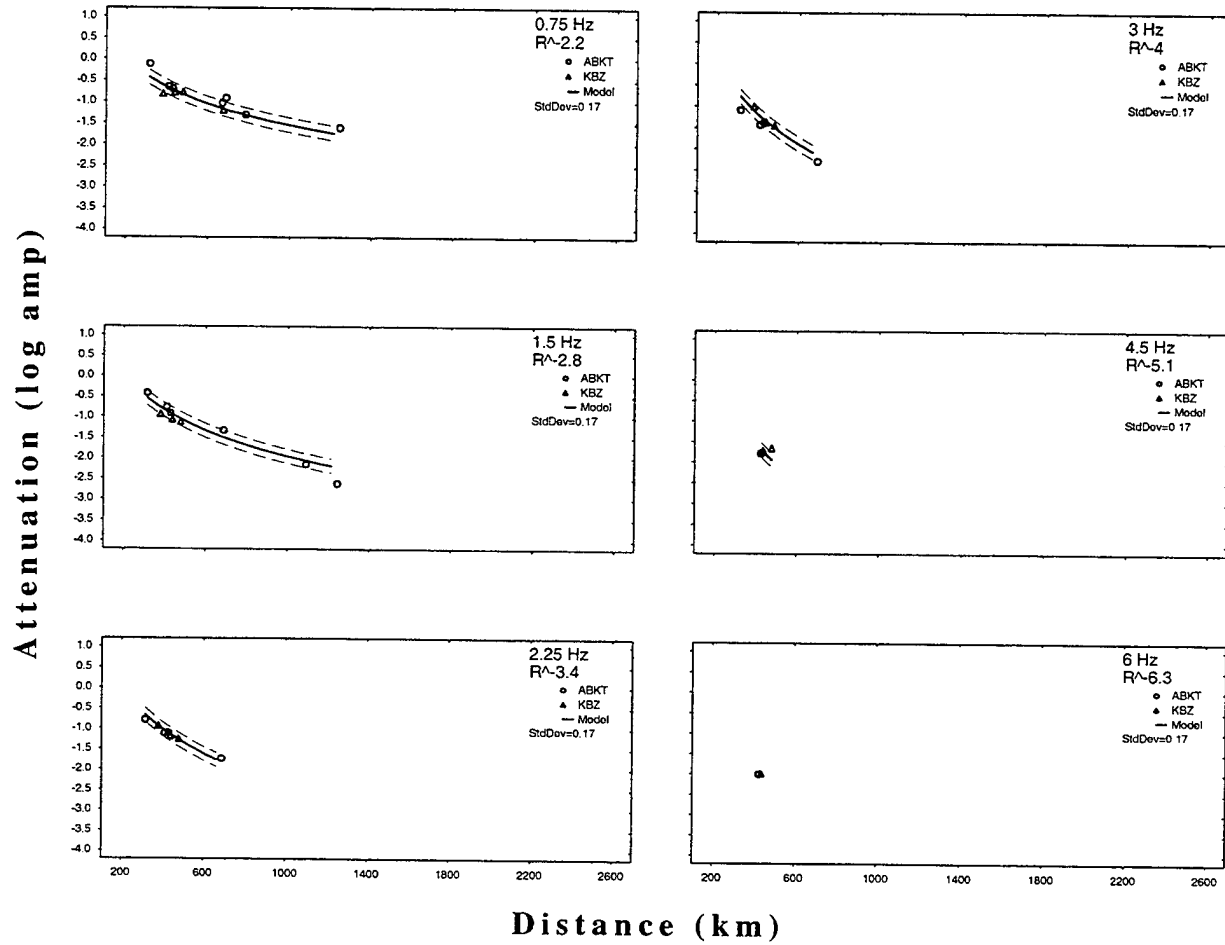
Figure B.5.2 Continued.

B.6 Central Asia

B.6.1 Inversion Results

Table B.6:   Inversion Results for the central Asia subnetwork

phase	*count*	*c*	κ	α	*a*	*b*	*|site|*	σ
Pn	48	10.0	0.00	-0.37	-0.02	2.17	0.12	0.34
Pg	11	10.0	1.76	-0.20	0.16	5.08	0.23	0.19
Sn	20	10.0	0.63	-0.42	0.08	2.33	0.17	0.26
Lg	49	10.0	1.57	-0.13	0.39	2.56	0.18	0.28

B.6.2 Source
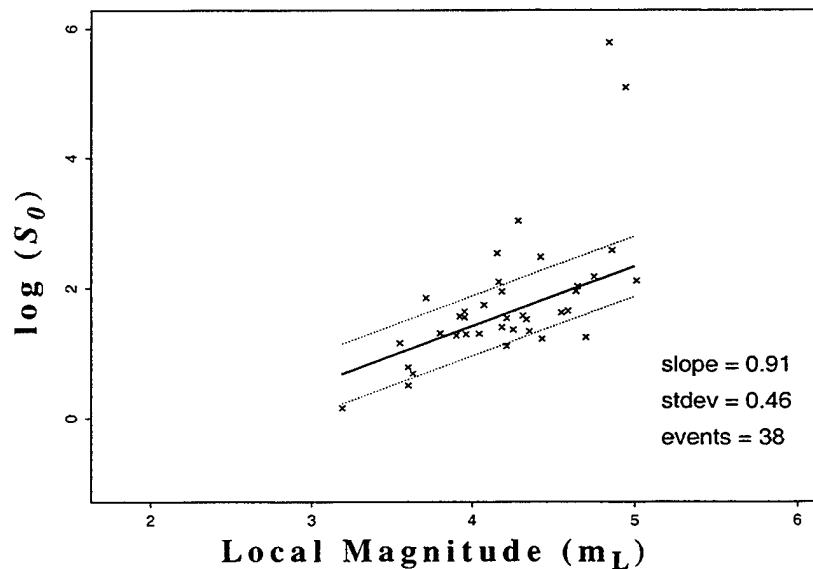
Figure B.6.1 Estimated long period source level (S_0) plotted against local magnitude for the central Asia subnetwork. The best-fit curve was calculated without consideration of two outlier points. These events had a larger body wave magnitudes (m_b 5.17 and 5.62) larger than any of the other events.
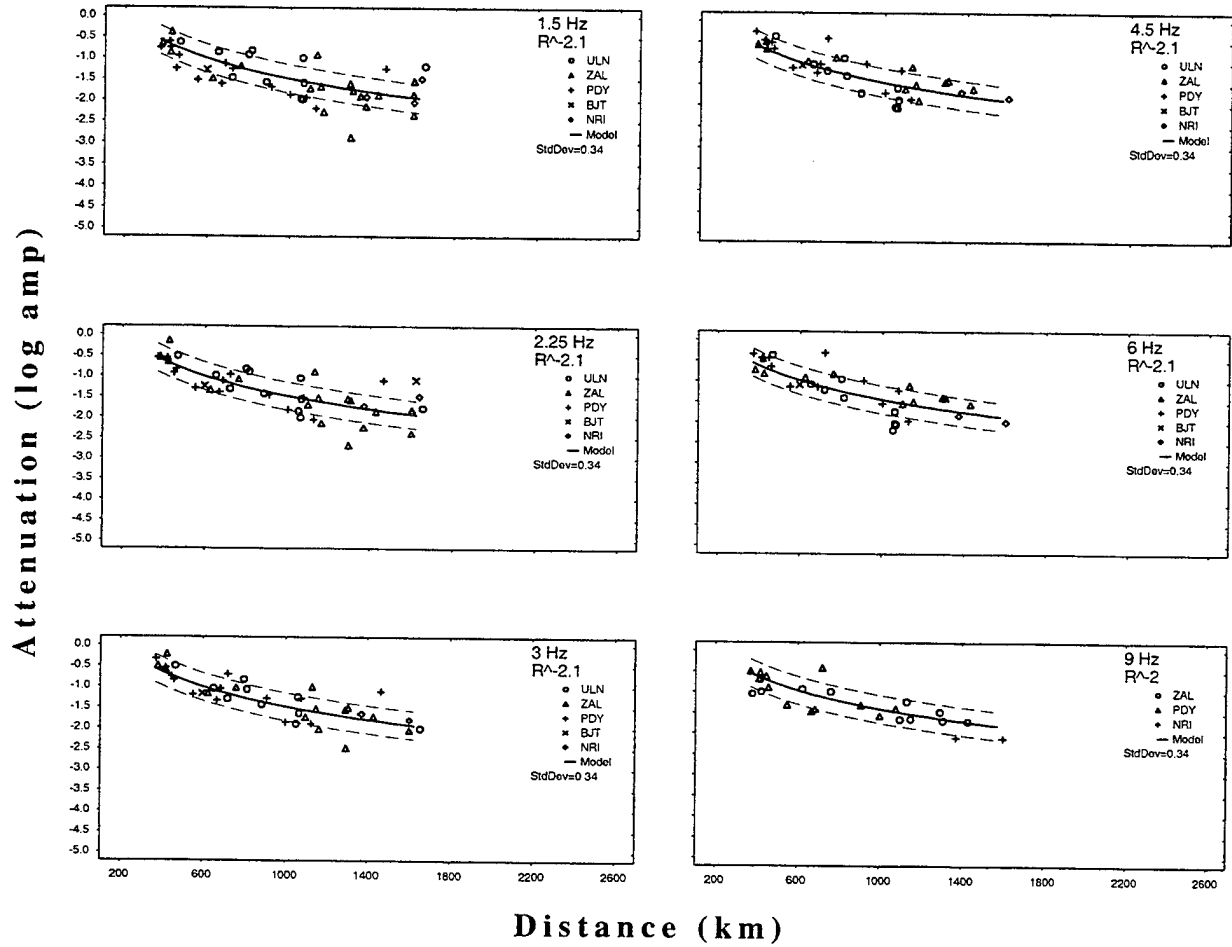
Central Asia Pn

Figure B.6.2 Attenuation curves at various frequencies for *Pn*, *Pg*, *Sn*, and *Lg* phases determined with the central Asia subnetwork.

Central Asia Pg
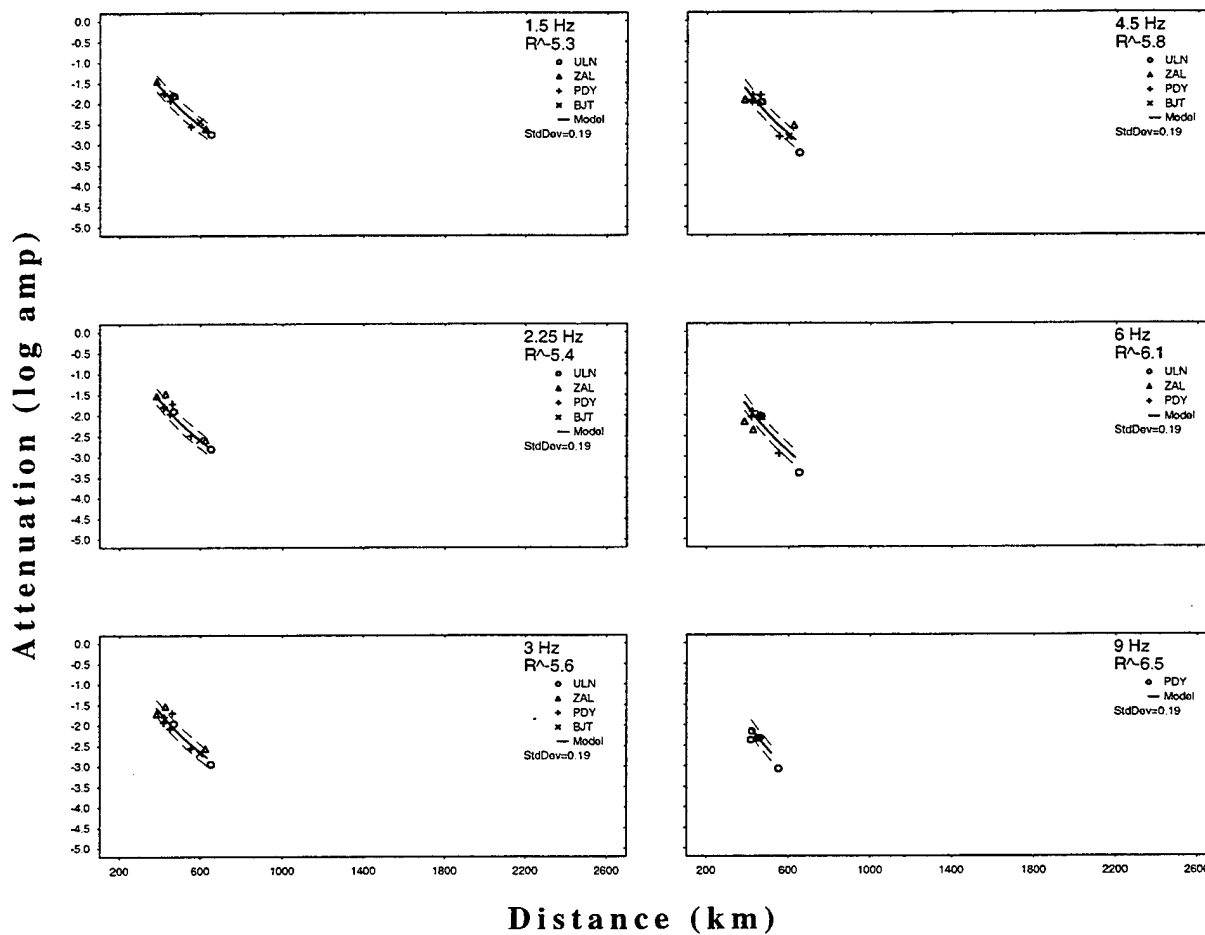
Figure B.6.2 Continued.

Central Asia Sn
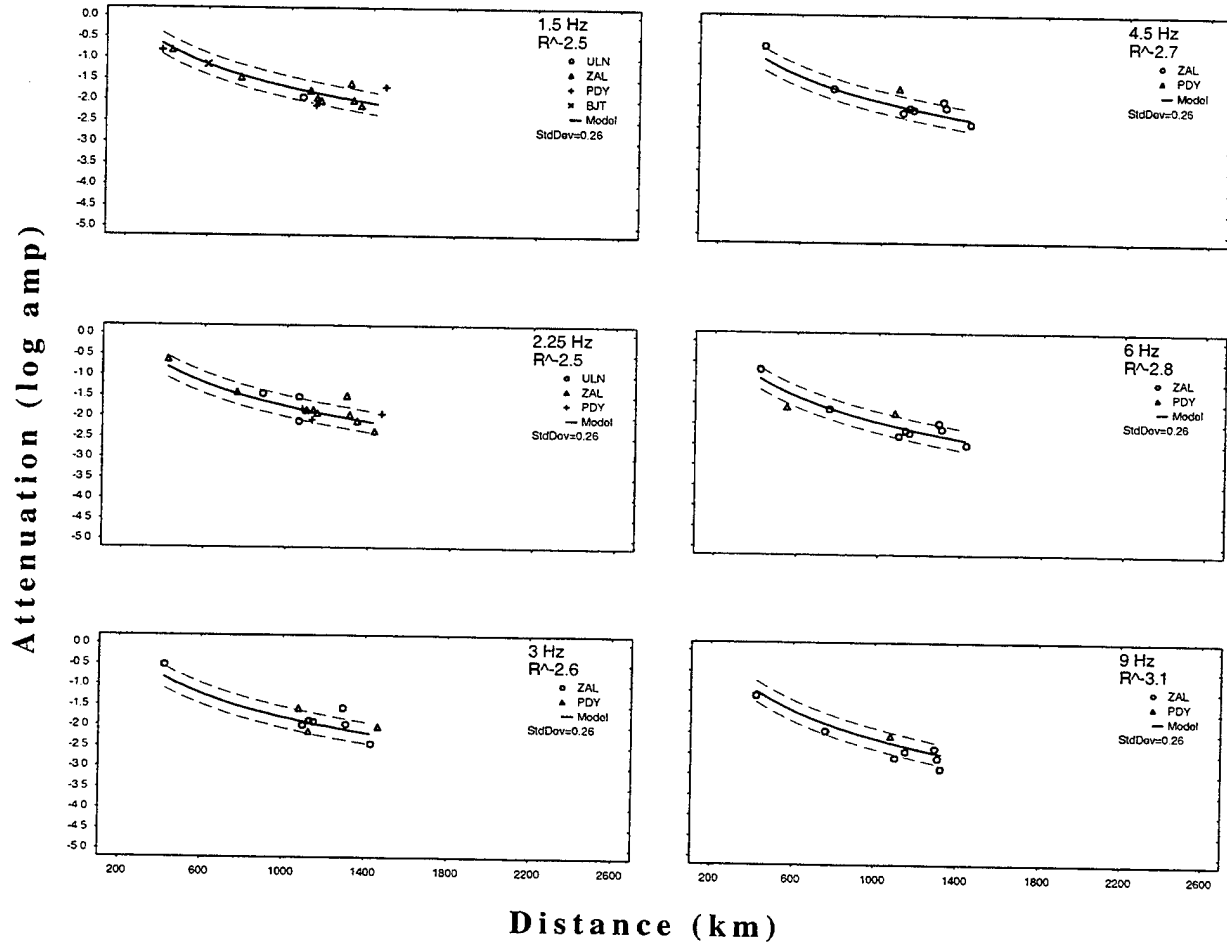
Figure B.6.2 Continued.

Central Asia Lg
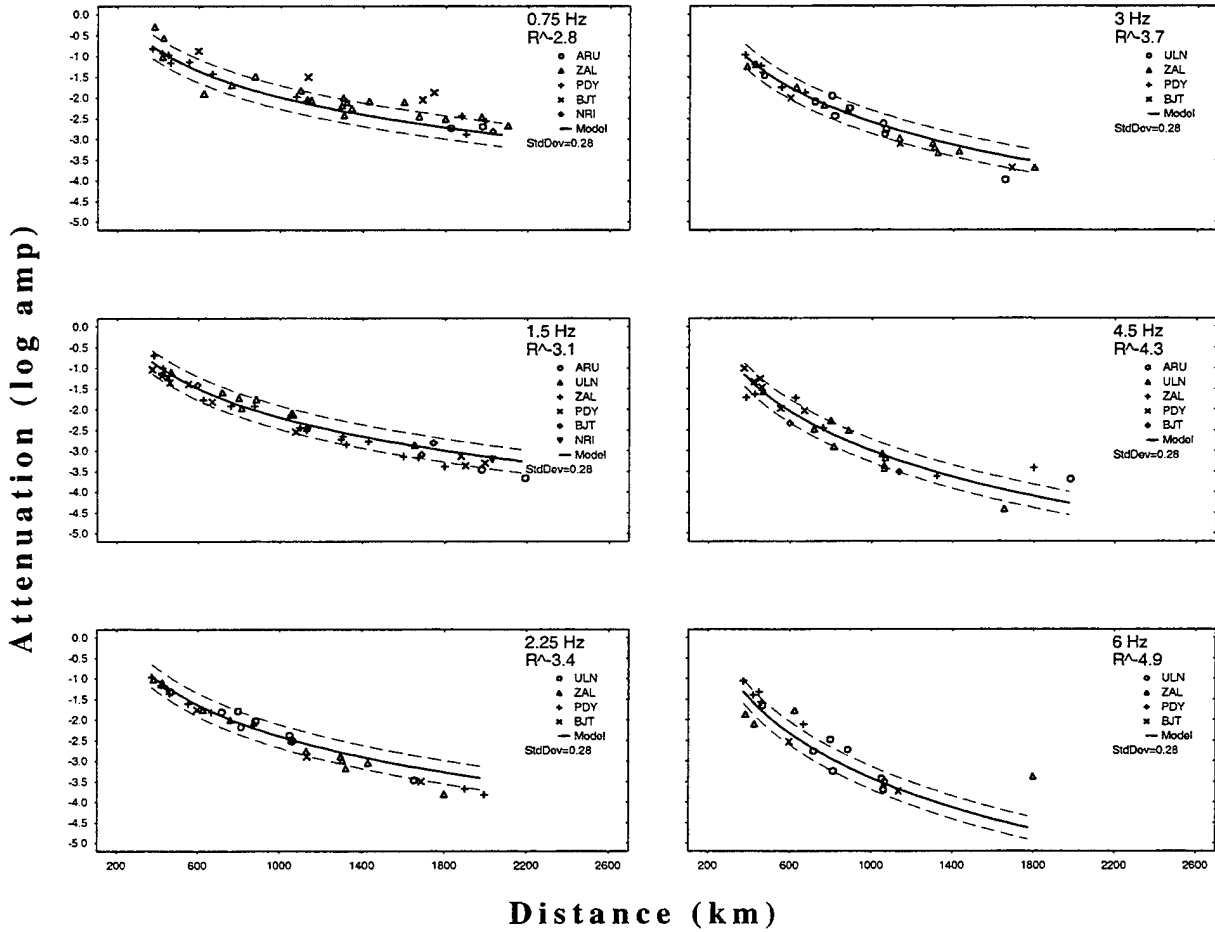
Figure B.6.2 Continued.

B.7 Australia

B.7.1 Inversion Results

Table B.7: Inversion Results for the Australia subnetwork

phase	*count*	*c*	κ	α	*a*	*b*	*|site|*	σ
Pn	295	15.0	0.00	-0.38	0.18	0.80	0.13	0.25
Pg	30	15.0	0.25	-0.16	0.51	-0.08	0.17	0.21
Sn	180	15.0	0.91	-0.32	0.16	1.61	0.14	0.20
Lg	142	15.0	1.18	-0.01	0.43	1.17	0.10	0.20

B.7.2 Source

slope = 0.83
stdev = 0.22
events = 107

Figure B.7.1 Estimated long period source level (S_0) plotted against local magnitude for the Australia subnetwork.

104

B.7.3 Path

Australia Pn
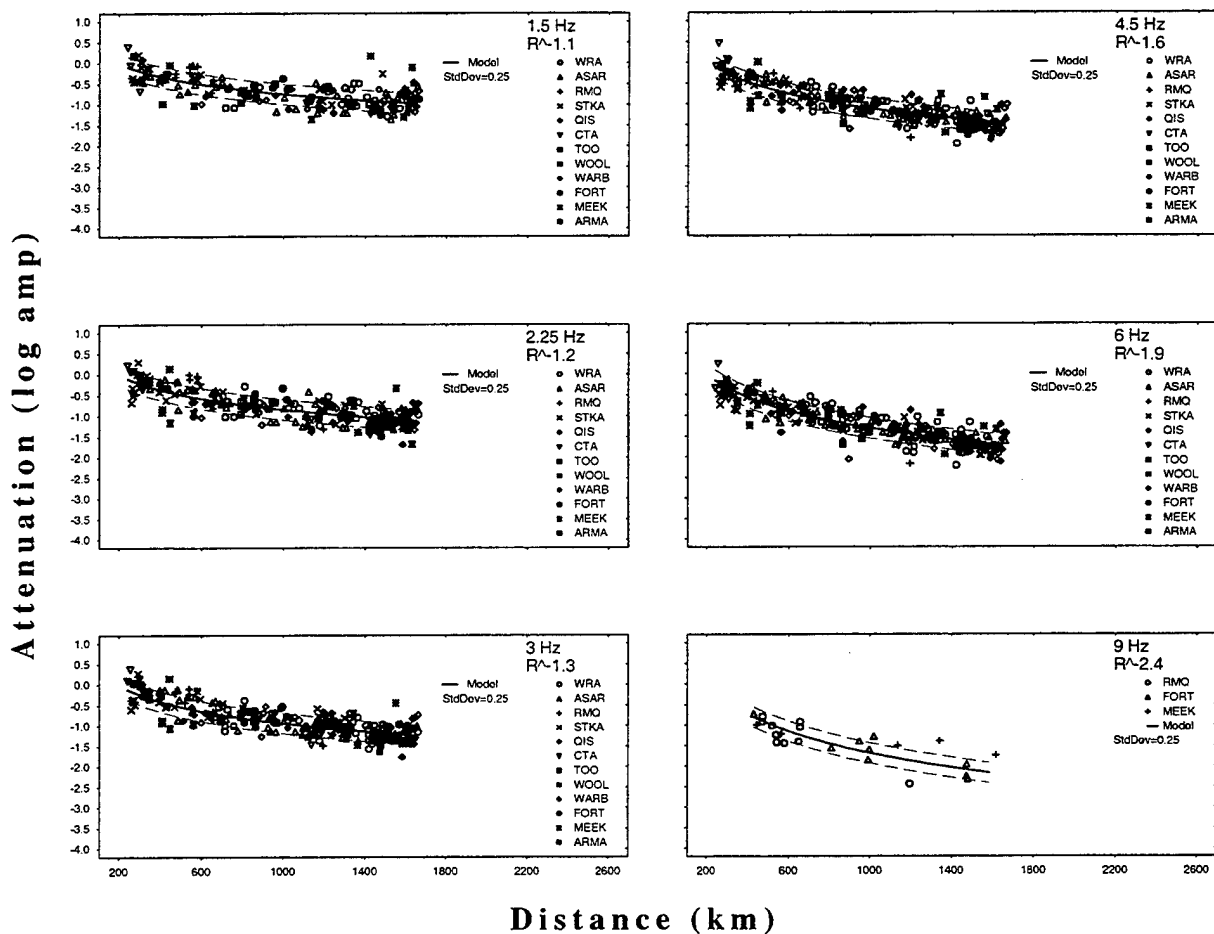
Figure B.7.2 Attenuation curves at various frequencies for *Pn, Pg, Sn,* and *Lg* phases determined with the Australia subnetwork.

Australia Pg

Figure B.7.2 Continued.

Australia Sn

Figure B.7.2 Continued.

Australia Lg
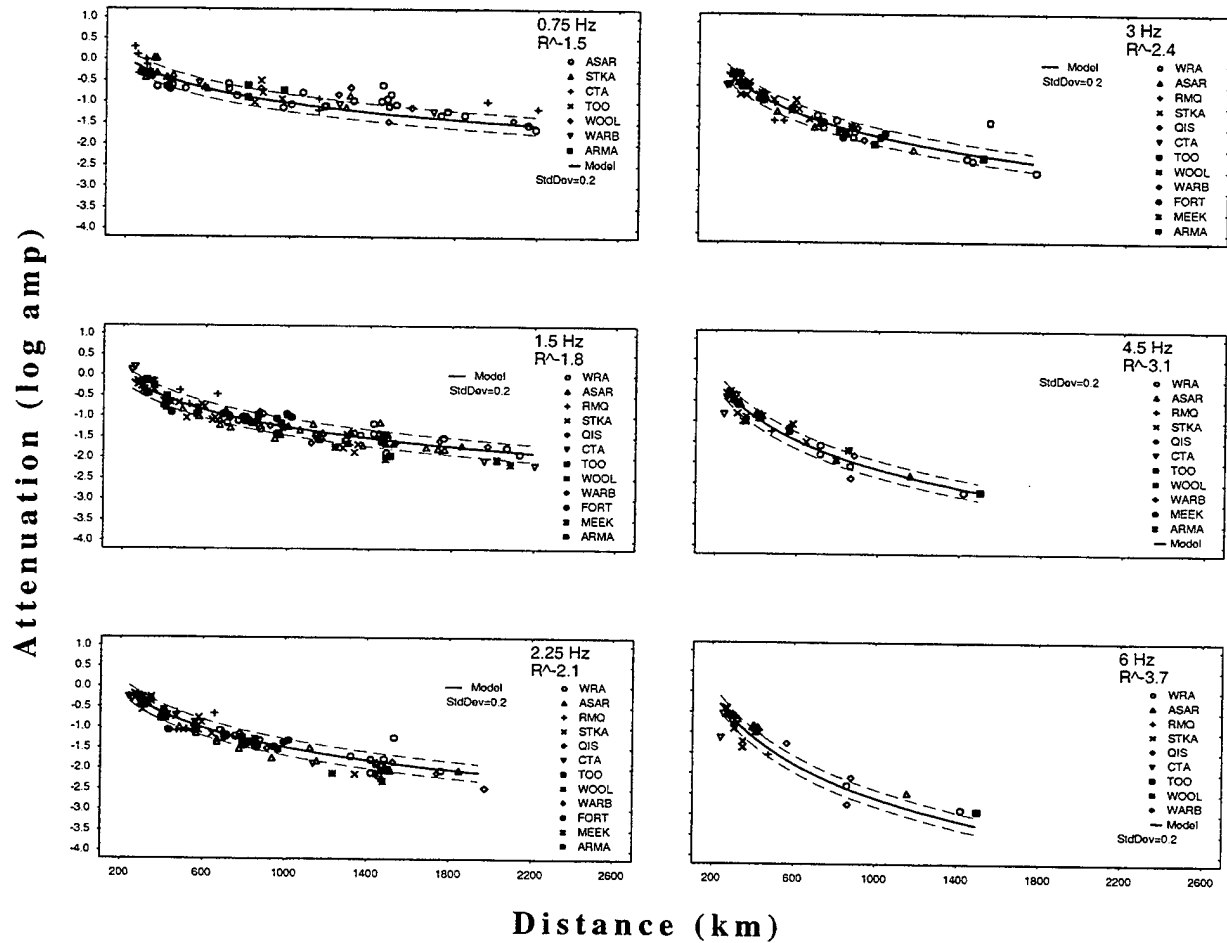
Figure B.7.2 Continued.

B.8 Japan

B.8.1 Inversion Results

Table B.8: Inversion Results for the Japan subnetwork

phase	count	c	κ	α	a	b	|site|	σ
Pn	632	25.0	0.00	0.04	0.01	1.76	0.32	0.25
Pg	38	25.0	0.02	0.27	0.24	0.57	0.20	0.22
Sn	124	25.0	0.31	0.03	-0.14	2.34	0.33	0.21
Lg	42	25.0	0.47	0.53	-0.11	1.70	0.26	0.17

B.8.2 Source
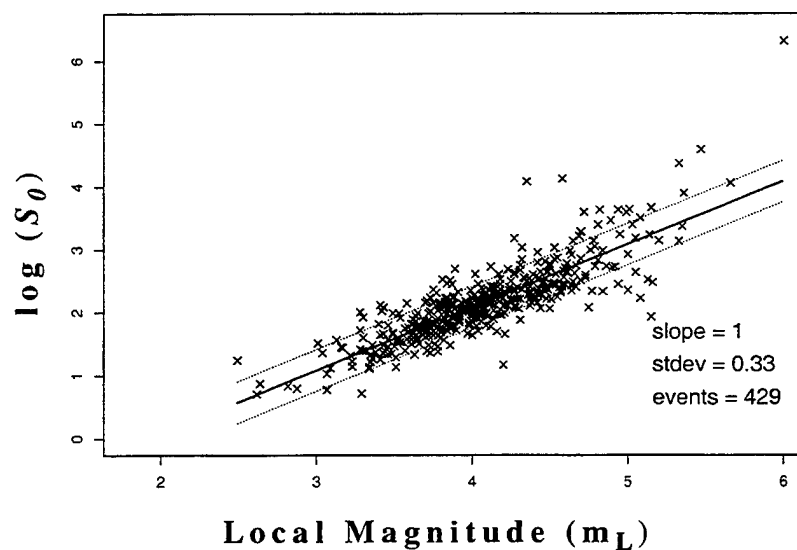
Figure B.8.1 Estimated long period source level (S_0) plotted against local magnitude for the Japan subnetwork.

B.8.3 Path

Japan Pn
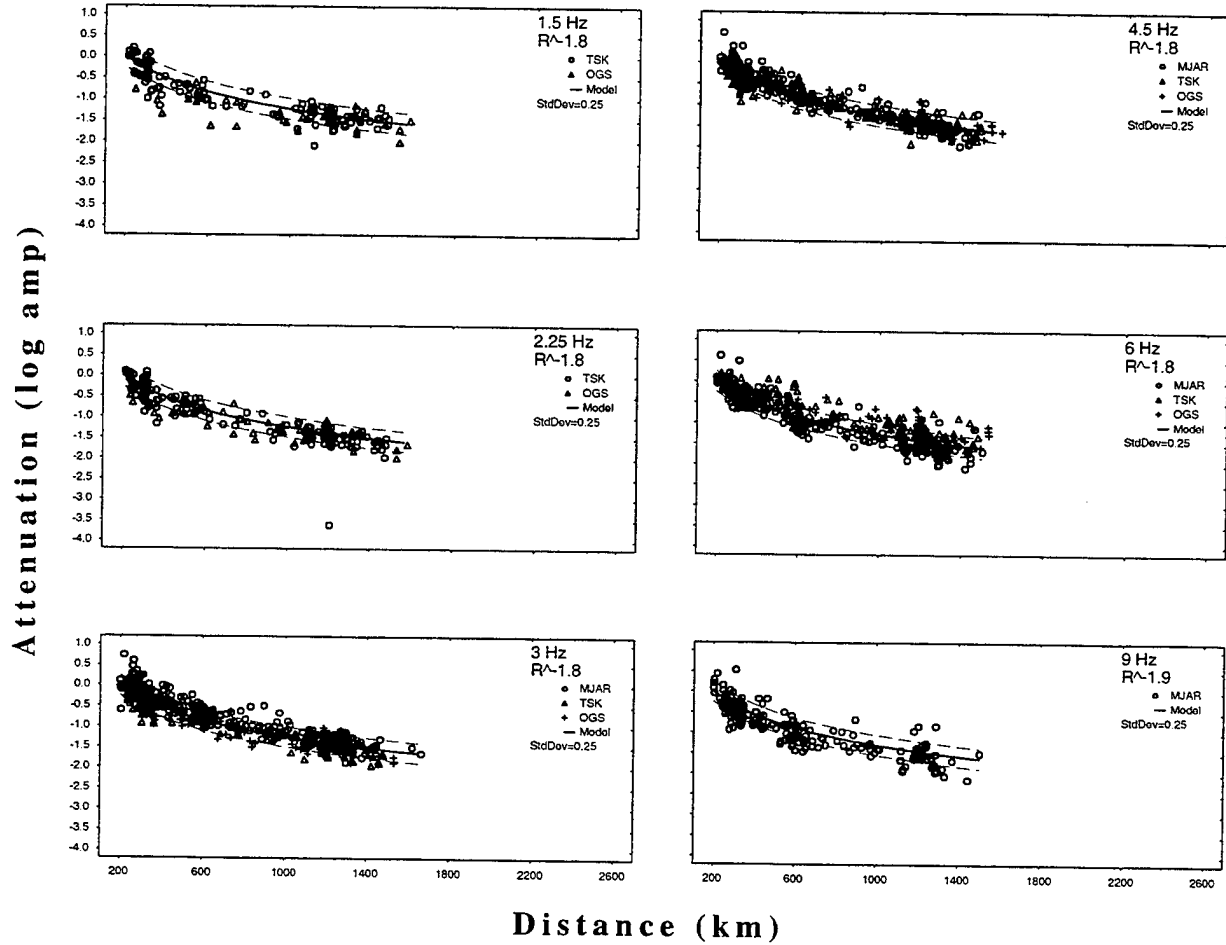
Figure B.8.2 Attenuation curves at various frequencies for *Pn*, *Pg*, *Sn*, and *Lg* phases determined with the Alaska subnetwork.

Japan Pg
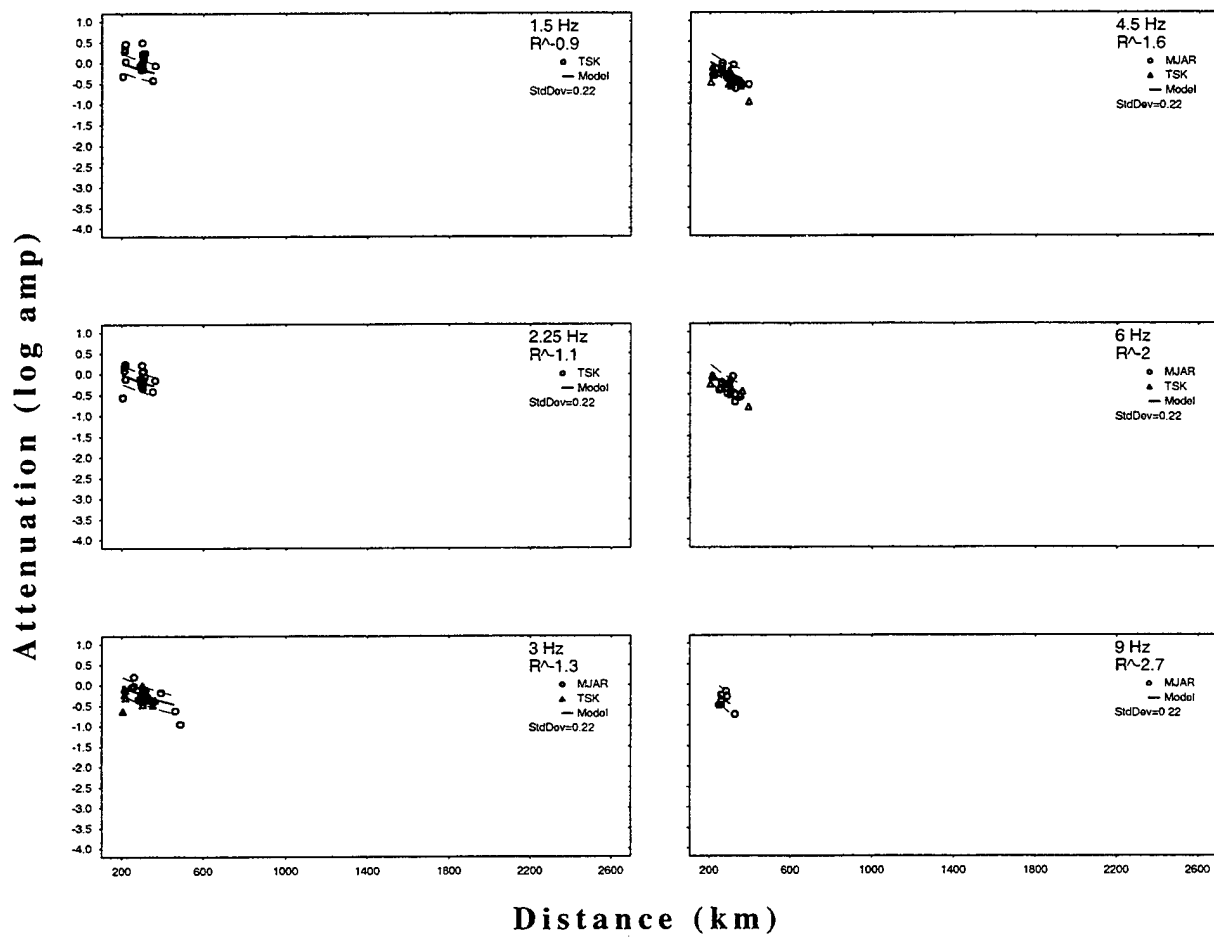
Figure B.8.2 Continued.

Japan Sn
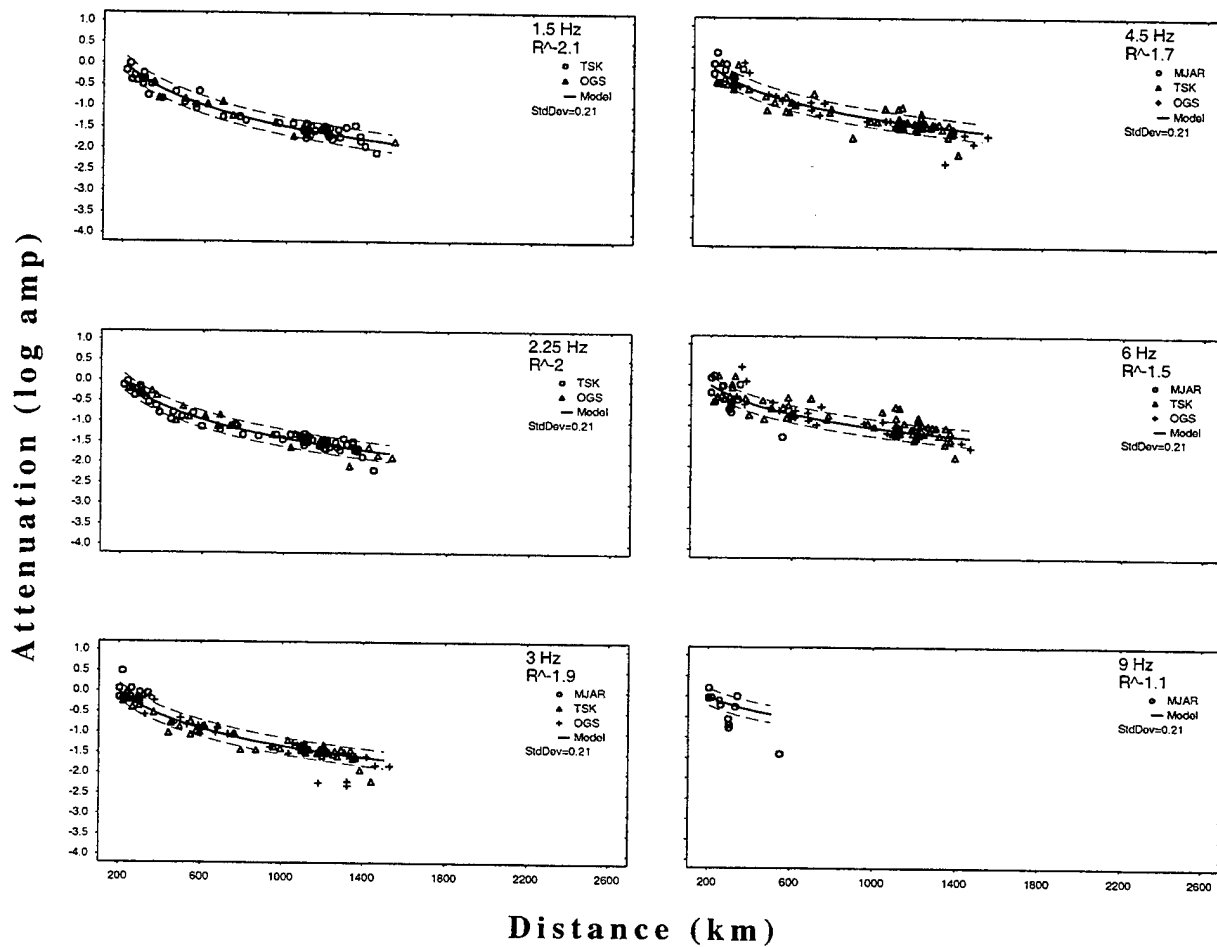
Figure B.8.2 Continued.

Japan Lg
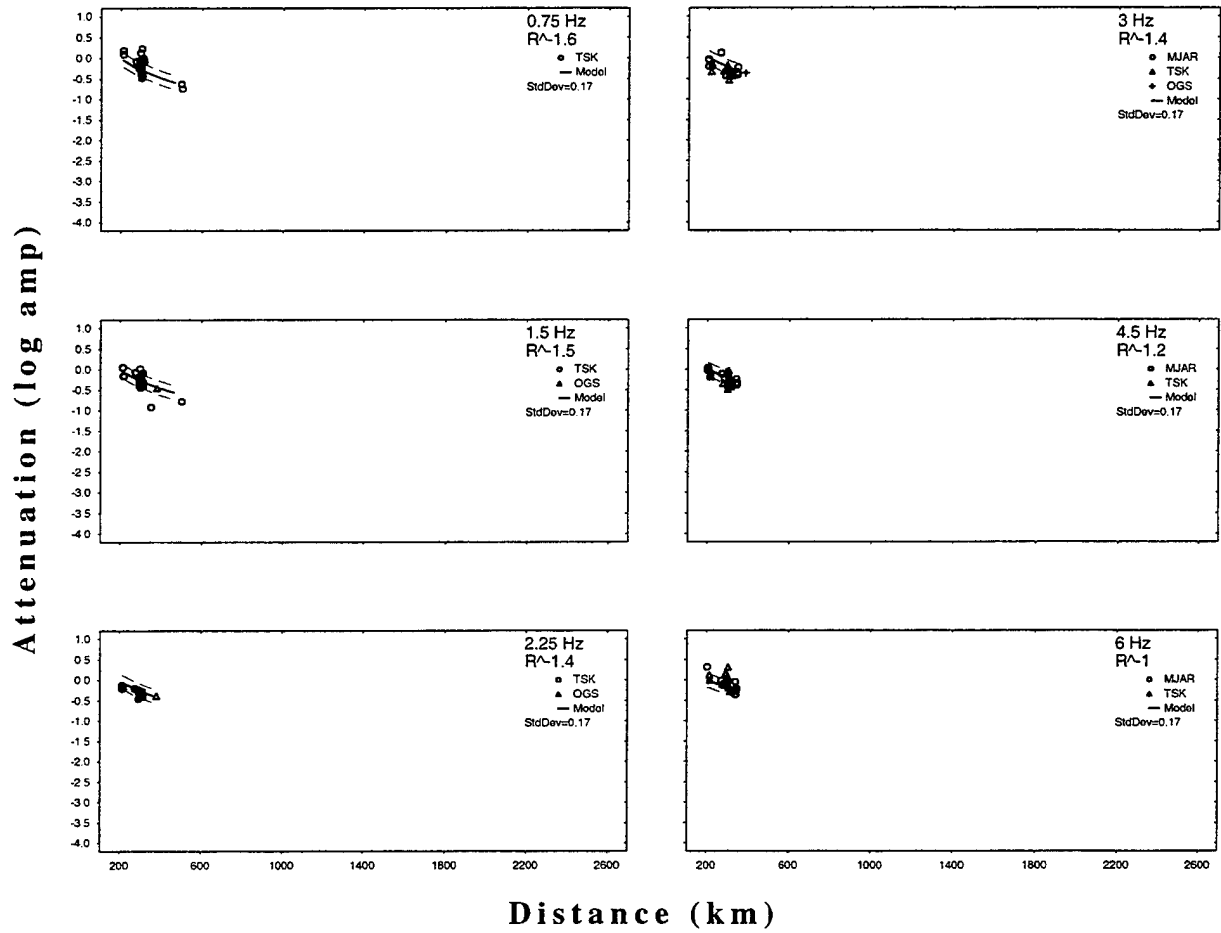
Figure B.8.2 Continued.

B.9 South America

B.9.1 Inversion Results

Table B.9: Inversion Results for the South America subnetwork

phase	*count*	*c*	κ	α	*a*	*b*	*|site|*	σ
Pn	59	15.0	0.00	-0.08	0.06	1.86	0.22	0.15
Pg	1	15.0	0.22	0.30	0.43	-0.71	0.00	0.21
Sn	8	15.0	0.75	0.04	0.12	1.85	0.29	0.14
Lg	4	15.0	0.12	-2.68	2.36	0.26	0.37	0.22

B.9.2 Source
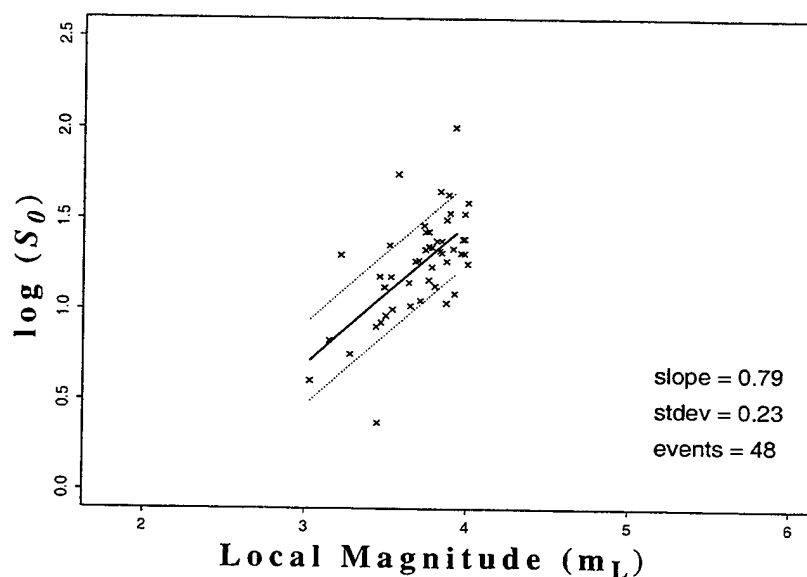
Figure B.9.1 Estimated long period source level (S_0) plotted against local magnitude for the South America subnetwork.

B.9.3 Path

South America Pn
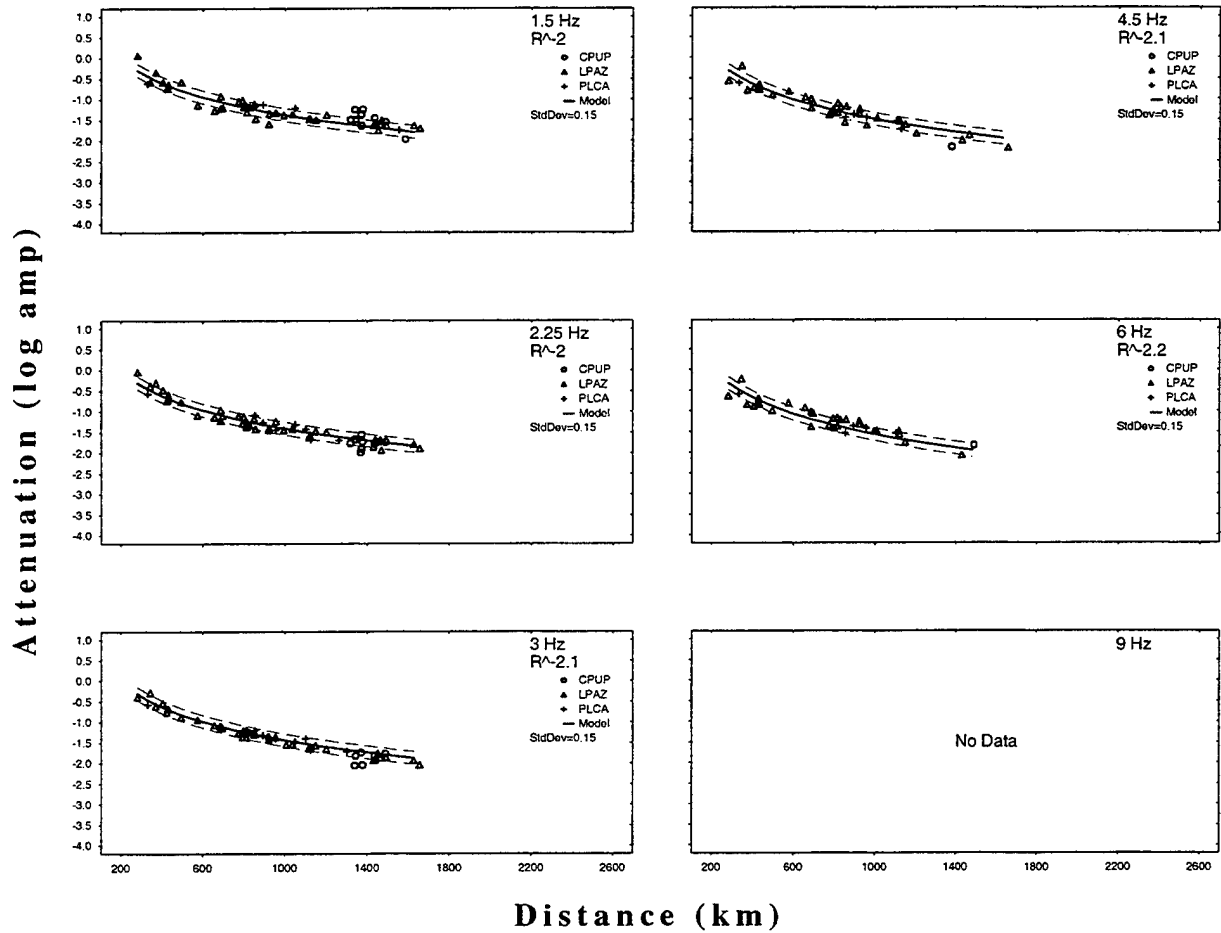
Figure B.9.2 Attenuation curves at various frequencies for *Pn, Pg, Sn,* and *Lg* phases determined with the South America subnetwork.

South America Pg
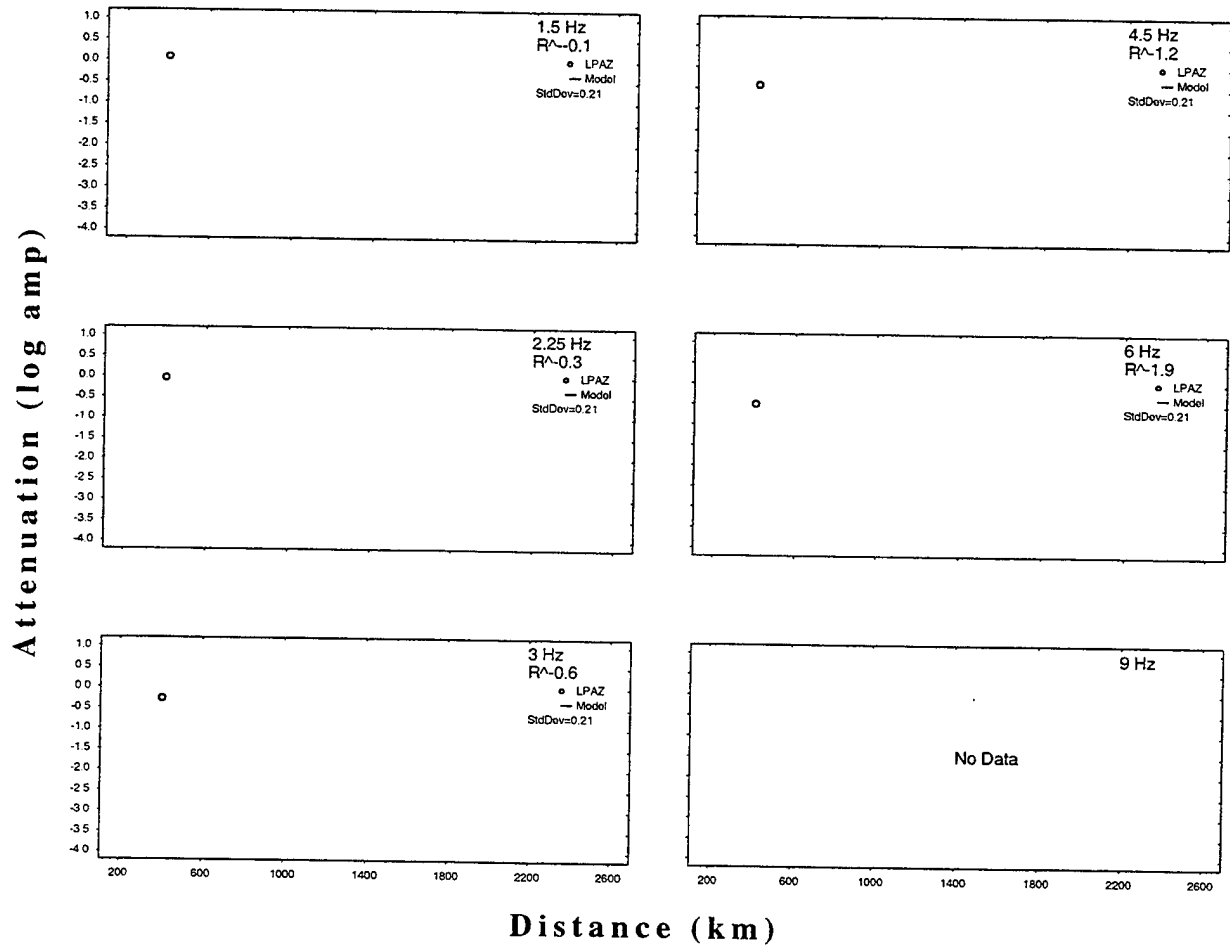
Figure B.9.2 Continued.

South America Sn
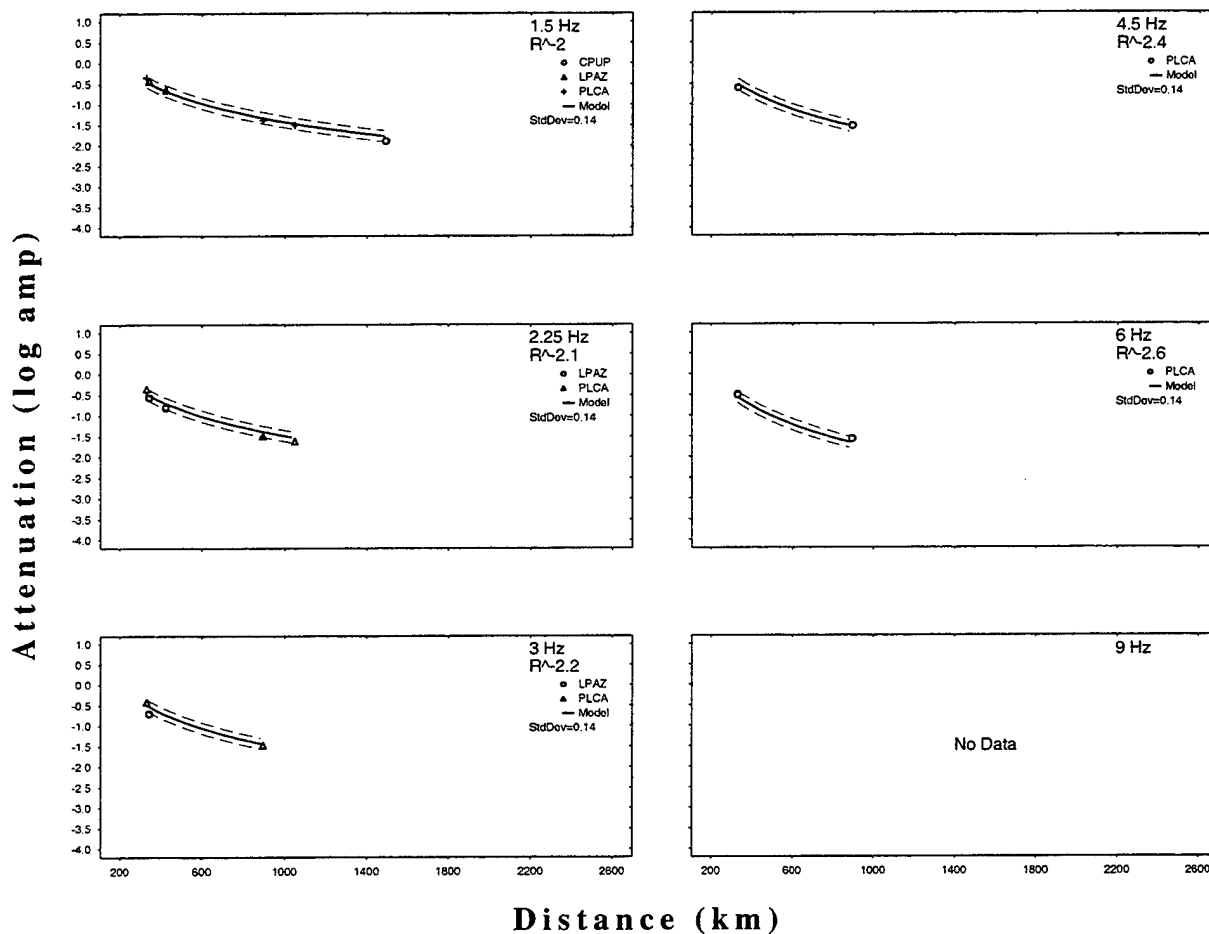
Figure B.9.2 Continued.

South America Lg
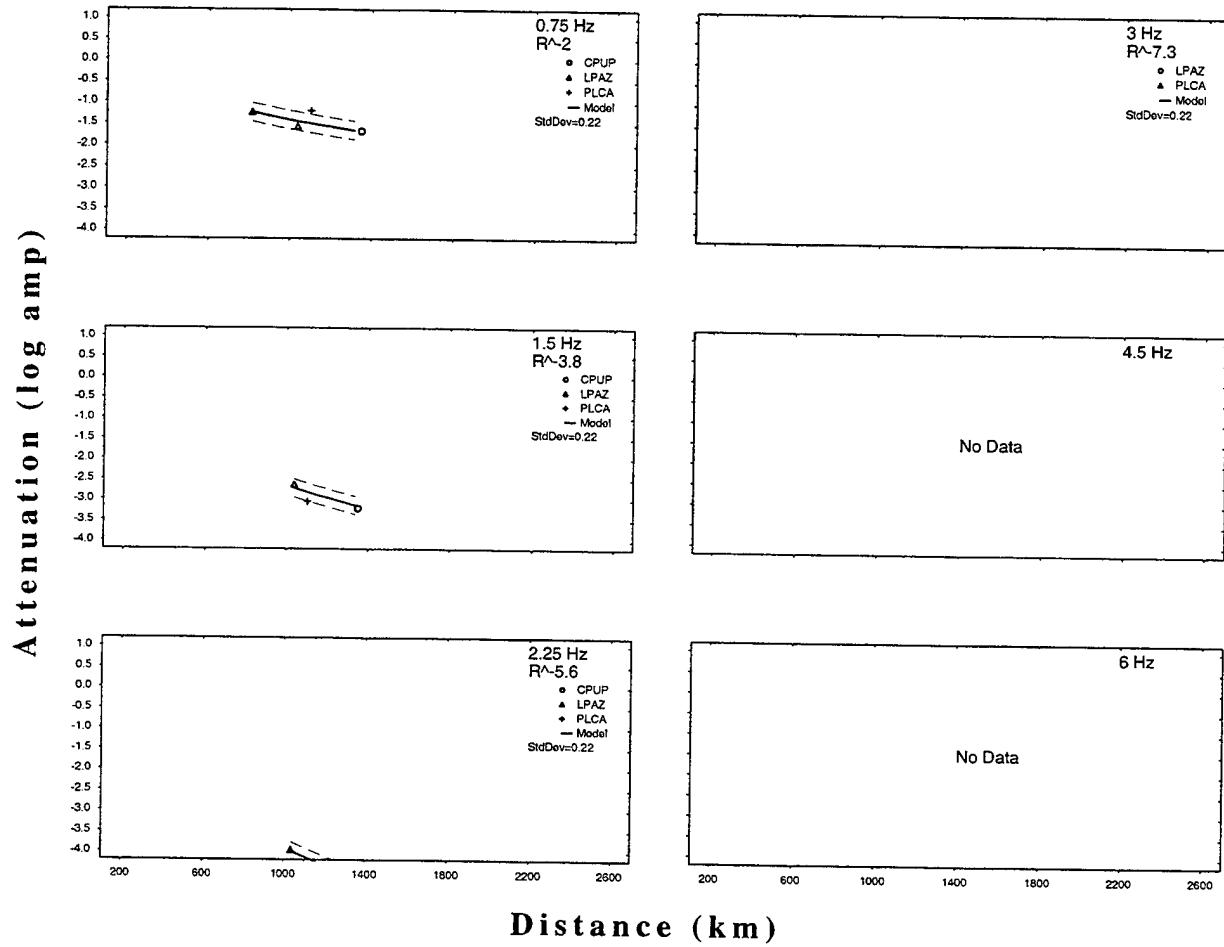
Figure B.9.2 Continued.

Appendix C: *S/P* Discriminants

This appendix contains uncorrected and normalized *S/P* ratios along with normalized *S/P* discriminant histograms for eight subnetworks: 1) Alaska, 2) western North America, 3) eastern North America, 4) southern Europe, 5) southern Asia, 6) central Asia, 7) Australia, and 8) Japan. The results are grouped by subnetwork. Each subnetwork has seven pages associated with it. Note that the western North America, eastern North America, southern Europe, central Asia, and Australia subnetworks contain several suspected mine blasts, while the southern and central Asia subnetworks record four known nuclear explosions.

The first page associated with each subnetwork contains uncorrected and distance-corrected plots of the *S/P* ratio. We plot the log amplitude ratio of the largest *S* (*Sn* or *Lg*) and earliest *P* (*Pn* or *Pg*) against distance to show the distance dependence that exists. The three plots in the left-hand column illustrate the uncorrected *S/P* ratio in the frequency bands 1-2, 3-6, and 6-12 Hz (i.e., referred to as 1.5, 4.5, and 9 Hz). The plots in the right-hand column show the ratio in each of these frequency bands after applying distance corrections based on our attenuation models. Note that the 6-12 Hz band only contains *Sn* amplitudes since *Lg* amplitudes were not allowed above 6 Hz for this study. The corrected ratio plots were generated with the slope fixed at zero. In the lower right-hand corner of each plot, the fall-off rate (R^{-n}), standard deviation, and number of measurements are listed.

The second through seventh pages are *S/P* discrimination histograms. These histograms are subdivided into three sections, each two pages in length. The first section shows histograms of normalized *Sn/Pn* amplitude ratios at various frequency bands, the second shows *Lg/Pn* ratios, and the third shows largest *S* / earliest *P* ratios. Each histogram has been produced with amplitude measurements from different frequency bands. The central frequency of the band in which the *S* amplitude was measured increases from left to right in each section, while the central frequency in which the *P* amplitude was measured increases from top to bottom. Note again that no *Lg* phases were measured in the 6-12 Hz band. *S/P* ratios were not computed when the central *S* frequency was larger than the central *P* frequency. In a few cases, one or more *S/P* ratio measurements extended beyond the boundaries of the histogram. In these circumstances, the outlier was added to the nearest end column, and a tick mark was placed inward and below the histogram (i.e., western North America, *Sn* 0.75 Hz, *Pn* 9.0 Hz). Different shading was used for earthquakes, industrial explosions, and nuclear explosions.

C.1. Alaska

C.1.1 Validation

Uncorrected   **Corrected**
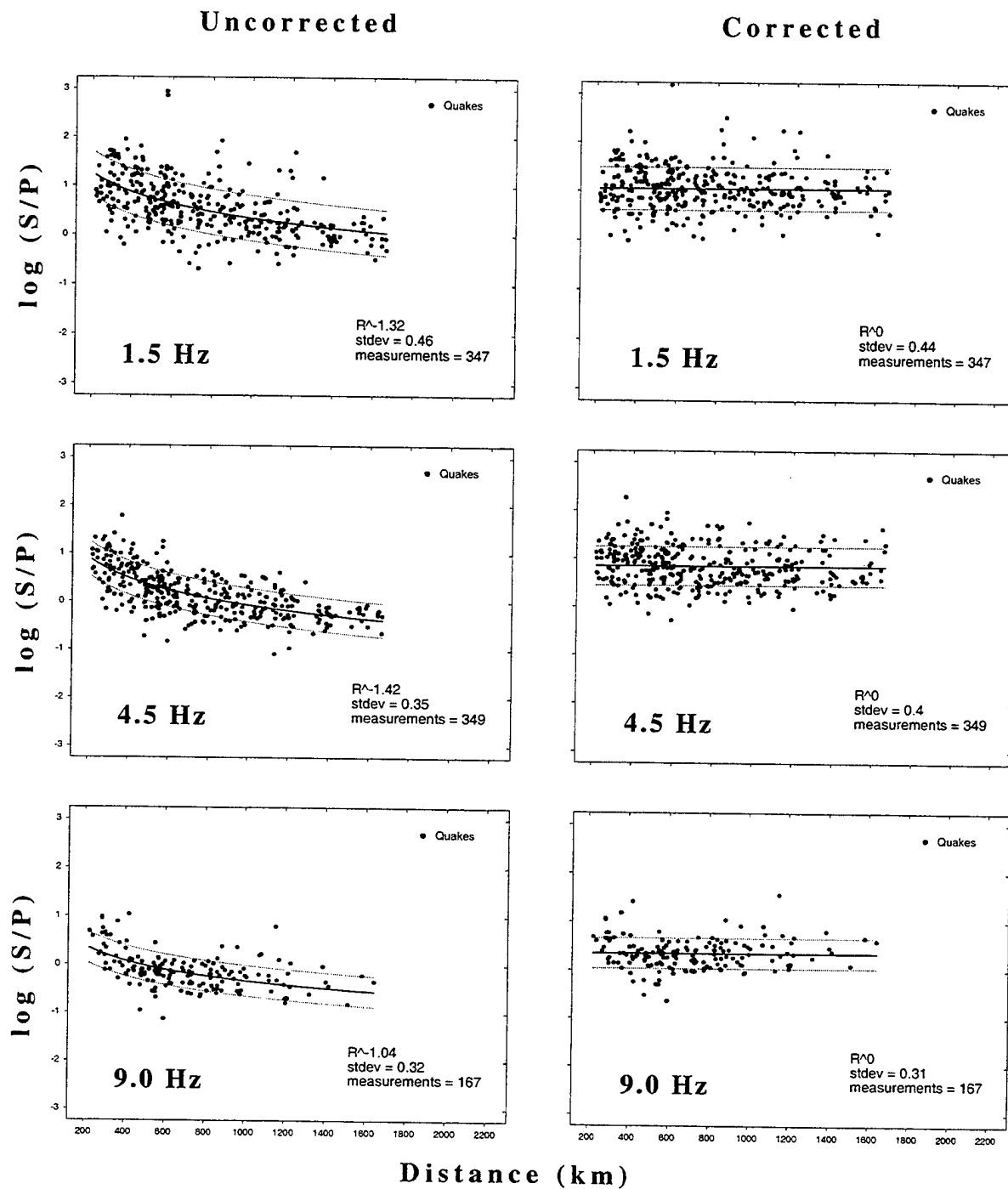
Figure C.1.1 Uncorrected and distance-corrected S/P ratio plots of measurements made in 1-2, 3-6, and 6-12 Hz (referred to as 1.5, 4.5, and 9.0 Hz) frequency bands for Alaska.

C.1.2 *S/P* Ratios

Alaska *Sn/Pn* Ratios
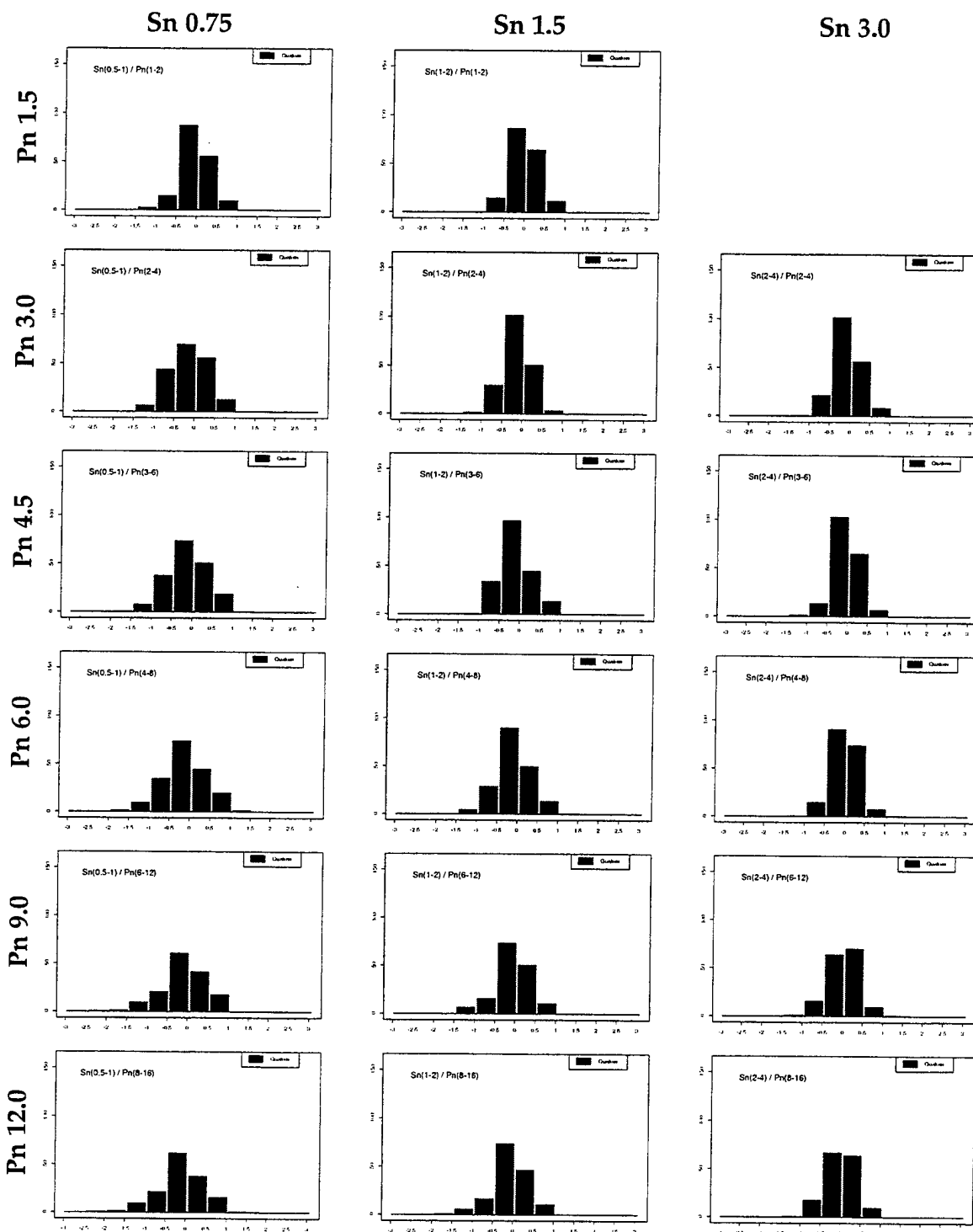
Figure C.1.2 Comparison of normalized *Sn/Pn* amplitude ratios for earthquake population found in Alaska.

Alaska *Sn/Pn* Ratios

Sn 4.5 **Sn 6.0** **Sn 9.0**
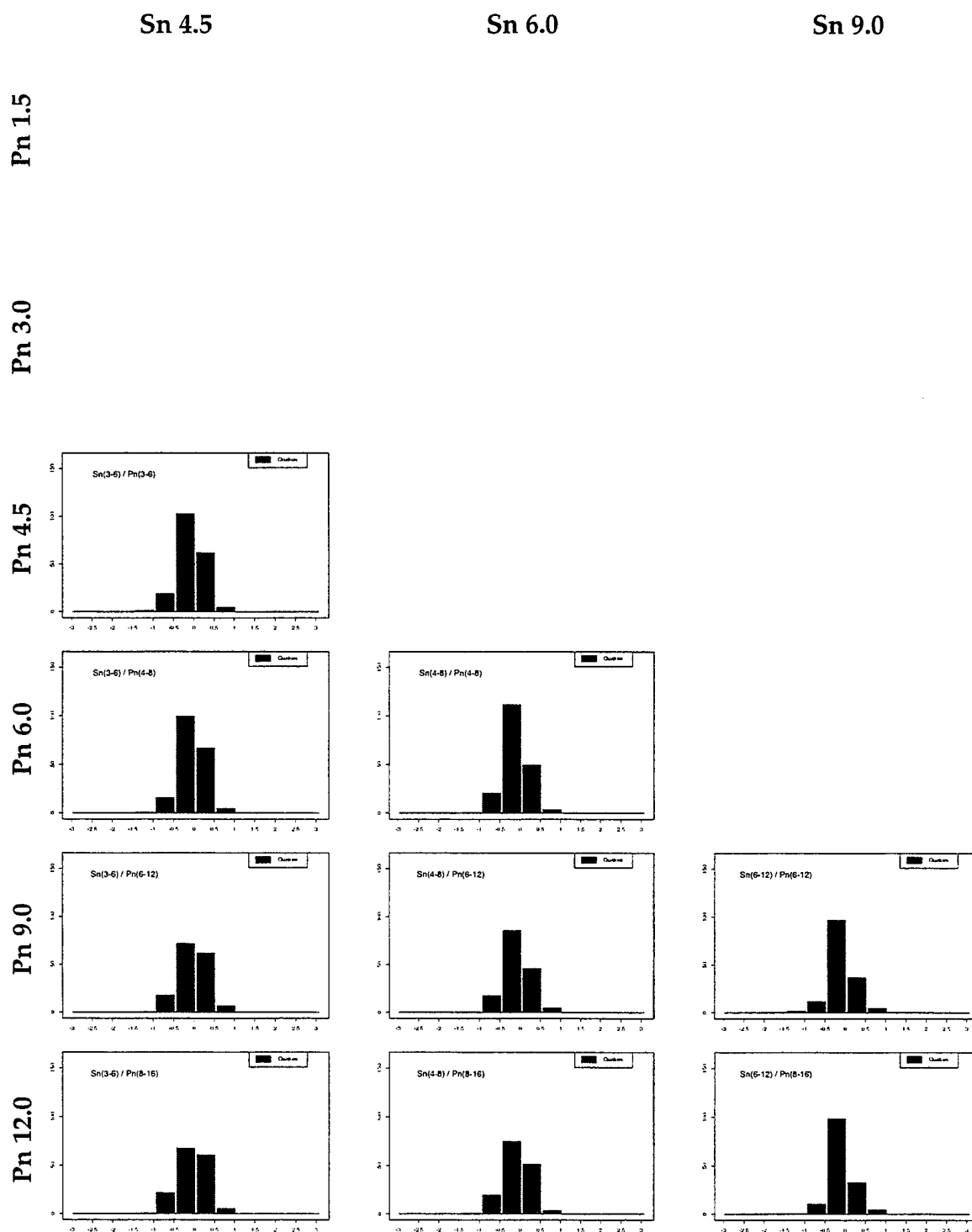
Figure C.1.2 Continued.

Alaska *Lg/Pn* Ratios
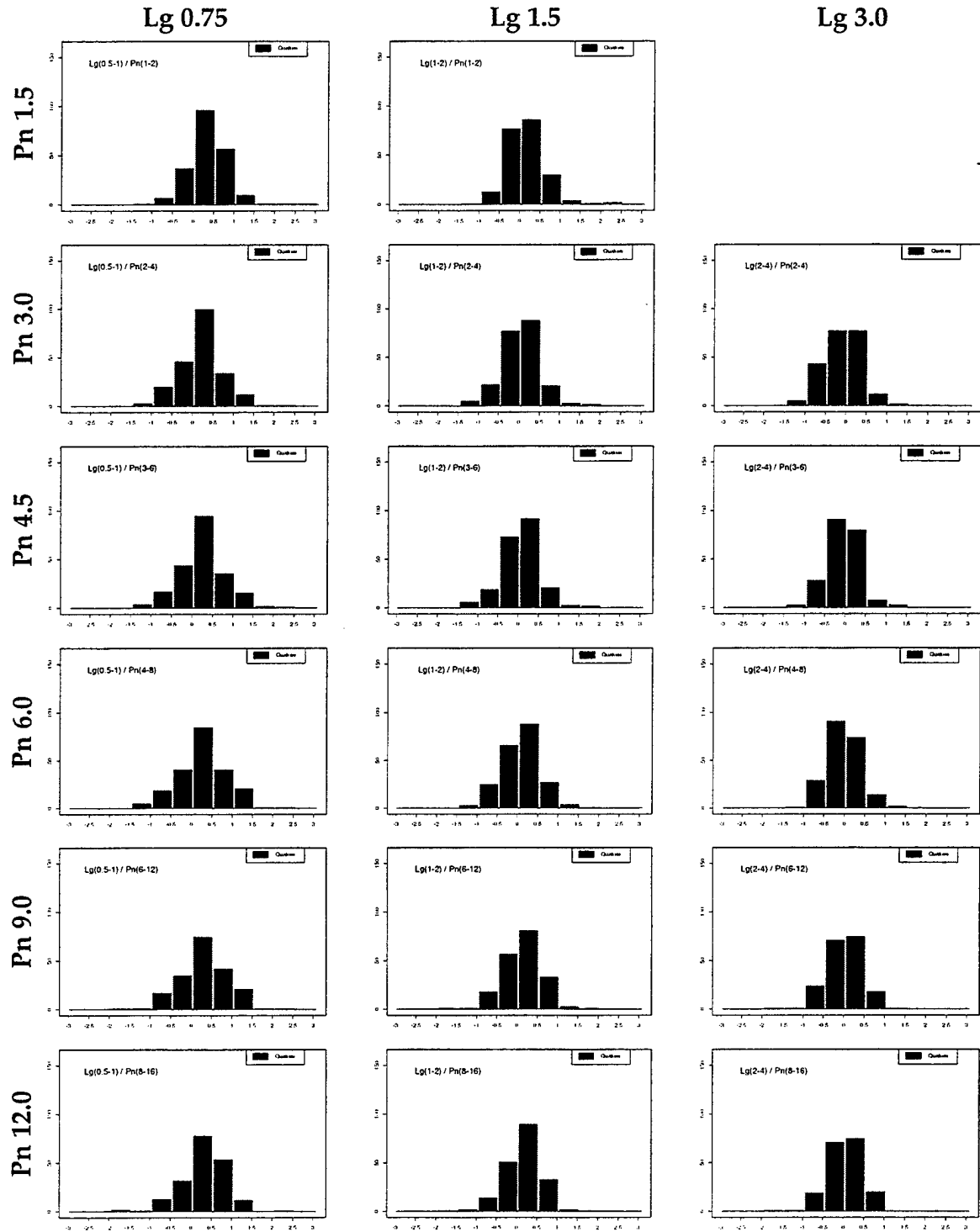
Figure C.1.3 Comparison of normalized *Lg/Pn* amplitude ratios for earthquake population found in Alaska.

123

Alaska *Lg/Pn* Ratios

Lg 4.5   **Lg 6.0**

Pn 1.5

Pn 3.0

Pn 4.5

Pn 6.0

Pn 9.0

Pn 12.0
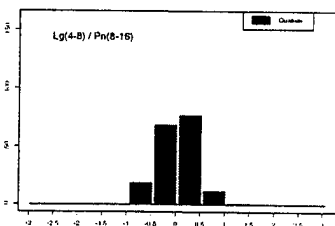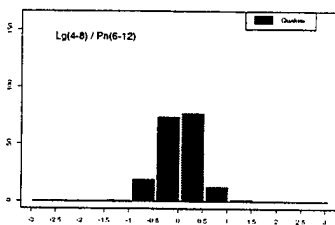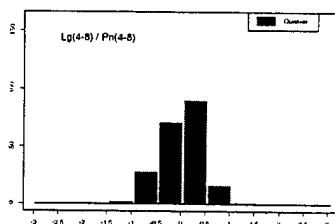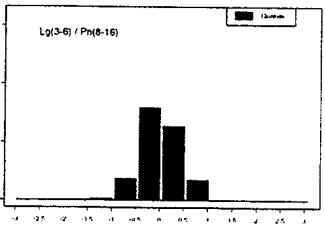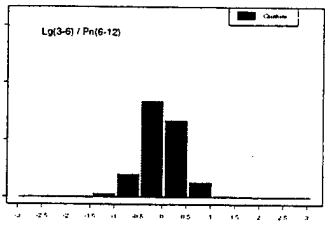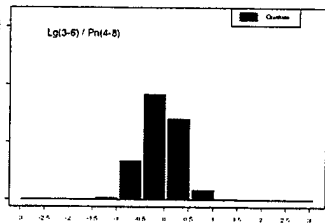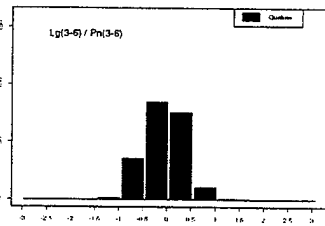
Figure C.1.3 Continued.

124

Alaska Largest *S* / Earliest *P* Ratios
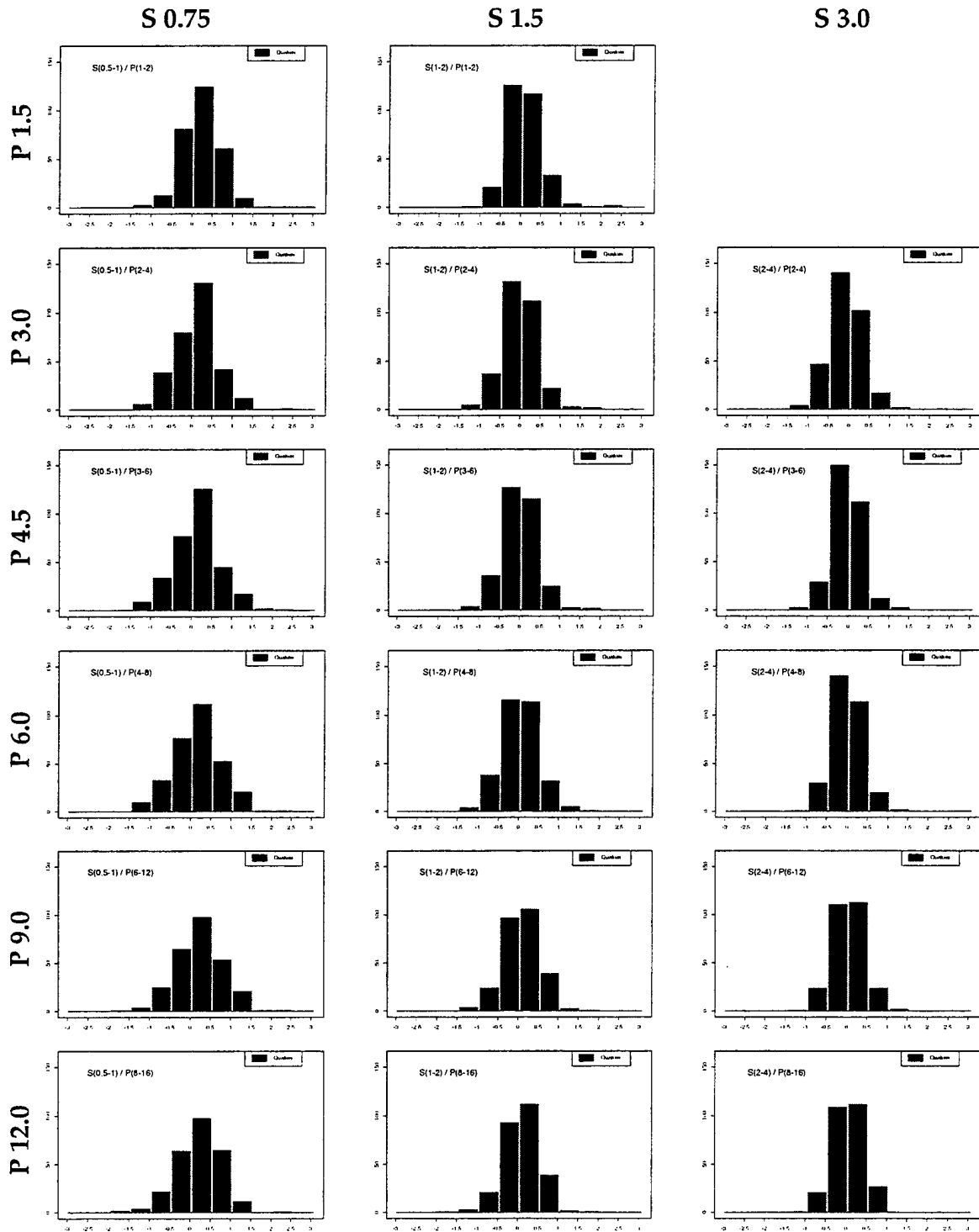
Figure C.1.4 Comparison of normalized largest *S* / earliest *P* amplitude ratios for earthquake population found in Alaska.

Alaska Largest *S* / Earliest *P* Ratios

S 4.5   S 6.0   S 9.0
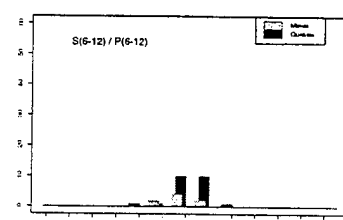
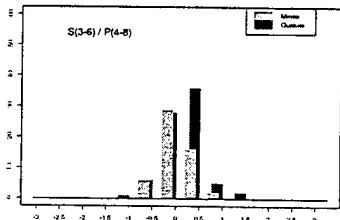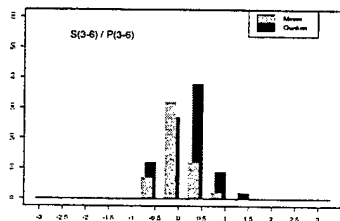P 1.5

P 3.0
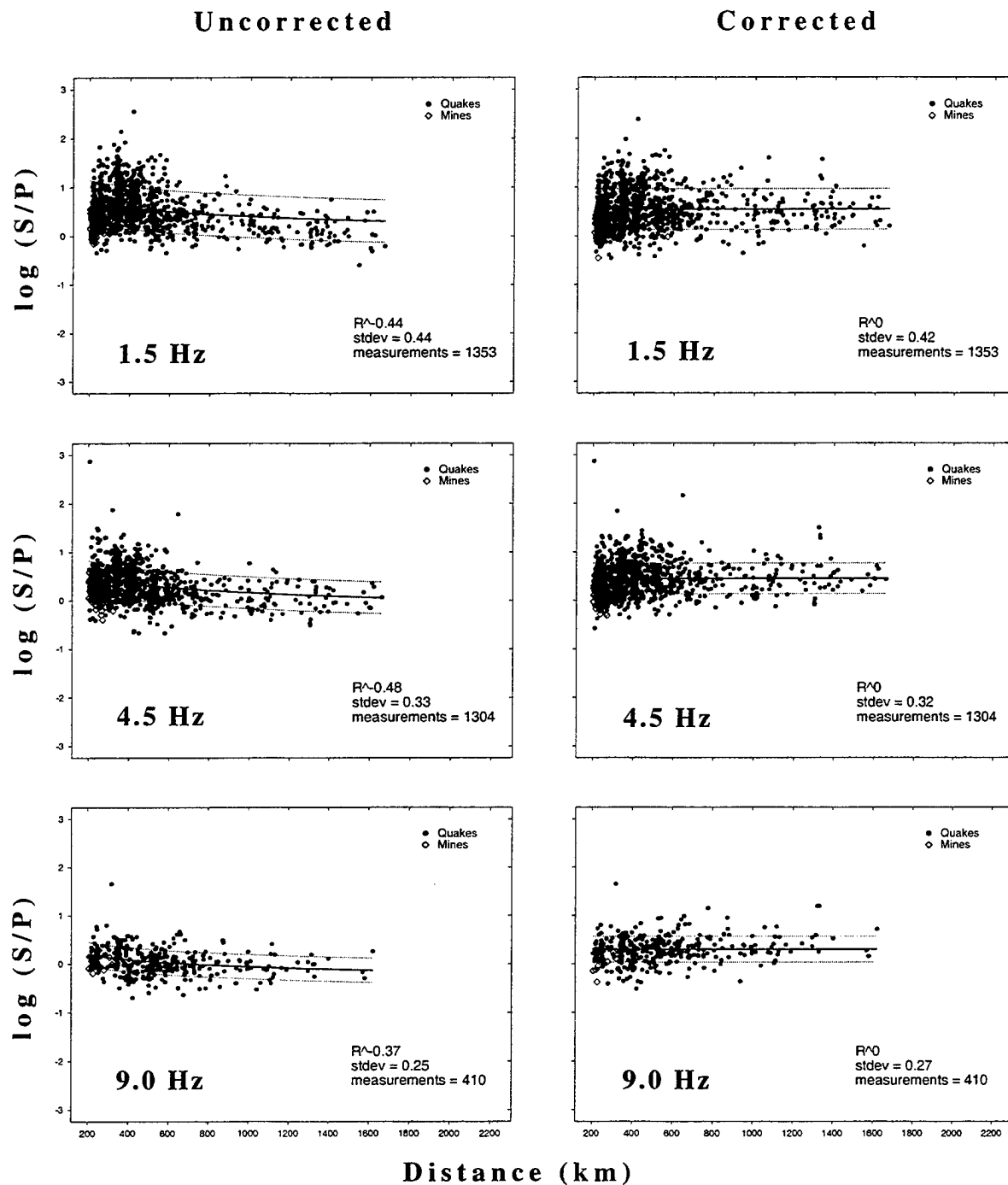
P 4.5

P 6.0

P 9.0

P 12.0
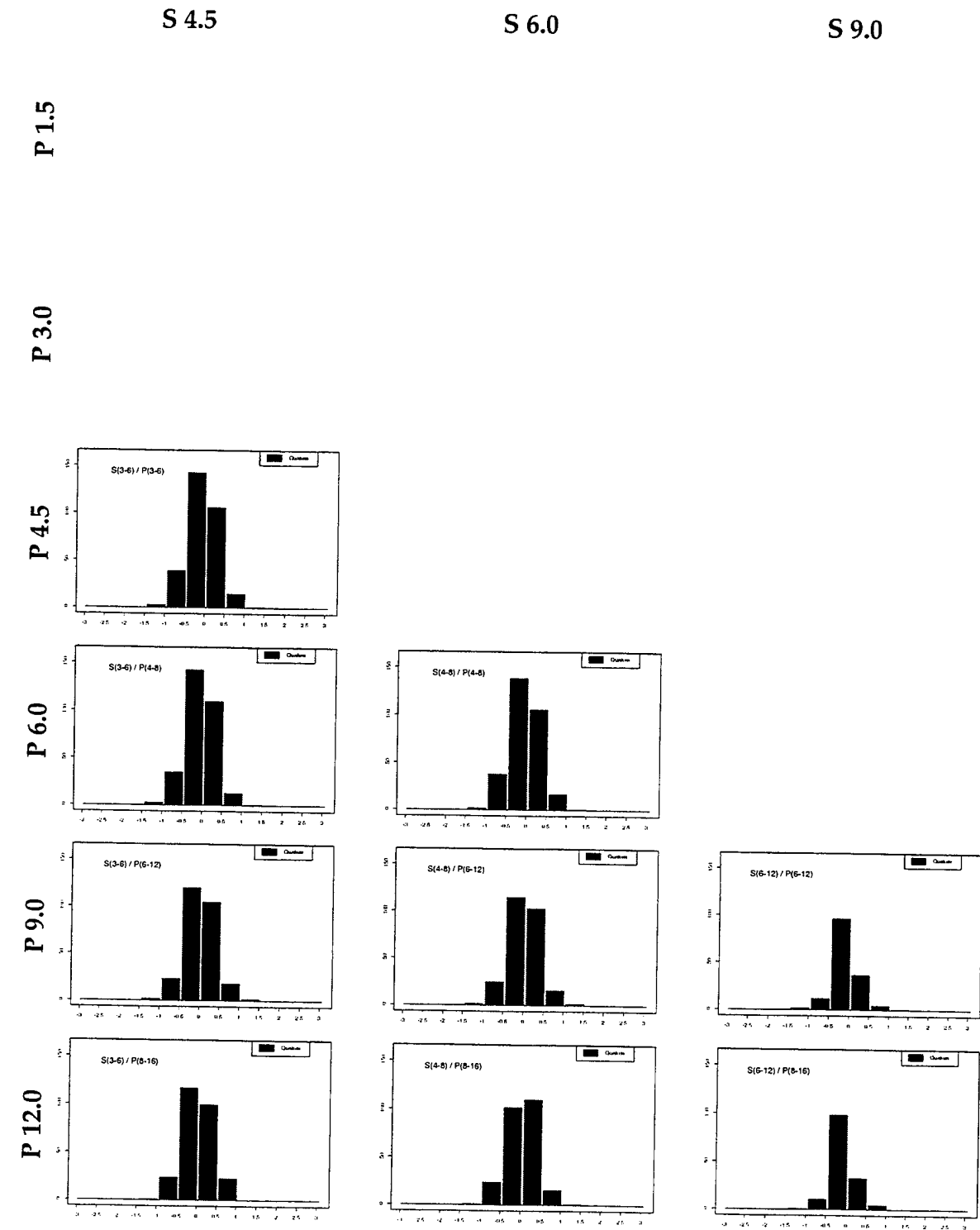
Figure C.1.4 Continued.

C.2. Western North America

C.2.1 Validation
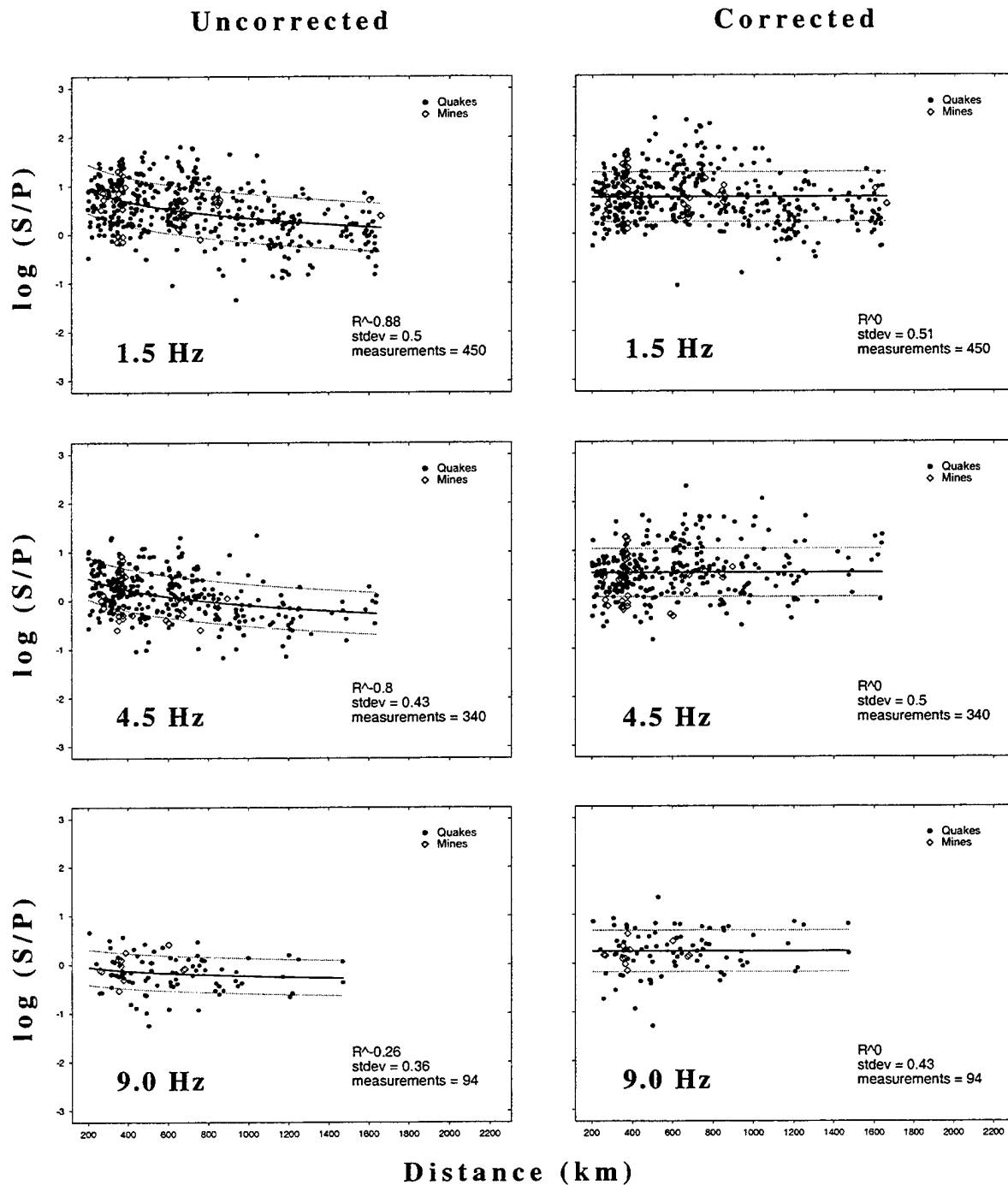
Figure C.2.1 Uncorrected and distance-corrected S/P ratio plots of measurements made in 1-2, 3-6, and 6-12 Hz (referred to as 1.5, 4.5, and 9.0 Hz) frequency bands for western North America.

C.2.2 *S/P* Ratios

Western North America *Sn/Pn* Ratios
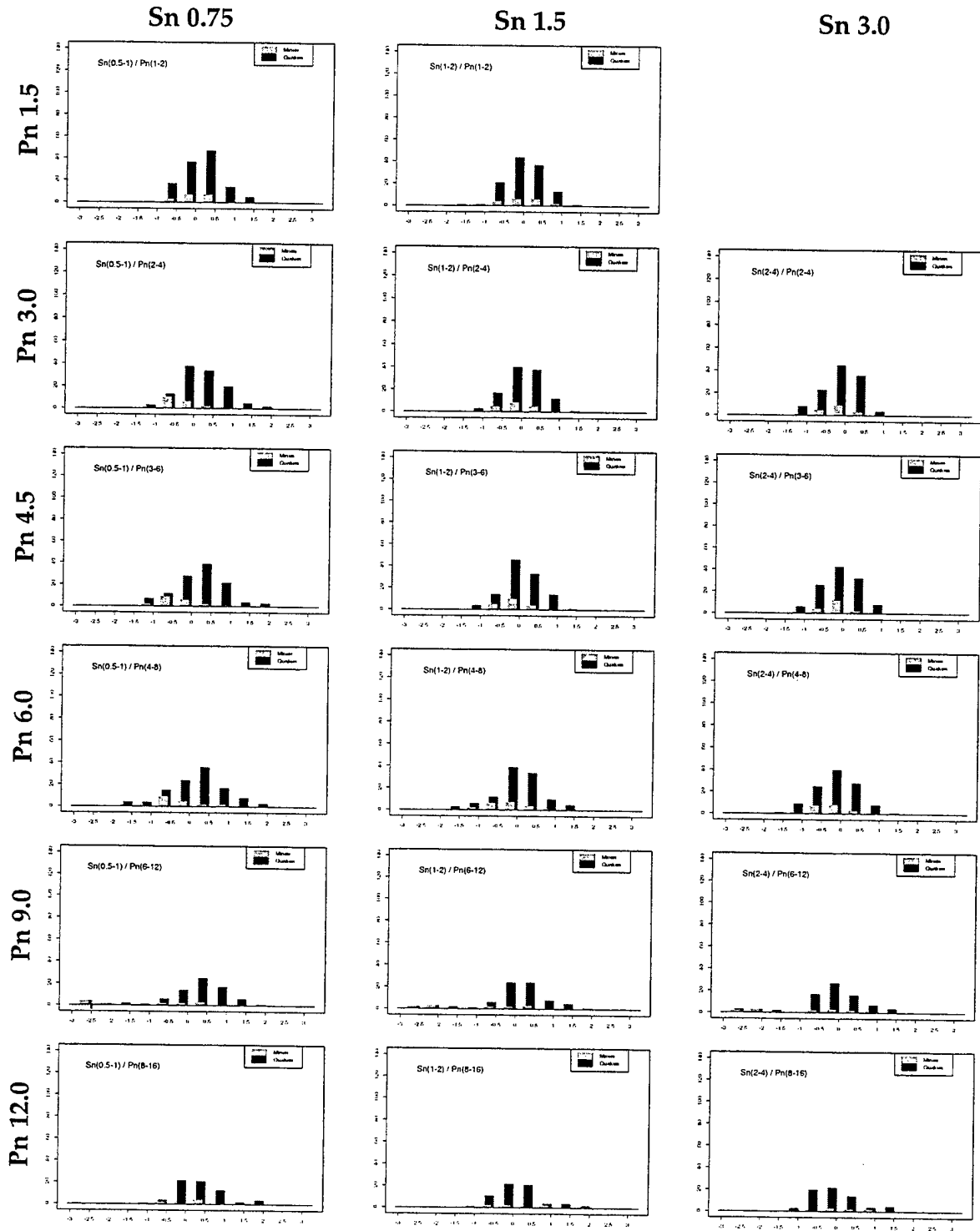
Figure C.2.2 Comparison of normalized *Sn/Pn* amplitude ratios for earthquake and explosion populations found in western North America.

Western North America *Sn/Pn* Ratios

Sn 4.5   Sn 6.0   Sn 9.0

Pn 1.5

Pn 3.0

Pn 4.5

Pn 6.0

Pn 9.0

Pn 12.0
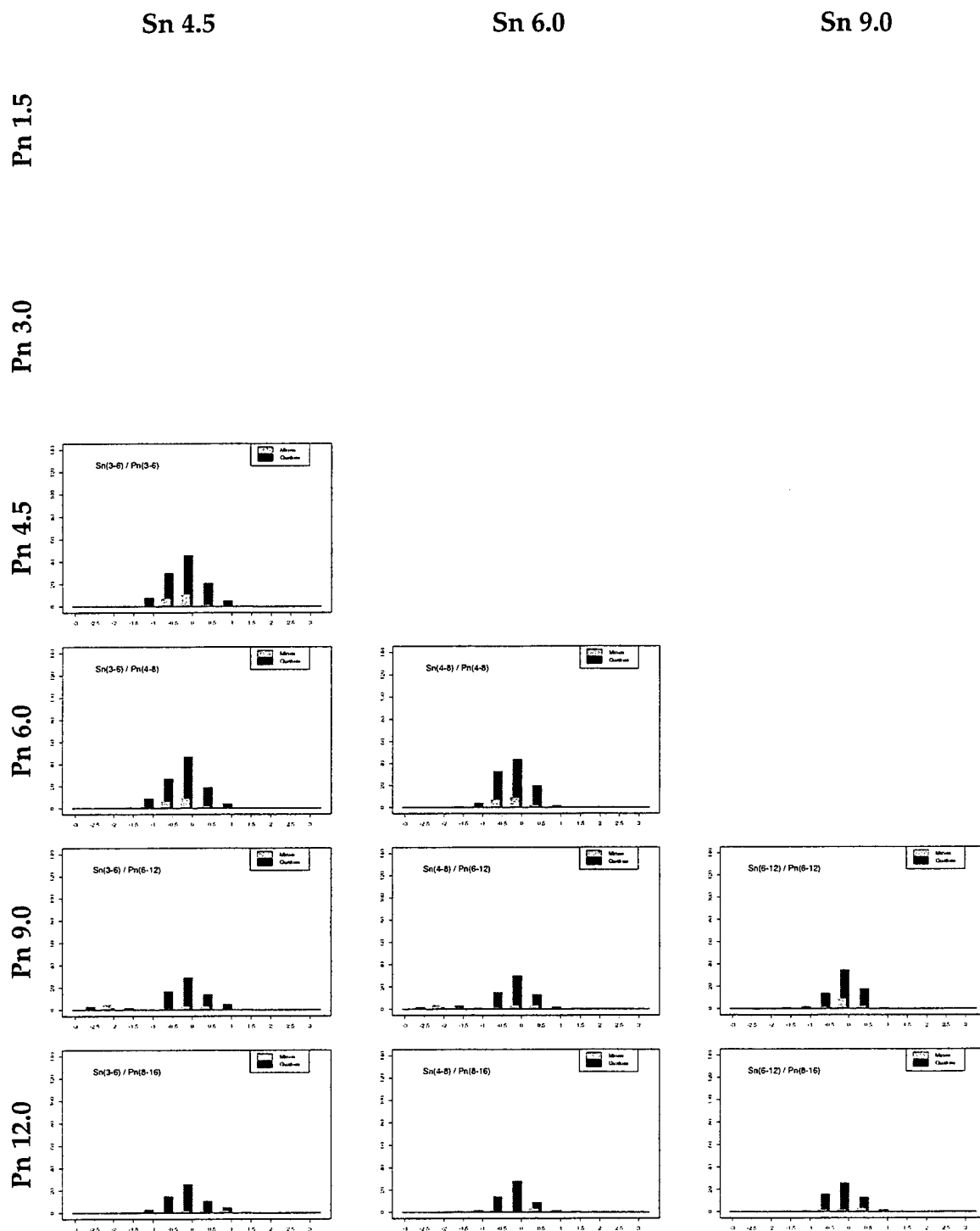
Figure C.2.2 Continued.

Western North America *Lg/Pn* Ratios
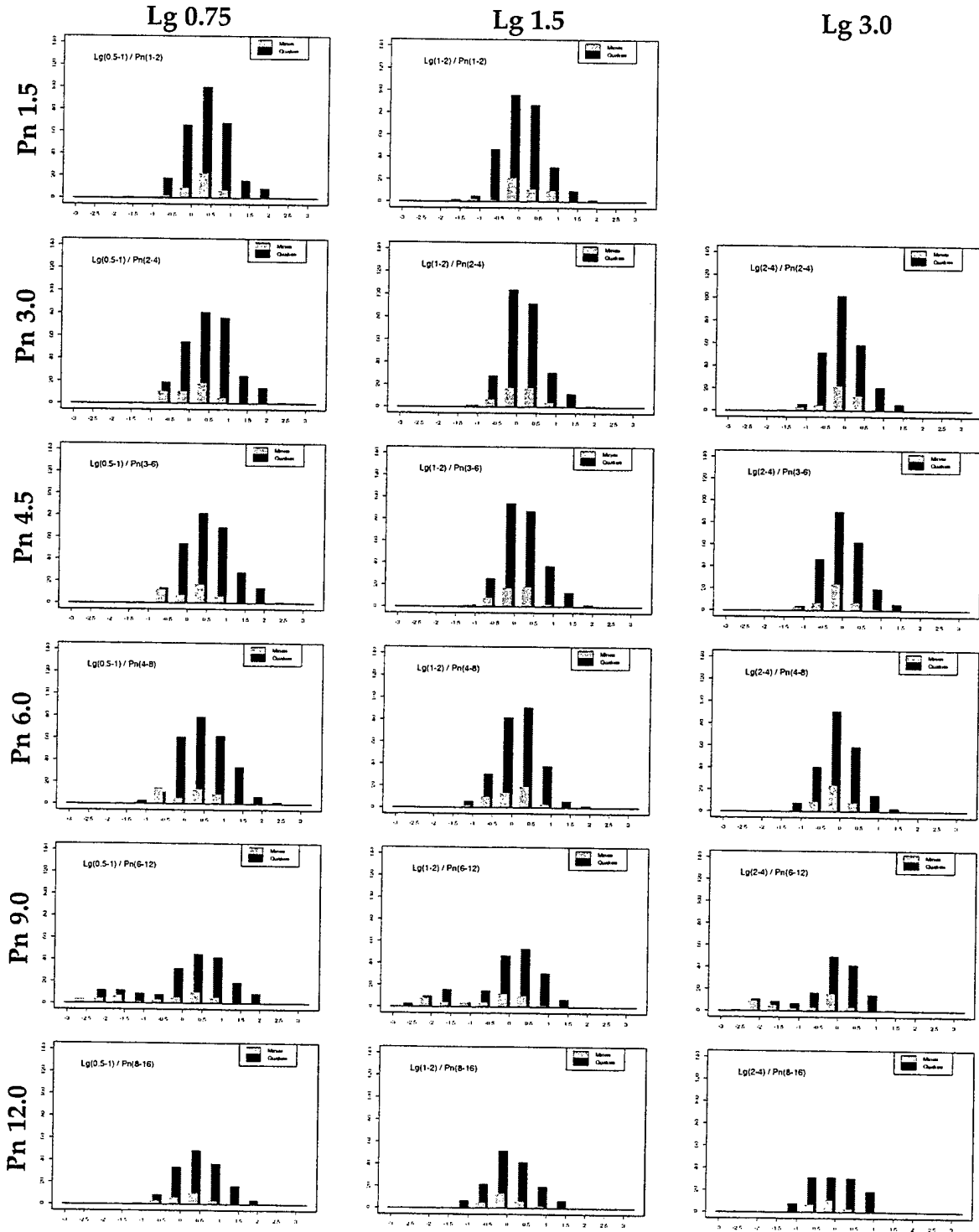
Figure C.2.3 Comparison of normalized *Lg/Pn* amplitude ratios for earthquake and explosion populations found in western North America.

Western North America *Lg/Pn* Ratios

Lg 4.5   Lg 6.0

Pn 1.5

Pn 3.0

Pn 4.5

Lg(3-6) / Pn(3-6)

Pn 6.0

Lg(3-6) / Pn(4-8)

Lg(4-8) / Pn(4-8)

Pn 9.0

Lg(3-6) / Pn(6-12)

Lg(4-8) / Pn(6-12)

Pn 12.0

Lg(3-6) / Pn(8-16)

Lg(4-8) / Pn(8-16)
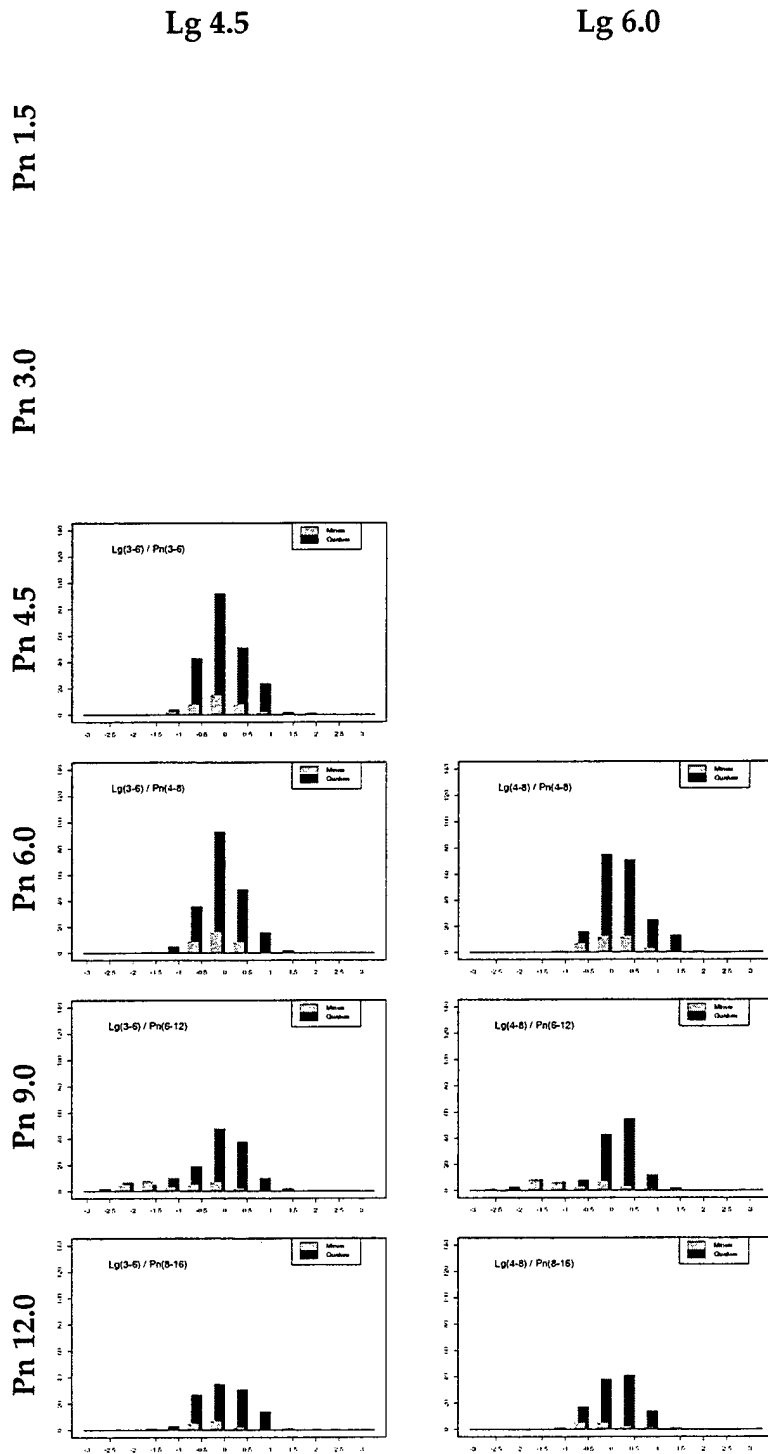
Figure C.2.3 Continued.

Western North America Largest *S* / Earliest *P* Ratios
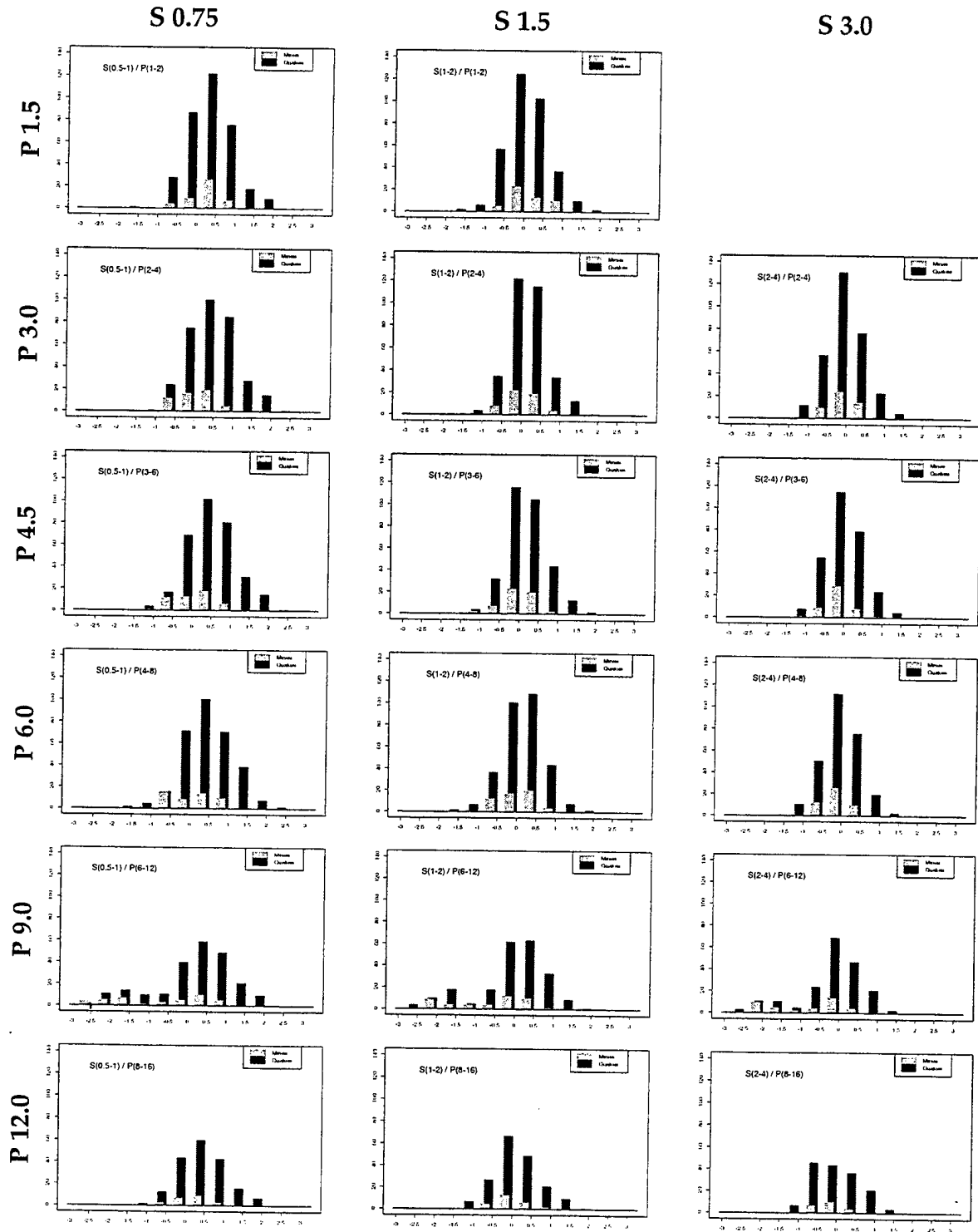
Figure C.2.4 Comparison of normalized largest *S* / earliest *P* amplitude ratios for earthquake and explosion populations found in western North America.

Western North America Largest *S* / Earliest *P* Ratios

	S 4.5	S 6.0	S 9.0

P 1.5

P 3.0

P 4.5

P 6.0

P 9.0

P 12.0
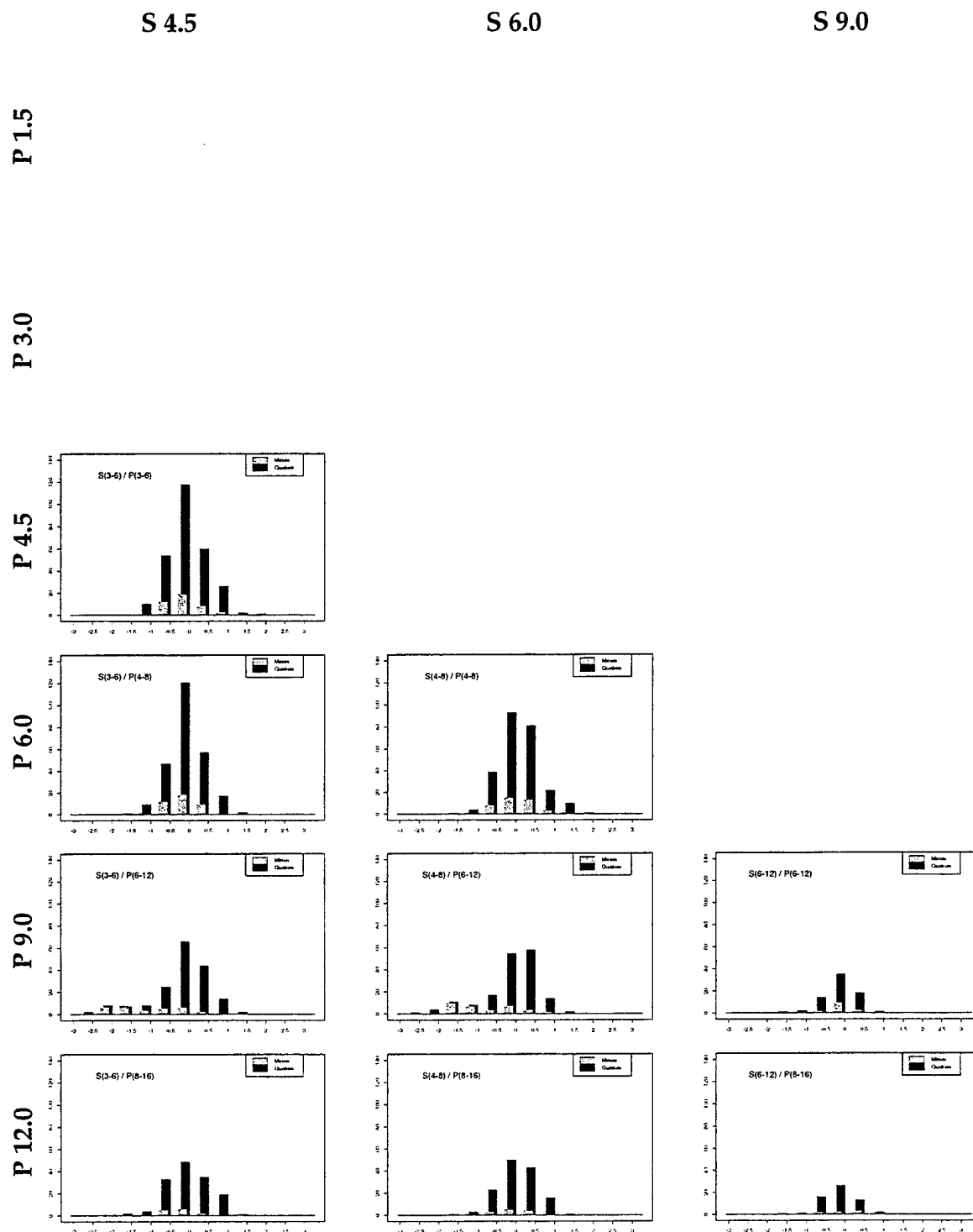
Figure C.2.4 Continued.

133

C.3. Eastern North America

C.3.1 Validation

Uncorrected   **Corrected**
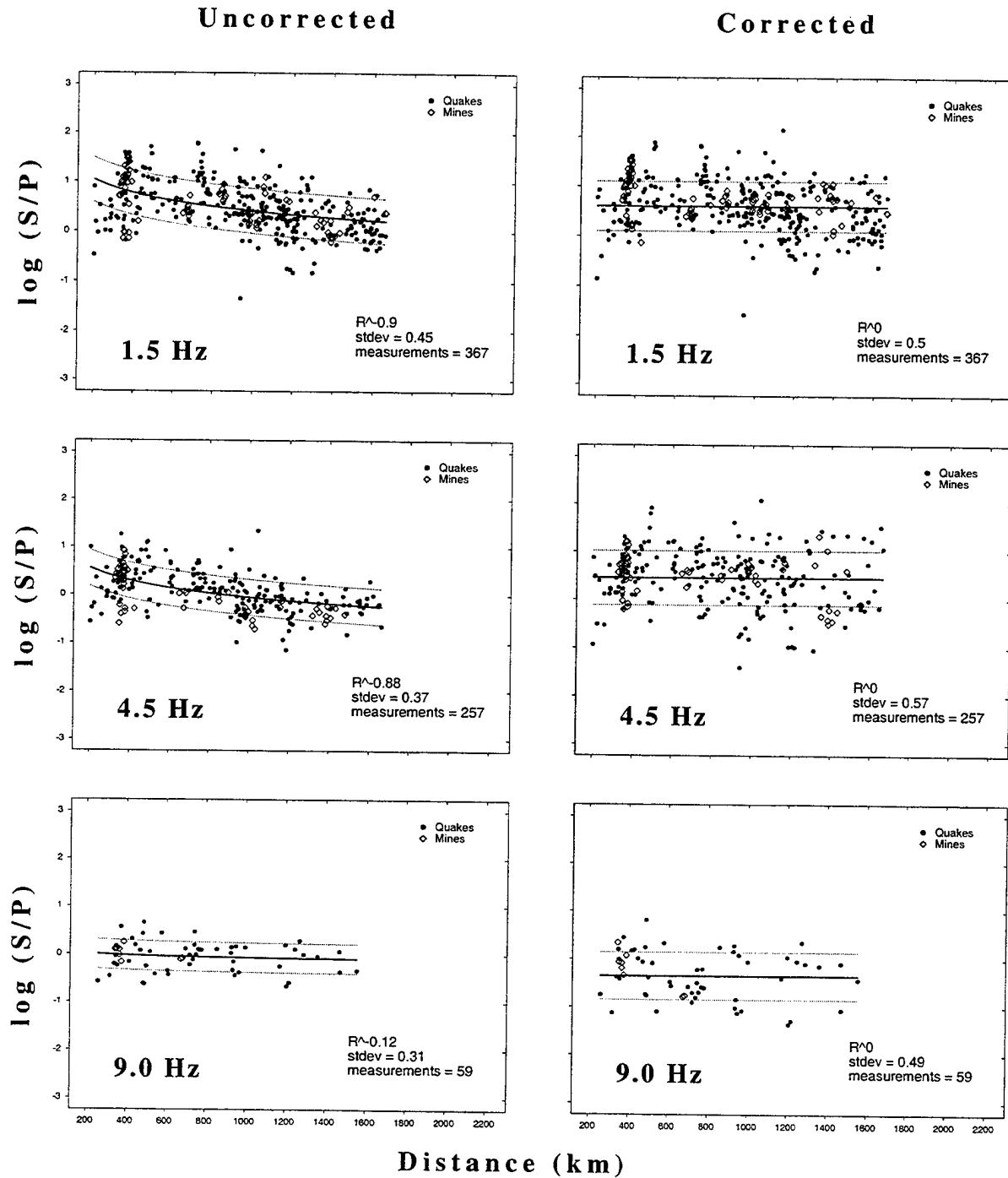
Figure C.3.1 Uncorrected and distance-corrected S/P ratio plots of measurements made in 1-2, 3-6, and 6-12 Hz (referred to as 1.5, 4.5, and 9.0 Hz) frequency bands for eastern North America.

C.3.2 *S/P* Ratios

Eastern North America *Sn/Pn* Ratios
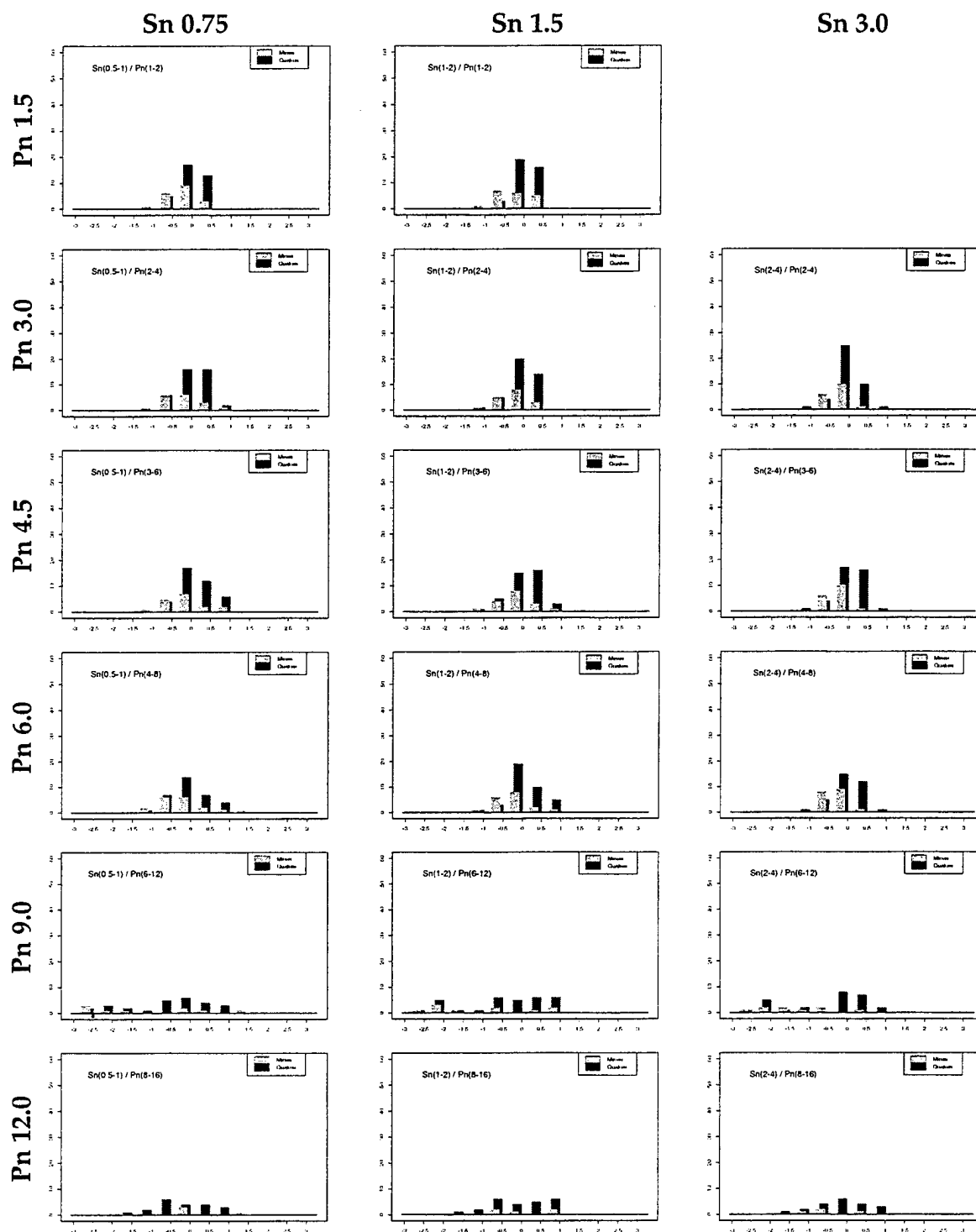
Figure C.3.2 Comparison of normalized *Sn/Pn* amplitude ratios for earthquake and explosion populations found in eastern North America.

Eastern North America *Sn/Pn* Ratios
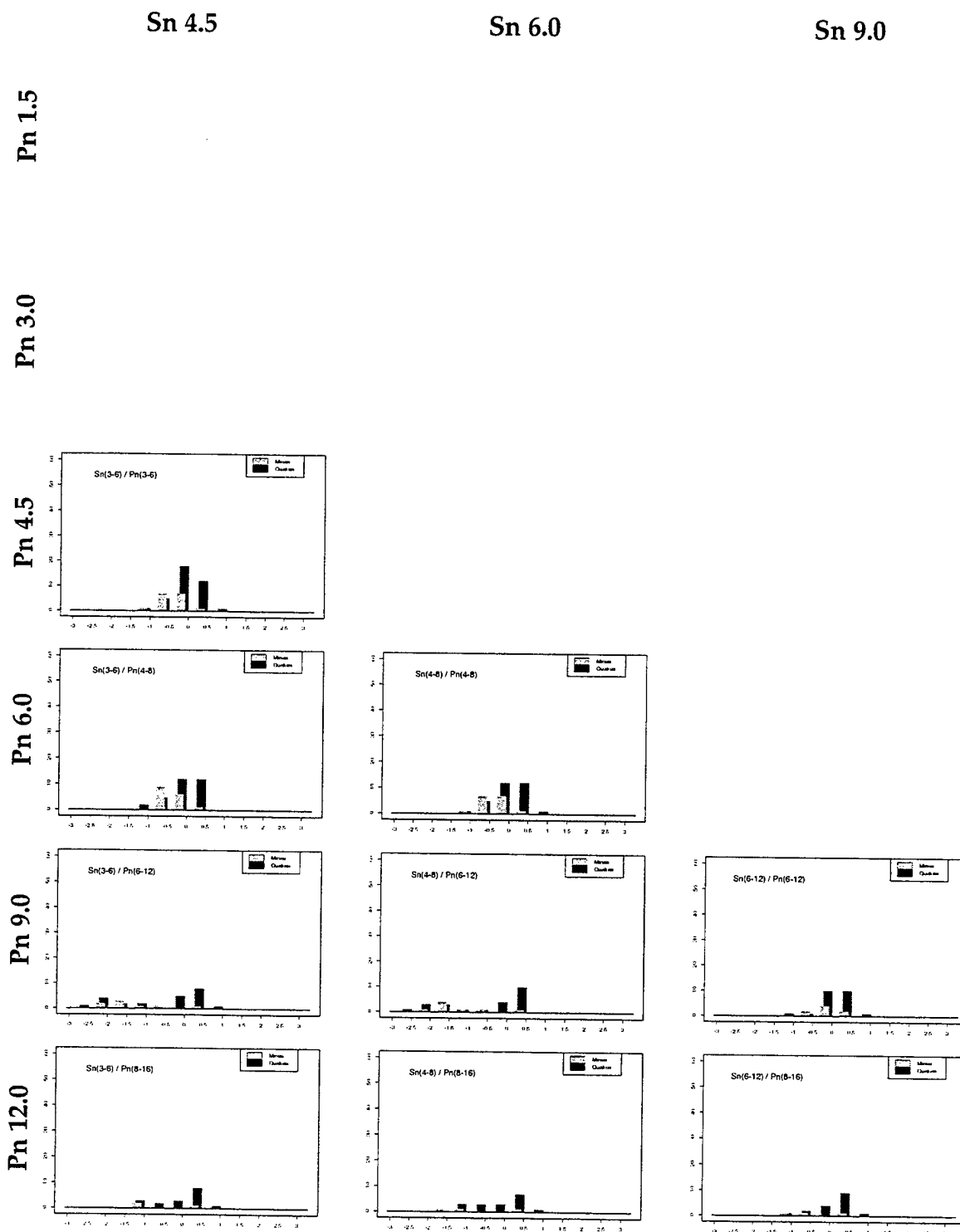
Figure C.3.2 Continued.

Eastern North America *Lg/Pn* Ratios
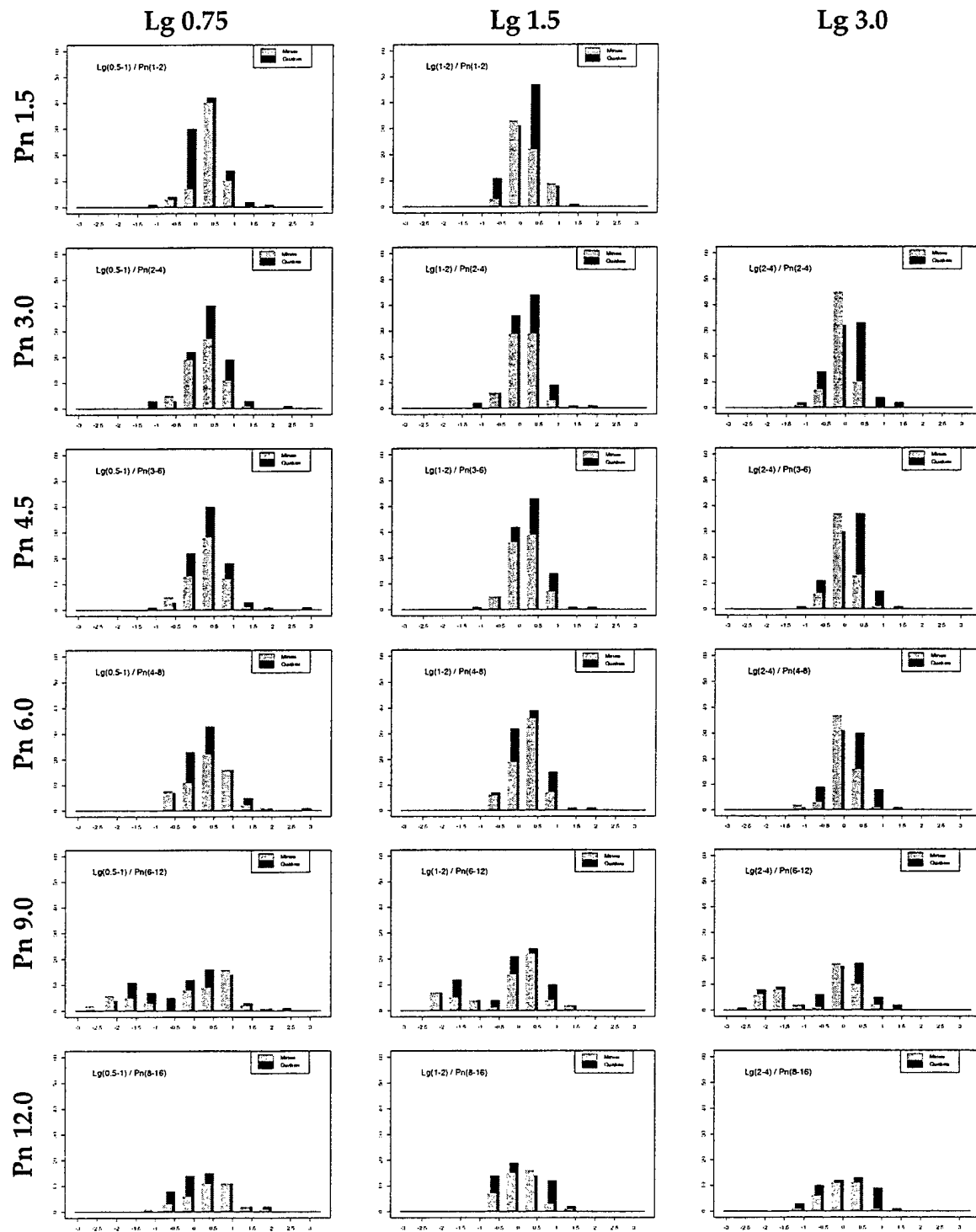
Figure C.3.3 Comparison of normalized *Lg/Pn* amplitude ratios for earthquake and explosion populations found in eastern North America.

137

Eastern North America *Lg/Pn* Ratios

Lg 4.5   Lg 6.0

Pn 1.5

Pn 3.0

Pn 4.5

Pn 6.0

Pn 9.0

Pn 12.0
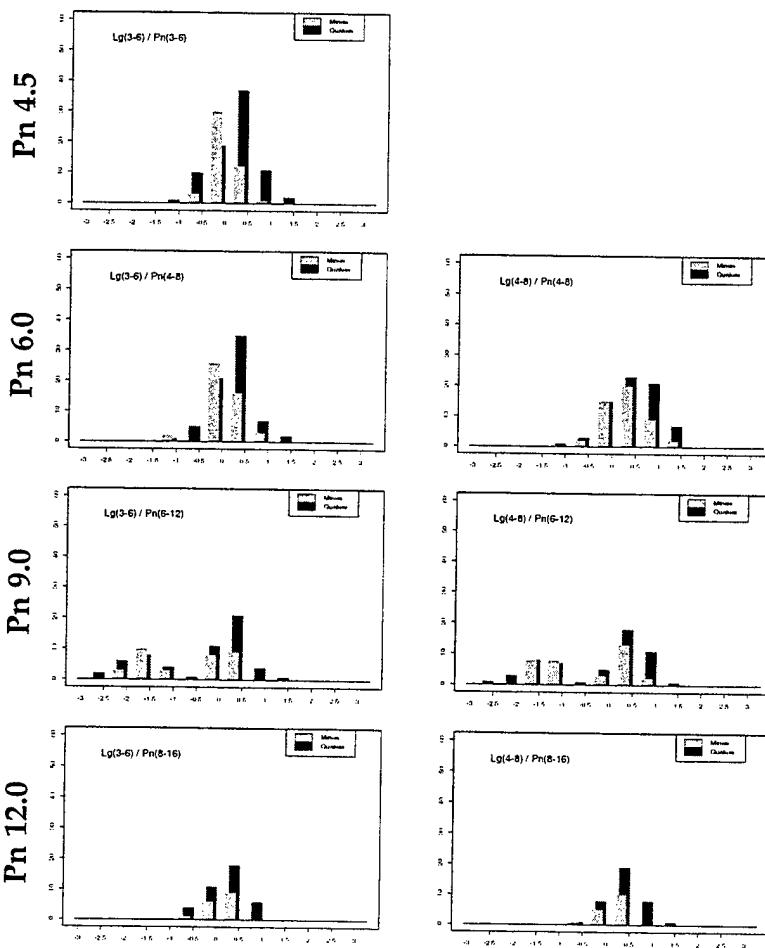
Figure C.3.3 Continued.

Eastern North America Largest *S* / Earliest *P* Ratios
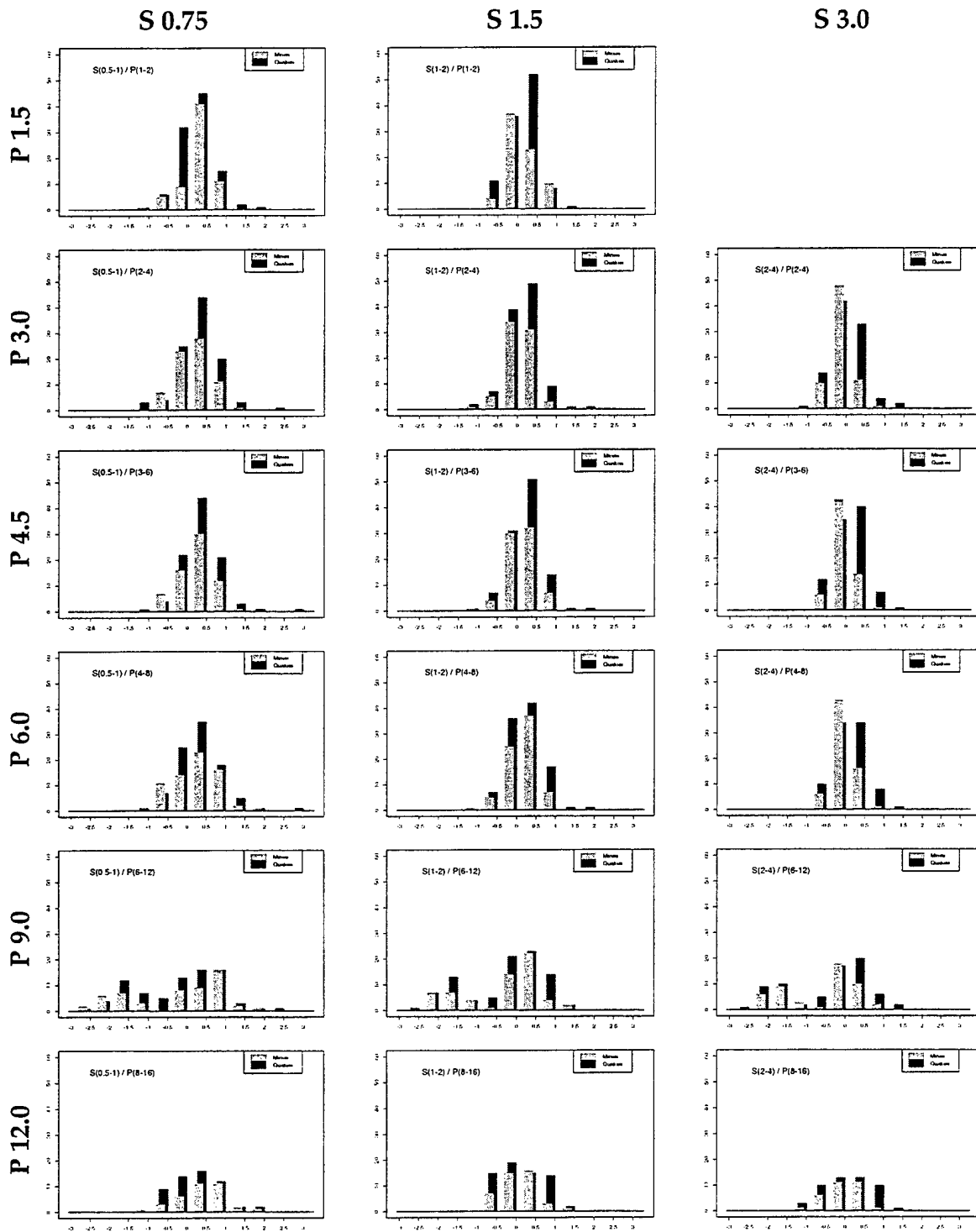
Figure C.3.4 Comparison of normalized largest *S* / earliest *P* amplitude ratios for earthquake and explosion populations found in eastern North America.

Eastern North America Largest *S* / Earliest *P* Ratios

S 4.5   S 6.0   S 9.0

P 1.5

P 3.0

P 4.5

S(3-6) / P(3-6)

P 6.0

S(3-6) / P(4-8)

S(4-8) / P(4-8)

P 9.0

S(3-6) / P(6-12)

S(4-8) / P(6-12)

S(6-12) / P(6-12)

P 12.0

S(3-6) / P(8-16)

S(4-8) / P(8-16)

S(6-12) / P(8-16)
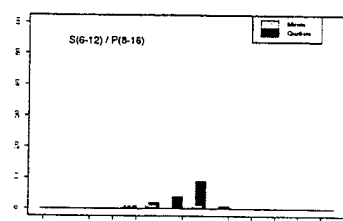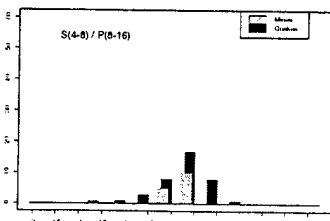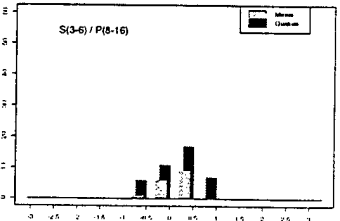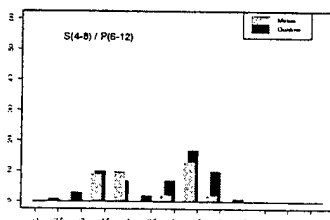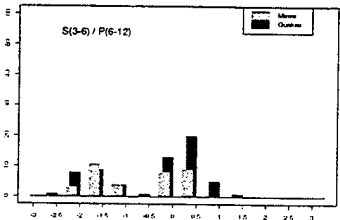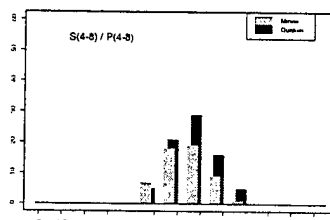
Figure C.3.4 Continued.

C.4. Southern Europe

C.4.1 Validation

Uncorrected   Corrected

Figure C.4.1 Uncorrected and distance-corrected S/P ratio plots of measurements made in 1-2, 3-6, and 6-12 Hz (referred to as 1.5, 4.5, and 9.0 Hz) frequency bands for southern Europe.

C.4.2 *S/P* Ratios

Southern Europe *Sn/Pn* Ratios
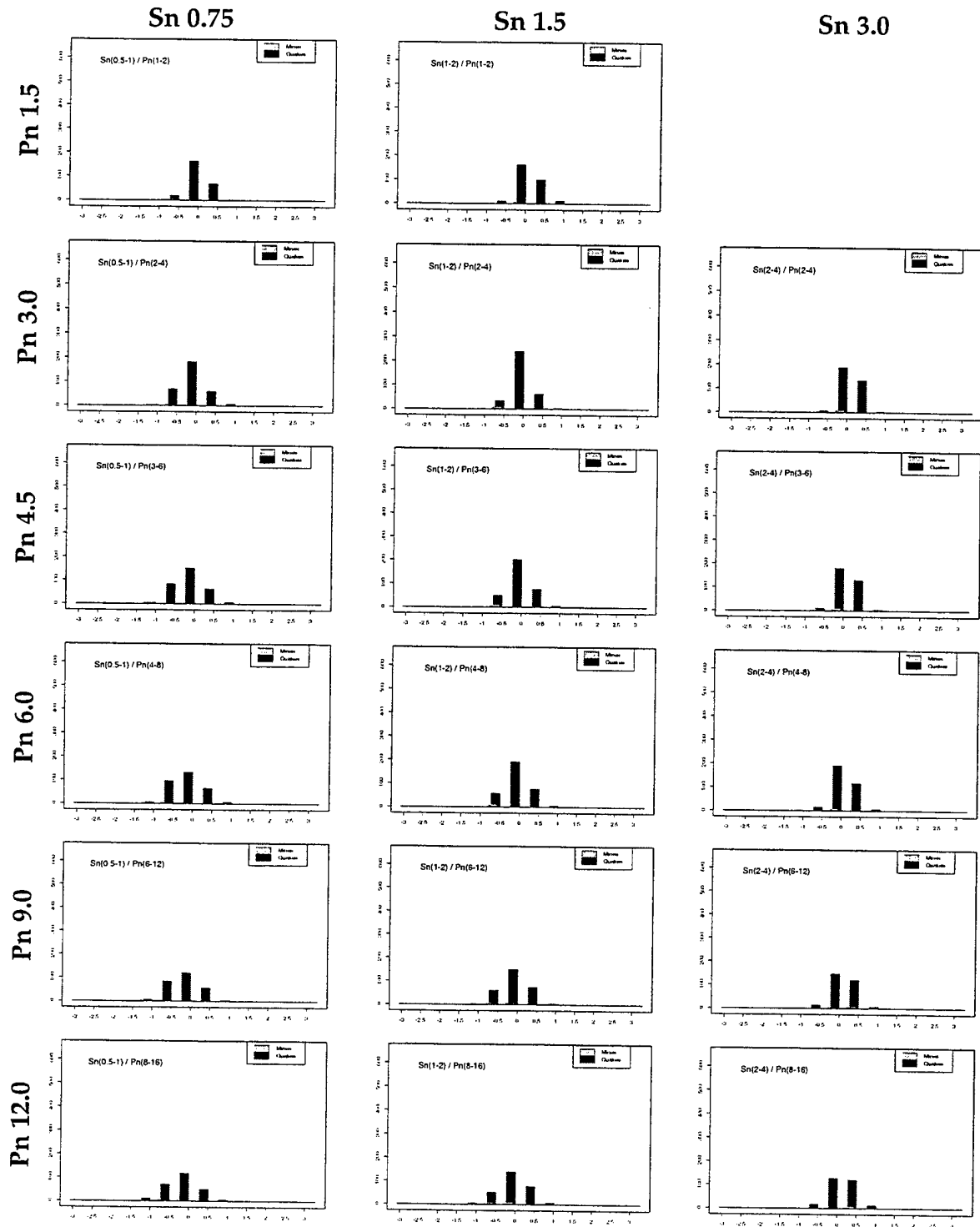
Figure C.4.2 Comparison of normalized *Sn/Pn* amplitude ratios for earthquake and explosion populations found in southern Europe.

Southern Europe *Sn/Pn* Ratios

Sn 4.5   Sn 6.0   Sn 9.0
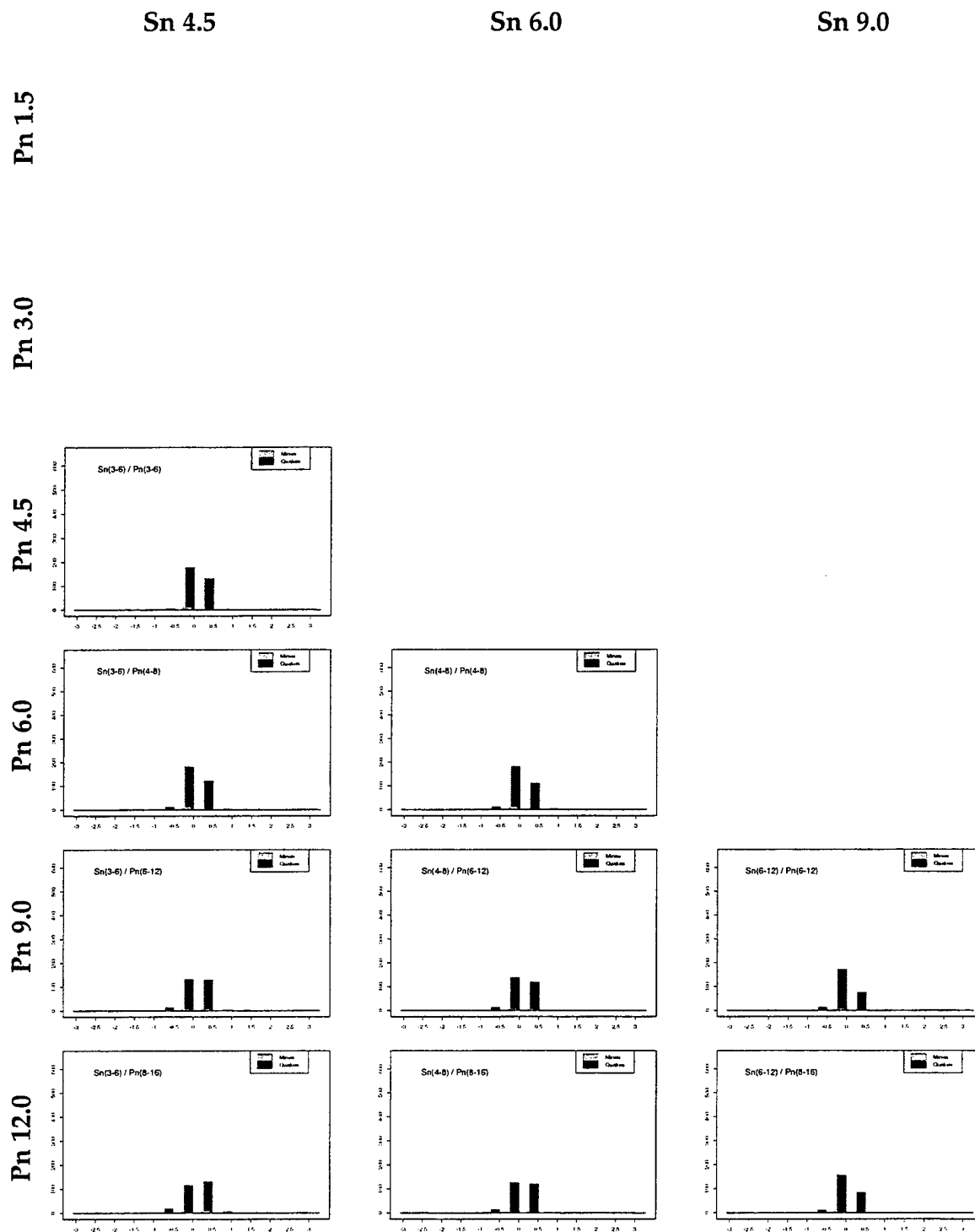
Figure C.4.2 Continued.

Southern Europe *Lg/Pn* Ratios

Lg 0.75   Lg 1.5   Lg 3.0
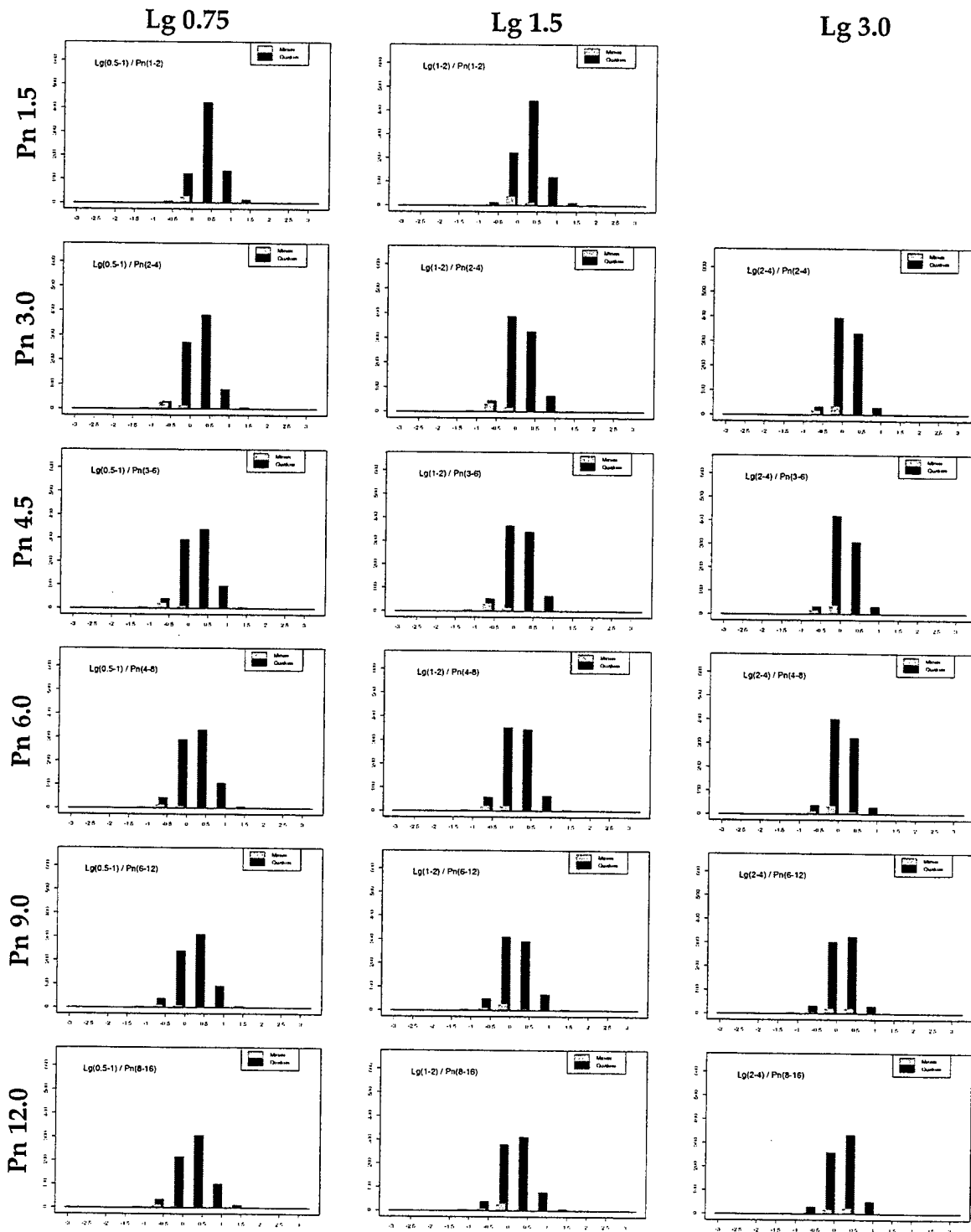
Figure C.4.3 Comparison of normalized *Lg/Pn* amplitude ratios for earthquake and explosion populations found in southern Europe.

Southern Europe *Lg/Pn* Ratios

Lg 4.5   Lg 6.0

Figure C.4.3 Continued.
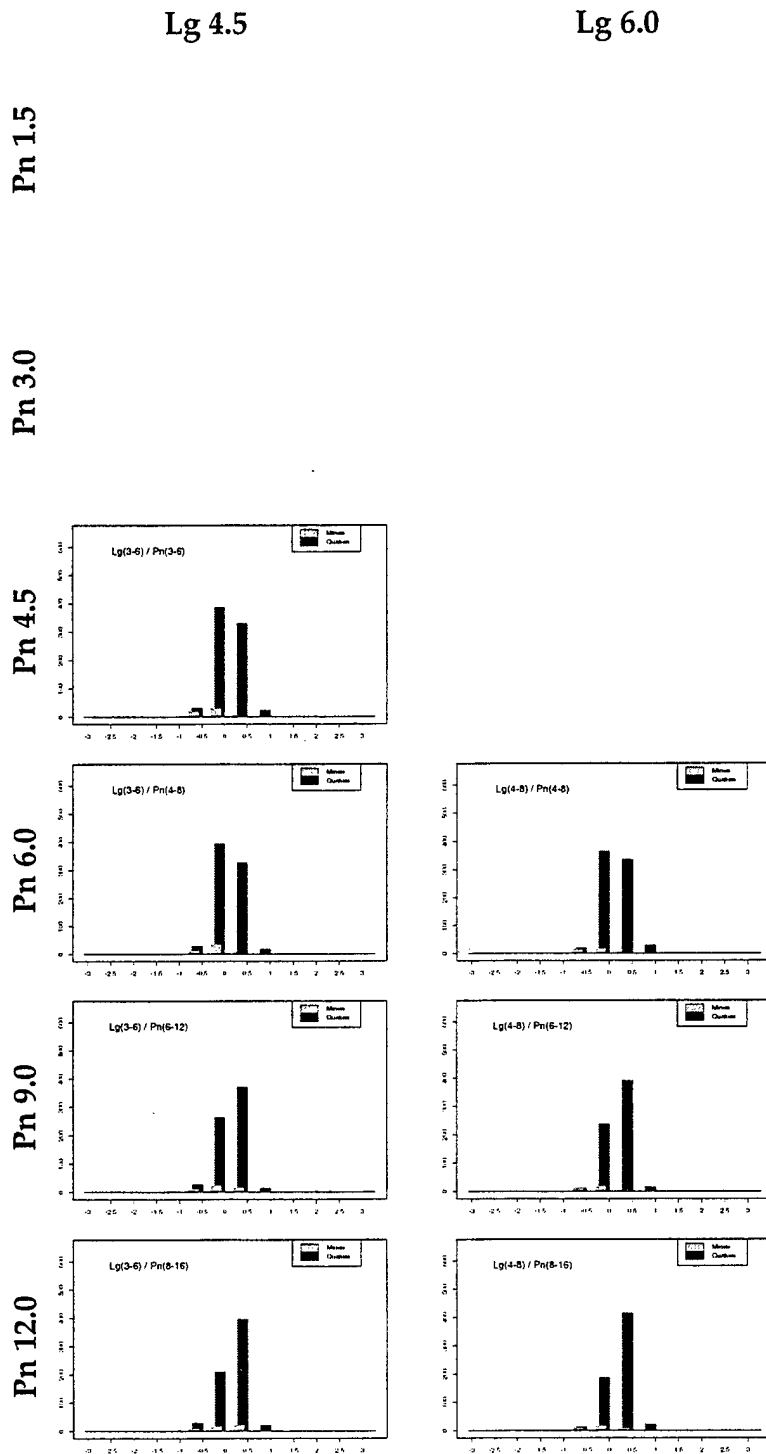
Southern Europe Largest *S* / Earliest *P* Ratios
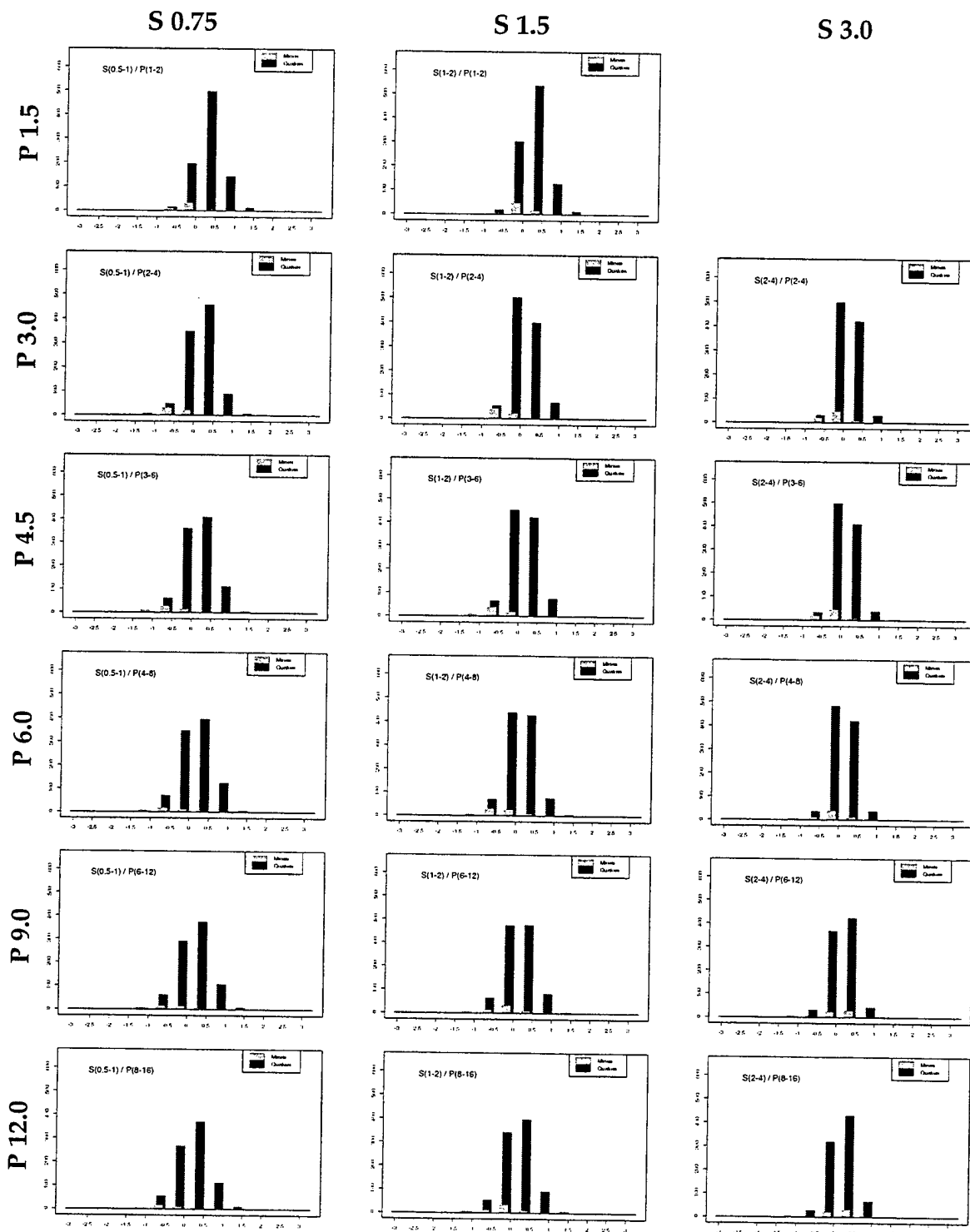
Figure C.4.4 Comparison of normalized largest *S* / earliest *P* amplitude ratios for earthquake and explosion populations found in southern Europe.
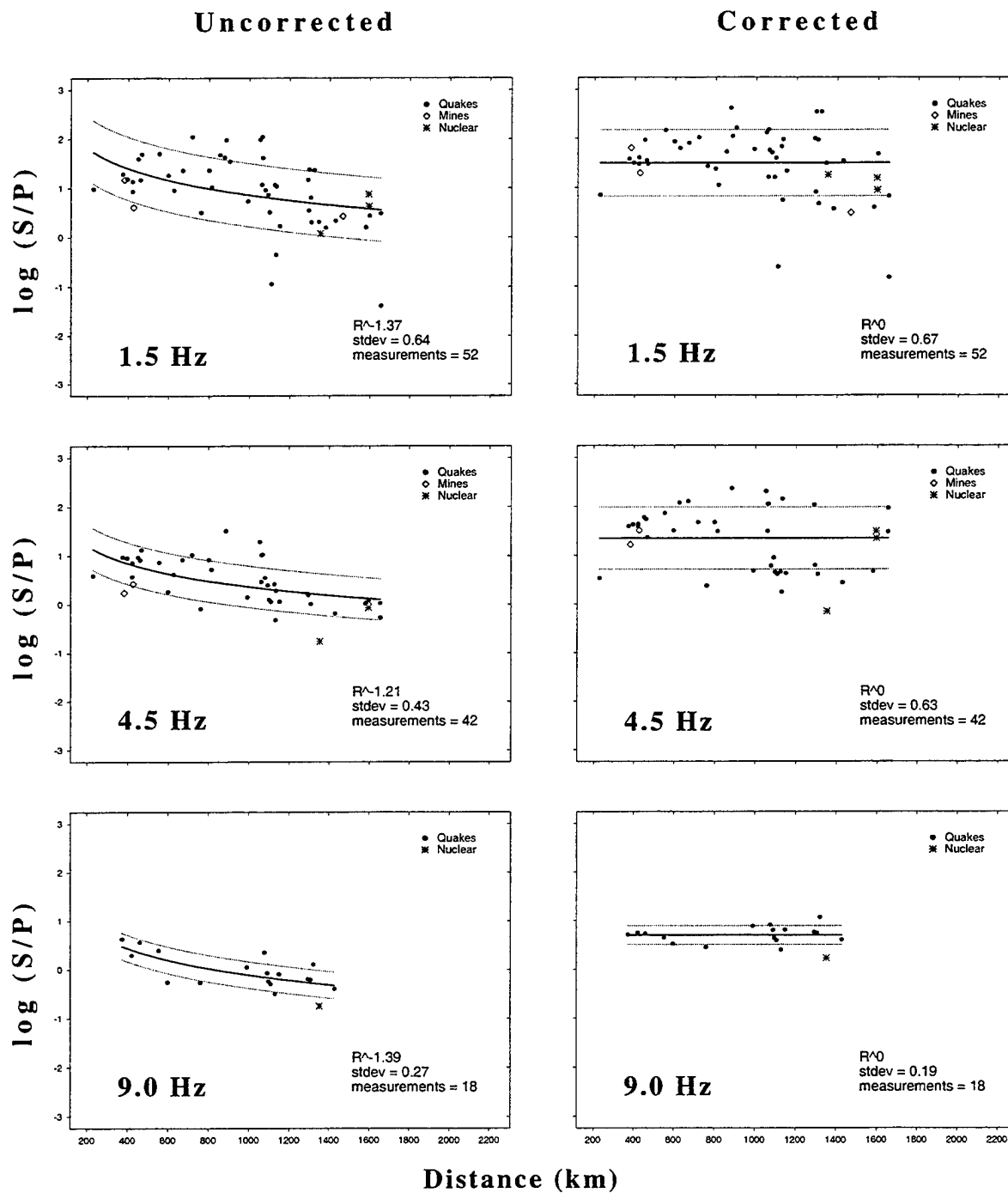
146

Southern Europe Largest *S* / Earliest *P* Ratios

S 4.5　　　　　　　　　　S 6.0　　　　　　　　　　S 9.0

P 1.5

P 3.0

P 4.5

P 6.0

P 9.0

P 12.0
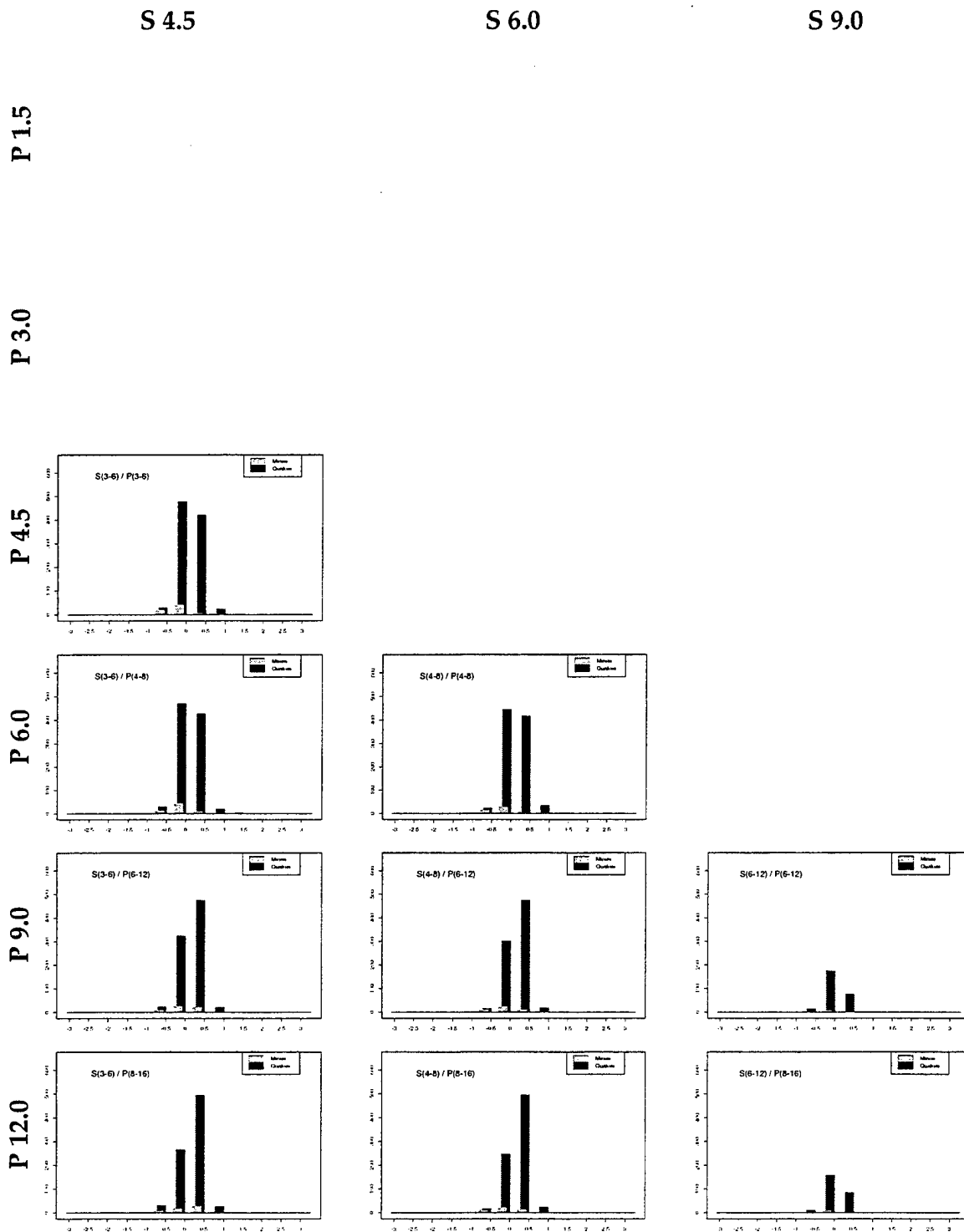
Figure C.4.4 Continued.

C.5. Southern Asia

C.5.1 Validation

Uncorrected   **Corrected**
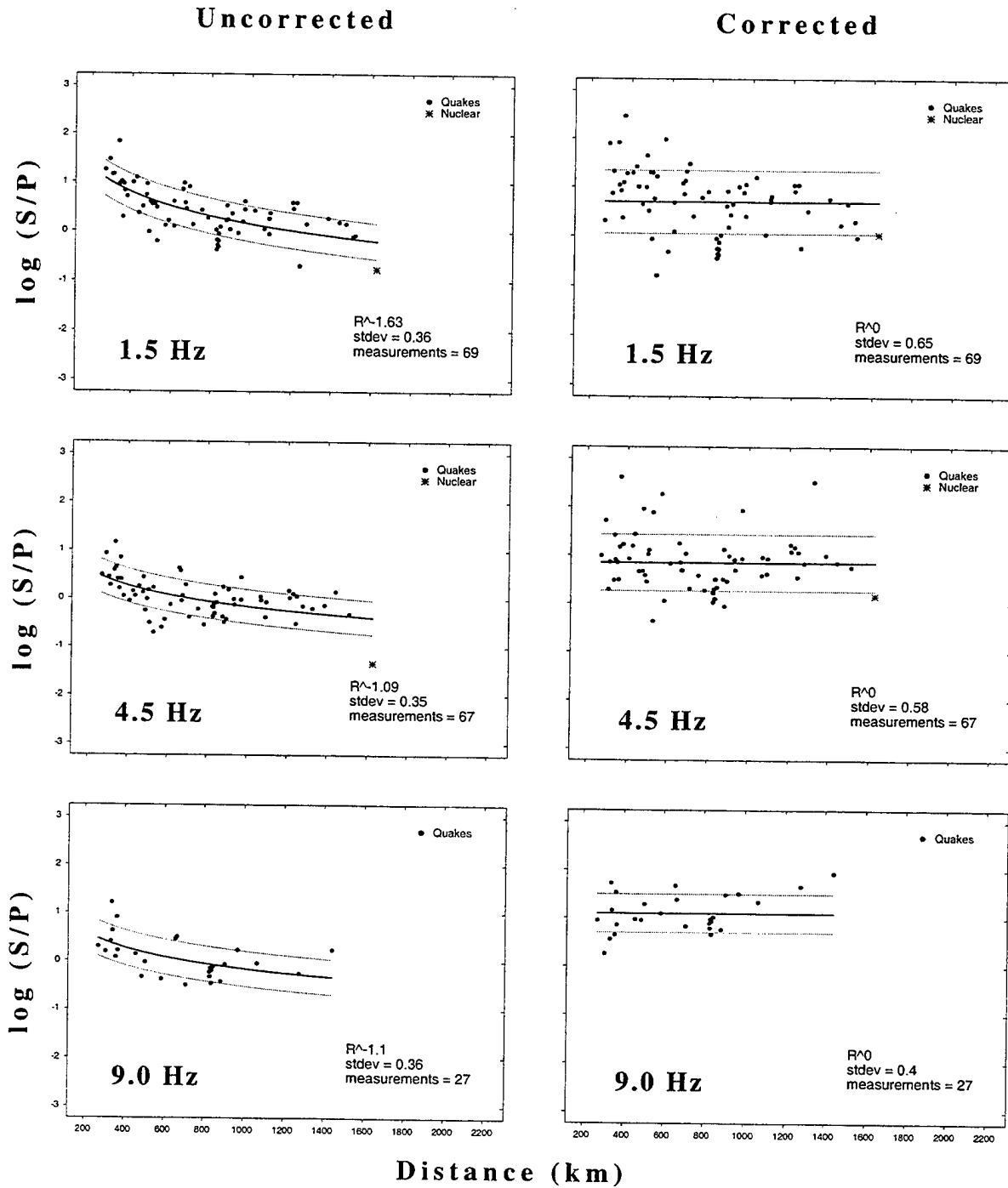
Figure C.5.1 Uncorrected and distance-corrected S/P ratio plots of measurements made in 1-2, 3-6, and 6-12 Hz (referred to as 1.5, 4.5, and 9.0 Hz) frequency bands for southern Asia.

148

C.5.2 *S/P* Ratios

Southern Asia *Sn/Pn* Ratios
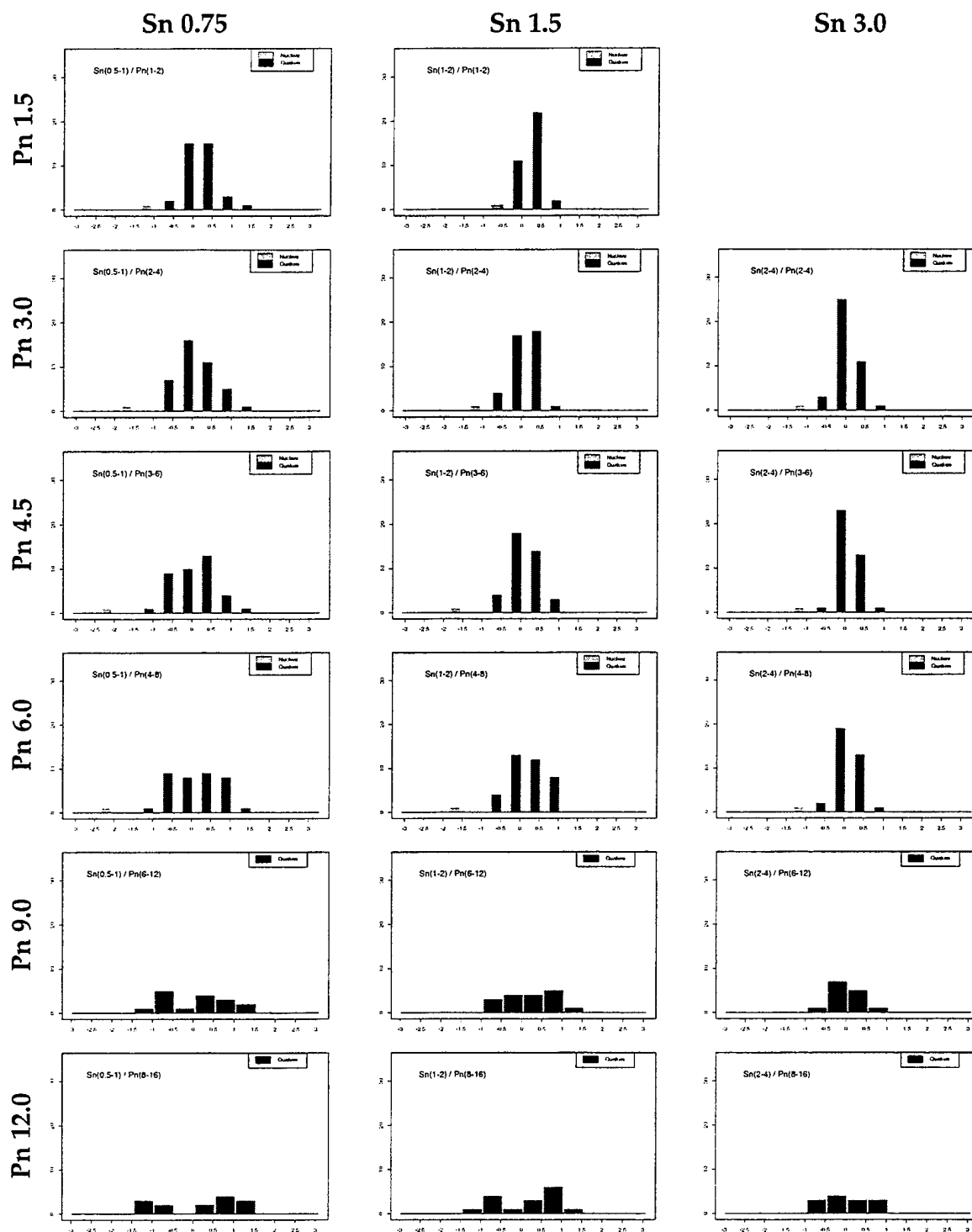
Figure C.5.2 Comparison of normalized *Sn/Pn* amplitude ratios for earthquake and explosion populations found in southern Asia.
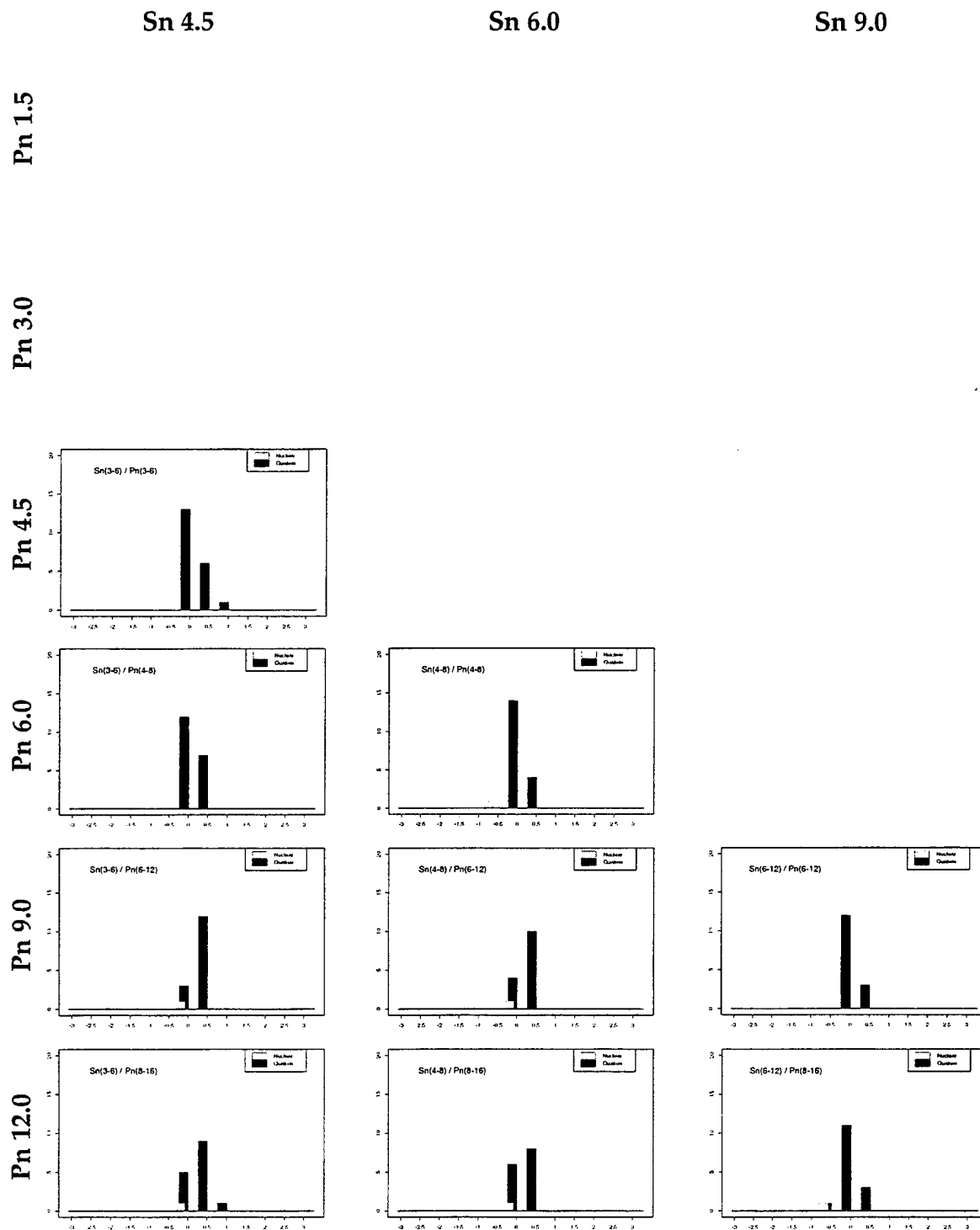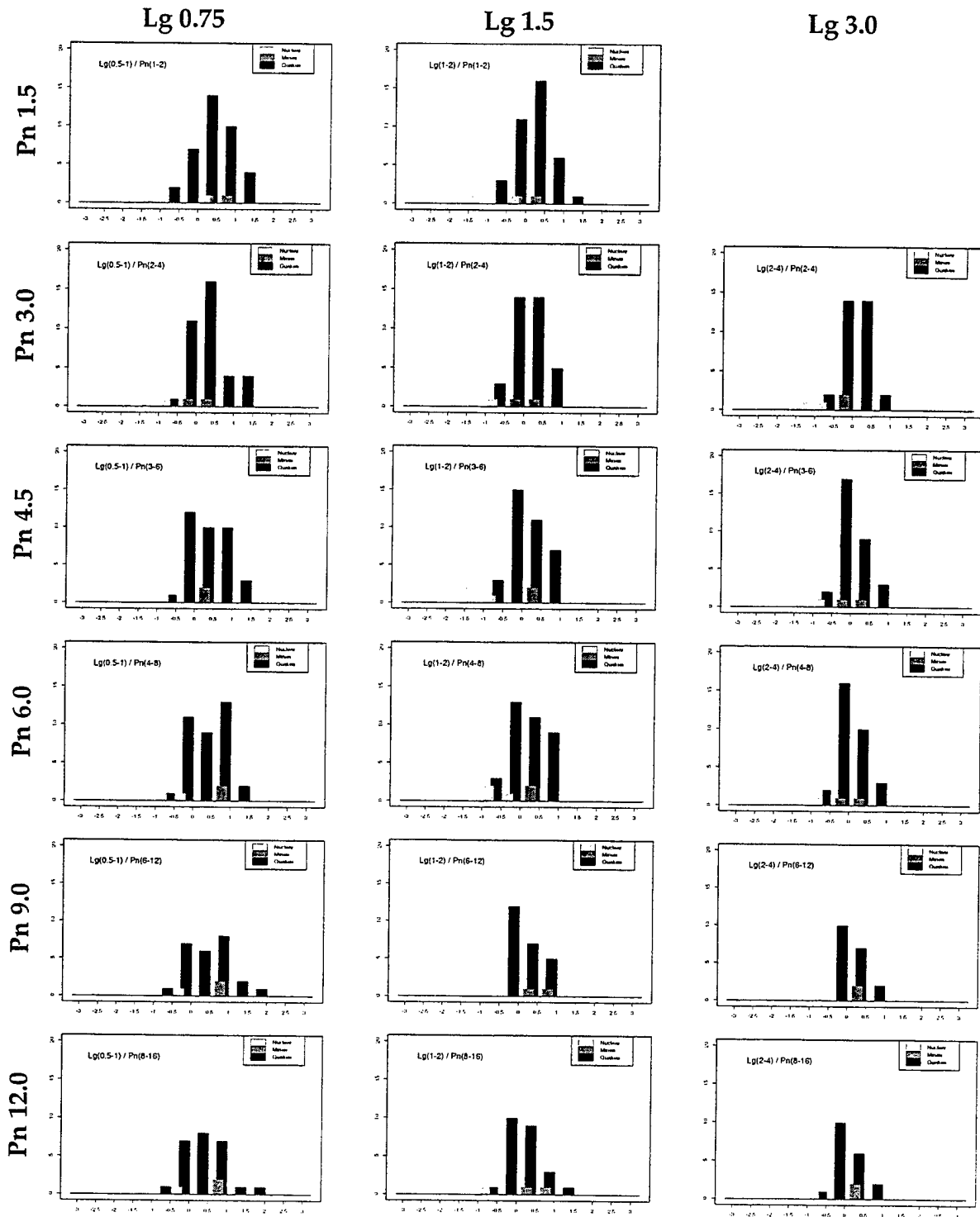
Southern Asia *Sn/Pn* Ratios
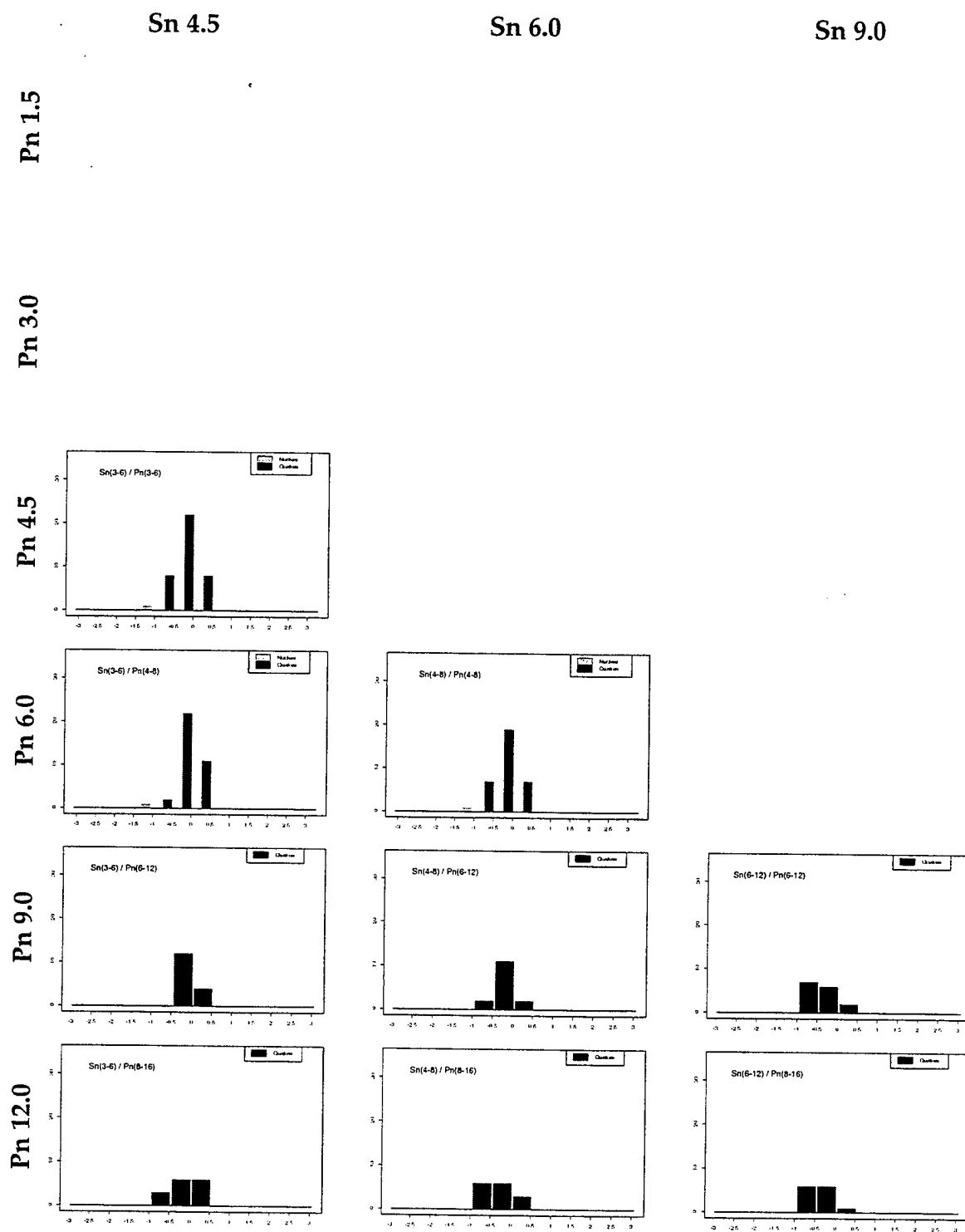
Figure C.5.2 Continued.

Southern Asia *Lg/Pn* Ratios
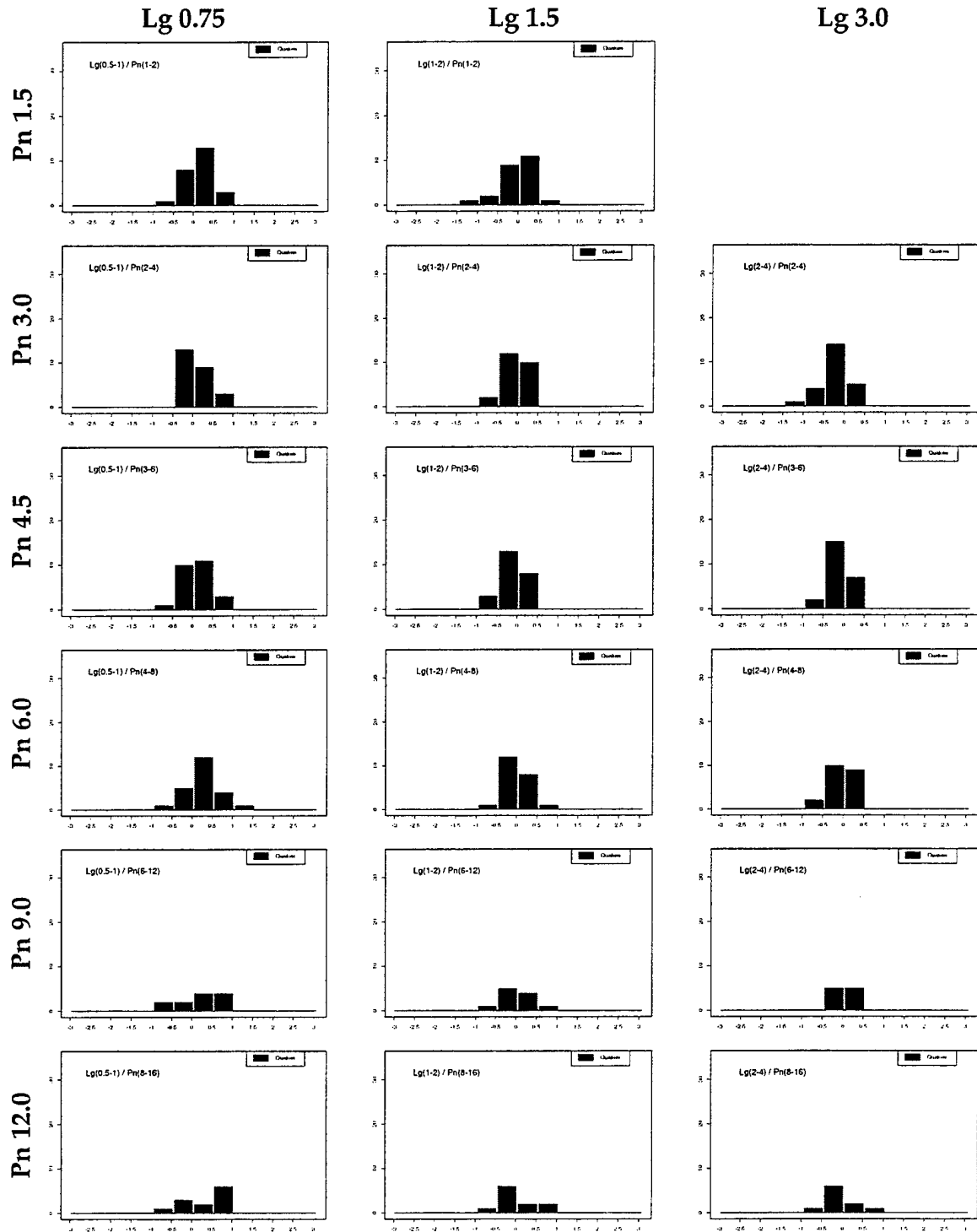
Figure C.5.3 Comparison of normalized *Lg/Pn* amplitude ratios for earthquake and explosion populations found in southern Asia.
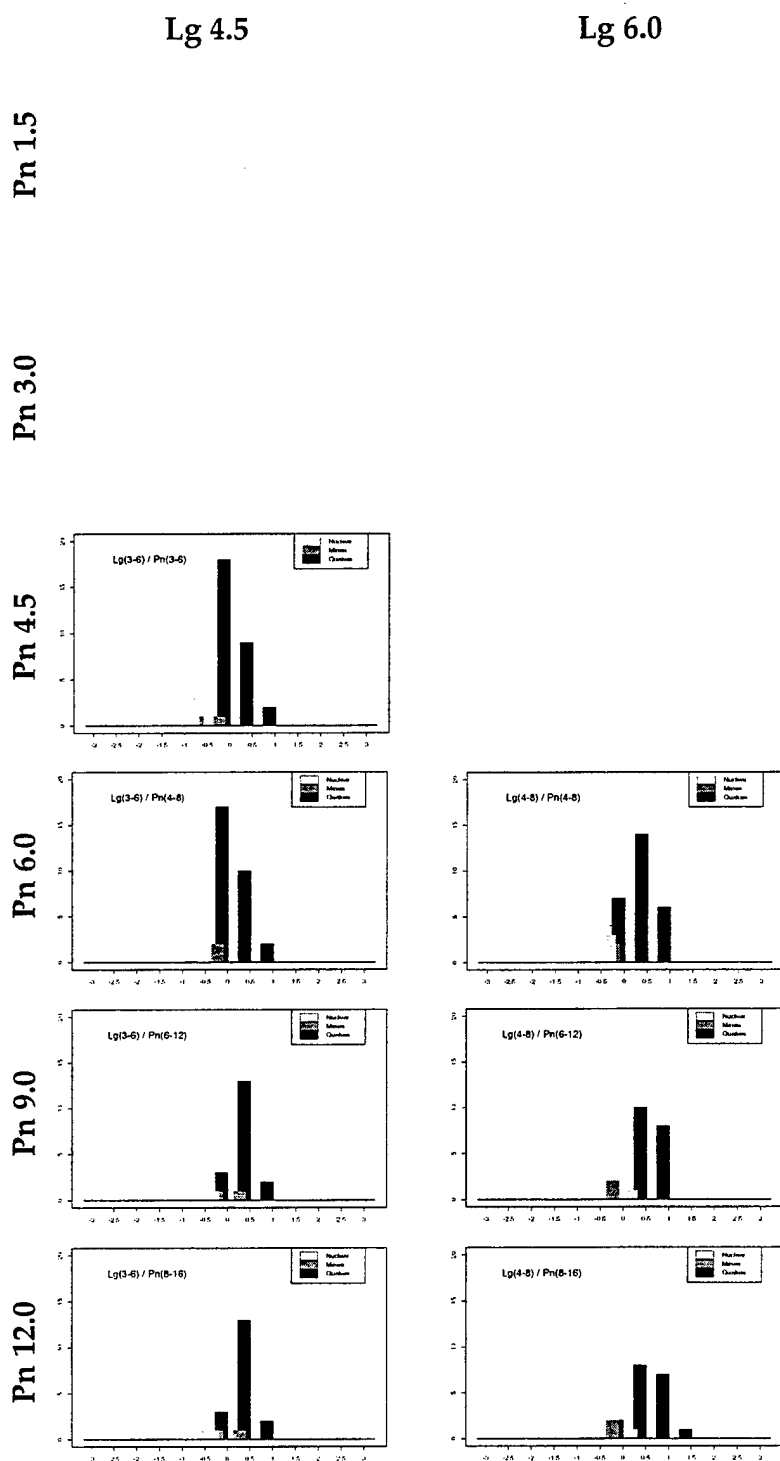
Southern Asia *Lg/Pn* Ratios

Lg 4.5   **Lg 6.0**
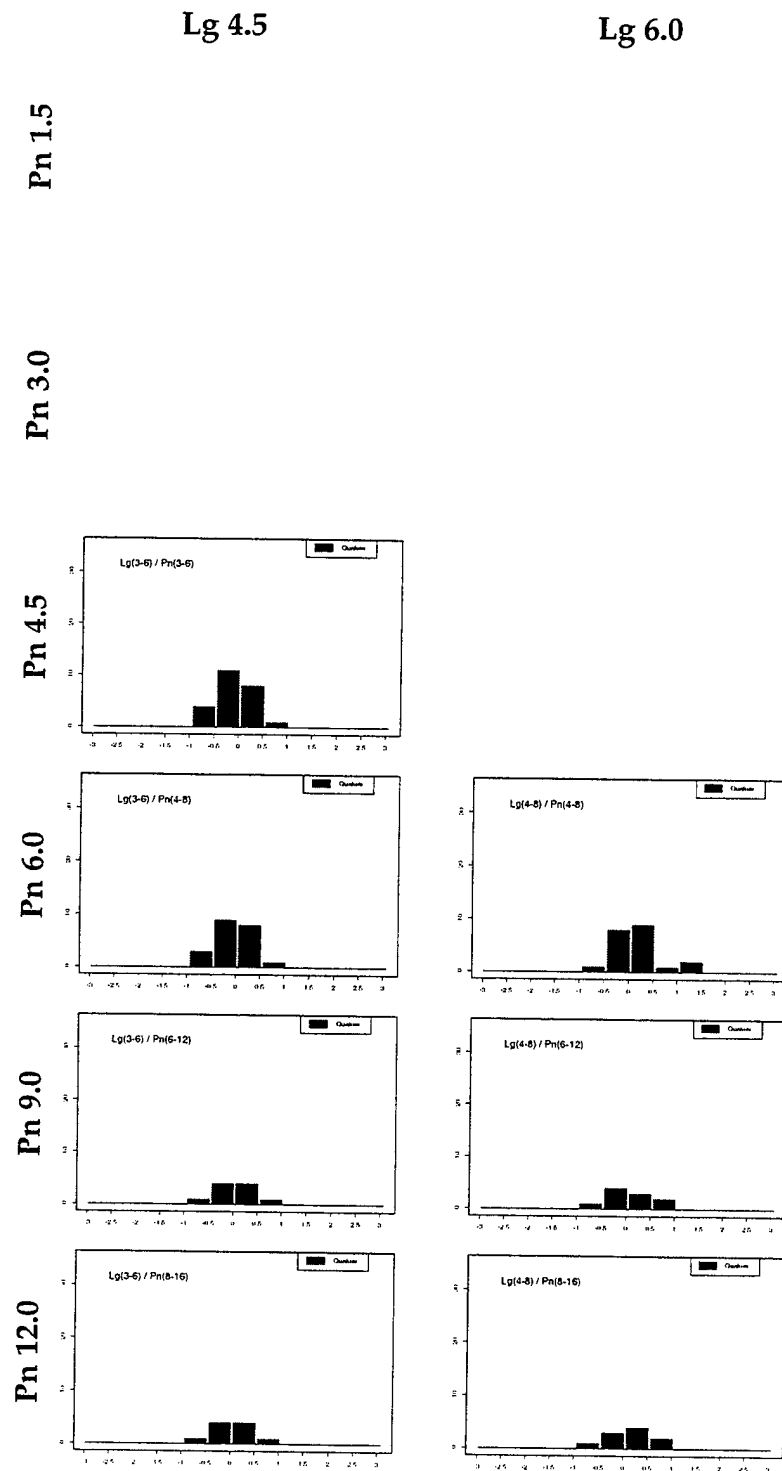
Figure C.5.3 Continued.

Southern Asia Largest *S* / Earliest *P* Ratios
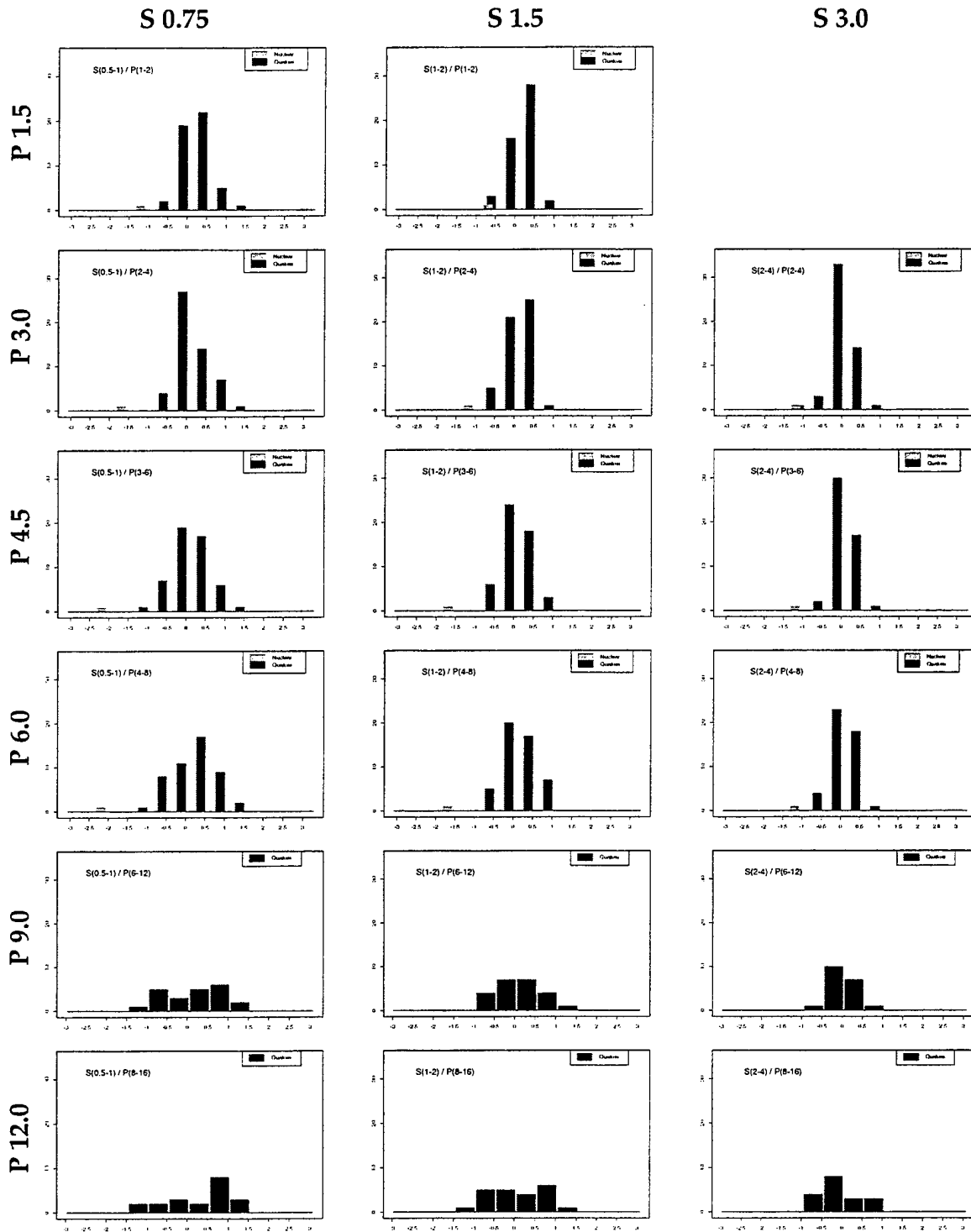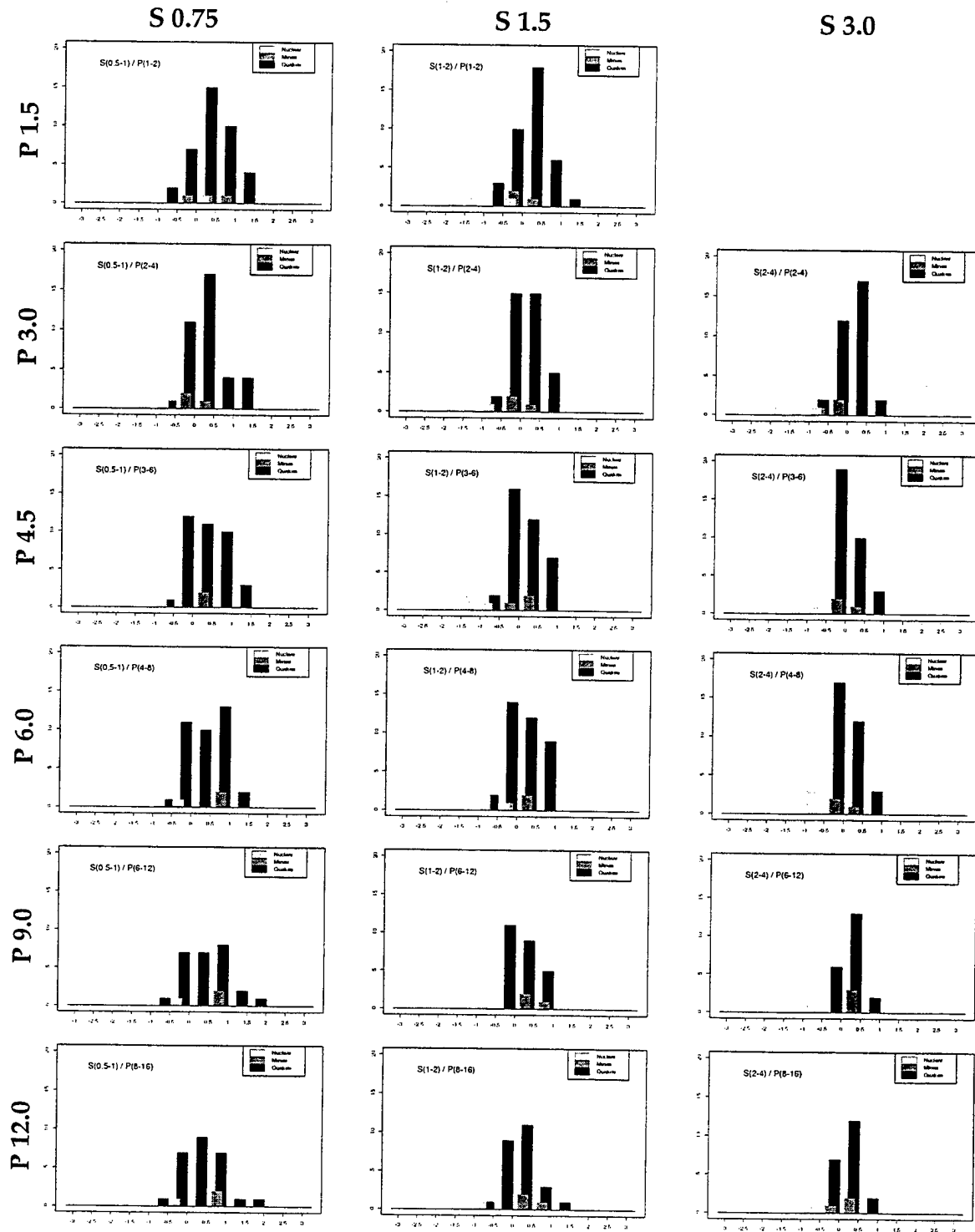

Figure C.5.4 Comparison of normalized largest *S* / earliest *P* amplitude ratios for earthquake and explosion populations found in Southern Asia.
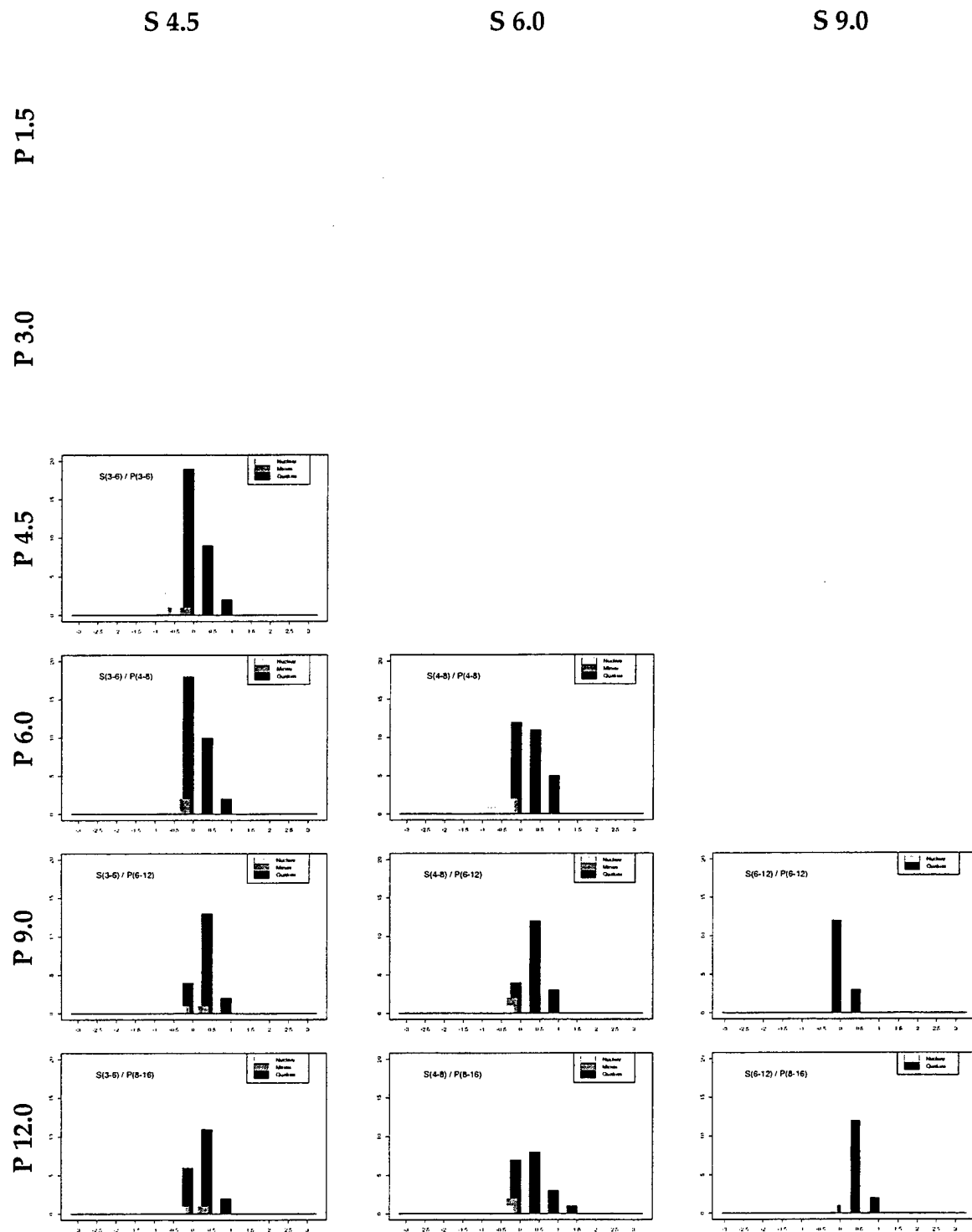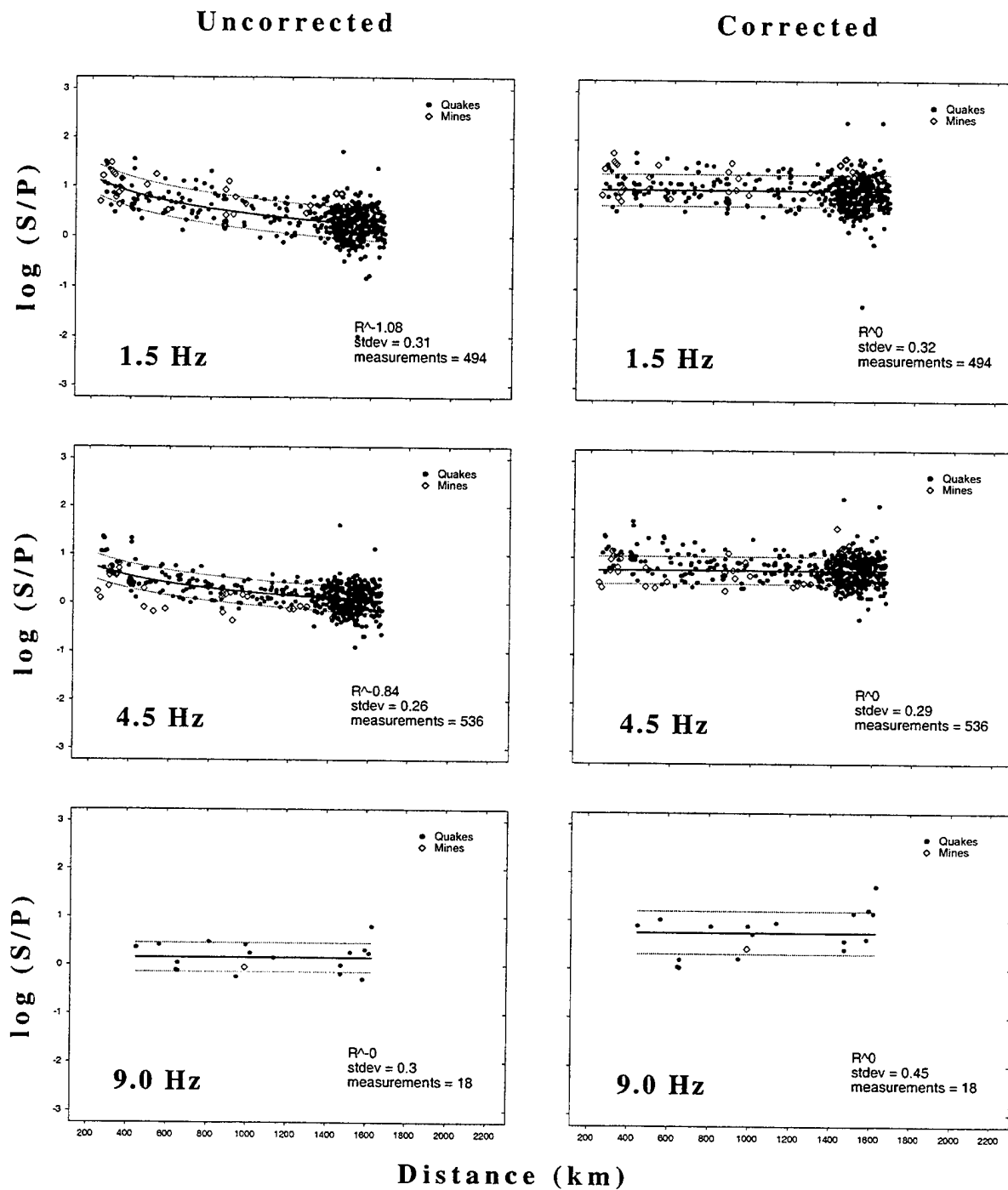
Southern Asia Largest *S* / Earliest *P* Ratios

<div align="center">S 4.5   S 6.0   S 9.0</div>

P 1.5

P 3.0

P 4.5

P 6.0

P 9.0

P 12.0
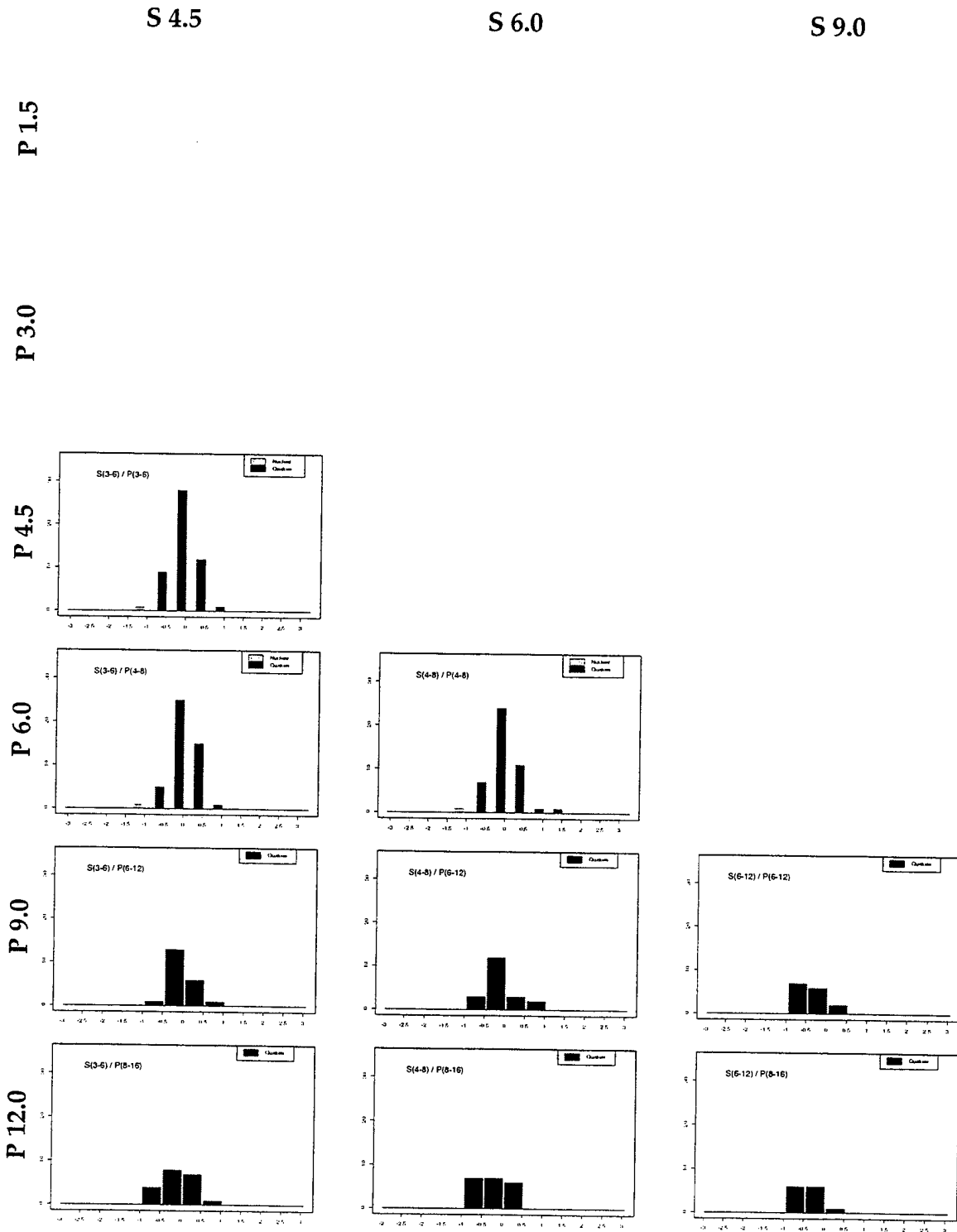
Figure C.5.4 Continued.

C.6. Central Asia

C.6.1 Validation

Uncorrected   **Corrected**

Figure C.6.1 Uncorrected and distance-corrected S/P ratio plots of measurements made in 1-2, 3-6, and 6-12 Hz (referred to as 1.5, 4.5, and 9.0 Hz) frequency bands for central Asia.
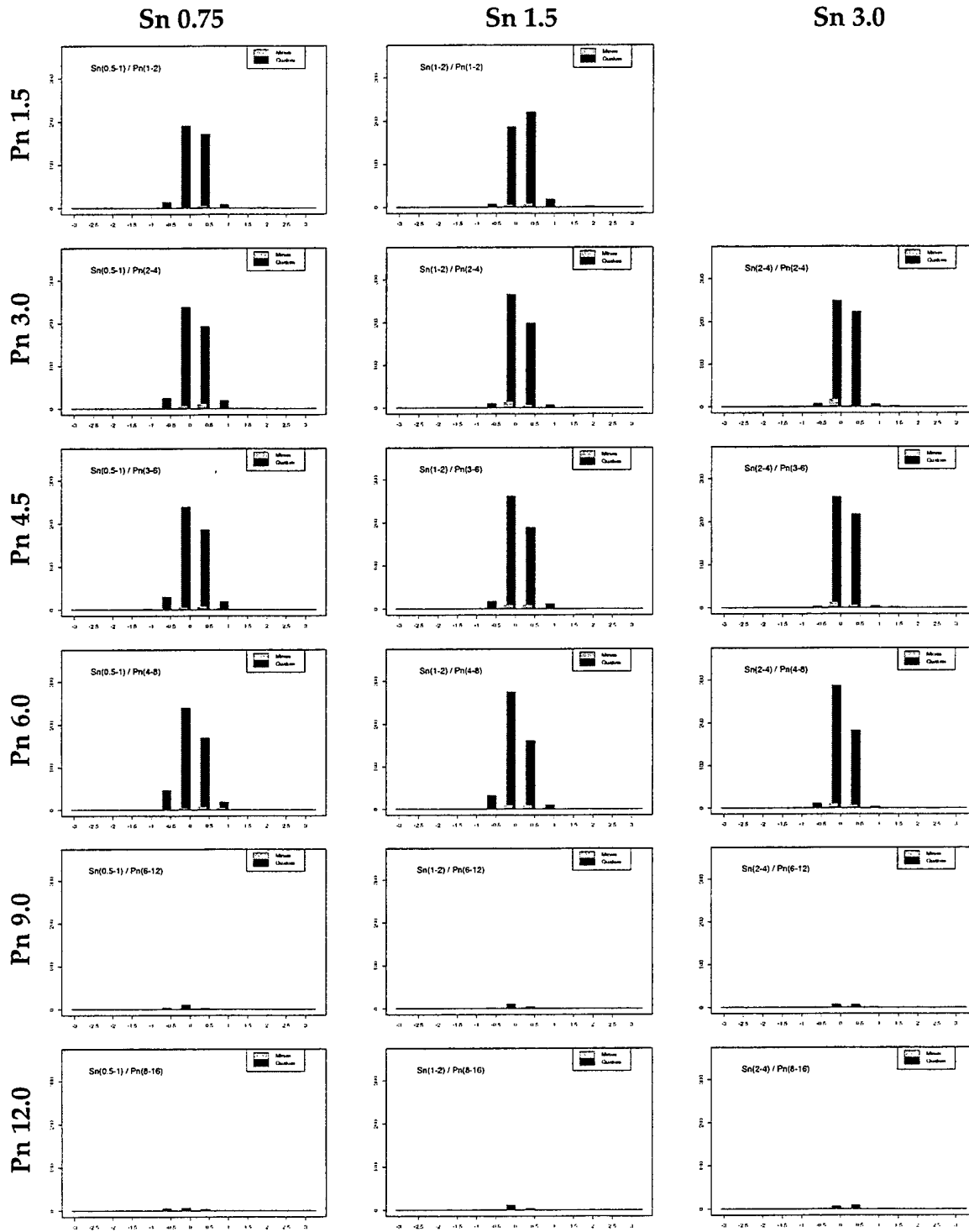
C.6.2 *S/P* Ratios

Central Asia *Sn/Pn* Ratios
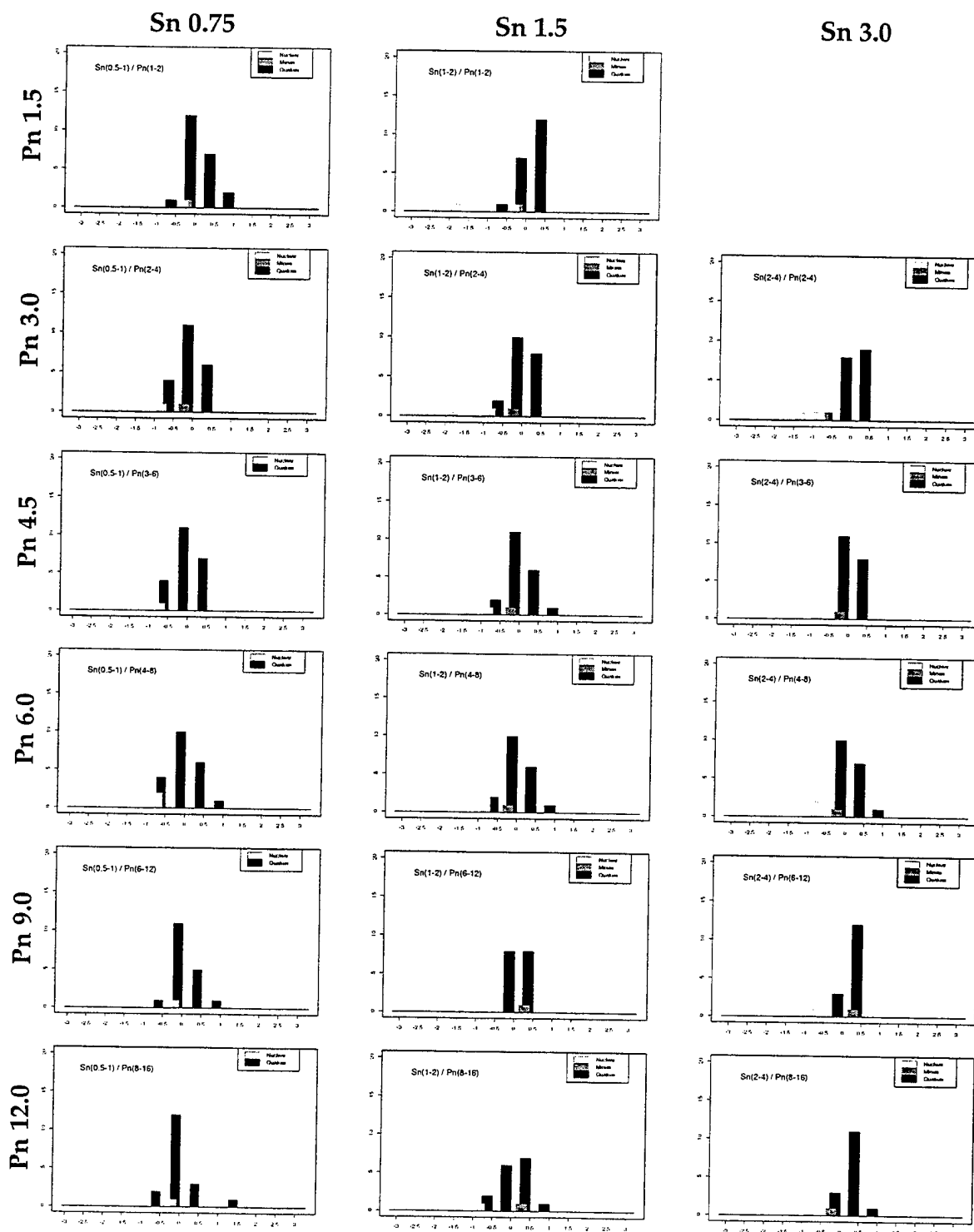
Figure C.6.2 Comparison of normalized *Sn/Pn* amplitude ratios for earthquake and explosion populations found in central Asia.

Central Asia *Sn/Pn* Ratios

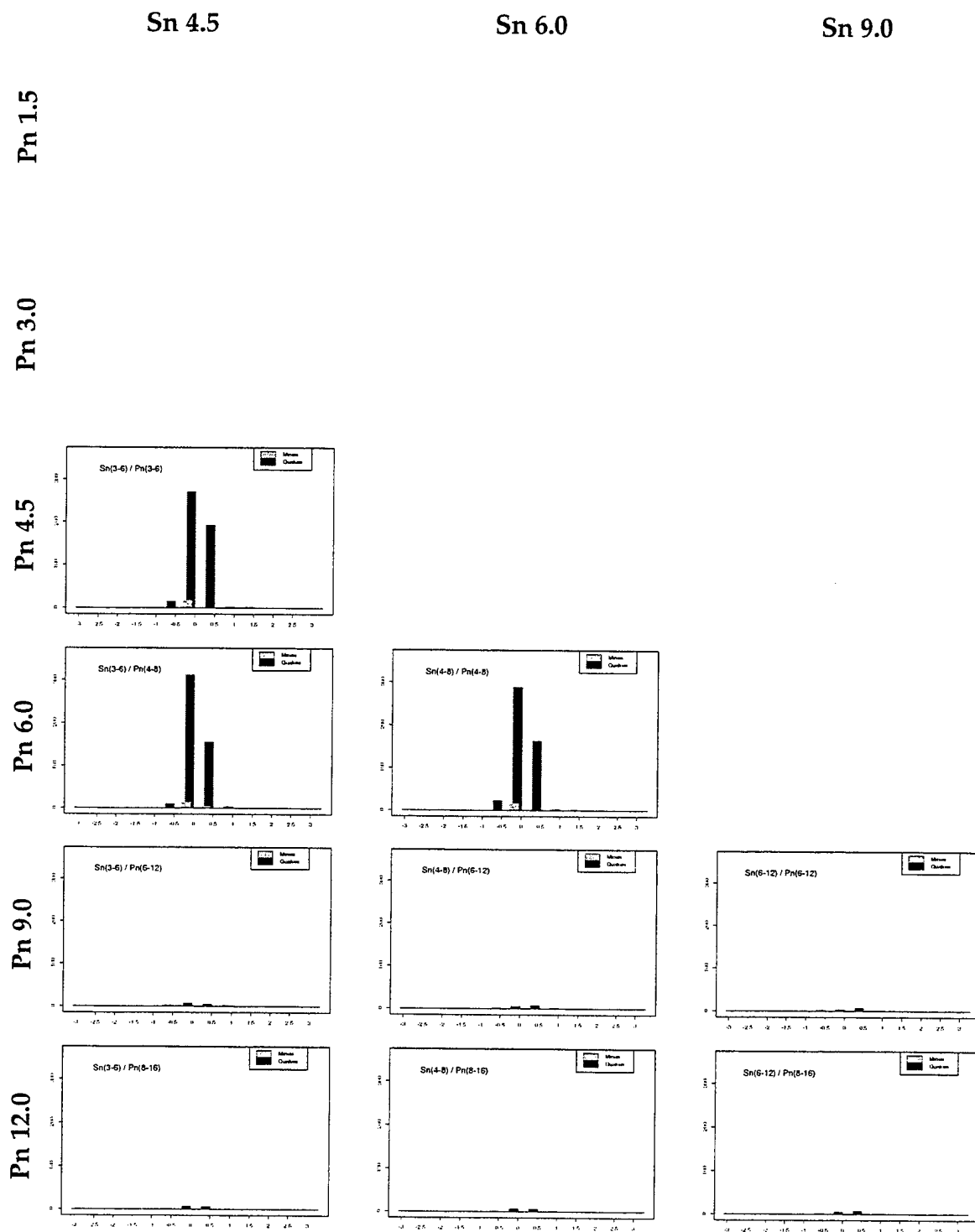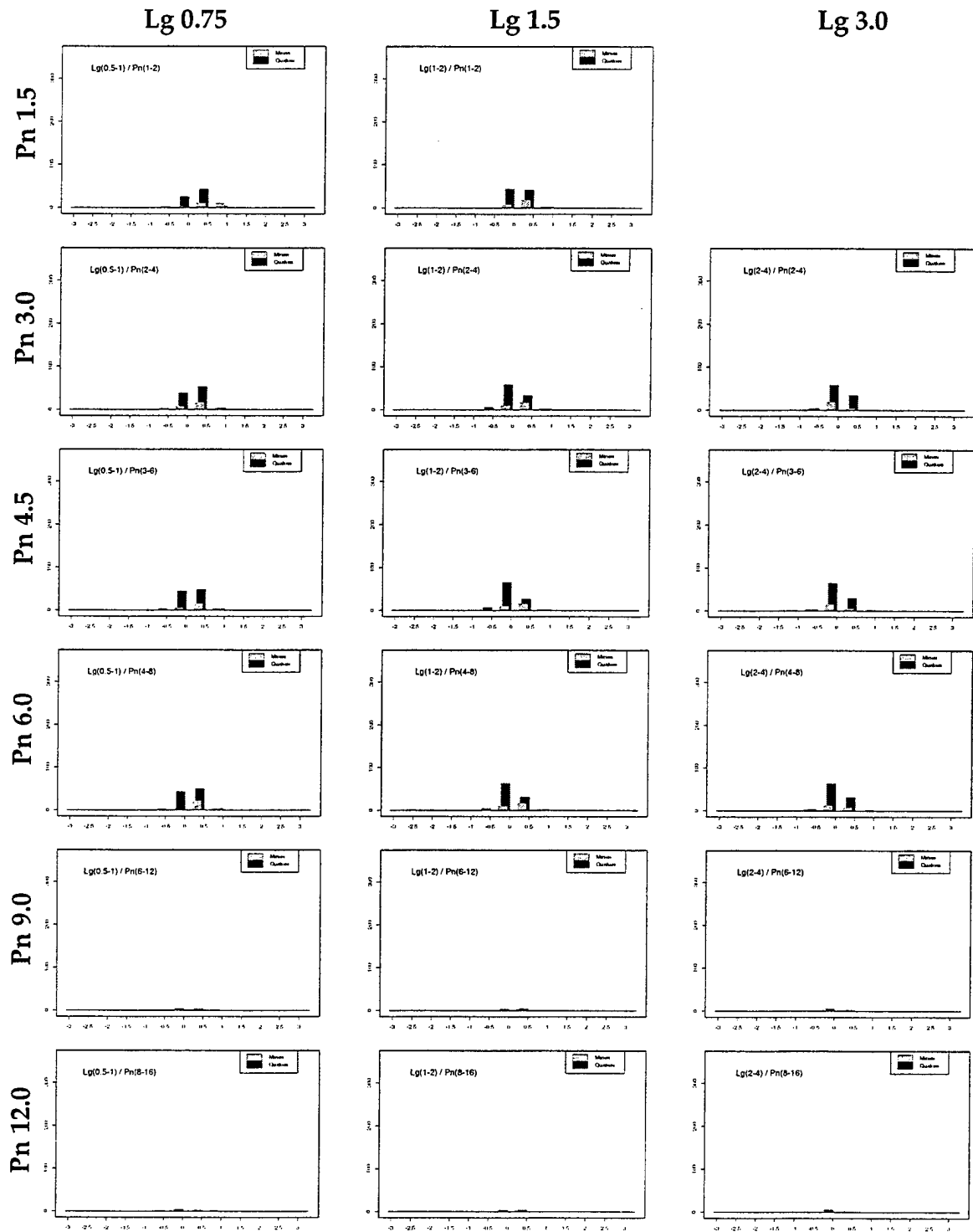Sn 4.5   Sn 6.0   Sn 9.0

Figure C.6.2 Continued.

Central Asia *Lg/Pn* Ratios

Figure C.6.3 Comparison of normalized *Lg/Pn* amplitude ratios for earthquake and explosion populations found in central Asia.

Central Asia *Lg/Pn* Ratios

Lg 4.5   Lg 6.0

Pn 1.5

Pn 3.0

Pn 4.5

Pn 6.0

Pn 9.0
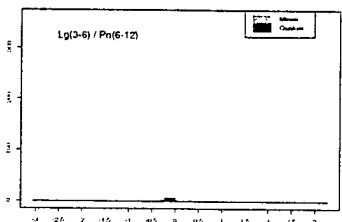
Pn 12.0

Figure C.6.3 Continued.

Central Asia Largest *S* / Earliest *P* Ratios

Figure C.6.4 Comparison of normalized largest *S* / earliest *P* amplitude ratios for earthquake and explosion populations found in central Asia.

160

Central Asia Largest *S* / Earliest *P* Ratios

S 4.5   S 6.0   S 9.0

P 1.5

P 3.0

P 4.5

S(3-6) / P(3-6)

P 6.0

S(3-6) / P(4-8)   S(4-8) / P(4-8)

P 9.0

S(3-6) / P(6-12)   S(4-8) / P(6-12)   S(6-12) / P(6-12)

P 12.0

S(3-6) / P(8-16)   S(4-8) / P(8-16)   S(6-12) / P(8-16)

Figure C.6.4 Continued.

161

C.7. Australia

C.7.1 Validation

Uncorrected   **Corrected**

Figure C.7.1 Uncorrected and distance-corrected S/P ratio plots of measurements made in 1-2, 3-6, and 6-12 Hz (referred to as 1.5, 4.5, and 9.0 Hz) frequency bands for Australia.

C.7.2 S/P Ratios

Australia *Sn/Pn* Ratios

Figure C.7.2 Comparison of normalized *Sn/Pn* amplitude ratios for earthquake and explosion populations found in Australia. See text for discussion.

Australia *Sn/Pn* Ratios

Sn 4.5   Sn 6.0   Sn 9.0

Figure C.7.2 Continued.

Australia *Lg/Pn* Ratios

Figure C.7.3 Comparison of normalized *Lg/Pn* amplitude ratios for earthquake and explosion populations found in Australia.

Australia *Lg/Pn* Ratios

Lg 4.5   **Lg 6.0**

Pn 1.5

Pn 3.0

Pn 4.5

Lg(3-6) / Pn(3-6)

Pn 6.0

Lg(3-6) / Pn(4-8)

Lg(4-8) / Pn(4-8)

Pn 9.0

Lg(3-6) / Pn(6-12)

Lg(4-8) / Pn(6-12)

Pn 12.0

Lg(3-6) / Pn(8-16)

Lg(4-8) / Pn(8-16)
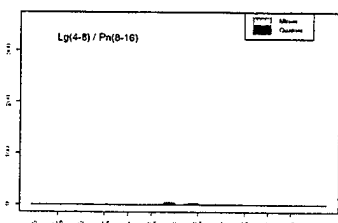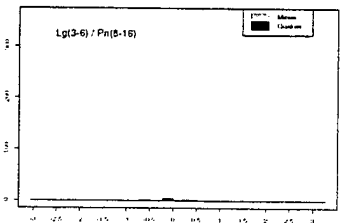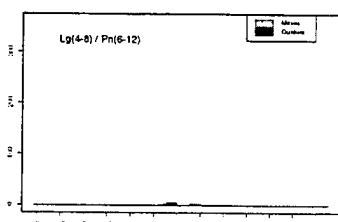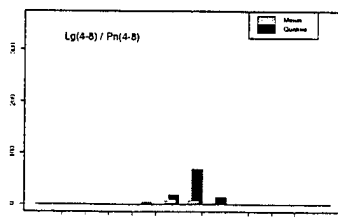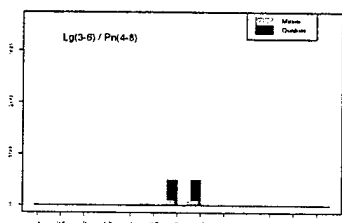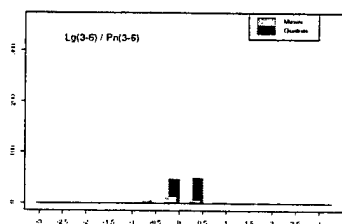
Figure C.7.3 Continued.

Australia Largest *S* / Earliest *P* Ratios
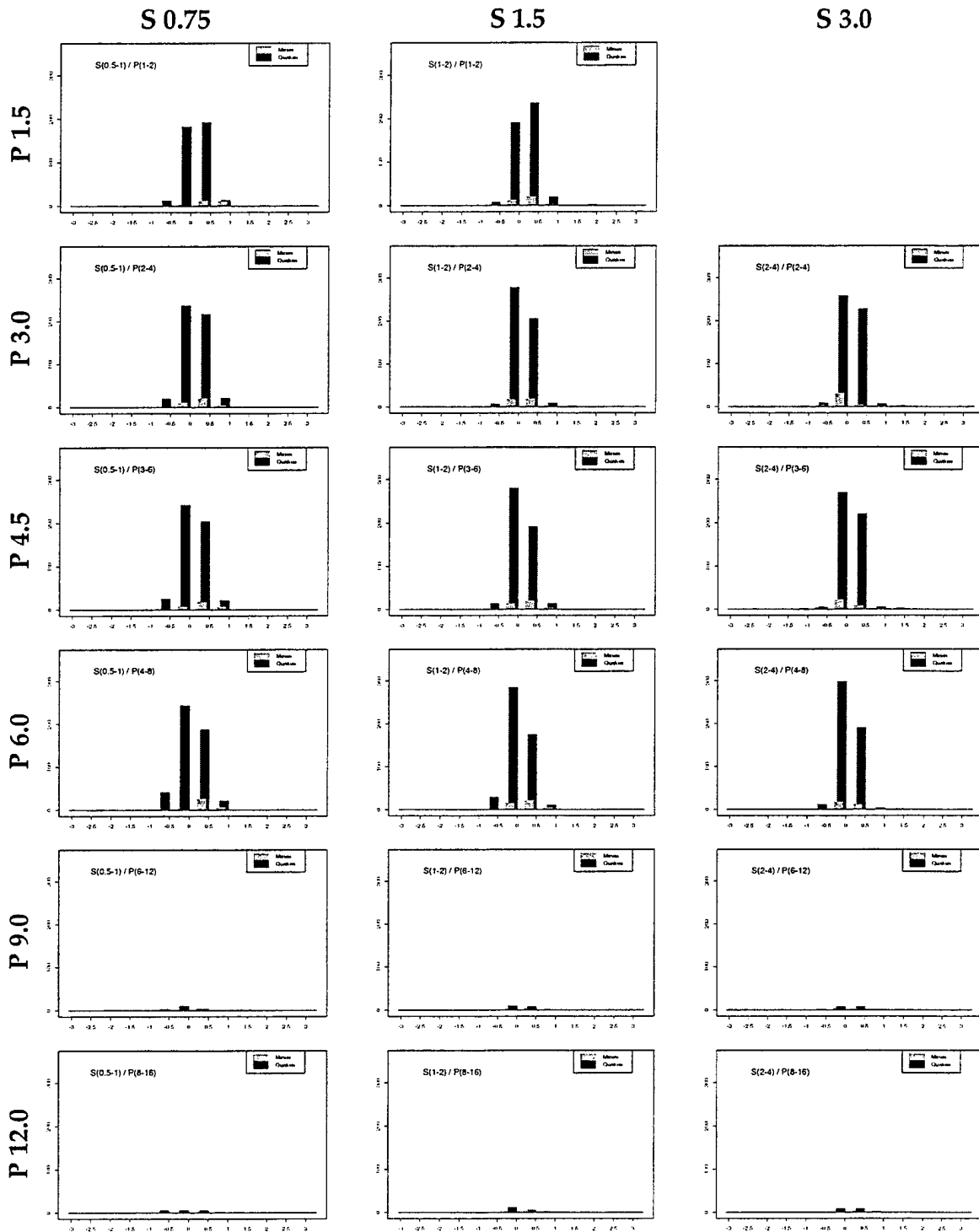
Figure C.7.4 Comparison of normalized largest *S* / earliest *P* amplitude ratios for earthquake and explosion populations found in Australia.

Australia Largest *S* / Earliest *P* Ratios

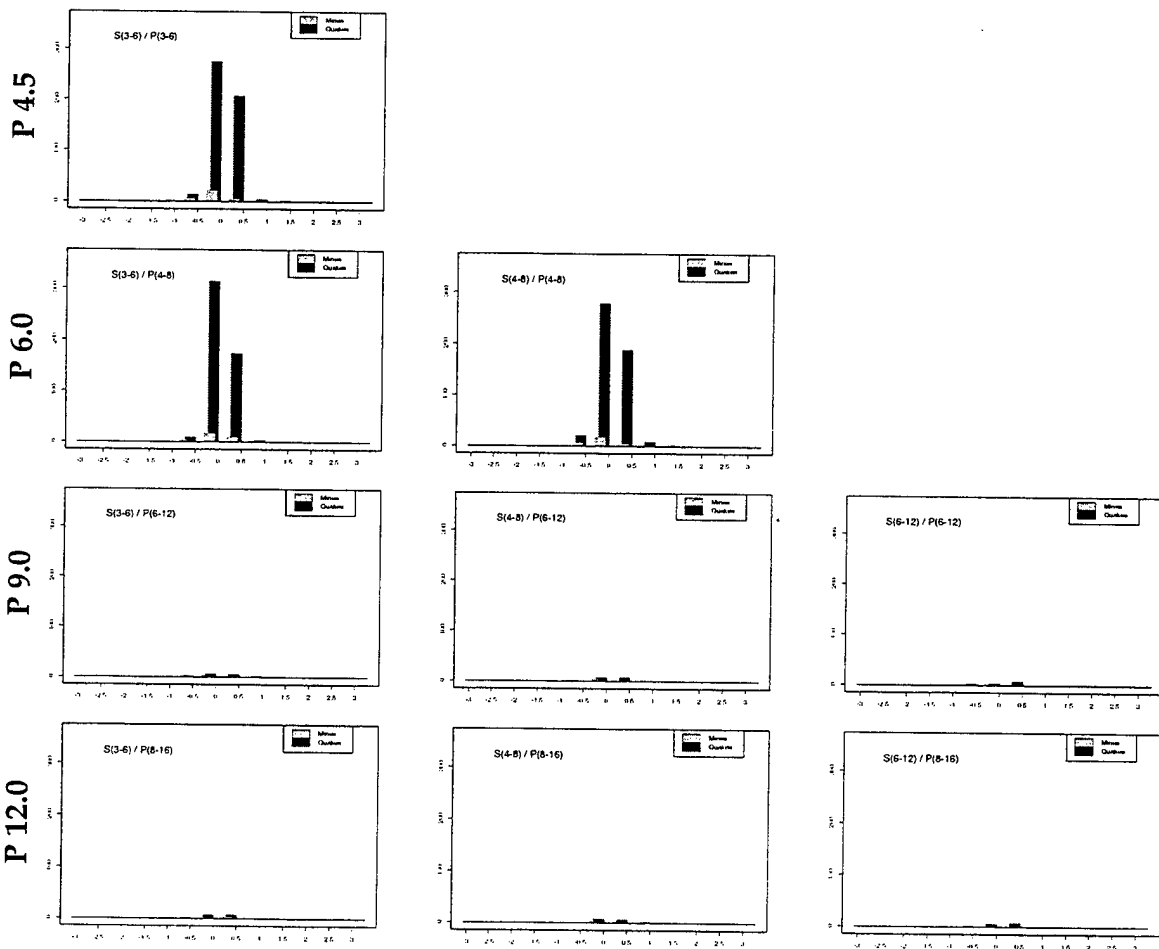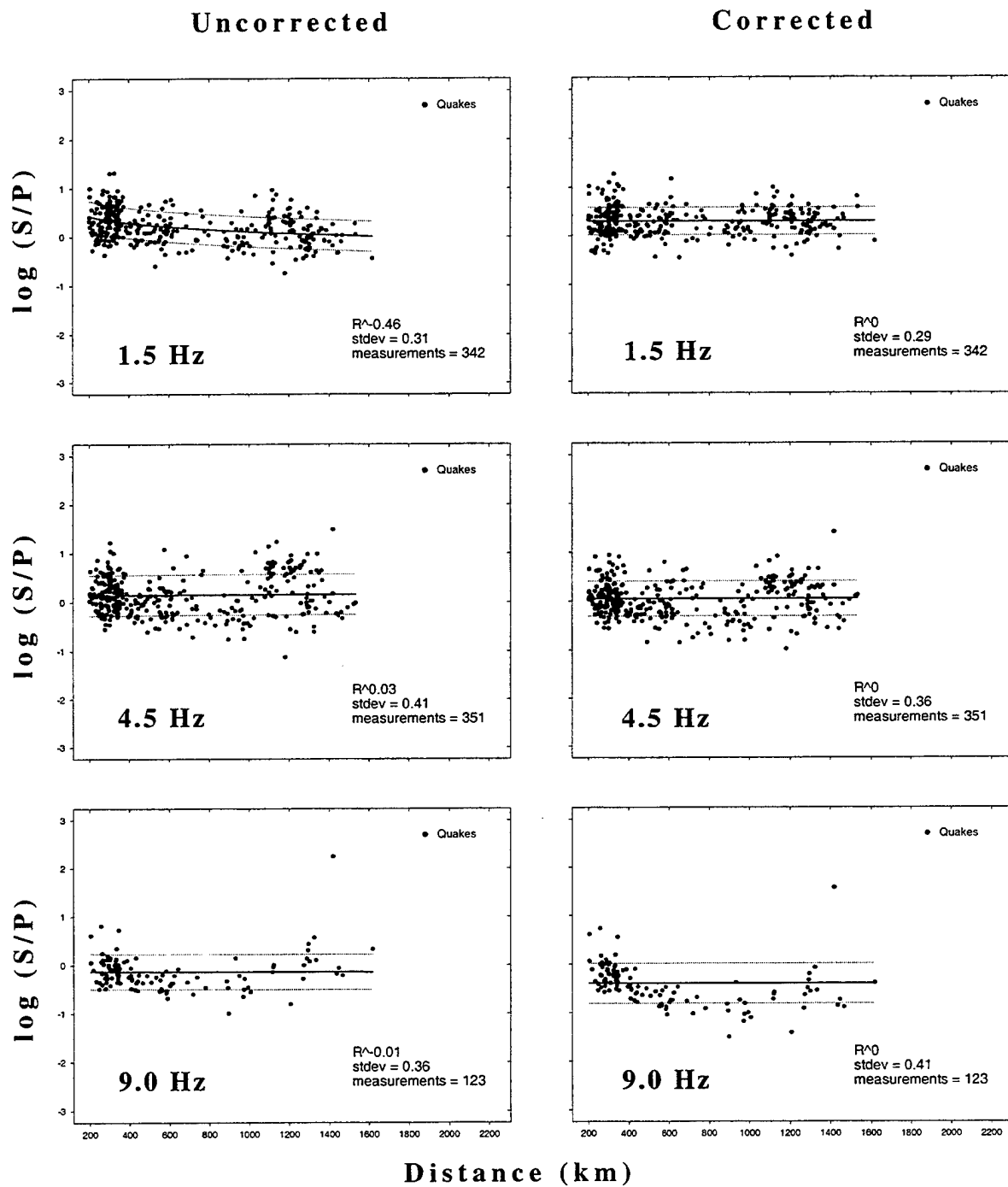S 4.5   S 6.0   S 9.0

P 1.5

P 3.0

P 4.5

P 6.0

P 9.0

P 12.0

Figure C.7.4 Continued.

C.8. Japan

C.8.1 Validation

Uncorrected   **Corrected**

Figure C.8.1 Uncorrected and distance-corrected S/P ratio plots of measurements made in 1-2, 3-6, and 6-12 Hz (referred to as 1.5, 4.5, and 9.0 Hz) frequency bands for Japan.
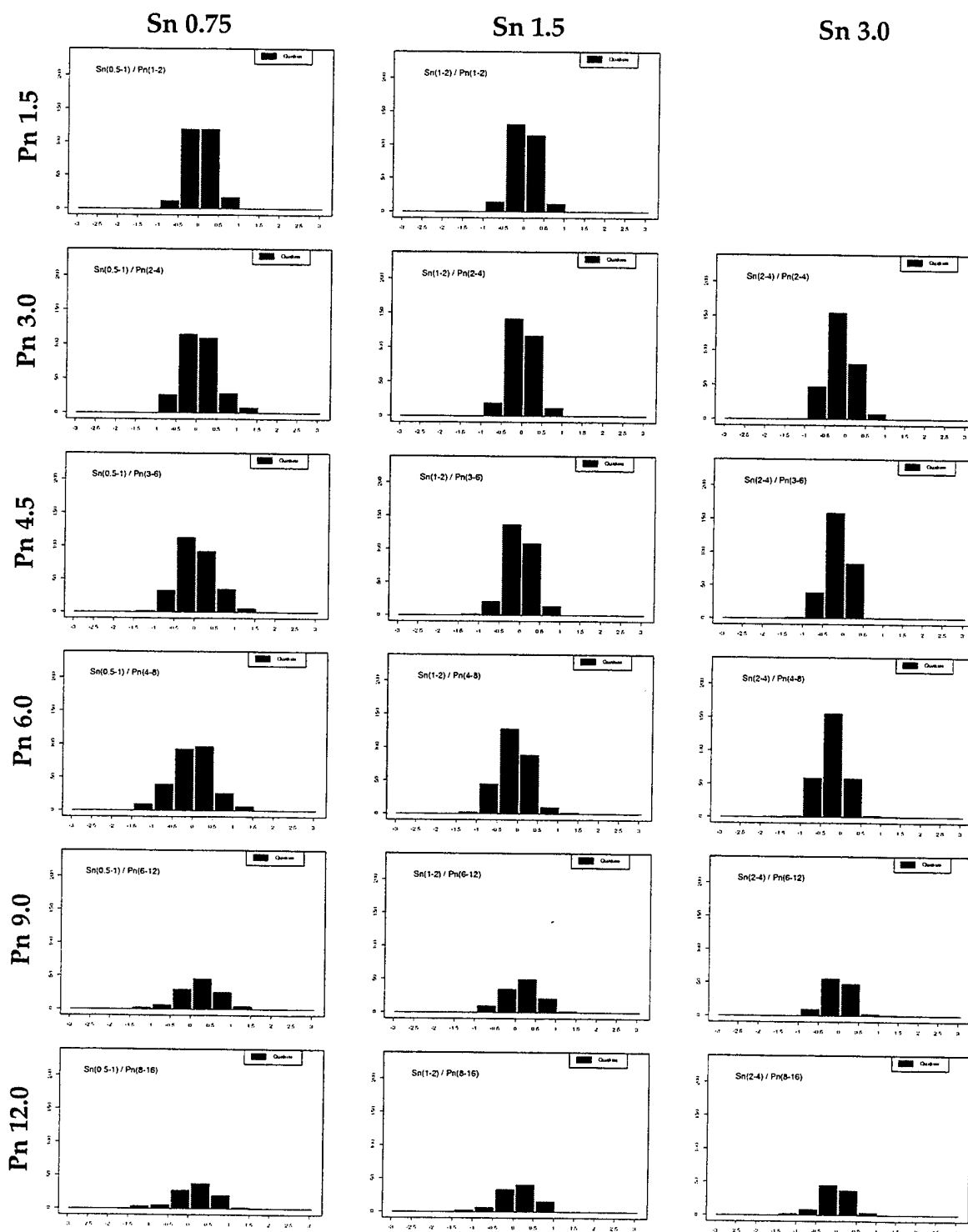
C.8.2 *S/P* Ratios

Japan *Sn/Pn* Ratios

Figure C.8.2 Comparison of normalized *Sn/Pn* amplitude ratios for earthquake population found in Japan.
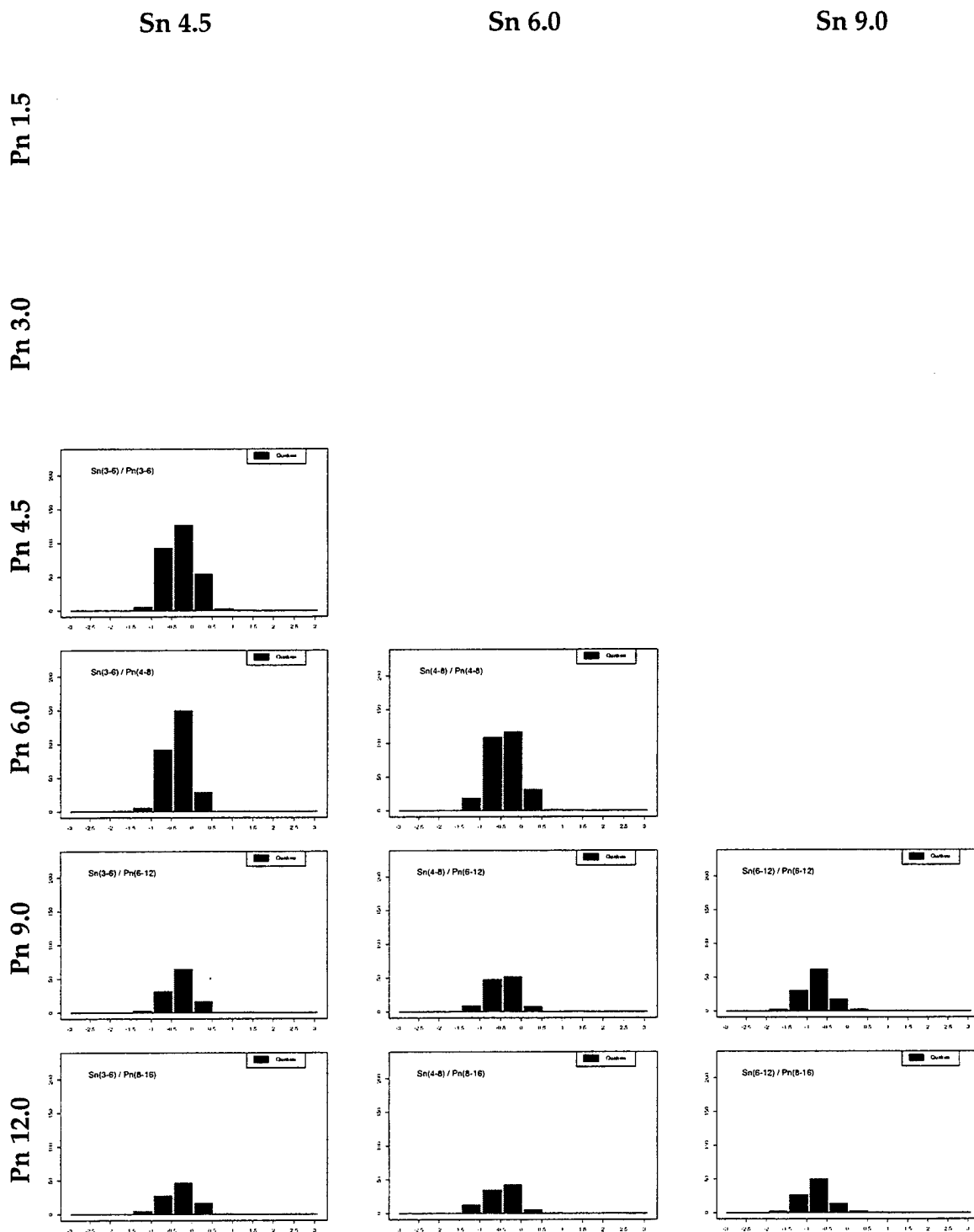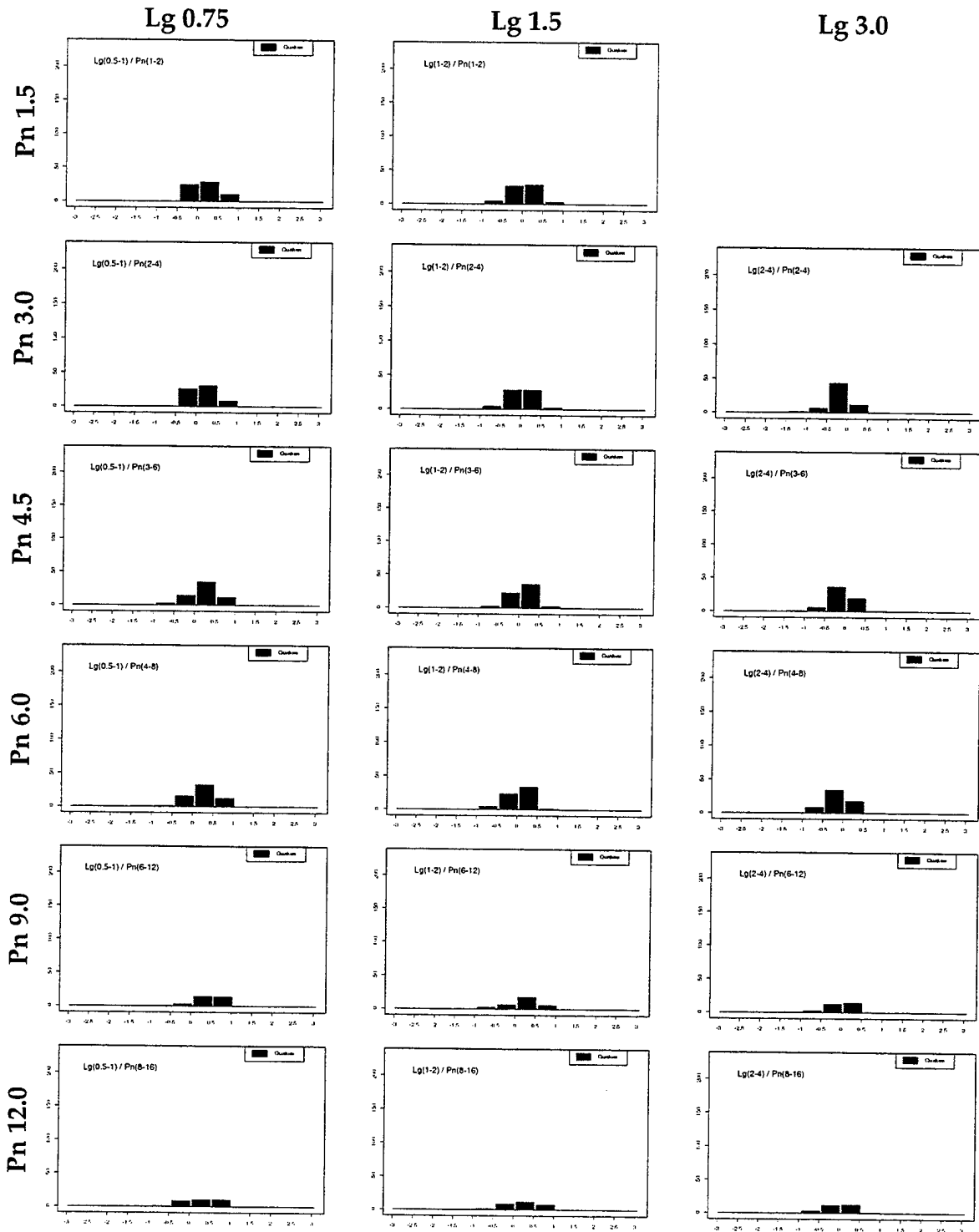
Japan *Sn/Pn* Ratios

Sn 4.5   Sn 6.0   Sn 9.0
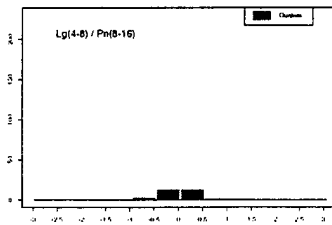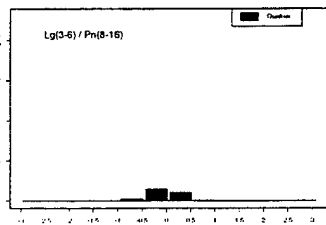
Pn 1.5

Pn 3.0

Pn 4.5

Pn 6.0

Pn 9.0

Pn 12.0

Figure C.8.2 Continued.

Japan *Lg*/*Pn* Ratios

Figure C.8.3 Comparison of normalized *Lg*/*Pn* amplitude ratios for earthquake population found in Japan.

Japan *Lg/Pn* Ratios

Lg 4.5   **Lg 6.0**

Pn 1.5

Pn 3.0

Pn 4.5

Pn 6.0

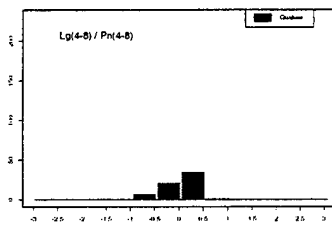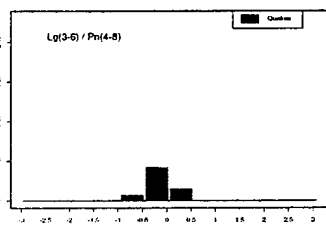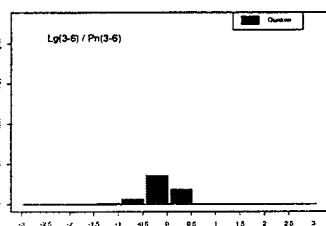**Pn 9.0**

Pn 12.0
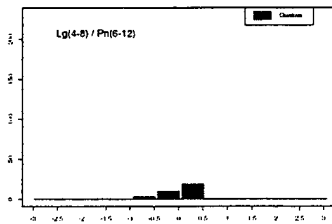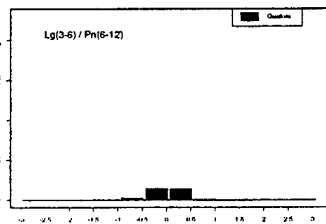
Figure C.8.3 Continued.

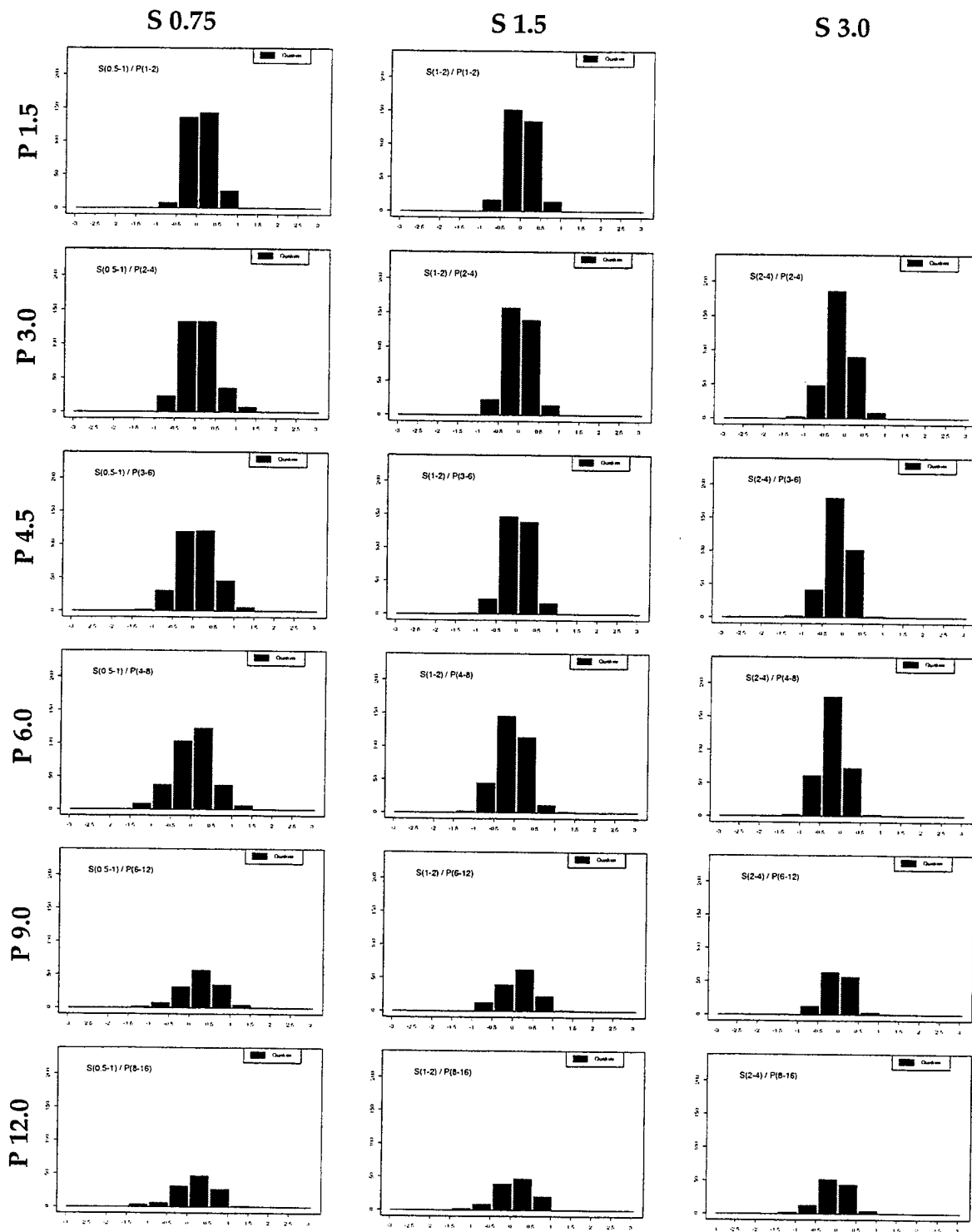173

Japan Largest *S* / Earliest *P* Ratios

Figure C.8.4 Comparison of normalized largest *S* / earliest *P* amplitude ratios for earthquake population found in Japan.

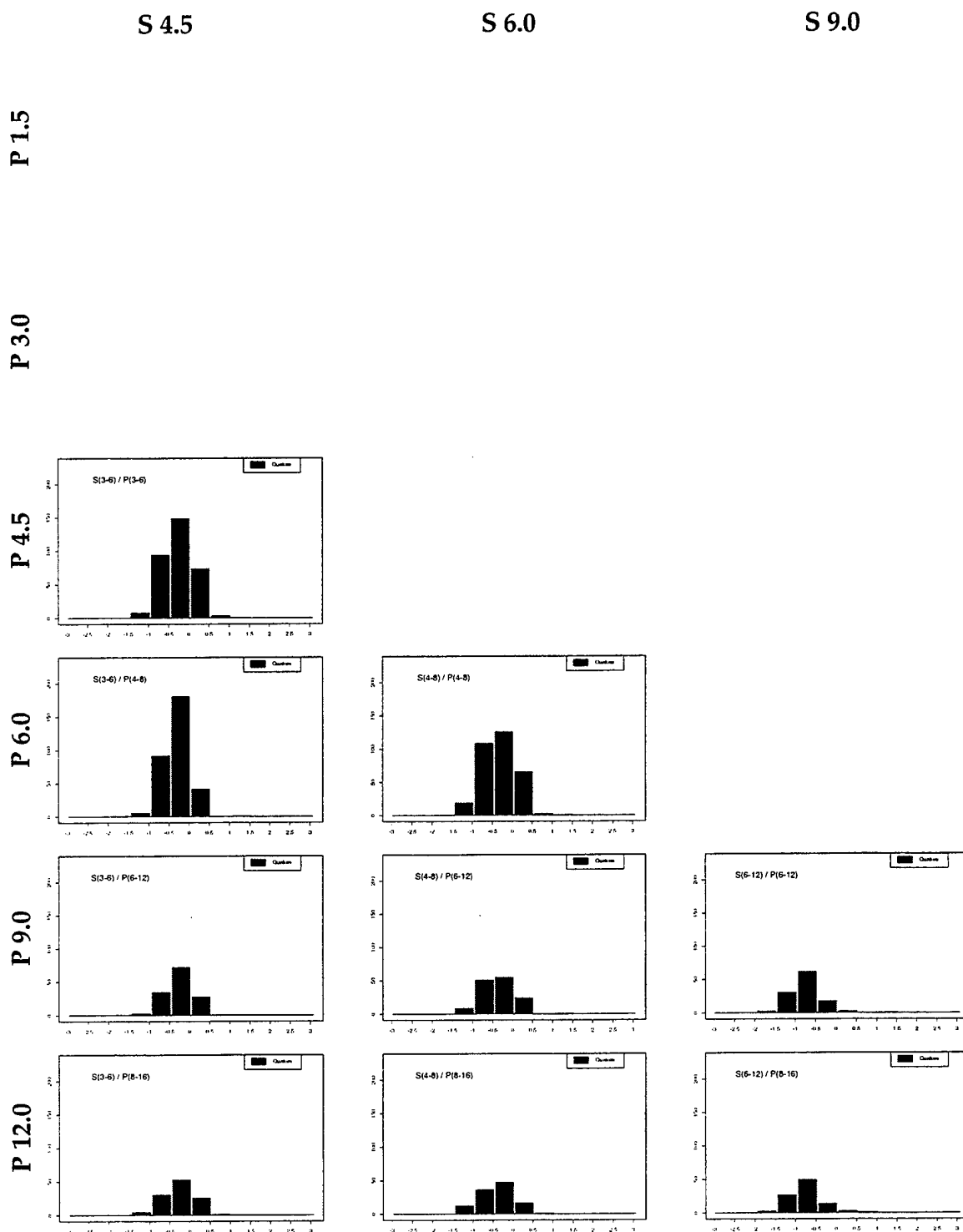# Japan Largest *S* / Earliest *P* Ratios

Figure C.8.4 Continued.

THOMAS AHRENS
SEISMOLOGICAL LABORATORY 252-21
CALIFORNIA INST. OF TECHNOLOGY
PASADENA, CA 91125

AIR FORCE RESEARCH LABORATORY
ATTN: VSOP
29 RANDOLPH ROAD
HANSCOM AFB, MA 01731-3010   (2 COPIES)

AIR FORCE RESEARCH LABORATORY
ATTN: RESEARCH LIBRARY/TL
5 WRIGHT STREET
HANSCOM AFB, MA 01731-3004

AIR FORCE RESEARCH LABORATORY
ATTN: AFRL/SUL
3550 ABERDEEN AVE SE
KIRTLAND AFB, NM 87117-5776 (2 COPIES)

RALPH ALEWINE
NTPO
1901 N. MOORE STREET, SUITE 609
ARLINGTON, VA 22209

G. ELI BAKER
MAXWELL TECHNOLOGIES
8888 BALBOA AVE.
SAN DIEGO, CA 92123-1506

MUAWIA BARAZANGI
INSTOC
3126 SNEE HALL
CORNELL UNIVERSITY
ITHACA, NY 14853

DOUGLAS BAUMGARDT
ENSCO INC.
5400 PORT ROYAL ROAD
SPRINGFIELD, VA 22151

THERON J. BENNETT
MAXWELL TECHNOLOGIES
11800 SUNRISE VALLEY
SUITE 1212
RESTON, VA 22091

WILLIAM BENSON
NAS/COS
ROOM HA372
2001 WISCONSIN AVE. NW
WASHINGTON DC 20007

JONATHAN BERGER
UNIV. OF CALIFORNIA, SAN DIEGO
SCRIPPS INST. OF OCEANOGRAPHY IGPP, 0225
9500 GILMAN DRIVE
LA JOLLA, CA 92093-0225

ROBERT BLANDFORD
AFTAC
1300 N. 17TH STREET
SUITE 1450
ARLINGTON, VA 22209-2308

LESLIE A. CASEY
DEPT. OF ENERGY/NN-20
1000 INDEPENDENCE AVE. SW
WASHINGTON DC 20585-0420

CENTER FOR MONITORING RESEARCH
ATTN: LIBRARIAN
1300 N. 17th STREET, SUITE 1450
ARLINGTON, VA 22209

FRANCESCA CHAVEZ
LOS ALAMOS NATIONAL LAB
P.O. BOX 1663, MS-D460
LOS ALAMOS, NM 87545   (5 COPIES)

ANTON DAINTY
DTRA/PMA
45045 AVIATION DRIVE
DULLESVA 20166-7517

CATHERINE DE GROOT-HEDLIN
UNIV. OF CALIFORNIA, SAN DIEGO
IGPP
8604 LA JOLLA SHORES DRIVE
SAN DIEGO, CA 92093

DIANE DOSER
DEPT. OF GEOLOGICAL SCIENCES
THE UNIVERSITY OF TEXAS AT EL PASO
EL PASO, TX 79968

DTIC
8725 JOHN J. KINGMAN ROAD
FT BELVOIR, VA 22060-6218 (2 COPIES)

MARK D. FISK
MISSION RESEARCH CORPORATION
735 STATE STREET
P.O. DRAWER 719
SANTA BARBARA, CA 93102-0719

LORI GRANT
MULTIMAX, INC.
311C FOREST AVE. SUITE 3
PACIFIC GROVE, CA 93950

HENRY GRAY
SMU STATISTICS DEPARTMENT
P.O. BOX 750302
DALLAS, TX 75275-0302

I. N. GUPTA
MULTIMAX, INC.
1441 MCCORMICK DRIVE
LARGO, MD 20774

DAVID HARKRIDER
BOSTON COLLEGE
24 MARTHA'S PT. RD.
CONCORD, MA 01742

THOMAS HEARN
NEW MEXICO STATE UNIVERSITY
DEPARTMENT OF PHYSICS
LAS CRUCES, NM 88003

MICHAEL HEDLIN
UNIVERSITY OF CALIFORNIA, SAN DIEGO
SCRIPPS INST. OF OCEANOGRAPHY
9500 GILMAN DRIVE
LA JOLLA, CA 92093-0225

DONALD HELMBERGER
CALIFORNIA INST. OF TECHNOLOGY
DIV. OF GEOL. & PLANETARY SCIENCES
SEISMOLOGICAL LABORATORY
PASADENA, CA 91125

EUGENE HERRIN
SOUTHERN METHODIST UNIVERSITY
DEPT. OF GEOLOGICAL SCIENCES
DALLAS, TX 75275-0395

ROBERT HERRMANN
ST. LOUIS UNIVERSITY
DEPT. OF EARTH & ATMOS. SCIENCES
3507 LACLEDE AVENUE
ST. LOUIS, MO 63103

VINDELL HSU
HQ/AFTAC/TTR
1030 S. HIGHWAY A1A
PATRICK AFB, FL 32925-3002

RONG-SONG JIH
DTRA/PMA
45045 AVIATION DRIVE
DULLES, VA 20166-7517

THOMAS JORDAN
MASS. INST. OF TECHNOLOGY
BLDG 54-918
CAMBRIDGE, MA 02139

LAWRENCE LIVERMORE NAT'L LAB
ATTN: TECHNICAL STAFF (PLS ROUTE)
PO BOX 808, MS L-208
LIVERMORE, CA 94551

LAWRENCE LIVERMORE NAT'L LAB
ATTN: TECHNICAL STAFF (PLS ROUTE)
PO BOX 808, MS L-205
LIVERMORE, CA 94551

LAWRENCE LIVERMORE NAT'L LAB
ATTN: TECHNICAL STAFF (PLS ROUTE)
PO BOX 808, MS L-200
LIVERMORE, CA 94551

THORNE LAY
UNIV. OF CALIFORNIA, SANTA CRUZ
EARTH SCIENCES DEPARTMENT
EARTH & MARINE SCIENCE BUILDING
SANTA CRUZ, CA 95064

ANATOLI L. LEVSHIN
DEPARTMENT OF PHYSICS
UNIVERSITY OF COLORADO
CAMPUS BOX 390
BOULDER, CO 80309-0309

JAMES LEWKOWICZ
WESTON GEOPHYSICAL CORP.
325 WEST MAIN STREET
NORTHBORO, MA 01532

LOS ALAMOS NATIONAL LABORATORY
ATTN: TECHNICAL STAFF (PLS ROUTE)
PO BOX 1663, MS D460
LOS ALAMOS, NM 87545

LOS ALAMOS NATIONAL LABORATORY
ATTN: TECHNICAL STAFF (PLS ROUTE)
PO BOX 1663, MS F665
LOS ALAMOS, NM 87545

LOS ALAMOS NATIONAL LABORATORY
ATTN: TECHNICAL STAFF (PLS ROUTE)
PO BOX 1663, MS C335
LOS ALAMOS, NM 87545

GARY MCCARTOR
SOUTHERN METHODIST UNIVERSITY
DEPARTMENT OF PHYSICS
DALLAS, TX 75275-0395

KEITH MCLAUGHLIN
CENTER FOR MONITORING RESEARCH
SAIC
1300 N. 17TH STREET, SUITE 1450
ARLINGTON, VA 22209

BRIAN MITCHELL
DEPT OF EARTH & ATMOSPHERIC SCIENCES
ST. LOUIS UNIVERSITY
3507 LACLEDE AVENUE
ST. LOUIS, MO 63103

RICHARD MORROW
USACDA/IVI
320 21ST STREET, N.W.
WASHINGTON DC 20451

JOHN MURPHY
MAXWELL TECHNOLOGIES
11800 SUNRISE VALLEY DRIVE
SUITE 1212
RESTON, VA 22091

JAMES NI
NEW MEXICO STATE UNIVERSITY
DEPARTMENT OF PHYSICS
LAS CRUCES, NM 88003

ROBERT NORTH
CENTER FOR MONITORING RESEARCH
1300 N. 17th STREET, SUITE 1450
ARLINGTON, VA 22209

OFFICE OF THE SECRETARY OF DEFENSE
DDR&E
WASHINGTON DC 20330

JOHN ORCUTT
INST. OF GEOPH. & PLANETARY PHYSICS
UNIV. OF CALIFORNIA, SAN DIEGO
LA JOLLA, CA 92093

PACIFIC NORTHWEST NAT'L LAB
ATTN: TECHNICAL STAFF (PLS ROUTE)
PO BOX 999, MS K5-12
RICHLAND, WA 99352

FRANK PILOTTE
HQ AFTAC/TT
1030 S. HIGHWAY A1A
PATRICK AFB, FL 32925-3002

KEITH PRIESTLEY
DEPARTMENT OF EARTH SCIENCES
UNIVERSITY OF CAMBRIDGE
MADINGLEY RISE, MADINGLEY ROAD
CAMBRIDGE, CB3 OEZ UK

JAY PULLI
BBN SYSTEMS AND TECHNOLOGIES, INC.
1300 NORTH 17TH STREET
ROSSLYN, VA 22209

DELAINE REITER
WESTON GEOPHYSICAL CORP.
73 STANDISH ROAD
WATERTOWN, MA 0472

PAUL RICHARDS
COLUMBIA UNIVERSITY
LAMONT-DOHERTY EARTH OBSERV.
PALISADES, NY 10964

MICHAEL RITZWOLLER
DEPARTMENT OF PHYSICS
UNIVERSITY OF COLORADO
CAMPUS BOX 390
BOULDER, CO 80309-0309

DAVID RUSSELL
HQ AFTAC/TTR
1030 SOUTH HIGHWAY A1A
PATRICK AFB, FL 32925-3002

CHANDAN SAIKIA
WOOODWARD-CLYDE FED. SERVICES
566 EL DORADO ST., SUITE 100
PASADENA, CA 91101-2560

SANDIA NATIONAL LABORATORY
ATTN: TECHNICAL STAFF (PLS ROUTE)
DEPT. 5704
MS 0979, PO BOX 5800
ALBUQUERQUE, NM 87185-0979

SANDIA NATIONAL LABORATORY
ATTN: TECHNICAL STAFF (PLS ROUTE)
DEPT. 9311
MS 1159, PO BOX 5800
ALBUQUERQUE, NM 87185-1159

SANDIA NATIONAL LABORATORY
ATTN: TECHNICAL STAFF (PLS ROUTE)
DEPT. 5736
MS 0655, PO BOX 5800
ALBUQUERQUE, NM 87185-0655

AVI SHAPIRA
SEISMOLOGY DIVISION
IPRG
P.O.B. 2286 NOLON 58122 ISRAEL

MATTHEW SIBOL
ENSCO, INC.
445 PINEDA CT.
MELBOURNE, FL 32940

JEFFRY STEVENS
MAXWELL TECHNOLOGIES
8888 BALBOA AVE.
SAN DIEGO, CA 92123-1506

TACTEC
BATTELLE MEMORIAL INSTITUTE
505 KING AVENUE
COLUMBUS, OH 43201 (FINAL REPORT)

LAWRENCE TURNBULL
ACIS
DCI/ACIS
WASHINGTON DC 20505

FRANK VERNON
UNIV. OF CALIFORNIA, SAN DIEGO
SCRIPPS INST. OF OCEANOGRAPHY
9500 GILMAN DRIVE
LA JOLLA, CA 92093-0225

RU SHAN WU
UNIV. OF CALIFORNIA, SANTA CRUZ
EARTH SCIENCES DEPT.
1156 HIGH STREET
SANTA CRUZ, CA 95064

JAMES E. ZOLLWEG
BOISE STATE UNIVERSITY
GEOSCIENCES DEPT.
1910 UNIVERSITY DRIVE
BOISE, ID 83725

SANDIA NATIONAL LABORATORY
ATTN: TECHNICAL STAFF (PLS ROUTE)
DEPT. 5704
MS 0655, PO BOX 5800
ALBUQUERQUE, NM 87185-0655

THOMAS SERENO JR.
SAIC
10260 CAMPUS POINT DRIVE
SAN DIEGO, CA 92121

ROBERT SHUMWAY
410 MRAK HALL
DIVISION OF STATISTICS
UNIVERSITY OF CALIFORNIA
DAVIS, CA 95616-8671

DAVID SIMPSON
IRIS
1200 NEW YORK AVE., NW
SUITE 800
WASHINGTON DC 20005

BRIAN SULLIVAN
BOSTON COLLEGE
INSITUTE FOR SPACE RESEARCH
140 COMMONWEALTH AVENUE
CHESTNUT HILL, MA 02167

NAFI TOKSOZ
EARTH RESOURCES LABORATORY
M.I.T.
42 CARLTON STREET, E34-440
CAMBRIDGE, MA 02142

GREG VAN DER VINK
IRIS
1200 NEW YORK AVE., NW
SUITE 800
WASHINGTON DC 20005

TERRY WALLACE
UNIVERSITY OF ARIZONA
DEPARTMENT OF GEOSCIENCES
BUILDING #77
TUCSON, AZ 85721

JIAKANG XIE
COLUMBIA UNIVERSITY
LAMONT DOHERTY EARTH OBSERV.
ROUTE 9W
PALISADES, NY 10964

180